

NOTE TO USERS

This reproduction is the best copy available.

UMI[®]

Creep-Fatigue Interaction in Aircraft Gas Turbine Components by Simulation and Testing at Scaled Temperatures

Mohammad Hossein Sabour

A Thesis

in

The Department

Of

Mechanical and Industrial Engineering

Presented in Partial Fulfillment of the Requirements
for the Degree of Doctor of Philosophy at
Concordia University
Montreal, Quebec, Canada

February 2005

© Mohammad H. Sabour



Library and
Archives Canada

Bibliothèque et
Archives Canada

Published Heritage
Branch

Direction du
Patrimoine de l'édition

395 Wellington Street
Ottawa ON K1A 0N4
Canada

395, rue Wellington
Ottawa ON K1A 0N4
Canada

Your file *Votre référence*

ISBN: 0-494-04063-7

Our file *Notre référence*

ISBN: 0-494-04063-7

NOTICE:

The author has granted a non-exclusive license allowing Library and Archives Canada to reproduce, publish, archive, preserve, conserve, communicate to the public by telecommunication or on the Internet, loan, distribute and sell theses worldwide, for commercial or non-commercial purposes, in microform, paper, electronic and/or any other formats.

The author retains copyright ownership and moral rights in this thesis. Neither the thesis nor substantial extracts from it may be printed or otherwise reproduced without the author's permission.

AVIS:

L'auteur a accordé une licence non exclusive permettant à la Bibliothèque et Archives Canada de reproduire, publier, archiver, sauvegarder, conserver, transmettre au public par télécommunication ou par l'Internet, prêter, distribuer et vendre des thèses partout dans le monde, à des fins commerciales ou autres, sur support microforme, papier, électronique et/ou autres formats.

L'auteur conserve la propriété du droit d'auteur et des droits moraux qui protègent cette thèse. Ni la thèse ni des extraits substantiels de celle-ci ne doivent être imprimés ou autrement reproduits sans son autorisation.

In compliance with the Canadian Privacy Act some supporting forms may have been removed from this thesis.

Conformément à la loi canadienne sur la protection de la vie privée, quelques formulaires secondaires ont été enlevés de cette thèse.

While these forms may be included in the document page count, their removal does not represent any loss of content from the thesis.

Bien que ces formulaires aient inclus dans la pagination, il n'y aura aucun contenu manquant.


Canada

ABSTRACT

Creep-Fatigue Interaction in Aircraft Gas Turbine Components by Simulation and Testing at Scaled Temperatures

Mohammad Hossein Sabour, Ph.D.

Concordia University, 2005

Advanced gas turbine engines which use hot section airfoil cooling, present a wide range of design problems. The frequencies of applied loads and the natural frequencies of the blade also are important since they have significant effects on failure of the component due to fatigue phenomenon. Due to high temperature environment the thermal creep and fatigue are quite severe. One-dimensional creep model, using ANSYS has been formulated in order to predict the creep life of a gas turbine engine blade. Innovative mathematical models for the prediction of the operating life of aircraft components, specifically gas turbine blades, which are subjected to creep-fatigue at high temperatures, are proposed. The components are modeled by FEM, mathematically, and using similitude principles. Three models have been suggested and evaluated numerically and experimentally. Using FEM method for natural frequencies causes phenomena such as curve veering which is studied in more detail.

The simulation studies on the life-limiting modes of failure, as well as estimating the expected lifetime of the blade, using the proposed models have been carried out. Although the scale model approach has been used for quite some time, the thermal scaling has been used in this study for the first time. The only thermal studies in literature

using scaling for structures is by NASA in which materials of both the prototype and the model are the same, but in the present study materials also are different.

The finite element method is employed to model the structure. Because of stress redistribution due to the creep process, it is necessary to include a full inelastic creep step in the finite element formulation. Otherwise over-conservative creep life predictions will be estimated if only the initial elastic stresses are considered.

The experimental investigations are carried out in order to validate the models.

The main contributions in the thesis are:

1. Using similitude theory for life prediction of components in general, and specifically using thermal scaling for the first time for prototype and model with two different materials.
2. Developing 1-D creep ANSYS macro to study creep effects to get meaningful results for industrial applications of gas turbine blade.
3. Analyzing the curve veering and flattening phenomena in rotating blade at thermal environment, using Lagrange-Bhat method.
4. Simple constitutive models in creep-fatigue interaction are proposed that can predict the lifetime in complicated situations of creep-fatigue, using the pure creep and pure fatigue test data.

**DEDICTED TO MY LATE FATHER, MOTHER, FAMILY, AND
TEACHERS**

AKNOWLEDGMENTS

All praises are due to the GOD who blessed me with kind professors and gave me support during the writing and research for this thesis.

I would like to express my deepest gratitude to professor Rama Bhat and Dr. Hany Moustapha, Department of Mechanical and Industrial Engineering, Faculty of Engineering and Computer Sciences, Concordia University, for their continuous guidance, effective support, and suggestions during the various stages of this work. Dr. Bhats' patience, understanding nature and technical excellence were the constant source of inspiration to the author throughout the course of this work.

The financial support provided by the Pratt and Whitney Canada and Department of Mechanical and Industrial Engineering of Concordia University is acknowledged.

Special thanks are for the NRC team, Dr. John Pierre, Dr. Silvio Kruger, and Mr. Martin Lord for allowing the use of their thermal fatigue and computer facilities and their help in carrying out the tests.

I would like to thank the group of technicians and department administrative staff for giving all the assistance needed to facilitate the work in the project. The strong endorsement of Dr. Mukhaerjee, the distinguished professor at University of California at Davis, for doing thermal scaling studies is also acknowledged.

I also wish to express my warm love and sincere appreciation to my wife Afsaneh, and children Mahya, Mahdi, and Amin for their encouragement and support. They were a constant source of strength and the author is grateful to them.

TABLE OF CONTENTS

Title	Page
<u>CHAPTER 1</u>	
INTRODUCTION AND LITERATURE REVIEW	
1.1. INTRODUCTION.....	1
1.2. LITERATURE REVIEW	3
1.2.1. Lifetime Prediction in Creep-Fatigue Interaction.....	3
1.2.2. Curve Veering in Rotating Blade in Thermal Environment.....	10
1.2.3. Scale Model Analysis and Testing at Scaled Temperatures	12
1.3. OBJECTIVES AND SCOPE OF THE THESIS.....	23
1.3.1. Model 1.....	23
1.3.2. Model 2.....	23
1.3.3. Model 3	24
 <u>CHAPTER 2</u>	
CREEP LIFE PREDICTION IN GAS TURBINE COMPONENTS	
2.1. THE HIGH-TEMPERATURE MATERIALS PROBLEM.....	27
2.2. THE CREEP CURVE.....	28
2.3. THE STRESS RUPTURE TEST.....	32
2.4. STRUCTURAL CHANGES DURING CREEP.....	33
2.5. FRACTURE AT ELEVATED TEMPERATURE.....	35
2.6. HIGH-TEMPERATURE ALLOYS	37
2.7. PRESENTATION OF ENGINEERING CREEP DATA.....	37
2.8. PREDICTION OF LONG -TERM PROPERTIES.....	39

2.8.1. Abridged Method	40
2.8.2. Mechanical Acceleration Method	41
2.8.3. Thermal Acceleration Method.....	42
2.9. ONE-DIMENSIONAL CREEP MODELING USING ANSYS.....	45
2.10. THEORIES FOR CREEP CALCULATIONS	46
2.10.1. Tabular Material Format (Primary and Secondary Creep)	47
2.10.2. Creep Strain Calculation for a Mission in Terms of T_4 and Angular Velocity.....	49
2.11. ONE DIMENSIONAL CREEP MACRO	49
2.11.1. ANSYS Material Input for Creep.....	50
2.11.2. ANSYS Creep Model # 6 (Primary Creep)	51
2.11.3. ANSYS Creep Model # 11 (Primary and Secondary Creep).....	52
2.11.4. Geometry.....	52
2.11.5. Temperature History	53
2.11.6. Stress History	54
2.12. ANALYSIS	55
2.12.1. Mathematical Material Model Versus ANSYS Creep Model # 6	55
2.12.2. Tabular Material Format and ANSYS Creep Model # 11	56
2.12.3. Parameter Sensitivity	57
2.13. CONCLUSIONS	59
2.13.1. The Mathematical Material Model and ANSYS Creep Model # 6	59
2.13.2. The Tabular Material Format and ANSYS Creep Model # 11	60

CHAPTER 3

CUMULATIVE FATIGUE AND LIFE PREDICTION

3.1. INTRODUCTION	61
3.2. CYCLIC LOADING	63
3.3. FATIGUE FAILURE MODELS	66
3.3.1. Stress-Life Approach	67
3.3.2. Strain-Life Approach	68
3.3.3. General Approach	69
3.4. ALTERNATING STRESS (ZERO MEAN STRESS)	71
3.5. MEAN STRESS EFFECTS	72
3.6. DIFFERENT AMPLITUDES	74

CHAPTER 4

CREEP-FATIGUE INTERACTION AND CONSTITUTIVE MODELS

4.1. INTRODUCTION	77
4.2. HOLD-TIME EFFECTS IN STRAIN-CONTROLLED FATIGUE	79
4.3. EFFECT OF RUPTURE DUCTILITY	81
4.4. EFFECTS OF ENVIRONMENT	82
4.5. DAMAGE RULES AND LIFE PREDICTION	82
4.6. EVALUATION OF LIFE-PREDICTION METHODS	86
4.7. FAILURE-MECHANISM MAPS	87
4.8. THERMAL FATIGUE	88
4.9. MODELS OF CREEP-FATIGUE INTERACTION	92

4.9.1. Introduction	92
4.9.2. Model 1	93
4.9.3. Model 2	97
4.9.4. Model 3	100
4.10. MECHANICAL TESTING	103
4.10.1. Test Schedule for Model 1	104
4.10.2. Test Schedule for Model 2	105
4.10.3. Test Schedule for Model 3	106

CHAPTER 5

APPROXIMATE METHODS IN DYNAMIC ANALYSIS OF ROTATING BLADE

5.1. LAGRANGE-BHAT METHOD	110
5.2. DYNAMIC ANALYSIS OF ROTATING BLADE	112
5.3. BLADE MODEL	113
5.3.1. Strain Energy	114
5.3.2. Kinetic Energy	115
5.4. TEMPERATURE EFFECTS ON NATURAL FREQUENCY	129
5.4.1. Longitudinal Vibrations	131
5.4.2. Transverse Vibrations	134
5.5. DYNAMIC OF ROTARY BLADE AT HIGH TEMPERATURE	135
5.6. CURVE VEERING	136
5.7. FLATTENING	140

CHAPTER 6

EXPERIMENTAL INVESTIGATION ON SCALED MODELS, INCLUDING TEMPERATURE SCALING

6.1. THEORETICAL ANALYSIS	144
6.1.1. Non-linear Elastic Behavior	145
6.1.2. Linear Elastic Behavior	146
6.1.3. Characteristics of Observations	146
6.1.4. Scale Model In Creep-Fatigue	147
6.2. SCALE MODEL OF CANTILEVER BEAM IN CREEP-FATIGUE	151
6.2.1. Frequency Scaling	151
6.2.2. Amplitude Scaling	153
6.2.3. Acceleration Scaling	154
6.2.4. Stress Scaling	158
6.2.5. Strain Scaling	159
6.2.6. Temperature effect	161
6.3. SCALE MODEL OF GAS TURBINE BLADE IN CREEP-FATIGUE	164
6.3.1. Natural Frequencies Scaling	165
6.3.2. Stress Scaling	166
6.3.3. Strain Scaling	167
6.3.4. Displacement Scaling	169
6.3.5. Temperature Effect	169
6.4. TEST ANALYSIS	179
6.4.1. Accelerated Testing	179
6.4.2. Experimental Procedure	182

6.5. FRACTOGRAPHY (SEM)201

CHAPTER 7

DISCUSSION AND CONCLUSIONS

7.1. GENERAL214

7.2. CONCLUSIONS217

7.3. RECOMANDATIONS FOR FUTURE WORK218

REFERENCES219

APPENDIX242

 Appendix A242

 Appendix B243

 Appendix C244

 Appendix D247

 Appendix E248

 Appendix F249

 Bibliography255

LIST OF FIGURES

Figure	Page
Figure 1 Segmented model of aircraft carrier [109].....	21
Figure 2 Diffusion of smoke above and within shear layer 1/400 scale model of part of.	23
Figure 3 Model and full-scale saturn vibration test vehicles [116].....	25
Figure 4 First bending mode of saturn, maximum dynamic pressure weight [116].....	25
Figure 5 Model Glacier made from Kaolin. Faults.....	26
Figure 6 Typical creep curve showing the three stages of creep. curve.....	35
Figure 7 Andrade's analysis of the competing processes.....	36
Figure 8 Schematic of the effect of stress on creep curves at constant temperature.....	38
Figure 9 Method of plotting stress-rupture data (schematic).....	39
Figure 10 Strain rate in creep test as function of total strain.....	40
Figure 11 The equicohesive temperature [134].....	42
Figure 12 Plot of stress vs. minimum creep rate, for 16-25-6 alloy [134].....	44
Figure 13 Deformation-time curves at 1300°F for 16-25-6 alloy [134].....	45
Figure 14 Abridged method of creep testing.....	47
Figure 15 Mechanical acceleration method of creep testing.....	48
Figure 16 Thermal acceleration method of creep testing.....	49
Figure 17 Stress-rupture data at various stresses plotted according to Equation (5).....	50

Figure 19 Strain hardening rule.....	54
Figure 20 Creep strain of the mathematical material model and ANSYS creep model 6.61	
Figure 21 Creep strain of the tabular material format and ANSYS creep model # 11....	62
Figure 22 Temperature histories.....	64
Figure 23 Typical cyclic loading.....	69
Figure 24 Typical S-N curve.....	71
Figure 25 Total fatigue life parts.....	72
Figure 26 Plastic strain amplitude versus reversals to failure.....	74
Figure 27 General approach curve.....	77
Figure 28 Compressive and tensile mean stress effect (schematic).....	78
Figure 29 (a) The effects of mean stress; (b) The comparison between different failure..	79
Figure 30 S-N curve in varying amplitude loads.....	81
Figure 31 Effects of hold time and tensile vs compressive hold on cyclic endurance life	86
Figure 32 Effect of ductility on endurance of ferritic steels [153].....	88
Figure 33 Creep-rupture/low-cycle-fatigue damage interaction curve.....	91
Figure 34 Creep-fatigue failure-mechanism map for 1Cr-Mo-V steel at 565 °C [169]....	95
Figure 35 Failure prediction diagram for combined creep and fatigue under constant...	105
Figure 36 Failure prediction for combined creep and fatigue in constant temperature...	105
Figure 37 The load waveform in mechanical testing.....	109
Figure 38 Rotating cantilever beam.....	120

Figure 39 Beam – hub radii assembly.....	123
Figure 40 Beam element before and after deflection showing the relative.....	126
Figure 41 Configuration of two coordinate systems.....	129
Figure 42 Schematic of the cantilever beam.....	135
Figure 43 Curve veering in nonthermal rotating blade, $\Delta T=0^{\circ}\text{C}$	144
Figure 44 Curve veering in thermal rotating blade, $\Delta T=400^{\circ}\text{C}$	145
Figure 45 Flattening in nonthermal rotating blade, $\Delta T=0^{\circ}\text{C}$	147
Figure 46 Flattening in thermal rotating blade, $\Delta T=400^{\circ}\text{C}$	148
Figure 47 Amplitude vs. frequency of the 0.5 meter model.....	162
Figure 48 Amplitude vs. frequency of the 1 meter prototype.....	162
Figure 49 Acceleration vs. frequency of the 0.5 meter model.....	163
Figure 50 Acceleration vs. frequency of the 1 meter prototype.....	163
Figure 51 Stress vs. length of the 0.5 meter model.....	164
Figure 52 Stress vs. length of the 1 meter prototype.....	165
Figure 53 Strain vs. length of the 0.5 meter model.....	166
Figure 54 Strain vs. length of the 1 meter prototype.....	166
Figure 55 Strain vs. length of the 0.5 meter model.....	168
Figure 56 Strain vs. length of the 1 meter prototype.....	168
Figure 57 Displacement vs. length of the 0.5 meter model.....	169
Figure 58 Displacement vs. length of the 1 meter prototype.....	169
Figure 59 Stress vs. length of the 0.164 meter model.....	172
Figure 60 Stress vs. length of the 0.328 meter prototype.....	173

Figure 61 Strain vs. length of the 0.164 meter model.....	174
Figure 62 Strain vs. length of the 0.328 meter prototype.....	174
Figure 63 Displacement vs. length of the 0.168 meter model.....	176
Figure 64 Strain vs. length of the 0.328 meter prototype.....	176
Figure 65 Principle stress vs. length of the 0. 164 meter model.....	177
Figure 66 Principle stress vs. length of the 0.328 meter prototype.....	177
Figure 67 Von-Mises stress vs. length of the 0. 164 meter model.....	178
Figure 68 Von-Mises stress vs. length of the 0.328 meter prototype.....	178
Figure 69 Force vs. length of the 0. 164 meter model.....	179
Figure 70 Force length of the 0.328 meter prototype.....	180
Figure 71 Von-Mises strain vs. length of the 0.164 meter model.....	181
Figure 72 Von-Mises strain vs. length of the 0.328 meter prototype.....	181
Figure 73 Elastic strain vs. length of the 0.164 meter model.....	182
Figure 74 Elastic strain vs. length of the 0.328 meter prototype.....	182
Figure 75 Thermal strain vs. length of the 0.164 meter model.....	183
Figure 76 Thermal strain vs. length of the 0.328 meter prototype.....	183
Figure 77 Displacement vs. length of the 0.168 meter model.....	184
Figure 78 Displacement vs. length of the 0.328 meter prototype.....	184
Figure 79 Thermal acceleration method of creep testing.....	187
Figure 80 Geometry of fatigue, creep, and creep-fatigue specimen, steel 4340.....	189
Figure 81 Gleeble-3500 for different creep, fatigue and creep-fatigue tests.....	190
Figure 82 Load waveform for creep, fatigue, and creep-fatigue tests.....	191
Figure 83 Stress waveform for creep tests.....	193
Figure 84 Force waveform for creep tests.....	194

Figure 85 Creep strain vs. time at 800°C in creep test.....	195
Figure 86 Creep strain vs. time at 850°C in creep test.....	195
Figure 87 Creep strain vs. time at 853°C in creep test.....	196
Figure 88 Creep strain vs. time at 875°C in creep test.....	196
Figure 89 Stress waveform for fatigue test.....	199
Figure 90 Force waveform for fatigue test.....	199
Figure 91 Strain vs. time in fatigue test.....	200
Figure 92 Stress waveform for creep-fatigue test.....	202
Figure 93 Force waveform for creep-fatigue test.....	202
Figure 94 Strain vs. time in creep-fatigue test.....	203
Figure 95 Fractography of Al-2023 at creep condition, 400X.....	208
Figure 96 Fractography of St-4340 at creep condition, 1100X.....	209
Figure 97 Fractography of St-4340 at creep-fatigue condition, 800X.....	210
Figure 98 Geometry of fatigue, creep, and creep-fatigue specimen Al 2024.....	212
Figure 99 Total strain vs. time in thermal scaling.....	214
Figure 100 Total strain vs. time in thermal scaling.....	215
Figure 101 Total strain vs. time in temperature-force scaling.....	215
Figure 102 Total strain vs. time in temperature-force scaling.....	216

LIST OF TABLE

Table	Page
Table 1 Compression of operating conditions based on Larson- Miller parameter.....	53
Table 2 Test table for justifying model 1.....	113
Table 3 Typical material data from pure creep test.....	114
Table 4 Typical material data from pure creep test.....	115
Table 5 Results of model 3 for creep-fatigue interaction.....	116
Table 6 Parameters involved in modeling.....	157
Table 7 Parameters involved in modeling.....	161
Table 8 Parameters involved in modeling.....	161
Table 9 Parameters involved in modeling.....	163
Table 10 Parameters involved in modeling.....	164
Table 11 Parameters involved in modeling.....	173
Table 12 Parameters involved in modeling.....	174
Table 13 Chemical properties of steel 4340.....	191
Table 14 Physical properties of steel 4340.....	191
Table 15 Mechanical properties of steel 4340.....	191
Table 16 Creep test results for steel 4340.....	194
Table 17 Chemical properties of Al 2023.....	214
Table 18 Physical properties of Al 2023.....	214
Table 19 Mechanical properties of Al 2023.....	214
Table 20 Parameters involved in modeling.....	216

Nomenclature

- A : cross-sectional area, material constant
- A_0 : initial cross-sectional area
- C, C_1 : Larson-Miller constant often assumed to be 20
- C_i : arbitrary constants, coefficients, generalized coordinate
- D : damage, exhaustion
- D_c : creep damage
- D_f : fatigue damage
- D_t : total damage
- E : Young's modulus of elasticity
- F : force
- H : height
- I : moment of inertia
- K : stiffness matrix
- K_1, K_2 : material constants
- L : characteristic length
- L_1 : Lagrangian
- M : mass, mass matrix
- N : number of cycles at stress σ and temperature T, rotary speed
- N_f : number of cycles to failure at stress σ and temperature T
- N_{f_i} : number of cycles to failure at stress σ_i
- N_i : number of cycles at stress σ_i

- Q : activation energy for creep
- Q_i : the generalized force along the coordinate C_i
- R : the gas constant, 8.3145 joules per kelvin per mole ($J \cdot K^{-1} \cdot mol^{-1}$)
- \bar{R} : dimensionless radius
- S_f : fatigue strength
- T : temperature in deg. F, in Kelvin, $^{\circ}R = ^{\circ}F + 460$, kinetic energy
- T_{max} : maximum kinetic energy
- U : potential energy
- U_{max} : maximum potential energy
- W : work, shape function, width
- Y : shape function
- Z : axis along the beam
- a : characteristic acceleration of vibration
- b : fatigue strength exponent or Basquin's exponent (≈ -0.05 to -0.12), width
- b_i : material constants
- c : temporary notation in modeling the Young's modulus of elasticity
- h : height
- i : number of load case
- n : material constants, number of cycles completed
- r : the ratio of transient creep rate to the transient creep strain
- t : the total analysis time, time
- t_h : hold time at stress σ and temperature T
- t_i : time spend at stress σ_i and temperature T_i
- t_m : flight duration (mission time)

- t_R : rupture time in hours stress σ and temperature T
 u : longitudinal displacement
 v : transverse displacement
 y : deflection, response
 z : axis along the beam
 \bar{z} : dimensionless z
 Δ : elongation
 $\Delta\varepsilon_e$: elastic strain range
 $\Delta\varepsilon_p$: plastic strain range
 Δt : spend time in hours
 $\Delta\varepsilon_{tot}$: total strain range
 Φ_i : shape functions
 α : thermal Expansion
 δ : deflection
 ε : total strain
 ε_0 : the instantaneous strain on loading
 ε_e : elastic strain
 ε_f : failure strain
 ε_p : plastic strain
 ε_t : the limit for transient creep
 $\dot{\varepsilon}_s$: the steady-state creep rate
 π : dimensionless group, Buckingham's pi

- ρ : density
- σ : Von-Misses effective stress, mean stress
- σ_a : alternating stress
- σ_{cr} : creep strength (creep stress for corresponding time to rupture)
- σ_m : mean stress
- σ_{UTS} : ultimate tensile stress
- σ'_f : fatigue strength coefficient (for most metals $\approx \sigma_f$, the true fracture strength)
- ω : characteristic frequency, rotary speed

CHAPTER 1

INTRODUCTION AND LITERATURE REVIEW

In this chapter the historical evolution of the creep-fatigue lifetime prediction and the scale model analysis are explained and the present study is placed in the context. The survey of literature on the life estimation and the one about similitude are presented.

1.1. INTRODUCTION

There is a general tendency towards more severe operating conditions, i.e. higher mechanical loadings and temperatures, in order to increase the efficiency of gas and steam turbines, internal combustion engines, heat exchangers, conventional and nuclear electric power generation equipment and other engineering components and devices. This trend has resulted in starting, growth and interaction of complex damaging processes within the materials of these devices. They can lead to the failure of a component and, consequently, a whole structure, and thus limit their lifetime. Therefore, a safe assessment of lifetime is very important for the prevention of such failures which may have disastrous consequences; too conservative predictions, however, unnecessarily increase the cost of production and maintenance of such systems.

Advanced gas turbine engines which use cooling at hot sections of airfoil, present a range of design problems. The blades operate in a damaging environment of high

temperatures, centrifugal and gas pressure forces and thermal cycling. These conditions combine at every point in the blade to create an interaction between creep and thermo-mechanical fatigue damage. Blades which have geometrically simple cooling passages can be analyzed using basic techniques if the thermal and stress conditions are known. To obtain meaningful results, finite element methods must be employed. Also, because of stress redistribution due to the creep process, it is necessary to include a full inelastic creep step in the finite element analysis. Otherwise over-conservative creep life predictions will be estimated if only the initial elastic stresses are considered.

The creep model uses a Norton power law, Larson-Miller and Robinson's rule approach, while the fatigue model combines Miner's rule and the universal slopes method. In both creep and fatigue cases, crack initiation should be considered as defining the design life. The simplest model, which has been suggested till now, is the linear summation of both damage parameters. A linear summation of the creep and fatigue damage parameters provides the analyst with a measure of the total damage at any point on the blade at any time in the load history, and a breakdown into the failure mode components. But it is not clear as to what is the best model that is as close as possible to reality. It is also important to know whether such a model is valid for gas turbine blade.

1.2. LITERATURE REVIEW

In the current investigation several aspects of lifetime prediction are of interest. They include the damage due to creep, fatigue, and creep-fatigue interactions, modeling using FEM, and experimental validation. Many researchers have dealt with these issues over the years. The simulation studies on the life-limiting modes of failure, as well as estimating the expected lifetime of the blade, using the proposed models have been carried out. Although the scale model approach has been used for quite some time, the thermal scaling has been used in this study for the first time. Approximate methods such as the Rayleigh-Ritz or the Finite Element Methods some times wrongly predict a veering away phenomenon among the natural frequencies of the structure. Such wrong predictions adversely affect any response quantities using such techniques resulting in either over or under designs. A review of the research is presented below in order to better understand the underlying phenomena and improve the predictions. The literature survey is presented on each topic below.

1.2.1. Lifetime Prediction in Creep-Fatigue Interaction

Turbine blades of aeroengine work under the most severe conditions. They have the most complex structure and are in danger of fracture. The turbine blades carry on the compound loads at high temperatures all the time when the engine is working. Therefore, to determine the working life of the blade, the creep and fatigue life cannot be treated

separately. On the contrary, the interactive effects of fatigue and creep must be fully considered.

Since aeroengine turbine blades and other high-temperature components are operated at high temperature and under cyclic loading, damage resulting from fatigue and even creep-fatigue interaction is one of the factors which must be dealt with in this type of application. The situation is often simulated in laboratories as high-temperature low-cycle fatigue. Incorporation of hold time at constant strain or stress in high-temperature low-cycle fatigue is one of the methods of studying creep-fatigue interaction.

Many investigators have examined creep-fatigue crack initiation [1, 2, 3] and propagation modes [1,4-11] in general. Some of them focused on studying the effect of specific parameters such as hold time [12-13] or creep stress effect [14], environment [5, 15] a new evidence of orientation [16, 17], geometry [18], and material parameters [19, 20, 21], and some of them studied the metallurgical problems [22], or discussed on design rules [23]. In design field, some of them developed a system for assessment [24], used numerical method [25] or damage concept [26] for life prediction, or suggested their own constitutive model [27, 28]. Since it is easier, many of them used thermo-mechanical loading [29-32] for the tests. It was shown in the above references that the origin of failure under low-cycle fatigue is mainly related to the geometrical discontinuities on the specimen surface and creep-fatigue-environment interactions may enhance the cracking problem.

In low cycle fatigue (LCF) tests, it has been reported that as the hold time is increased, the fatigue life is decreased at a fixed test temperature, and the reason for life reduction is reported to be due to the creep effect of stress relaxation, which makes an additional plastic strain enlarging the hysteresis loop during hold time. It is reported that the creep mechanisms of stress relaxation, which are the main reasons for fatigue life reduction under creep-fatigue interactions, after a long enough hold time, are the same as that of the general monotonic creep [33].

A significant reduction in fatigue life is observed with hold time in compression or in both tension and compression. The influence of tensile hold on fatigue life is more complicated. The mean stress develops during tensile and compressive hold tests. The scanning electron Microscopy (SEM) analysis of fracture surfaces shows that crack initiation and first stage of growth is transgranular, but crack growth in second stage is intergranular [34]. In fact, it has been noted that high-temperature tensile yield strength is an important parameter in studying high-temperature low cycle fatigue properties, crack growth in creep and the effect of cyclic loading on growth in creep-fatigue [10]. Considerable effort has been made to understand crack growth behavior under fatigue loading at elevated temperatures, where creep, fatigue and oxidation may contribute to failure at the same time. Depending on the specific materials and loading conditions, the role of each damage component may change significantly. To date, there is no “unified” approach with which the problem of fatigue crack growth at high temperature can be solved in a general manner.

The results show that mixed time and cycle dependent crack growth seems to be the dominant fatigue crack growth mode in the two powder metallurgy (PM) nickel alloys studied, whilst limited creep may be present at the crack tip, particularly under static and long dwell loading conditions [35]. Coffine [36] produced the first significant evidence to suggest that the oxidation is primarily responsible for high temperature low cycle fatigue damage. A variety of studies have been carried out on different alloys, especially directionally solidified superalloy Mar [37, 38], Inconel [39], Co-base [40, 41], Cr-base [4, 42], Ti-base [43, 44, 45], and Al [46]. In the 300 series austenitic stainless steels, such as 304, 316 and 316L used in high temperature applications, many studies have been devoted to understand the creep-fatigue interaction behavior by employing the hold-time tests [32-55]. It has been observed in these investigations that at relatively high temperatures, continuous cycling endurance is corrupted when a hold-period is included in the cycle. In general, the imposition of holds at tension peak strain tended to be more harmful than those imposed at compression peak strain. Further, there has been conflicting reports on the influence of the tension-hold duration on fatigue life. Hales [56] reported a continuous reduction in life with increase in the length of tension hold-time, while others [13, 57, 58] noted a saturation effect in the life reduction. The creep-fatigue effect in stainless steels is mainly recognized to be due to the inherent weakness of the grain boundaries which lend themselves to the formation of creep induced grain boundary voids that can enlarge into intergranular cavities and cracks [44]. Nickel base superalloys are so called “creep-brittle” materials because of their superior tensile strength and low creep ductility. Nickel base superalloys have been used with high reliability for blades and vane applications in gas turbines. Many investigations have been done on these types

of alloys either in single crystal or in general types. The application of directionally-solidified and single crystal alloys has become common in advanced gas turbines, because of their superior creep and fatigue properties compared with conventionally cast polycrystalline materials. At a given stress intensity factor range, small cracks showed growth rates significantly higher than physically long cracks, not only under the fatigue-dominant conditions but also under the creep-fatigue conditions. This is confirmed in air and in vacuum: thus the difference between the small and long cracks is independent of environment [59]. In general, creep-fatigue design considerations are intended to prevent crack initiation, where crack initiation may be defined arbitrarily as the presence of cracks which can be detected visually, say one mm in size. The difference between crack initiation and failure life in a small specimen is often a small proportion of the total life, and it can be argued that the failure endurance of a small specimen corresponds to the endurance at crack initiation in a large component. Several damage rules have been suggested for estimating the cumulative damage under creep-fatigue conditions. Interest has tended to focus on four basic types of approaches [60]:

1. The damage-summation method
2. The frequency-modified strain-range method
3. The strain-range-partitioning method
4. The ductility-exhaustion method.

In addition to these, several other less known approaches have also been applied. The most common approach is based on linear superposition of fatigue and creep damage.

Indeed, the foundation of the present design procedure is the linear life-fraction rule, which forms the basis of the ASME Boiler and Pressure Vessel Code, Section III, Code Case N-47 [61]. This approach combines the damage summations of Robinson for creep [62] and of Miner for fatigue [63].

The frequency modification approach is essentially a modification of the Coffine-Manson relationship for pure fatigue by incorporating a frequency term [64]. The strain-range-partitioning (SRP) approach involves partitioning of the total inelastic strain range into four possible components (depending on the direction of straining tension or compression) and the type of inelastic strain accumulated (creep or time-independent plasticity) [65-69]. A damage function has been proposed by Ostergren for predicting low-cycle fatigue at elevated temperatures [70, 71]. The relative qualities of one or more of the damage rules described so far in predicting the lives of specific materials have been assessed by a number of investigators. With respect to Cr-Mo-V rotor steels, Leven compared the linear-damage (LD), frequency-modified strain-range (FM), and strain-range-partitioning (SRP) approaches and concluded that all of them could predict life within a factor of 2 [72]. Similar conclusions were reached by Kuwabara and Nitta [73] and by Batte [74]. Batte has claimed, however, that in the low strain ranges the LD approach is better than the others. Curran and Wundt reported that the LD approach gave non-conservative predictions [75]. Melton compared the FM and SRP approaches and the Ostergren damage function and found the data to be best described by the FM approach [76]. Bisego, Fossati, and Ragazzoni claimed better fit of data to the SRP approach than to the LD approach [77].

There are divergent opinions regarding which damage approach provides the best basis for life prediction. It is quite clear that a number of variables, such as test temperature, strain range, frequency, time and type of hold, waveform, ductility of the material, and damage characteristics, affect the fatigue life. The conclusions drawn in any investigation may therefore apply only to the envelope of material and test conditions used in that study. The validity of any damage approach has to be examined with reference to the material and service conditions relevant to a specific application. One of the major problems in evaluating the applicability of different life-prediction methods is that in many cases it is necessary to use all the available data in deriving the life-prediction method and thus it is possible to examine only up to the accuracy with which a given method describes the data. Results from most studies show that even the best of the available methods can predict life only to within a factor of 2 to 3. Some of the mentioned reasons for these inaccuracies are: failure of the methods to model changing stress-relaxation and creep characteristics caused by strain softening or hardening, use of monotonic creep data instead of cyclic creep data, and lack of sufficiently extended-duration test data. All of the damage rules available today involving empirical constants are material-dependent and difficult to evaluate. Extrapolation of the rules to materials and conditions outside the envelope covered by the specific investigation often results in unsuccessful life predictions. For application to service components, the stress-strain variation for each type of transient and its time dependence must be known with accuracy.

1.2.2. Curve Veering in Rotating Blade in Thermal Environment

Analysis of fatigue requires information on the dynamic behavior of structures, and hence the natural frequencies, mode shapes etc. Analysis of complex structures such as a turbine blade cannot be carried out exactly and one must resort to approximate methods such as FEM. Under such circumstances the results may be corrupted by a phenomenon called “curve veering”.

Curve veering behavior has been observed in vibrating rectangular plates when natural frequencies were plotted against the side ratio by Warburton as early as 1954 [78]. When the variation of the structural eigenvalues was plotted against a system parameter, Claassen and Thorne [79] observed the phenomenon in 1962. A large number of references have either reported this behavior [79-85], or in some cases reported results without specifically referring to, but contained the curve veering behavior [86-90]. When such curve veering behavior is present, the responses calculated using the particular method of analysis cannot be completely relied upon in the design and against creep and fatigue requires the use of large safety factors. Hence it is very important to understand the curve veering phenomenon.

The phenomenon has been attributed to the approximate methods used in solving the eigenvalue problem. However, a study on a rotating string with a spring support, reported by Schajer [81] showed the curve veering behavior when analyzed by Rayleigh Ritz method as well as by exact analytical solutions as reported by Perkins and Mote [82]. The curve-veering phenomenon is evident in the studies reported on rotating disks and

plates [86-88] and in the exact analysis of clamped beams on intermediate elastic supports [89, 90] even though these authors did not allude to this behavior in their discussions. The phenomenon has been haunting researchers not only in the area of vibrations of regular systems but also in the vibrations of disordered systems [91], and in several other areas such as molecular physics [92]. In the vibration of square membranes or plates, the symmetry of the structures suggest that the natural frequencies corresponding to m, n modes must be identical to n, m modes when the structure is rotated by 90° about its transverse axis through the centre. In rectangular membranes or plates with all edges simply supported, where exact solutions are available, the variation of natural frequencies corresponding to m, n modes will intersect with those corresponding to n, m modes when the aspect ratio is one, showing that ω_{mn} is identically equal to ω_{nm} . However, Leissa [85] reported on a curve veering aberration when natural frequencies were obtained using an approximate method. When exact natural frequencies λ_{41}^2 , λ_{43}^2 , and λ_{31}^2 were plotted against the side ratio (a/b), the lines corresponding to λ_{43}^2 and λ_{31}^2 intersected at $(a/b)=1$. However, when a three-term solution was worked out using Galerkin's method these curves corresponding to the approximate eigenvalues never intersected. The line corresponding to λ_{43}^2 strangely veered away when they reached $(a/b) = 1$. At $(a/b) = 1$, these two natural frequencies stayed distinct and for $(a/b) > 1$, the line corresponding to λ_{43}^2 become that for λ_{31}^2 and vice versa. However when the problem was solved using finite difference method, the curve veering behavior disappeared. Sabour et al [93] showed that the curve veering in rotating blade is pseudo and depends on number of terms used for the shape function, the phenomenon shifts to the still higher modes.

1.2.3. Scale Model Analysis and Testing at Scaled Temperatures

Quite often it may not be possible to carry out experimental validation of design analysis on prototype structures at the design stage. Exact simulation of operating conditions such as thermal environments may not be possible. Under such conditions the designer may resort to study the structural behavior using scale model testing. Engineers and scientists have been using scale models for many years. Models for vibrating rods and plates were investigated by French mathematician A.L. Cauchy in 1829. The first water basin model for designing watercraft was made by W. Froude in 1869. O. Reynolds started using the concept of scaling in fluid machinery problem and he published classical model experiments on fluid motion in pipes in 1883 [94]. Model tests have many limitations but still they are invaluable for engineers and the use of model testing is increasing steadily. The principal purpose of modal analysis or dimensional analysis from engineering viewpoint is the arrangement of the variables of a physical relation so that, without destroying the generality of the relationship, it may be more easily determined experimentally [95]. Thus, the complexity and extent of an experiment may be greatly simplified by this approach. The origin of the modern theory of dimensional analysis is rooted in the concept of geometric similitude used first by Galileo for determining elastic properties of a single structural member as a function of their geometric dimensions. Newton used it in the study of the Laws of Motion, and Marriotte for work on shock and on fluid flow [96]. Great contributions were made to the analysis of physical phenomena during the eighteenth century, and yet very little attention was paid to matters of physical dimensions during most of that period. Euler broke this trend and showed in several of his

numerous writings the meaning of quantities and the mathematical expression of physical relationship [97]. Lagrange and Laplace continued the work that was initiated by Euler and formulated the principles of dimensional analysis; Fourier, in the last of his three successive versions (1807, 1811, and 1822) of the *Analytical Theory of Heat*, established the foundations of dimensional analysis [97]. Fourier not only showed special mathematical powers but also deep concerns about physical aspects of the problem of heat transfer. He recognized the existence of dimensionless groups in his equations. All the basic elements related to the principles of dimensional analysis are in Fourier's *Théorie Analytique de la Chaleur*, even though he did not derive the relations between variables involved [97]. Further, Fourier did not consider the flow of heat in similar bodies. After Fourier, no important development in dimensional analysis took place for half a century. There were considerations and discussions about system of units for old and newly created physical quantities; moreover- from both analytical treatments and considerations of similarity – dimensionless groups, or so-called “abstract coefficients”, started to appear in the literature. In the *Theory of Sound (1877-8)* Lord Rayleigh refers to “Method of Dimensions” which corresponds to the principles expressed by Fourier fifty years ago [97]. The first detailed application of the “method of dimensions” is described at the beginning of the first volume (1877) after a discussion of the theoretical solution of the problem of the vibration of a mass attached to the center of a stretched string. Carvallo and Vaschy were the first to attempt a formulation of a general theorem for the method of dimensions. Carvallo showed that the equation for the power of a dynamo could be expressed as a relation between two dimensionless variables [97].

Much work was carried out by Carvallo, Vaschy, and Riabouchinsky before Buckingham [98] in 1914 developed the Pi Theorem that forms the basis for investigating physical relationships within the framework of similarity. In 1915, Rayleigh [99] published a paper motivating the use of his method in dimensions among engineers; he gave several examples, including an analysis of Boussinesq's on the steady passage of heat from a solid conducting body immersed in a stream of fluid moving with a velocity, v , at infinity. Rayleigh assumed that the total heat, h , passing in unit of time was a function of only the linear dimension, a , of the solid, the temperature difference, θ , the velocity, v , the specific heat of the fluid, c , and the conductivity, k .

1.2.3.1. Fields of Application

Historically dimensional analysis and similarity theory were first used to study hydraulics and the flow of fluids in pipes and channels. Empirical rules were developed through model tests before laws of viscous flow were known. Since many areas of fluid dynamics are still too complicated and accurate analysis is mathematically very difficult, a lot of efforts have been devoted to develop accurate similarity methods for fluid dynamics, hydraulics, aerodynamics, and naval hydrodynamics [100]. Model test on water wheels were conducted in the eighteenth century by Smeaton [101]. At the beginning of the twentieth century model tests again began to be carried out by manufacturers for the development of modern types of hydraulic turbines. Hydraulic scaled models are frequently used in pump, turbine, hydraulic torque converters and other turbo machines. These scaled models are used to design the sump or intake, to establish

head, flow, efficiency, cavitations characteristics to ensure compliance with specified rated conditions, obtain flow patterns, and to acquire the best efficiency value [102-106]. The best known and perhaps one of the oldest applications of scale model experiments is in the field of naval architecture. Historical records show that experiments with models of ships have been performed since the time of Leonardo da Vinci [107]. However, it was not until W.E. Froude (1874) that model test predictions were established as a valuable engineering tool. He used it to obtain the resistance of a full-scale ship from model resistance experiments in a towing tank. For many decades model-testing tank, or water basin have been used for ship designing [108]. Frictional and wave making resistance, propeller performance, ship maneuverability in smooth and rough water, cavitations, ship bending vibrations due to wave impact and crashing, and many other performance would be impossible to predict without model experiments [108]. A 136:1 scale model of 820 feet World War II ESSEX-Class aircraft carrier prototype as shown in Figure 1 was tested

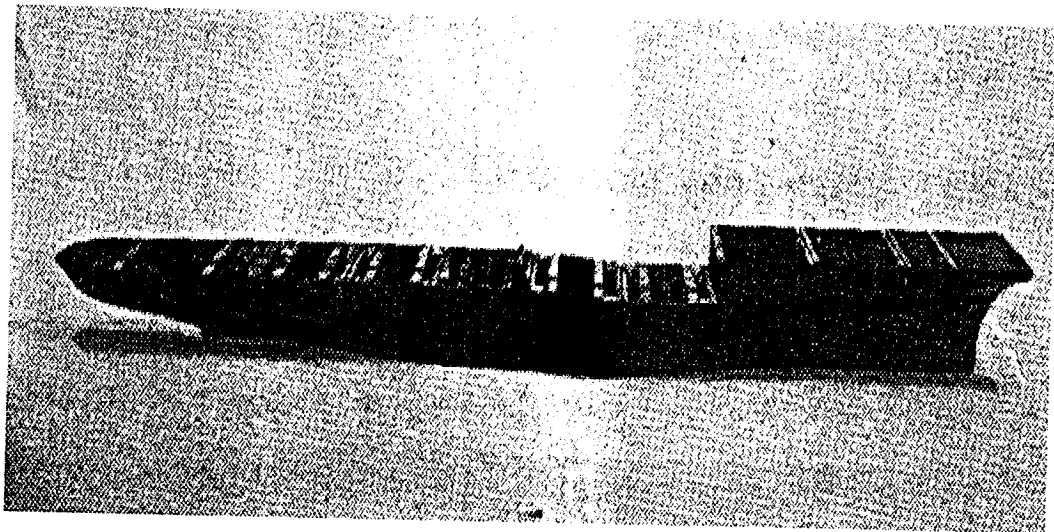


Figure 1 Segmented model of aircraft carrier [109].

at the David Taylor Model Basin in regular and irregular seas [109]. Just as the water basin was used in studying structural behavior in fluids, the wind tunnel was used to study the structural behavior in subsonic, supersonic, hypersonic, and hypervelocity air flow. Wind tunnels can simulate velocities ranging from a light breeze to many times the speed of sound. They can accommodate the scaled models of buildings and structures that are sensitive to winds [110], aircraft, and spacecraft for studies of turbulence, drag, lift, pressures, buffeting, flutter, and other phenomena [108]. After the dramatic and disastrous failure of Tacoma Narrows Bridge in 1940, intensive study of the aerodynamic stability of suspension bridges was carried out. Investigators used wind tunnels in order to study the aerodynamics of bridge sections. Use of dynamic “sectional” models, as opposed to complete or full bridge models, is now commonly accepted [111]. Larger model scale and lower modeling cost are advantages offered by sectional approach. The scale ratio for sectional models may be in the region of 1:30 or 1:50, and for full models in conventional wind tunnels may be 1:200 or higher. A 1/400-scale-model is shown in Figure 2 of about one mile of downtown Montreal that was used in the 6-ft×9-ft low speed wind tunnel to obtain mean pressures and the spectrum on unsteady pressures at different locations on a tall building in a simulated wind shear layer [112].

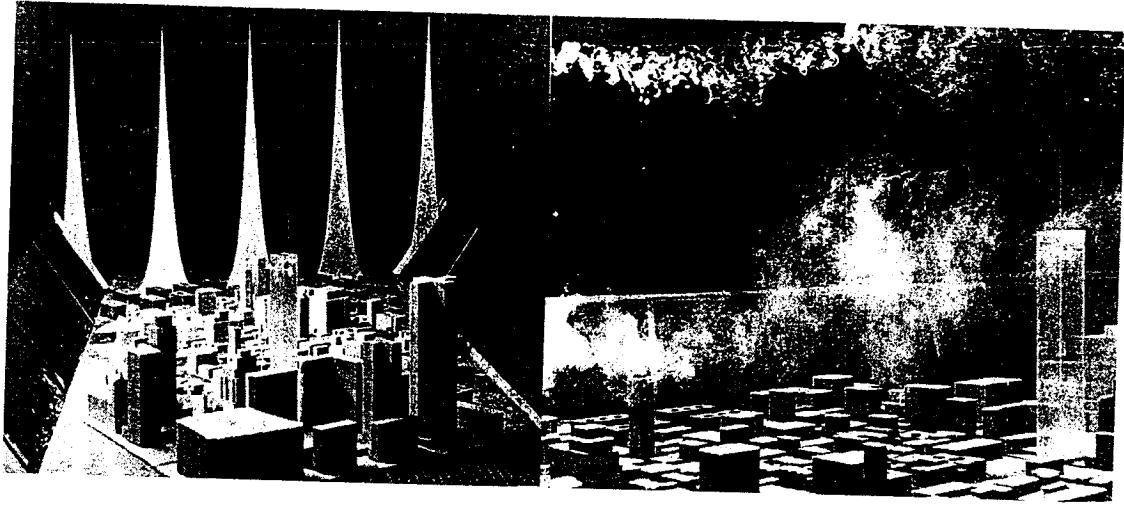


Figure 2 Diffusion of smoke above and within shear layer 1/400 scale model of part of downtown Montreal in 6-FT9-FT wind tunnel [112].

Again scaled models have been used extensively in the aeronautical field. In the past decades, dynamic models have made possible many refinements and helped in solving many problems which otherwise would have been impossible to solve economically. Dynamic scaled models have also been used extensively in the development of large launch vehicles in order to study fuel discharge, and the primary natural frequencies of the vehicle, buffet and response to ground winds, and also the determination of response due to acoustic excitation [113]. The importance of dynamic scaled models in aerospace research and development is demonstrated in reference [113]. Much of the work on dynamic scaled models in aerospace has been carried out at Langley Research center of NASA. In 1950 a one-tenth dynamic scaled model of large helicopter with a rotor diameter of about 13 feet was tested [114]. This model was designed to study the ground resonance and flutter problems.

A 1/6th scale model, equipped with wing tip tanks and representative of unsure fighter-type of conventional plan form, was tested for flutter [115]. For the design of the model, the model was dynamically scaled to flutter at the same speed as a full scale; in addition the principles followed in the scaling required that non-dimensional parameters important in flutter, such as mass ratio, frequency ratio, and reduced frequency, remain the same on the model as on the full-scale counter part.

A 1/5th scale dynamic replica of Saturn SA-1 launch vehicle was constructed again at Langley Research Center to establish the feasibility of obtaining the required experimental vibration data with a model [116]. For the resulting model which was 32 feet high (as compared to 160 feet full scale) and weighed about 7,500 pounds (as compared to 935,000 pounds on full scale) as shown in Figure 3, good agreements were obtained with the prototype results for the first bending mode as shown in Figure 4.

The modeling of concrete structures has received its greatest momentum in the post World War II years when many structural problems dealing with dynamic loads had to be resolved. Time dependent loadings, because of their complex nature and effects on structures, have enabled the experimental technique of using small-scaled models to

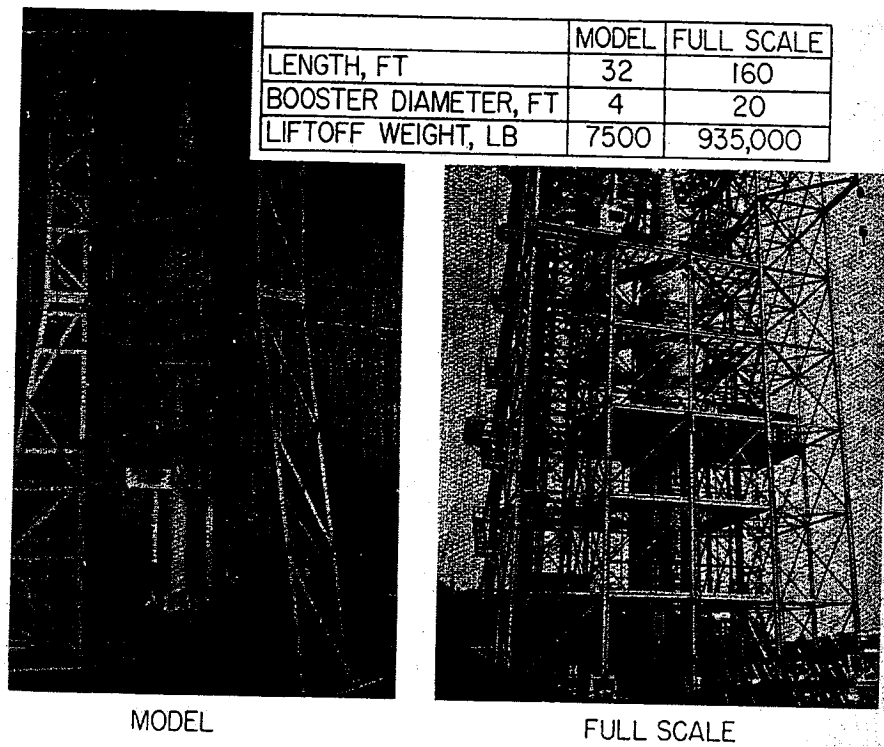


Figure 3 Model and full-scale saturn vibration test vehicles [116].

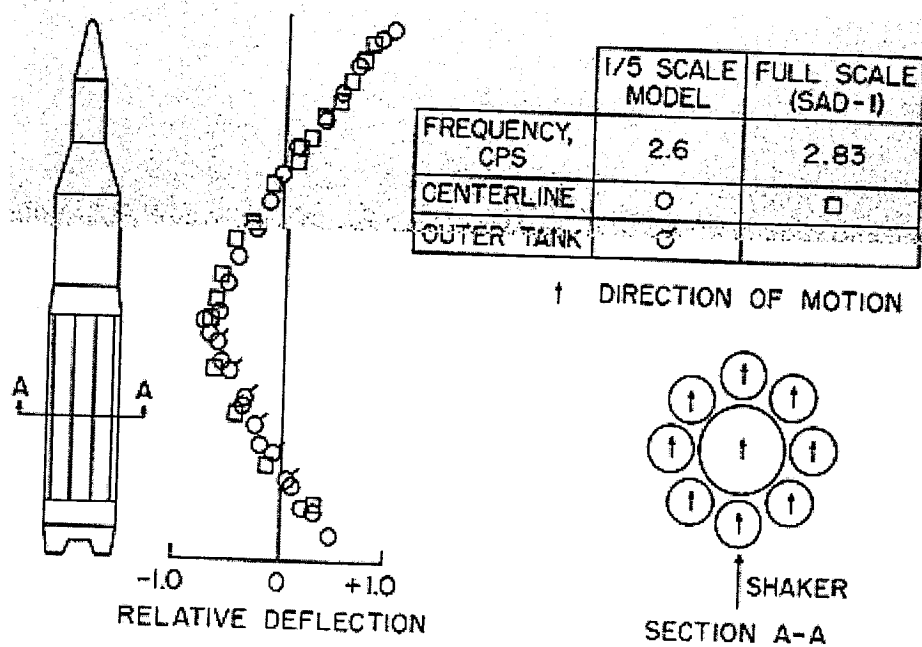


Figure 4 First bending mode of saturn, maximum dynamic pressure weight [116].

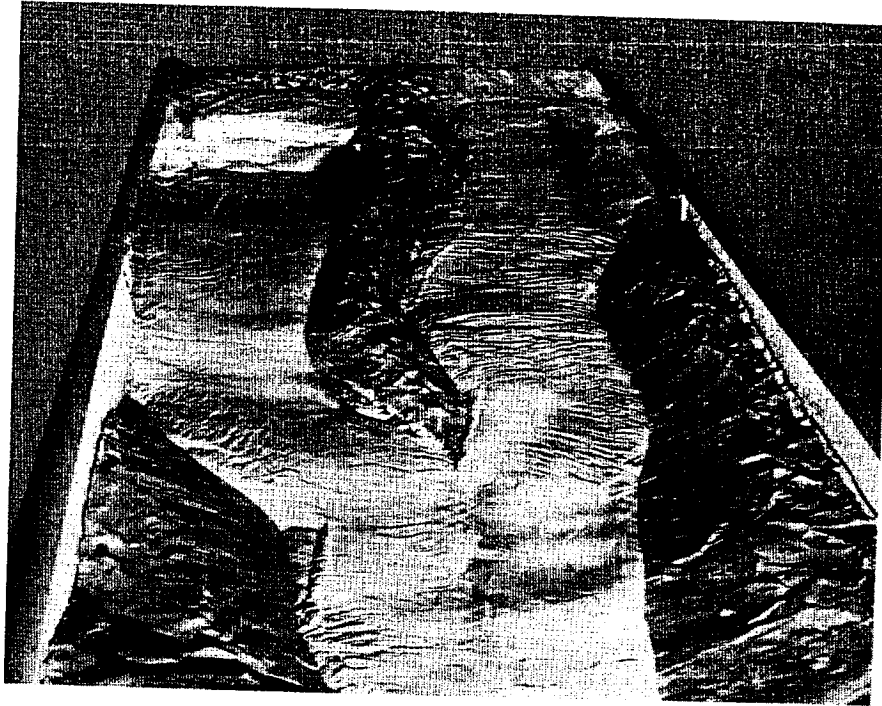


Figure 5 Model Glacier made from Kaolin. Faults and fields closely resemble those of field observations [108].

compete on an equal basis with more traditional analytical methods. Scaled models have been used for evaluating the dynamic properties of concrete material [117], response behavior of multipart building structures, dams and bridges due to earthquake [118-121], response due to wind pressures, soil mechanics, pile foundations, underground explosions [108]. Meteorologists and geophysicists are another group long interested in model experiments. As early as the late eighteenth century, an attempt was made to construct a laboratory model for cyclone. Now the study of geophysical phenomena in the laboratory on a miniature scale is well advanced. A model of extremely slow fluid flow, a miniature glacier composed of water and kaolin is shown in Figure 5 [108]. There is no limit to scale model experimentation within the range of quantifiable physical phenomena. Scaled models are used in every field that needs experimental results for the approximation of behavior of phenomena.

1.2.3.2. Temperature Scaling

Problems involving thermal environments are widespread within the framework of today's science and technology. In many engineering problems heat transfer is involved, and under certain conditions it may be desirable to use a model to assist in the solution of the problems. It is basically two axioms [122] that are inherent in methods of measurement and evaluation of quantities.

Axiom 1. Absolute numerical equality of quantities may exist only when the quantities are similar qualitatively.

Axiom 2. The ratio of the magnitudes of two like quantities is independent of the units used in their measurement, provided that the same units are used for evaluating each.

One of the characteristics involved in all thermal problems is temperature, which is normally measured in units of degrees F or degrees C. However, in solutions based on dimensional analysis, degrees Rankine or Kelvin must be used. The dimensional designation θ will be used for temperature. Quantity of heat, measured in units of BTU's and designated dimensionally as H is also a significant factor in the usual method of approach to thermal problems. It must be recognized, however, that H is dimensionally equivalent to $F \cdot L$, or capacity for doing mechanical work. Coefficient of Thermal Expansion, α , is the unit strain developed in an unrestrained specimen by a temperature change of one degree. It is expressed in units of strain per degree F, C, R, or K and in dimension of θ^{-1} . Specific Heat, c, is the quantity of heat required to increase the temperature of a unit mass of the material by one degree. It is expressed in units of BTU per degree, and dimensions of $HM^{-1}\theta^{-1}$ or $L^2T^{-2}\theta^{-1}$. Thermal Conductivity, k, is the rate of

heat flow through a unit thickness of the material for a one degree temperature difference. It is evaluated in BTU per hour per inch per degree F, and $HT^{-1}L^{-1}\theta^{-1}$ or $MLT^{-3}\theta^{-1}$. It is almost mandatory that model and prototype be constructed of identical materials [106]

1.2.3.3. Background of Investigations

The research till now is mainly focused on thermodynamic and heat transfer point of view. Ward [123] did some investigations in thermodynamic scale effects on pump suction performance, and Clark [124] carried out some studies on aircraft tire. Clark concluded that in general thermal modeling of aircraft tire temperature rise may not be possible without extensive experimentation and the development of suitable scaling factors based on experimental data. Ezra [125] believes that model experiments should be conducted at the same temperature as full scale. Most of the studies in thermal scaling are done at National Aeronautics and Space Administration (NASA), but all of them are concerning heat transfer on spaceships or aircrafts. For instance Katzoff's [126] studied the similitude in thermal models of spacecraft, and he concluded that the most difficult problems appear to be the accurate scaling of thermal conductivity and heat capacity. In his study four dimensionless similitude parameters are derived concerning heat radiation, internal heat generation, thermal conductivities of materials, and heat capacities of materials. William and O'Sullivan's [127] work is another comprehensive investigation of aircraft structural models subject to aerodynamic heating and external loads, but even in this study the prototype and model both are from the same material, and hence it is much simpler than the present study.

1.3. OBJECTIVES AND SCOPE OF THE THESIS

In this thesis, the creep, fatigue and creep-fatigue interaction have been studied and innovative mathematical models are proposed to predict the operating life of aircraft components, specifically gas turbine blades, which are subjected to creep-fatigue at high temperatures. The components are modeled by finite element methods, analytical method, and using similitude principles. Three constitutive models have been developed to predict the lifetime of the components experiencing creep-fatigue interactions.

1.3.1. Model 1

The main idea is that the total damage can be used for break point of the components, and the damages due to creep and fatigue can be accumulated linearly. In this model, the creep model uses a Norton power law, Larson-Miller and Robinson's rule approach, while the fatigue model combines Miner's rule and the universal slopes method. Each damage has been calculated separately and the total damage is found by linear summation in order to find the lifetime.

1.3.2. Model 2

The fluctuating stress is considered as a varying stress in fatigue-creep model. Since the fluctuating stress is combination of alternating and mean stress, it can be assumed that the mean part represents the static load which can cause creep at elevated

temperatures, whereas the alternating part is responsible for fatigue damage. This model is an extension to Goodman theory, except that instead of an intercept of ultimate stress (σ_u) on the σ_m axis, the intercept used is the creep-limited static stress (σ_{cr}).

1.3.3. Model 3

The approach for this model is that the creep-fatigue interaction can be considered as cyclic fatigue but with the hold time at maximum, minimum, or extreme stresses. This model has two strong points: 1) the required data can be used from pure creep and pure fatigue tests; 2) it has a safety factor (or a weakness factor) that is based on the material information and industrial experiences, between 0-1.

One-dimensional creep model, using ANSYS has been created to predict the creep life of a gas turbine engine blade. This application creates an ANSYS macro, which is called "Creep-1D". The macro is developed in ANSYS Parametric Design Language (APDL) using ANSYS creep models. Creep-1D macro creates a one-dimensional geometry to simulate an equivalent blade model. This geometry is based on the blade radial coordinates with the corresponding sectional areas using Link180 element- a 3D beam element. The macro stops when user defined criterion, which are number of missions and creep strain limit, are met. To execute the macro, four input files and eleven command line arguments are needed.

The simulation studies on the life-limiting mode of failure, as well as estimating the expected lifetime of the blade, using the proposed models have also been carried out. Although the scale model approach has been used for quite some time, the thermal scaling has been used in this study for the first time. The only thermal studies in literature using scaling for structures are by NASA in which materials of both the prototype and the model are the same, but in the present study materials also are different. The finite element method is employed to analysis the structure. Because of stress redistribution due to the creep process, it is necessary to include a full inelastic creep step in the finite element formulation. Otherwise over-conservative creep life predictions will be estimated if only the initial elastic stresses are considered.

The experimental investigations are carried out in order to validate the theories. In order to save the time, accelerated tests which are a sense time scaling concept were carried out. Two categories of tests were done at NRC Material Testing Laboratory, Boucherville, Quebec, the thermal scaling tests, and the creep-fatigue tests. In thermal scaling tests, the available steel 4340 and aluminum 2023 have been selected as prototype and model, respectively. The scaled temperatures are applied to the model, and the total strain of both prototype and model are measured and compared with those of simulation results and good agreement (less than 10% error) have been found. The fatigue, creep and creep-fatigue tests at upscale temperature are carried out on steel 4340 and the rupture time, total strain, and elongation are measured and compared with those of the mathematical models and good agreements are obtained.

The main contributions in the thesis are summarized as follows:

1. Using similitude theory for life prediction of components in general, and specifically using thermal scaling for the first time for prototype and model with two different materials.
2. Developing 1-D creep ANSYS macro to study creep effects to get meaningful results for industrial applications of gas turbine blade.
3. Analyzing the curve veering and flattening phenomena in rotating blade at thermal environment, using Lagrange-Bhat method and energy equation, in order to evaluate the vibratory stresses.
4. Suggesting the simple constitutive models in creep-fatigue interaction that can predict the lifetime in complicated situation of creep-fatigue, just by the simple pure creep and pure fatigue test data.

In this chapter the creep-fatigue lifetime prediction and the scale model analysis were discussed. A literature survey of the life estimation was presented and then the one about similitude. In next chapter, the creep life prediction in gas turbine components will be discussed and the 1-D creep model in ANSYS will be explained.

CHAPTER 2

CREEP LIFE PREDICTION IN GAS TURBINE COMPONENTS

In the previous chapter a literature survey was presented on the creep-fatigue lifetime prediction, curve veering phenomenon in structures and the scale model analysis including thermal scaling. The thesis objectives were also stated. In this chapter, the creep phenomenon and its effects on gas turbine blade will be explained, and the governing equations presented. The life prediction in gas turbine component will be discussed and the 1D creep model which was programmed in ANSYS will be explained.

2.1. THE HIGH-TEMPERATURE MATERIALS PROBLEM

The strength of metals decreases with increasing temperature. High temperature will also result in greater mobility of dislocations by the mechanism of climb. In some metals the slip system changes, or additional slip systems are introduced with increasing temperature. Deformation at grain boundaries becomes an added possibility in the high-temperature deformation of metals. The interaction of the metal with its environment at high temperature is very important. However, at elevated temperature the strength becomes very much dependent on both strain rate and time of exposure. A number of metals under these conditions behave in many respects like viscoelastic materials. A metal subjected to a constant tensile load at an elevated temperature will creep and undergo a time-dependent increase in length. A strong time dependence of strength

becomes important in different materials at different temperatures. What is high temperature for one material may not be so high for another. To compensate for this, temperature often is expressed as a homologous temperature, i.e., the ratio of the test temperature to the melting temperature on an absolute temperature scale. Generally, creep becomes of engineering significance at a homologous temperature greater than 0.4 [128]. The creep test measures the dimensional changes which occur from elevated-temperature exposure, while the stress-rupture test measures the effect of temperature on the long-time load-bearing characteristics.

2.2. THE CREEP CURVE

The progressive deformation of a material at constant stress is called creep. To determine the engineering creep curve of a metal, a constant load is applied to a tensile specimen maintained at a constant temperature, and the strain (extension) of the specimen is determined as a function of time. Although the measurement of creep resistance is quite simple in principle, in practice it is complicated. The elapsed time of such tests may extend to several months, while some tests have been run for more than 10 years [128]. Curve A in Figure 6 illustrates the idealized shape of a creep curve. The slope of this curve ($d\varepsilon/dt$ or $\dot{\varepsilon}$) is referred to as the creep rate. Following an initial rapid elongation of the specimen, ε_0 , the creep rate decreases with time, then reaches essentially a steady state in which the creep rate changes little with time, and finally the creep rate increases

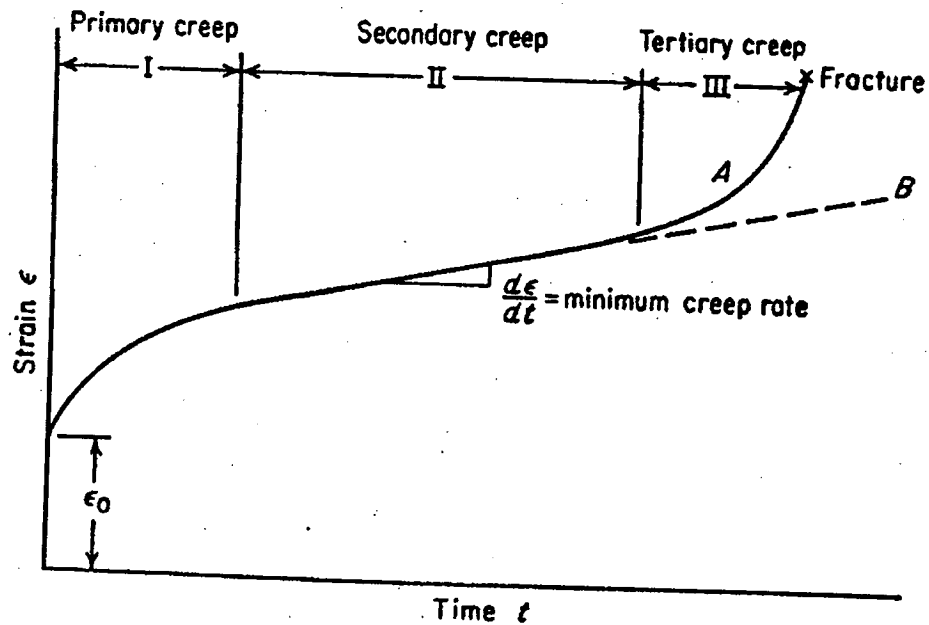


Figure 6 Typical creep curve showing the three stages of creep. Curve A, constant-load test; curve B, constant-stress test.

rapidly with time until fracture occurs. However, the degree to which these three stages are distinguishable depends strongly on the applied stresses and temperatures. Andrade's [129] pioneering work on creep had considerable influence on the subsequent research on the subject. He considered that the constant-stress creep curve represents the superposition of two separate creep processes which occur after the sudden strain which results from applying the load. The first component of the creep curve is a transient creep with a creep rate decreasing with time. The superposition of these creep processes is shown in Figure 7.

An equation which gives better fit than Andrade's equation, although it has been tested on a limited number of materials, was proposed by Garofalo [130].

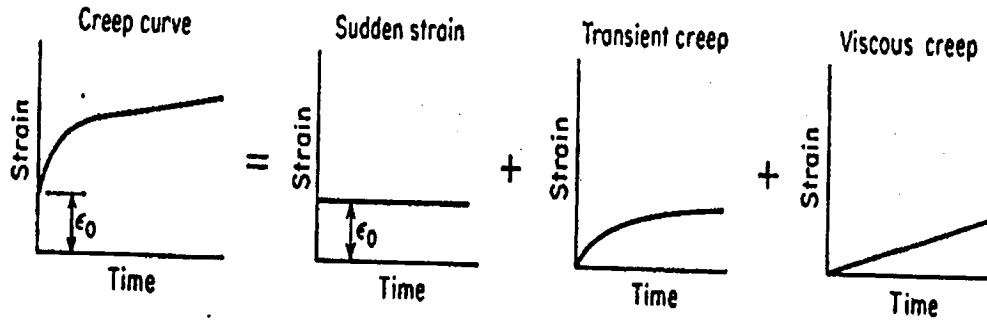


Figure 7 Andrade's analysis of the competing processes which determine the creep curve.

$$\epsilon = \epsilon_0 + \epsilon_t(1 - e^{-rt}) + \dot{\epsilon}_s t \quad (1)$$

where ϵ_0 = the instantaneous strain on loading

ϵ_t = the limit for transient creep

r = the ratio of transient creep rate to the transient creep strain

$\dot{\epsilon}_s$ = the steady-state creep rate

Although the instantaneous strain, ϵ_0 , is not really creep it is important because it may constitute a considerable fraction of the allowable total strain in machine parts. Sometimes the instantaneous strain is subtracted from the total strain in the creep specimen to give the strain due only to creep. In that case, the creep curve starts at the origin of coordinates. The first stage of creep, known as primary creep, represents a region of decreasing creep rate. Primary creep is a period of mainly transient creep in which the creep resistance of the material increases by its own capability to deform. For low temperature in the creep of lead at room temperature, primary creep is the major creep process. The second stage of creep, known also as secondary creep, is a period of

nearly constant creep rate which results from a balance between the competing processes of strain-hardening and recovery. For this reason, secondary creep is usually referred to as steady-state creep. The average value of the creep rate during secondary creep is called the minimum creep rate. For many relatively short-life creep situations (e.g., turbine blades in military aircraft and rocket motor nozzles), time to rupture or the rupture lifetime is the dominant design consideration. Empirical relationships have been developed in which the steady state creep rate as a function of stress is expressed as [131]:

$$\dot{\epsilon}_s = K_1 \sigma^n \quad (2)$$

where $\dot{\epsilon}_s$ is strain rate, σ is the mean stress, and K_1 and n are material constants. A plot of the logarithm of $\dot{\epsilon}_s$ versus the logarithm of σ yields a straight line with slope of n . Third-stage or tertiary creep mainly occurs in constant-load creep tests at high stresses and at high temperatures. Tertiary creep occurs when there is an effective reduction in cross-sectional area either because of necking or internal void formation. Third-stage creep is often associated with metallurgical changes such as coarsening of precipitate particles, re-crystallization, or diffusional changes in the phases that are present. Figure 8 shows the effect of applied stress on the creep curve at constant temperature. It is noticeable that a creep curve with three well-defined stages will be found for only certain combinations of stress and temperature. A similar family of curves is obtained for creep at constant stress for different temperatures. Higher temperature causes greater creep rate. The minimum creep rate is the most important design parameter derived from the creep curve. Two standards of this parameter are commonly used [60]:

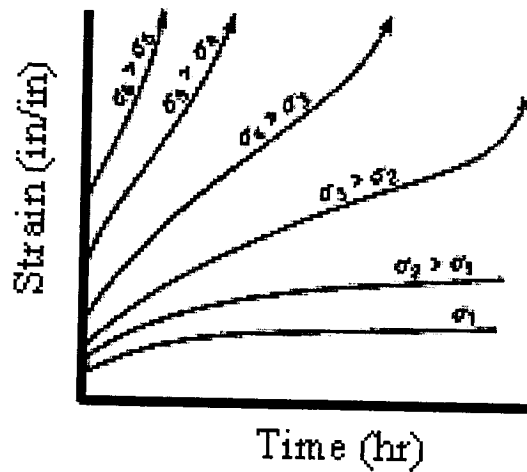


Figure 8 Schematic representation of the effect of stress on creep curves at constant temperature.

1. the stress to produce a creep rate of 0.0001 percent per hour or 1 percent/10,000 h
2. the stress for a creep rate of 0.00001 percent per hour or 1 percent/ 100,000 h (about 11.1 years).

The first criterion is more typical of the requirements for jet-engine alloys, while the last criterion is used for steam turbines and similar equipment. A log-log plot of stress versus minimum creep rate frequently results in a straight line. This type of plot is very useful for design purposes.

2.3. THE STRESS-RUPTURE TEST

The stress-rupture test is basically similar to the creep test except that the test is always carried out to the failure of material. Higher loads are used with the stress-rupture

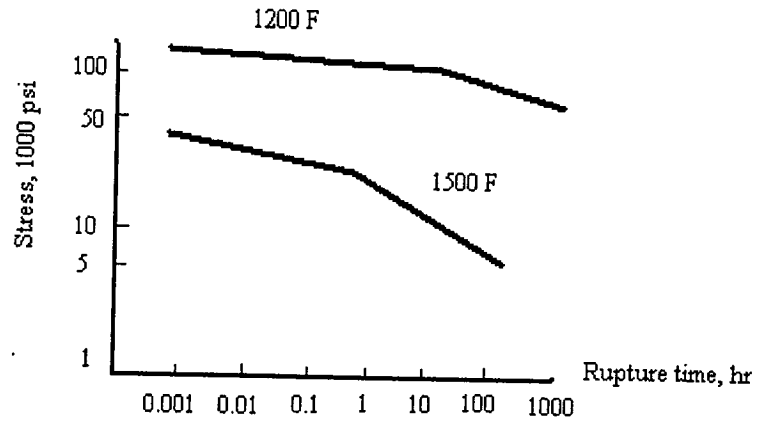


Figure 9 Method of plotting stress-rupture data (schematic).

test than in a creep test, and therefore the creep rates are higher. In the creep test the total strain is often less than 0.5 percent, while in the stress-rupture test the total strain may be around 50 percent. The stress is plotted against the rupture time on a log-log scale (Figure 9). A straight line will usually be obtained for each test temperature [60].

2.4. STRUCTURAL CHANGES DURING CREEP

The curve of creep rate versus total strain, Figure 10, illustrates the large change in creep rate which occurs during the creep test. Since the stress and temperature are constant, this variation in creep rate is the result of changes in the internal structure of the material with creep strain and time [60].

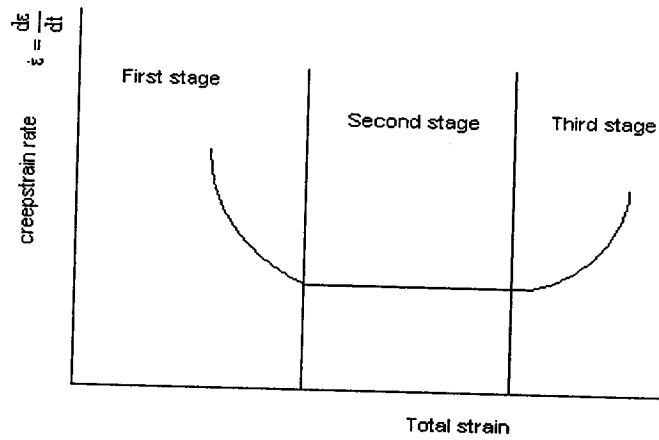


Figure 10 Strain rate in creep test as function of total strain.

The principal deformation processes at elevated temperature are slip, subgrain formation, and grain-boundary sliding. A number of secondary deformation processes such as grain-boundary migrations have been observed in metals at elevated temperature. Since different processes which occur at elevated temperature depend on the rate of strain as well as on the temperature, it is not always possible to extrapolate the results obtained for high strain-rate conditions to conditions of greater practical interest. If the deformation happens such that large strains can be achieved with essentially no strain hardening, it is called the hot working. Hot-working processes such as rolling, extrusion, or forging typically are used in the first step of converting a cast slab into a shaped product. The strain in hot-working is large compared with tension or creep tests. Hot-working usually is carried out at temperatures above $0.6T_m$. The temperature and stress dependence of the steady-state hot-working rate is given by Equation (3).

$$\dot{\epsilon}_s = Ae^{-Q/RT} \quad (3)$$

where $\dot{\epsilon}_s$ = the steady-state creep rate, h^{-1}

A = material constants

Q = activation energy for creep

R = the gas constant, 8.3145 joules per kelvin per mole ($J \cdot K^{-1} \cdot mol^{-1}$)

T = temperature, in Kelvin

and with the direct effect of both stress and temperature the following equation can be used [131],

$$\dot{\epsilon}_s = K_2 \sigma^n e^{-Q/RT} \quad (4)$$

where σ is the mean stress, and K_2 is constant. Further, Q is termed the activation energy for creep and it is the amount of energy which is needed to activate the creep function for the material.

2.5. FRACTURE AT ELEVATED TEMPERATURE

Early work of Rosenhain and Ewen [132] established that metals undergo a transition from transgranular fracture to intergranular fracture as the temperature is increased. When transgranular fracture occurs, the slip planes are weaker than the grain boundaries, while for intergranular fracture, the grain boundary is the weaker component. Jeffries [133] introduced the concept of the equicohesive temperature, ECT, which was defined as the temperature at which the grains and grain boundaries have equal strength (Figure 11a). Figure 11b shows that decreasing the strain rate lowers the ECT and

therefore increases the tendency for inter granular fracture. However, for high-purity material there is a wide range of temperature where the strengths of the grains and the grain boundaries are not very different (Figure 11c) so that transgranular fracture can occur up to rather high temperatures.

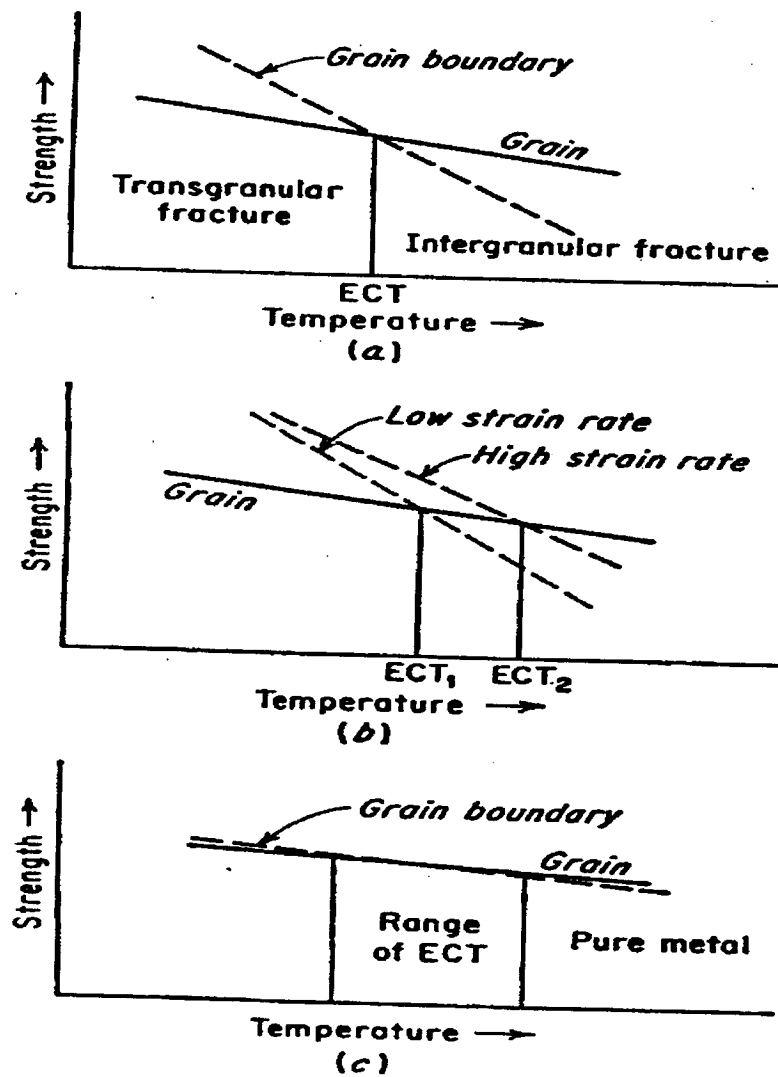


Figure 11 The equicohesive temperature [134].

2.6. HIGH-TEMPERATURE ALLOYS

High-temperature alloys are a class of complex materials developed for a specific application. Some of the metallurgical principles behind the development of these alloys are important. In general, the creep resistance alloys have higher melting point of the metals. The rate of self-diffusion is lower in metals with a high T_m .

2.7. PRESENTATION OF ENGINEERING CREEP DATA

For design purposes it is essential that decisions be based on experimental data. In reporting high-temperature strength data it is common to speak of creep strength or rupture strength. Creep strength is defined as the stress at a given temperature which produces a steady-state creep rate of a fixed amount, usually taken as 0.00001 or 0.0001 percent per hour. Alternatively, the creep strength may be defined as the stress to cause a creep strain of 1 percent at the given temperature. Rupture strength refers to the stress at a given temperature to produce a life to rupture of a certain amount, usually 1,000, 10,000, or 100,000 h. It frequently is important to be able to extrapolate creep or stress-rupture data into regions where data are not available. Therefore, the common methods of plotting creep data are based on plots which yield reasonable straight lines. Figure 12 shows the common method of presenting the influence of stress on the steady-state or minimum creep rate, which is a log-log plot. It has been shown [135] that the value of the minimum creep rate depends on the length of time that creep test has been carried out.

For precise determination of $\dot{\epsilon}_s$, creep curves which have entered the third stage of creep should be used. When $\dot{\epsilon}_s$ is based on creep curves of shorter duration, the value of minimum creep rate obtained is larger than the true value. Thus, the error is on the conservative side. Another method of presenting creep data is a plot of stress versus time to produce different amounts of total strain (instantaneous strain plus creep strain). The uppermost curve in Figure 13 is the stress-rupture curve. The percentages beside each data point are the percentage reduction of area at failure. For short-time high-temperature applications (such as in missiles and high speed aircraft), data are needed at higher temperatures and stresses and at shorter times than are usually determined for creep tests.

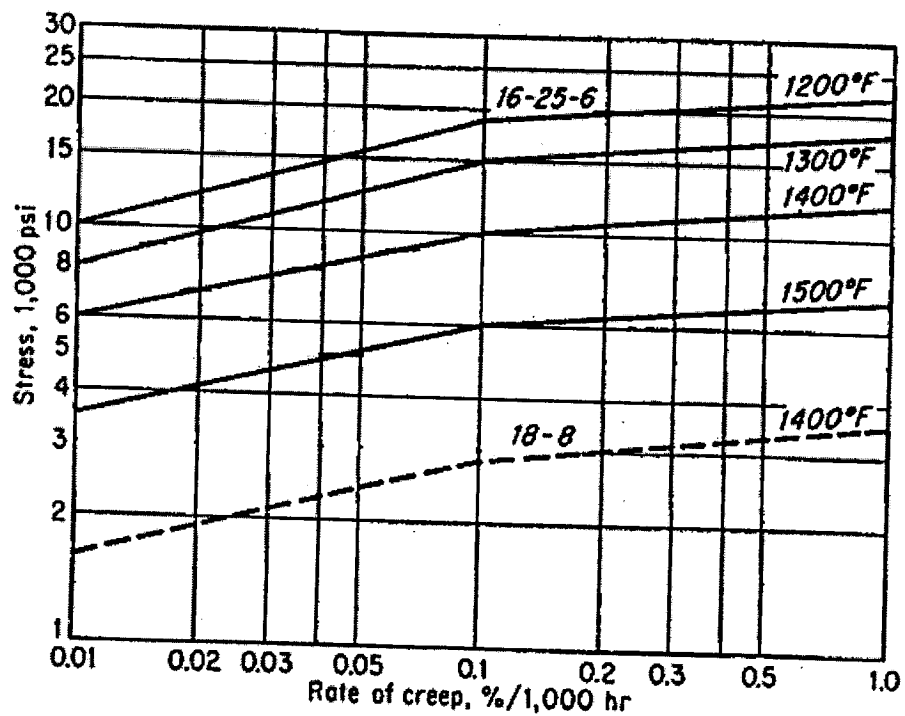


Figure 12 Plot of stress vs. minimum creep rate, for 16-25-6 alloy [134].

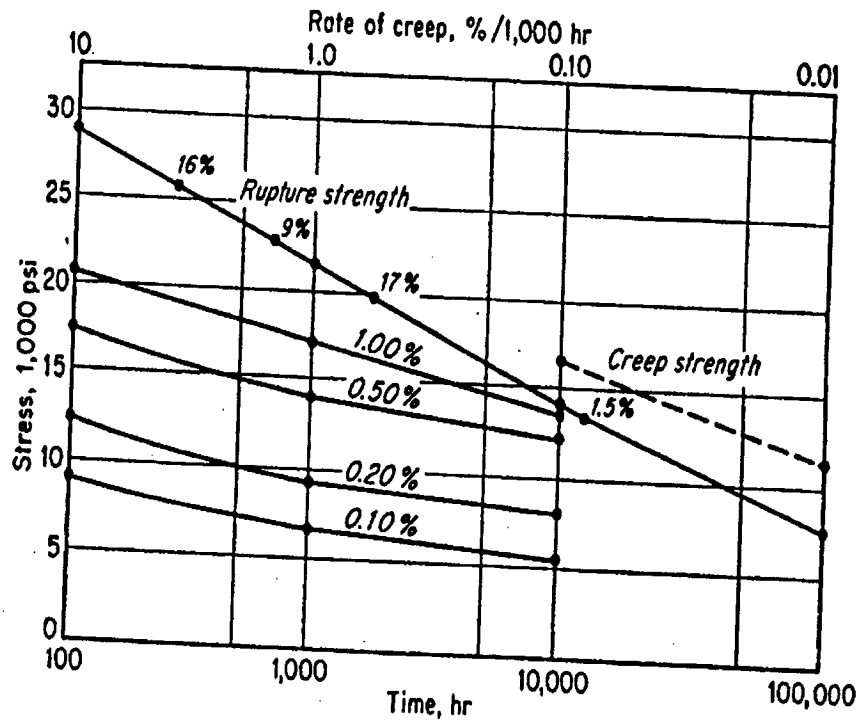


Figure 13 Deformation-time curves at 1300°F for 16-25-6 alloy [134].

2.8. PREDICTION OF LONG -TERM PROPERTIES

Frequently high-temperature strength data are needed for conditions for which there is no experimental information. This is particularly true of long-term creep and stress-rupture data, where it is quite possible to find that the creep strength to give 1 percent deformation in 100,000 h (11.4 years) is required, although the alloy has been in existence for only 2 years. Obviously, in such situations extrapolation of the data to longer term is required. Reliable extrapolation of creep and stress-rupture curves to longer times can be made only when it is certain that no structural changes occur in the region of extrapolation which would produce a change in the slope of the curve. Since structural

changes generally occur at shorter times for higher temperatures, one way of checking this point is to examine the log-stress-log-rupture life plot at a temperature several hundred degrees above the required temperature. For example, if in 1,000 h no change in slope occurs in the curve at 200° F above the required temperature, extrapolation of the lower temperature curve as a straight line to 10,000 h is probably safe and extrapolation even to 100,000 h may be possible.

Certain useful techniques have been developed for approximating long-term creep behavior based on a series of short-term tests. Data from creep testing may be cross plotted in a variety of different ways. The basic variables involved are stress, strain, time, temperature, and perhaps strain rate. Any two of these basic variables may be selected as plotting coordinates, with the remaining variables to be treated as parametric constants for a given curve. Three commonly used methods for extrapolating short-time creep data to long-term applications are the abridged method, the mechanical acceleration method, and the thermal acceleration method.

2.8.1. Abridged Method

In this method the tests are conducted at several different stress and temperature levels. As shown in Figure 14, the data are plotted as creep strain versus time for a family of stress levels, all run at constant temperature. The curves are plotted out to the laboratory test duration and then extrapolated to the required design life. The design specifications will dictate a limiting design strain that will intersect the design life.

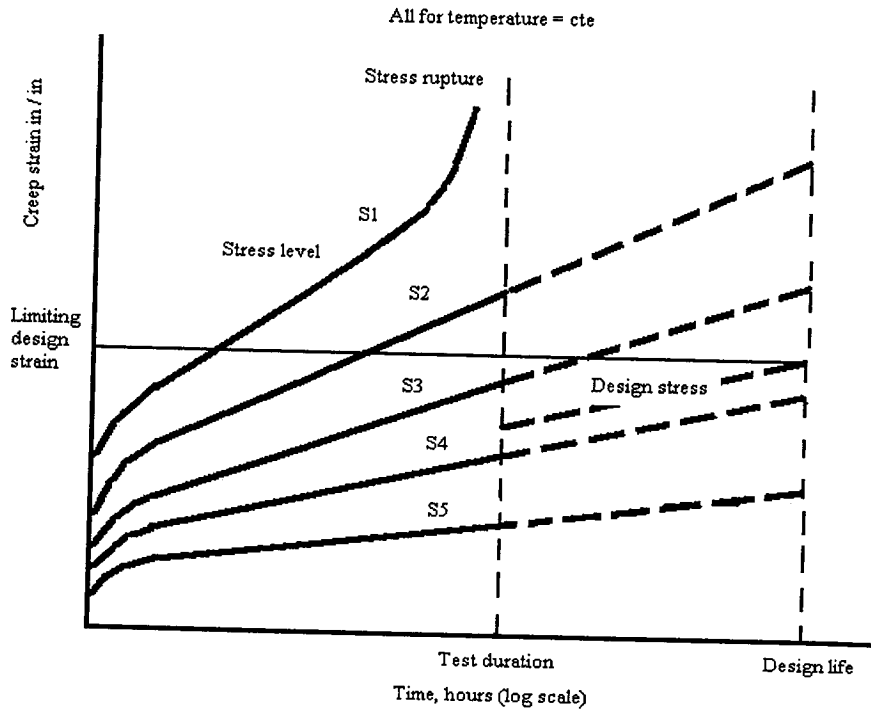


Figure 14 Abridged method of creep testing.

2.8.2. Mechanical Acceleration Method

In this method, the stress levels used in the laboratory tests are significantly higher than the contemplated design stress levels, so that the limiting design strains are reached in a much shorter time than in actual service. The data taken in the mechanical acceleration method are plotted as stress level versus time, as shown in Figure 15, for a family of constant strain curves, all run at a constant temperature. As shown in the figure, the stress rupture curve may also be plotted by this method. The constant strain curves are plotted out to the laboratory test duration and then extrapolated to the design life.

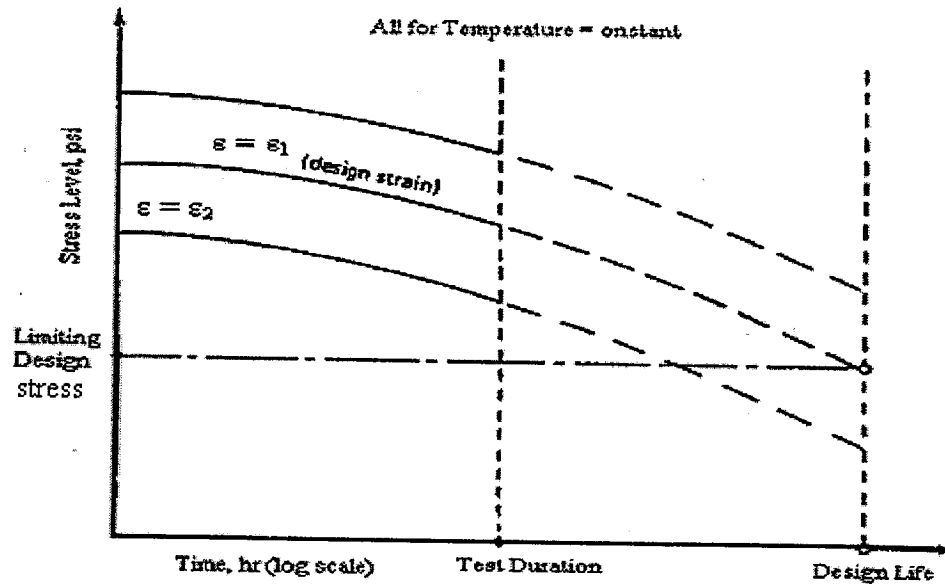


Figure 15 Mechanical acceleration method of creep testing.

2.8.3. Thermal Acceleration Method

The thermal acceleration method involves laboratory testing at temperatures much higher than the actual service temperature expected. As shown in Figure 16, the data are plotted as stress versus time for a family of constant temperatures where the creep strain produced is constant for the whole plot. It may be noted that stress rupture data may also be plotted in this way. As an aid in extrapolation of stress-rupture data, several time-temperature parameters have been proposed for trading off temperature for time. The basic idea of these parameters is that they permit the prediction of long-time rupture behavior from the results of shorter time tests at higher temperatures at the same stress. Noting that $\epsilon = te^{-Q/RT}$ in Equation (3) and taking the logarithm of both sides of this equation:

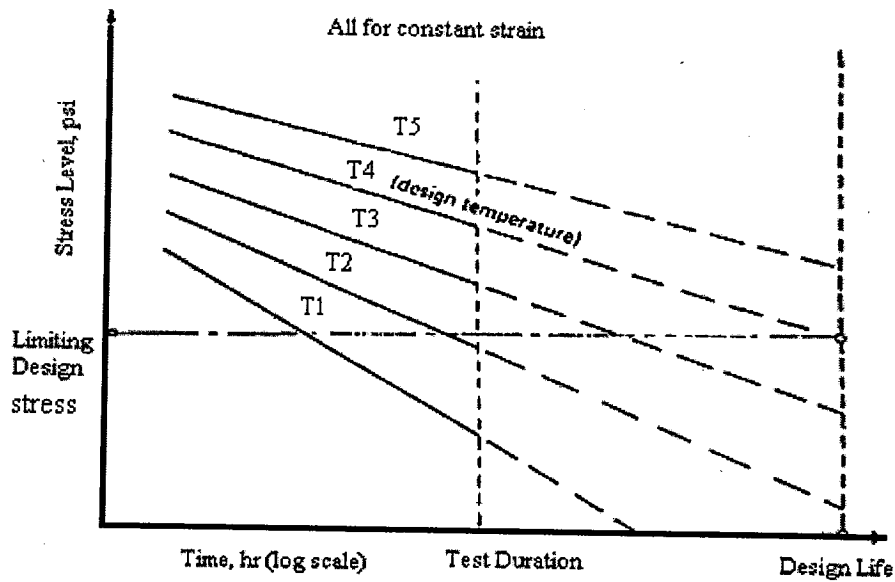


Figure 16 Thermal acceleration method of creep testing.

$$\text{Log } \epsilon = \text{Log } t - M (Q/RT)$$

$$\text{Log } t = \text{Log } \epsilon + MQ/RT \quad (5)$$

where $M = \text{Log } e = 0.434$. If ϵ and Q/R are functions of stress only, then Equation (5) is linear in $\text{Log } t$ and $1/T$. Larson and Miller [136] plotted experimental stress-rupture data in accordance with Equation (5), see Figure 17. Since the line for each constant stress converges to a common point on the $\text{log } t$ axis this plot indicates that Q varies with stress but ϵ does not. The point of convergence is $\text{log } \epsilon = -C_1$. For most alloys C_1 varies from about 15 to 25 depending on material. Figure 17 also indicates that the slope $b = (M/R)Q$ is a function of stress. From Equation (5) the Larson-Miller parameter can be formulated as:

$$T(C_1 + \text{Ln } t_R) = b = f(\sigma, T) = P \quad \text{or} \quad T(C_1 + \text{Ln } t_R) = P \quad (6)$$

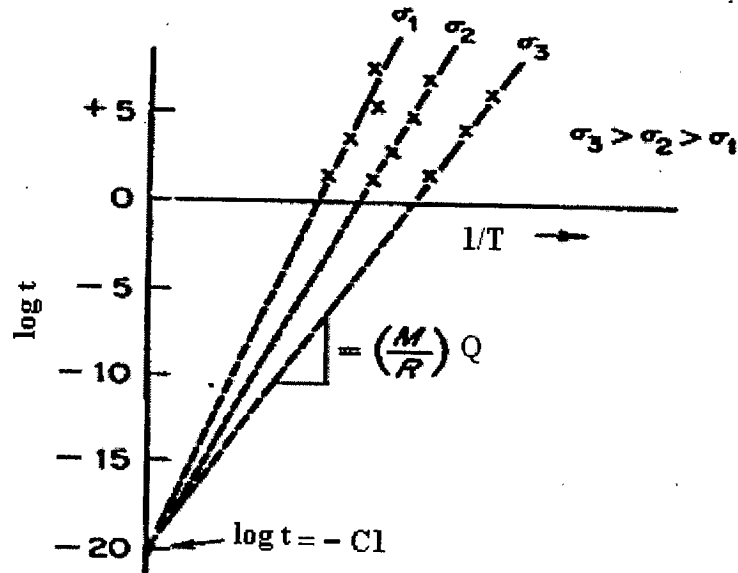


Figure 17 Stress-rupture data at various stresses plotted according to Equation (5) [134].

where T = the test temperature, $^{\circ}R = ^{\circ}F + 460$

t = the time to rupture (h)

C_1 = the Larson-Miller constant often assumed to be 20

Table 1 Time compression of operating conditions based on Larson- Miller parameter $C_1=20$.

<u>Operating conditions</u>	<u>Larson-Miller test conditions</u>
10,000 h at 1000°F	13 h at 1200°F
1,000 h at 1200°F	12 h at 1350°F
1,000 h at 1350°F	17 h at 1500°F

Table 1 illustrates how Equation (6) provides a time compression at the expense of increased temperature. When "trading-up" in temperature through the Larson-Miller

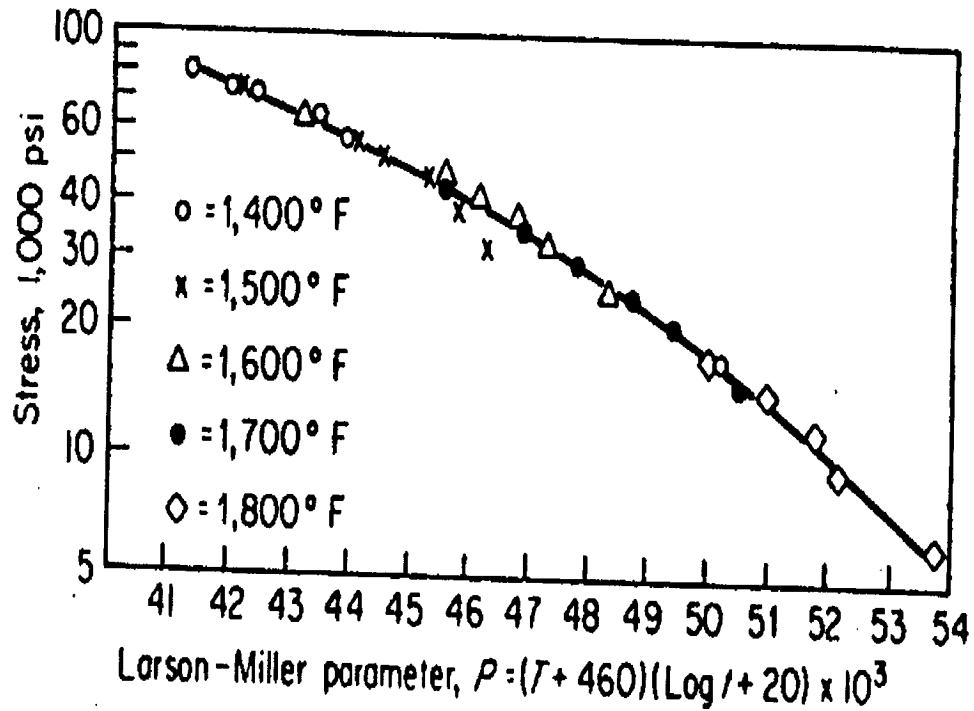


Figure 18 Master curve for Larson-Miller parameter for Astroloy [134].

parameter, it is important to be sure that the higher-temperature does not cause a change in metallurgical structure. If P_1 is evaluated for pairs of t and T obtained over a range of stress, a single master curve is obtained for the material (Figure 18).

2.9. ONE-DIMENSIONAL CREEP MODELING USING ANSYS

This section summarizes the details of an analytical application tool that has been created to predict the creep life of a gas turbine engine blade. This application creates an ANSYS [137] macro, which is called "Creep-1D". The macro is developed in ANSYS Parametric Design Language (APDL) using ANSYS creep models. Creep-1D macro

creates a one-dimensional geometry to simulate an equivalent blade model. This geometry is based on the blade radial coordinates with the corresponding sectional areas using Link180 element- a 3D beam element. The macro stops when user defined criteria, which are number of missions and creep strain limit, are met. To execute the macro, four input files and eleven command line arguments are needed. Hot section components of gas-turbine engines are subject to severe thermo-mechanical loads during each mission cycle. Life assessment of engine hot-section components requires knowledge of the thermal environment, material characterization, calibrated failure data, structural response at the critical location for crack initiation. Creep is one of the most important phenomena affecting the lifetime of the gas turbine engine components due to the exposure to high temperature. Creep behavior usually appear, for a metal alloy when temperature is more than 40% of melting point [131].

2.10. THEORIES FOR CREEP CALCULATIONS

In practice, creep often occurs under non-steady conditions. Methods have been devised to predict the behavior of the material under non-steady conditions from data obtained under steady conditions. There are basically four rules for creep calculations:

- Strain hardening
- Time hardening
- Life fraction
- Energy hardening

2.10.1. Tabular Material Format (Primary and Secondary Creep)

The creep data in tabular form is used to predict the creep strain in primary, secondary and tertiary regions. Experimental results stored in Tabular Material Format are used directly to predict the creep strain at different stations. The creep data table (one from each strain condition) consists of tabulated values of stress (at various temperatures) at different times. However, for stress rupture condition, the values of creep strain could be different for different temperatures. For some of the strain conditions, data have been obtained by an interpolation scheme. Three (0.5%, 1 %, and rupture) or four (0.5%, 1 %, 2% and rupture) strain data points available in the material manual are sufficient for the scheme used by this program to generate the creep curves. The temperature of station at time i , T_i , and the corresponding stress, σ_i , are calculated using Equations (3) and (4). The strain-hardening rule is used to determine the cumulative creep strain (Figure 19). Logarithmic interpolation is used to calculate the creep life at each station at time t_i given by:

$$\log_{10} t_i = \log(t_{i-1}) + \left[\frac{\log(\sigma_{i-1}) - \log(\sigma_i)}{\log(\sigma_{i-1}) - \log(\sigma_{i+1})} \right] \times [\log(t_{i+1}) - \log(t_{i-1})] \quad (7)$$

where

t_{i-1} : time corresponding to σ_{i-1}

t_{i+1} : time corresponding to σ_{i+1}

σ_{i-1} : stress at time t_{i-1}

σ : stress at time t_i

σ_{i+1} : stress at time t_{i+1}

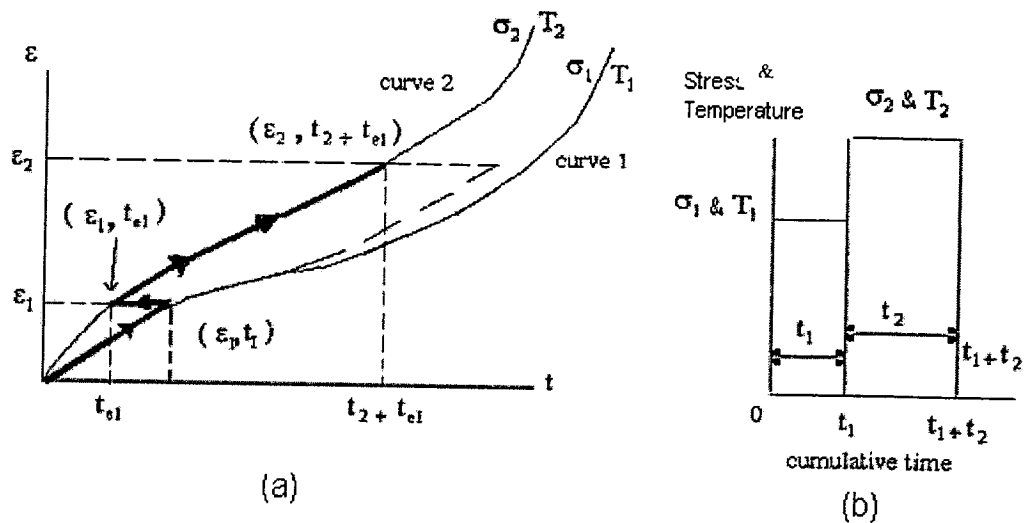


Figure 19 Strain hardening rule.

Typical example of experimental test data and also the procedure of creep strain calculations are presented in appendix B. The strain-hardening rule is based on the assumption that the major factor governing the creep is the amount of prior strain. This idea is shown in Figure 19, where the total creep strain would be calculated by adding the ϵ_i increments. Note that under this assumption the operational path moves horizontally from one curve to the other along lines of constant strain. Considering the case where a virgin material has been creeping under a stress σ_1 at a temperature T_1 for a time interval t_1 , and at the end of which, the values of these parameters are suddenly changed to σ_2, T_2 and remain there for another time interval t_2 (Figure 19b). During the first part of the test, the mathematical creep following the σ_1, T_1 follows curve 1 to reach a level of creep strain point (ϵ_1, t_1) . Under the several loading conditions the stress and temperature will be changed and the material will follow different curves. For instance, at point (ϵ_1, t_1) the curve (σ_2, T_2) will be followed, starting from a point ϵ_1 and t_{e1} (see arrows in Figure 19a).

The term t_{e1} is called the equivalent time, which is time required to undergo creep strain ϵ_1 when subjected to stress σ_2 and temperature T_2 .

2.10.2. Creep Strain Calculation for a Mission in Terms of T_4 and Angular Velocity

This option will be used to calculate temperatures and stresses at the blade station at various times from the given values of T_4 and angular velocity at a reference condition. It will be used just as an alternative for providing the temperature and stress data for all stations in detail.

2.11. ONE DIMENSIONAL CREEP MACRO

The 1-D Creep macro is the first step towards development for 3-D creep applications. ANSYS has 12 implicit models for creep strain calculations. Seven of those are for primary creep strain, three for secondary creep strains, and two for both primary and secondary creep strains. The macro runs ANSYS creep model number six for primary creep and model number 11 for primary and secondary creep. It then outputs maximum creep strain, temperature and stress at the corresponding element. In order to run the macro, the following ten arguments,

1. Number of missions
2. Material deterioration (temperature)

3. Creep option 1(on) or 0(off)
4. Nonlinear geometry 1(on) or 0(off)
5. Geometry filename
6. Load filename
7. Creep strain limit
8. Material properties filename
9. Creep constant filename
10. Creep ratio

and the following four input files;

1. Geometry
2. Load
3. Material properties
4. Creep constants

are required. Typical data and format of the input files are presented in Appendix C.

2.11.1. ANSYS Material Input for Creep

ANSYS has the capability of modeling the primary and secondary creep stages. The tertiary stage is usually not analyzed since it implies impending failure. ANSYS calculates the creep strain using either implicit or explicit time integration method. Both are applicable to static or transient analyses. The implicit creep method is robust, fast, accurate, and recommended for general use. It can handle temperature dependent creep

constants, as well as simultaneous coupling with isotropic hardening plasticity models. The explicit creep method is useful for cases where very small time steps are required.

2.11.2. ANSYS Creep Model # 6 (Primary Creep)

The ANSYS model number six is used for primary creep, since it is the only primary creep equation on the base of creep strain, while the others are on the base of creep strain rate. Model six predicts the creep strain using the following relationship:

$$\epsilon_{cr} = C_1 \sigma^{C_2} t^{C_3+1} e^{-C_4/T} / (C_3 + 1) \quad (8)$$

where

- ϵ_{cr} : the creep strain
- C_1 to C_4 : material creep constants defined by the TBDATA command
- T : metal temperature of each element in K (ANSYS help sec. 2.5.7)
- t : time at end of substep
- σ : equivalent stress at time t

ANSYS creep model six is equivalent to the Norton power creep law (Equation 9),

where: $C_1 = A \times N$, $C_2 = M$, $C_3 = N - 1$, $C_4 = 0.0$

$$\epsilon_{cr} = A \sigma^M t^N \quad (9)$$

2.11.3. ANSYS Creep Model # 11 (Primary and Secondary Creep)

ANSYS creep model 11 is used for primary creep, secondary creep as well as the rupture time, since it is the only equation on the base of creep strain, which calculates creep strain; the others calculate the creep strain rate. Model 11 uses the following equation to calculate the primary and secondary creep strains. The first part of the equation is exactly the same as Equation (6) and the second part is for the secondary creep:

$$\varepsilon_{cr} = C_1 \sigma^{C_2} t^{C_3+1} e^{-C_4/T} / (C_3 + 1) + C_5 \sigma^{C_6} t e^{-C_7/T} \quad (10)$$

where

- ε_{cr} : the equivalent creep strain
- C_1 to C_7 : material creep constants defined by the TBDATA command
- T : metal temperature of each element
- t : time at end of substep
- σ : equivalent stress at time t

2.11.4. Geometry

The macro creates the geometry of the blade based on the radial coordinates and corresponding area using Link180, a 3-D beam element. The average area between nodes i and $i+1$ is taken as the area of the i -th element. In the case of shrouded blades, in order to consider the effect of the sudden change of area and also, the concentrated huge mass

at the tip of the blade, the area of the shroud is considered as the area of the tip of the blade.

2.11.5. Temperature History

Initial temperatures of all nodes as a function of time, at different stations, can be input manually. Temperature can be calculated at different blade stations for a given T_4 , using temperature distribution input for at least two references T_4 . The temperature history of the blade at each station is calculated using linear interpolation between each reference temperature provided by the user.

$$T_{ij} = T_{1j} + \frac{T_{4i} - T_{41}}{T_{42} - T_{41}} (T_{2j} - T_{1j}) \quad (11)$$

where

T_4 : gas path temperature

T_{41} : minimum T_4

T_{42} : maximum T_4

T_{4i} : T_4 at time t_i

T_{ij} : temperature at station j at time t_i , in °F

T_{1j} : minimum blade temperature at station j , at T_{41}

T_{2j} : maximum blade temperature at station j , at T_{42}

The macro uses Equation (11) to calculate the temperature history. The macro reads the load from an input file. The load file includes time divisions of one mission t_i , blade angular speed at each time, N_i , T_4 at each time, T_{4i} , minimum and maximum T_4 , and minimum and maximum of blade metal temperature. Then it takes the temperature of the elements from the input file. In order to model the higher temperature conditions, temperature of node $j+1$ is used for element j .

2.11.6. Stress History

The macro follows the following equation to find the stress at element j representing the blade stress at cumulative time t :

$$\sigma = \frac{F + m_j R_j N^2}{A_j} \quad (12)$$

where

F : centrifugal force above element j

m_j : mass of the element

R_j : radius of rotation

N : angular speed at time t_i

A_j : average area of node j and $j+1$

2.12. ANALYSIS

2.12.1. Mathematical Material Model Versus ANSYS Creep Model # 6

The same geometry, load conditions and material of the existing FORTRAN code are applied in ANSYS creep model six. The stress output of the Mathematical Material Model and ANSYS creep model six are comparable (Appendix D). The creep strains versus time of both models are shown in Figure 20. The constant difference is due to nonlinear geometry and also changes of Modulus of Elasticity, E , by temperature that ANSYS takes into consideration. It can be seen that the ANSYS creep strain is always a bit more than the FORTRAN code creep strain. In other words, the life of the specified strain from FORTRAN code is a bit more than ANSYS life.

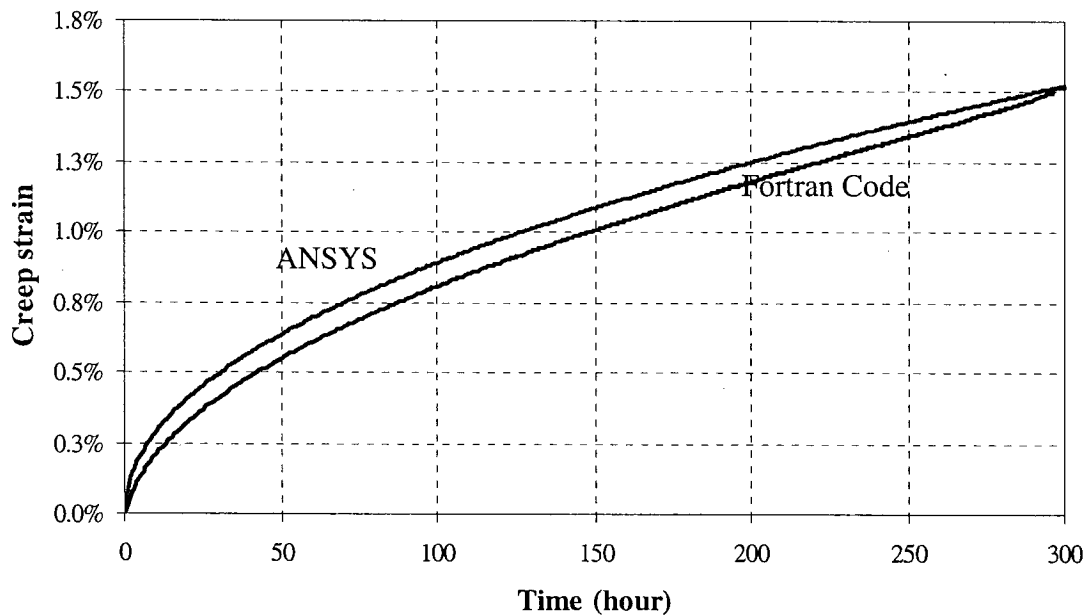


Figure 20 Creep strain of the mathematical material model and ANSYS creep model # 6.

2.12.2. Tabular Material Format and ANSYS Creep Model # 11

The same geometric and load conditions of the FORTRAN code Tabular Material Format are applied in ANSYS creep model 11. To compare the effects of linear and nonlinear geometry, the creep strain calculation using ANSYS model # six with constant stress also has been done. Figure 21 shows the creep strain of the Tabular Material Format, ANSYS creep model 11 with constant stress (linear geometry), and the creep curve of ANSYS equation with nonlinear geometry effect (1D creep macro). Figure 21 shows that ANSYS creep model # 11 with constant stress, for a given strain, predicts higher time. The time predicted by The Tabular Material Format at primary stage is lower than that given by the ANSYS creep model # 11, but at secondary stage it gives higher time, due to nonlinear

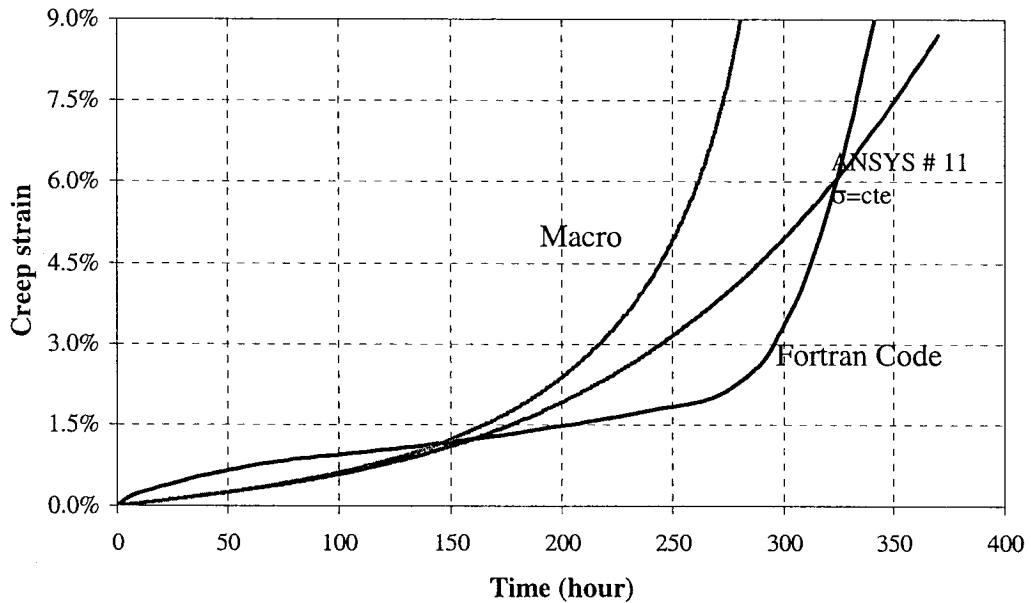


Figure 21 Creep strain of the tabular material format and ANSYS creep model # 11.

geometry and also changes of Modulus of Elasticity, E, by temperature that ANSYS takes into consideration. The difference for this stage is almost constant. The results of macro using ANSYS model 11, and Tabular Material Format of the FORTRAN code are illustrated in Appendix D.

2.12.3. Parameter Sensitivity

The effect of five different T_4 sequences on rupture strain has been investigated. The following sequences using material CPW658 have been selected to model the real situation of a mission in an aircraft flight. In this example, the total mission time is 1 hour. Power throttle movement between each condition is typically 5 sec., and therefore the transient duration between each mission condition was set to this value. Temperatures of four cases vary between 962.78°C (1765°F) and 1007.22° (1845°F) and case 3 has the constant average temperature of 1805°F. As an example, case 5 is explained as follows (Figure 22):

The mission starts at T_4 temperature of 962.78°C (1765°F) and continues for 900 seconds. In 5 seconds the T_4 shifts to 1006.11° (1843 °F) and continues up to 2700 seconds. Again in 5 seconds the T_4 drops to 962.78°C (1765°F), after which it remains constant to the end of the mission (3600 seconds). Some investigations were also done on creep ratio with ANSYS macro: In both The FORTRAN code and ANSYS, case 3 (constant average temperature) predicts about 20% higher lifetime, i.e. the temperature variations reduce the lifetime and creep strain. In the FORTRAN code, Case 3 analysis gives about 10% higher

rupture creep strain in comparison with the other four cases. However, for case 3 the ANSYS macro gives about $\pm 10\%$ difference in rupture creep strain with the other four loading cases. In both the FORTRAN code and ANSYS the sequence of the loading does not affect the lifetime and rupture creep strain.

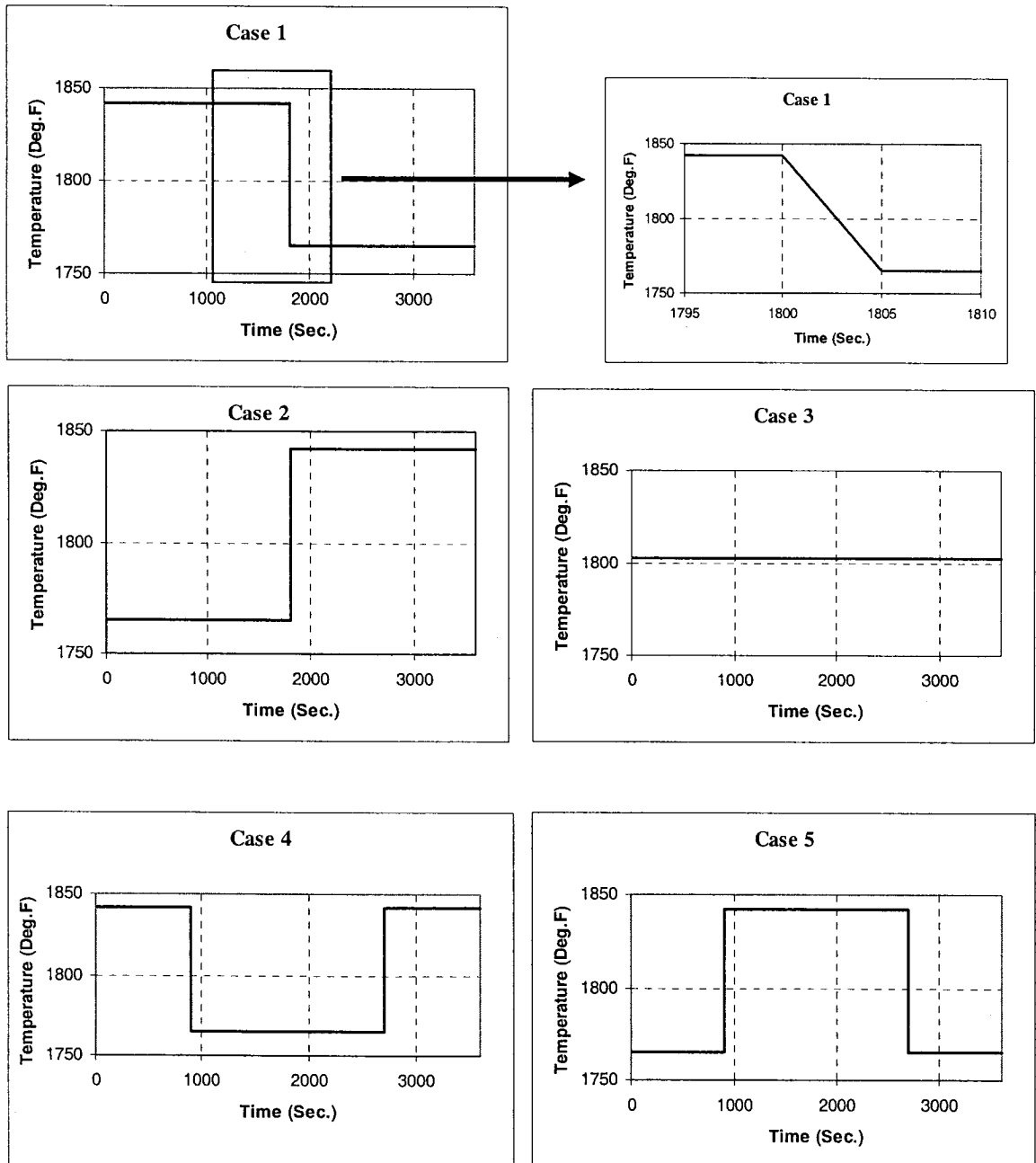


Figure 22 Temperature histories.

The ANSYS macro has been developed with a feature “Fast Run”. In this case instead of running for, “n” number of one-hour missions, we can run for one n-hour mission. The results show that with a creep ratio from 0.1 to 1, the lifetime and the rupture creep strain for this case is comparable with those of the FORTRAN code. When the creep ratios are more than 1, they do not give accurate results. Based on the required accuracy and the run time, any creep ratio from 0.1 to 1 can be selected (Appendix D). The main difference is for the tertiary part of the creep curve. The higher the creep ratio, the higher the lifetime and rupture creep strain and lower the run time.

It is worth noting that due to inherent nature of nonlinearity of the creep phenomenon, a creep run with linear geometry is meaningless. Thus for a creep run, we have to keep its relevant argument in the macro “on”.

2.13. CONCLUSIONS

A one-dimensional creep macro is created to calculate creep life of a gas turbine blade using ANSYS creep models 6 and 11. The FORTRAN code options as well as ANSYS models are compared.

2.13.1. The Mathematical Material Model and ANSYS Creep Model # 6

The creep strain of these two models is comparable with constant difference. The ANSYS creep model six always predicts shorter lifetime.

2.13.2. The Tabular Material Format and ANSYS Creep Model # 11

These two models calculate different “times” for a given strain, due to the fact that ANSYS takes into consideration the nonlinear geometry, and also changes of modulus of Elasticity, E , with temperature. The creep strain predicted by the FORTRAN code at primary stage is larger than that of the ANSYS one, but at secondary stage ANSYS calculates larger creep strain, due to above-mentioned facts. The FORTRAN code needs the initial stresses, which must be calculated, whereas the macro calculates the stresses using ANSYS. In FORTRAN code, the number of elements is limited to 15. Although there is no limitation for the number of elements in ANSYS, the number of elements in the macro is limited to 1000, and can be increased, if needed.

In this chapter, the creep phenomenon and its effects on gas turbine blade was explained, and the governing equations were presented. The life prediction in gas turbine component was discussed and the 1-D creep model which was programmed in ANSYS was explained. In the next chapter, the cumulative fatigue and the life prediction will be discussed. Also the universal slope and the effect of mean stress will be clearly explained.

CHAPTER 3

CUMULATIVE FATIGUE AND LIFE PREDICTION

In the previous chapter, the creep phenomenon and its effects on gas turbine blade was explained, and the governing equations were presented. The life prediction in gas turbine component was discussed and the 1-D creep model which was programmed in ANSYS was explained. In this chapter, the cumulative fatigue and the life prediction are discussed. Also the universal slope and the effect of mean stress are clearly explained.

3.1. INTRODUCTION

A metal subjected to repetitive or fluctuating stress will fail at a stress much lower than that required for failure on a single application of load. Failure occurring under cyclic loading is termed fatigue failure. Vibrational stresses on turbine blades, alternating bending loads on blades and shafts, and fluctuating thermal stresses during start-stop cycles and due to power changes are some examples of cyclic loading that can occur in a plant. For convenience two types of fatigue are distinguished: high cycle fatigue (HCF) and low cycle fatigue (LCF).

HCF resulting in the loss of gas turbine engine blades or disks is currently the predominant surprise engine failure mode after the completion of engine development. This is a direct result of the introduction of high thrust-to-weight ratio engines, accomplished by increasing the mass flow and utilizing fewer parts. HCF of turbomachinery blading is a significant design problem because fatigue failures can result from resonant vibratory stresses lasting over a relatively short time. Fatigue failure results from a combination of steady stress, vibratory stress, and material imperfections. Advanced turbomachinery blading is designed to have high steady stress levels. Thus, HCF occurs because of high mean stress - low amplitude vibratory loading of the airfoils. The root cause of the vibratory stress is flow-induced vibrations. It is not always possible to eliminate the sources of forced vibration from the operating range of a turbomachine. Because a blade may have as many critical points of high stress as it has natural modes, the designer must determine which particular modes have the greatest potential for aerodynamic excitation. This requires the prediction of the resonant aerodynamically forced vibration response and vibratory stress of the airfoil. Most failures in machinery are due to time-varying loads rather than to static loads. These failures typically occur at stress levels significantly lower than the yield strengths of the materials. Long before, the (Linear Elastic Fracture Mechanics) LEFM-based approaches (e.g. Paris Law, 1963) [138] to characterize fatigue failure were developed; the importance of cyclic (alternating) loading in causing failures (e.g. railroad axles) was recognized. Because of the severe conditions of gas turbine blades, specific features of fatigue crack growth in blades have been considered and a method for predicting their propagation taking into account the main factors has been justified [139].

3.2. CYCLIC LOADING

Most laboratory fatigue testing is done either with axial loading or bending, thus producing only tensile and compressive stresses. The stress usually is cycled either between a maximum and a minimum tensile stress or between a maximum tensile stress and a maximum compressive stress. The latter stress is considered a negative tensile, is assigned an algebraic minus sign, and therefore is known as the minimum stress. There are some necessary terms that should be explained first.

Definitions

A typical stress history during cyclic loading is depicted in Figure 23. Important parameters to characterize a given cyclic loading history are:

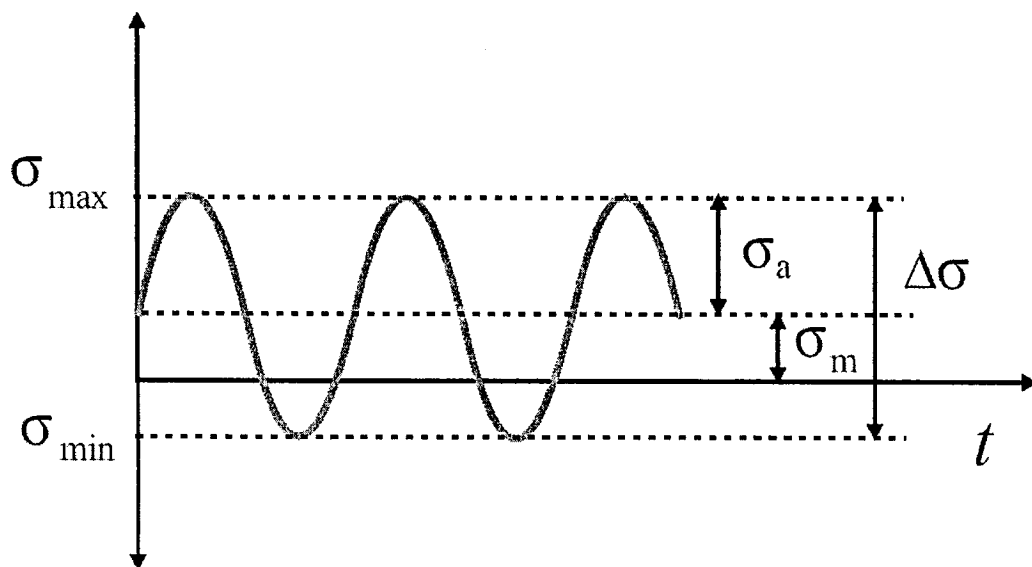


Figure 23 Typical cyclic loading.

Stress Range: $\Delta\sigma = \sigma_{\max} - \sigma_{\min}$

Stress Amplitude: $\sigma_a = \frac{1}{2}(\sigma_{\max} - \sigma_{\min})$ (13)

Mean Stress: $\sigma_m = \frac{1}{2}(\sigma_{\max} + \sigma_{\min})$

Load Ratio: $R = \frac{\sigma_{\min}}{\sigma_{\max}}$

Frequency

Frequency is the number of cycles per second and is denoted as ν or f in units of Hz. For instance for rotating machinery at 3000 rpm, $f \approx 50$ Hz. In general, only influences of fatigue are critical if there are environmental effects present, such as humidity or elevated temperatures. The waveform can be a sine wave, square wave, or some other waveforms.

S-N Curve

If a plot is made of the applied stress amplitude versus the number of cycles of stress reversals to failure (S-N curve) the behavior shown in Figure 24 is typically observed:

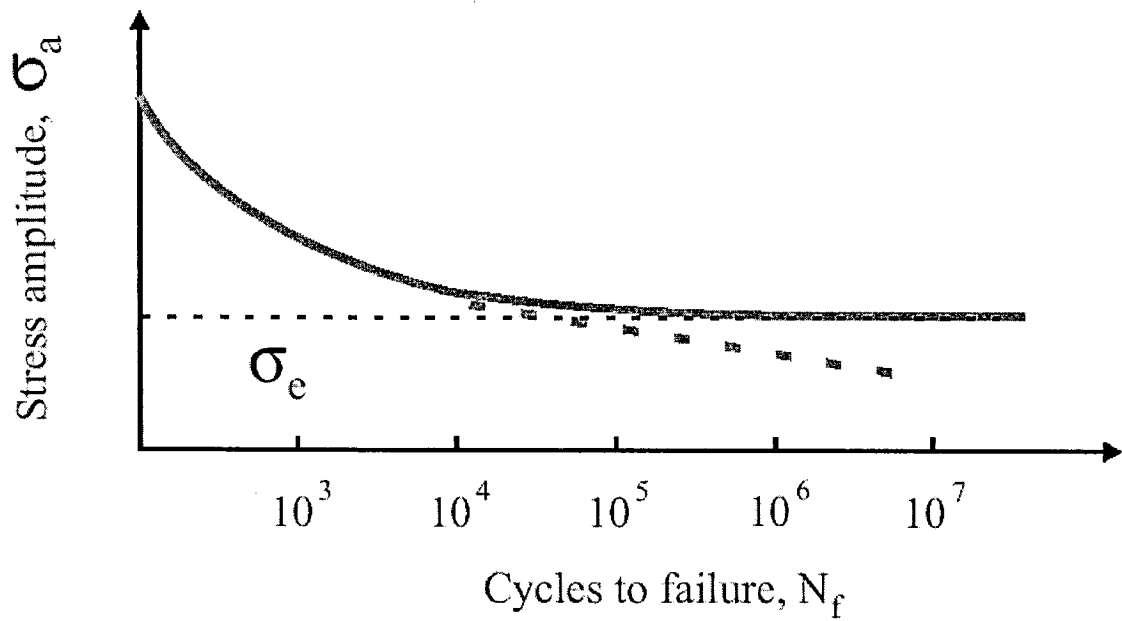


Figure 24 Typical S-N curve.

Endurance Limit

If the stress is below σ_e (the endurance limit or fatigue limit), the component has effectively infinite life. For most steels and copper alloys $0.35\sigma_{TS} \leq \sigma_e \leq 0.50\sigma_{TS}$.

If the material does not have a well defined σ_e , often σ_e is arbitrarily defined as the stress that gives

$$N_f = 10^7 \quad (14)$$

3.3. FATIGUE FAILURE MODELS

Based on the number of stress or strain cycles that the part is expected to undergo in its lifetime, it is either a low-cycle fatigue (LCF) regime or a high-cycle fatigue (HCF) regime. There is no sharp dividing line between the two regimes, and various investigators suggest slightly different divisions. On an average $N=1000$ cycles is a reasonable approximation of the divide between LCF and HCF. There are three fatigue failure models in current use and each has a place and purpose. They are the stress-life (S-N)¹ approach, the strain-life (ϵ -N) approach, and the linear-elastic-fracture-mechanics (LEFM) approach.

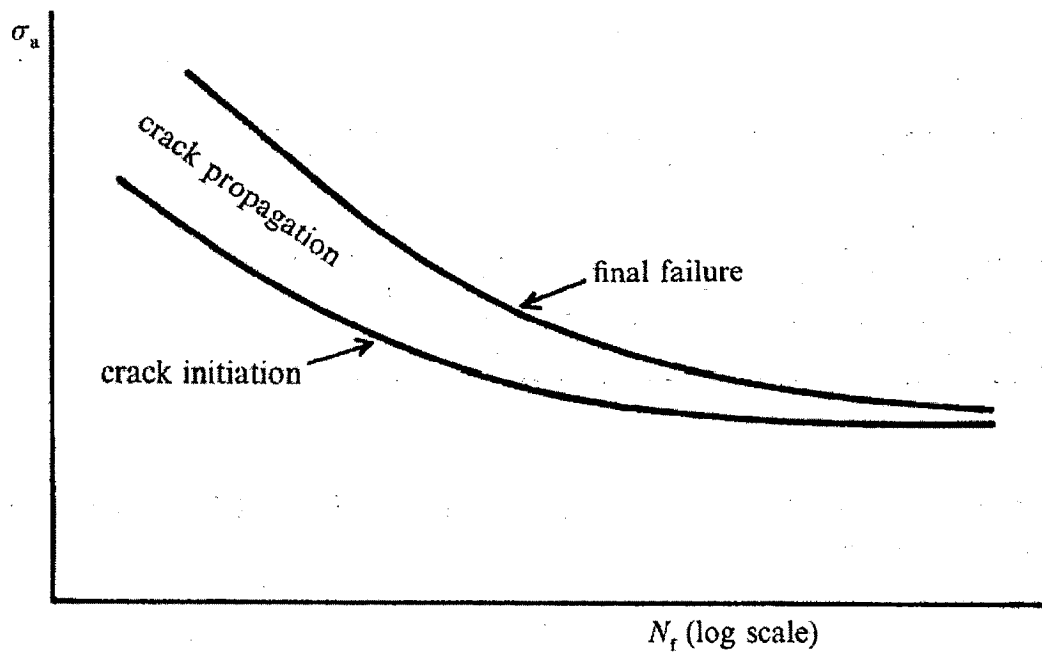


Figure 25 Total fatigue life parts.

¹. In this text two notations has been used for stress, S and σ .

3.3.1. Stress-Life Approach

If a plot is prepared of $\log(\sigma_a)$ versus $\log(2N_f)$ (where $2N_f$ represents the number of reversals to failure, one cycle equals two reversals) a linear relationship is commonly observed. Basquin [140] has proposed the following relationship between stress amplitude and lifetime:

$$\frac{\Delta\sigma}{2} = \sigma_a = \sigma'_f (2N_f)^b \quad (15)$$

In this expression σ'_f is the fatigue strength coefficient (for most metals $\approx \sigma_f$, the true fracture strength), b is the fatigue strength exponent or Basquin's exponent (≈ -0.05 to -0.12), and $2N_f$ is the number of reversals to failure. The total fatigue life of a component can be considered to have two parts, the initiation life and the propagation life, as depicted in Figure 25. The stress-life or S-N approach is the oldest and the least accurate of the three models and is the most often used for high-cycle fatigue (HCF) applications. It seeks to determine fatigue strength and/or endurance limit (σ_e) for the material so that the cyclic stress can be kept below that level and failure avoided for the required number of cycles. The assumption is that stresses and strains everywhere remain in the elastic region and no local yielding occurs to initiate a crack. If the stress is below σ_e (the endurance limit or fatigue limit), the component has effectively infinite life. For most steels and copper alloys $0.35\sigma_{TS} \leq \sigma_e \leq 0.50\sigma_{TS}$ is valid.

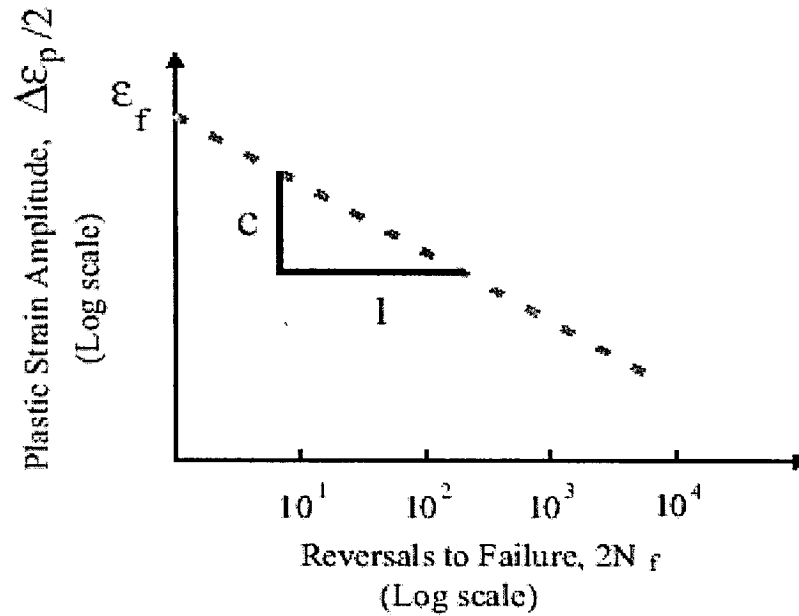


Figure 26 Plastic strain amplitude versus reversals to failure.

3.3.2. Strain-Life Approach

The stress-life approach just described is applicable for situations involving primarily elastic deformation. Under these conditions the component is expected to have a long lifetime. For situations involving high stresses, high temperatures, or stress concentrations such as notches, significant plasticity can be involved, and the approach is not appropriate. Under such conditions, rather than the stress amplitude σ_a , the loading is characterized by the plastic strain amplitude $(\frac{\Delta\epsilon_p}{2})$. If a plot is made of $\log(\frac{\Delta\epsilon_p}{2})$ versus $\log(2N_f)$, the linear behavior of Figure 26 is generally observed. To represent this behavior, Coffin-Manson [141] has proposed the following relationship:

$$\frac{\Delta \epsilon_p}{2} = \epsilon'_f (2N_f)^c \quad (16)$$

where $\frac{\Delta \epsilon_p}{2}$ is the plastic strain amplitude, ϵ'_f is the fatigue ductility coefficient (for most metals $\approx \epsilon_f$, the true fracture ductility) and c is the fatigue ductility exponent (-0.5 to -0.7 for many metals). The strain-life or ϵ - N approach gives a reasonably accurate picture of crack initiation stage. Combinations of fatigue loading and high temperature are better handled by this method, because the creep effect can be included. It is mostly applied for low-cycle fatigue (LCF). The LEFM approach gives the best model for crack propagation stage of the process. It is often used in conjunction with nondestructive testing (NDT) in a periodic service-inspection program, especially in the aerospace industry. It gives more accurate results when a detectable and measurable crack already exists. Fatigue loads are either fully reversed (without mean stress), repeated or fluctuating (with mean stress). In first case, the mean value is equal to alternating stress and in later case, all component values are nonzero and variable.

3.3.3. General Approach

Consider a fully reversed, strain-controlled loading. The total strain is composed of an elastic and plastic part, i.e.

$$\frac{\Delta \epsilon}{2} = \frac{\Delta \epsilon_e}{2} + \frac{\Delta \epsilon_p}{2} \quad (17)$$

The Coffin-Manson expression may be used to express the plastic strain term $\frac{\Delta\varepsilon_p}{2}$. The elastic strain term, $\frac{\Delta\varepsilon_e}{2}$ is obtained as follows. From the Basquin Law (stress-life approach):

$$\frac{\Delta\sigma}{2} = \sigma'_f (2N_f)^b \quad (18)$$

For 1-D, elastic loading $\frac{\Delta\varepsilon_e}{2} = \frac{\Delta\sigma}{2E} = \frac{\sigma_a}{E}$ and thus

$$\frac{\Delta\varepsilon_e}{2} = \frac{\sigma'_f}{E} (2N_f)^b \quad (19)$$

and we may write that:

$$\frac{\Delta\varepsilon}{2} = \frac{\sigma'_f}{E} (2N_f)^b + \varepsilon'_f (2N_f)^c \quad (20)$$

A plot of this equation is depicted below:

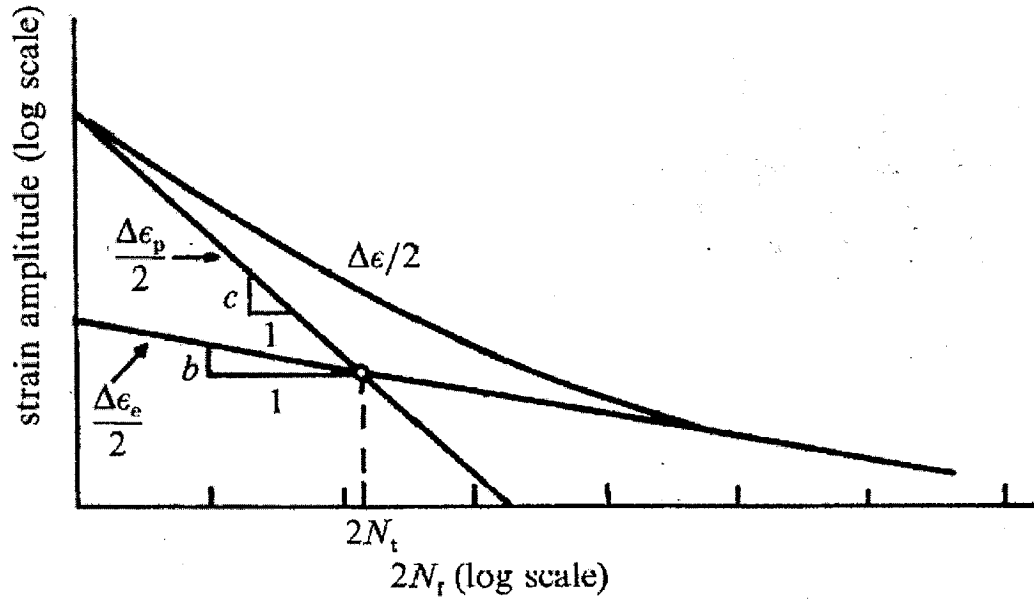


Figure 27 General approach curve.

3.4. ALTERNATING STRESS (ZERO MEAN STRESS)

In the absence of mean stress, the S-N curve is used and the method is called Stress-Life Approach. If a plot is prepared of $\log(\sigma_a)$ versus $\log(2N_f)$ (where $2N_f$ represents the number of reversals to failure, one cycle equals two reversals, and σ_a is alternating stress) a linear relationship is commonly observed. The following relationship between stress amplitude and lifetime [140] has been proposed:

$$\frac{\Delta\sigma}{2} = \sigma_a = \sigma'_f (2N_f)^b \quad (21)$$

where σ'_f is the fatigue strength coefficient (for most metals $\approx \sigma_f$, the true fracture strength), b is the fatigue strength exponent or Basquin's exponent (≈ -0.05 to -0.12), and $2N_f$ is the number of reversals to failure.

The total fatigue life of a component can be considered to have two parts, the initiation life and the propagation life.

3.5. MEAN STRESS EFFECTS

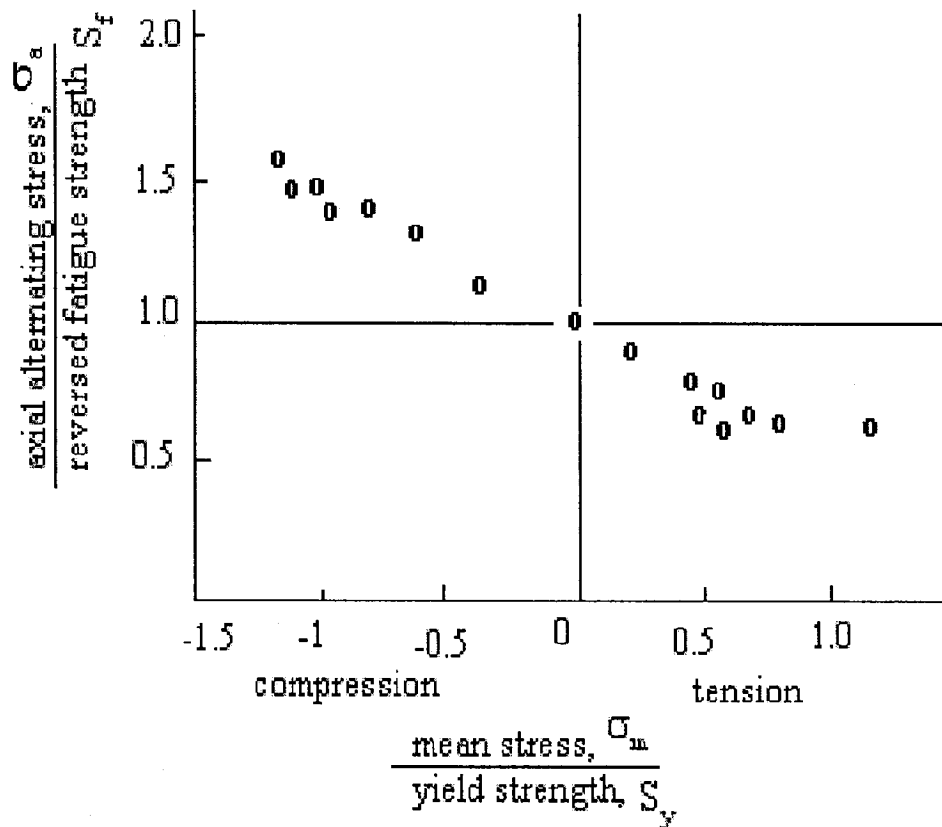


Figure 28 Compressive and tensile mean stress effect (schematic).

The presence of a mean-stress component has a significant effect on failure. When a tensile mean component of stress, σ_m , is added to the alternating component the material fails at lower alternating stress than it does under fully reversed loading. Figure 28 shows the effects of mean stresses (ranging from the compressive regime to the tensile regime) on failure when combined with alternating tensile stress for steels. The plot is normalized. The effect of the mean stress has been depicted in Figure 29a. For the same number of cycles to failure, the more mean stress that is applied, the less is the alternating stress. Different failure criteria for this case of loading with mean stress are compared schematically in Figure 29b.

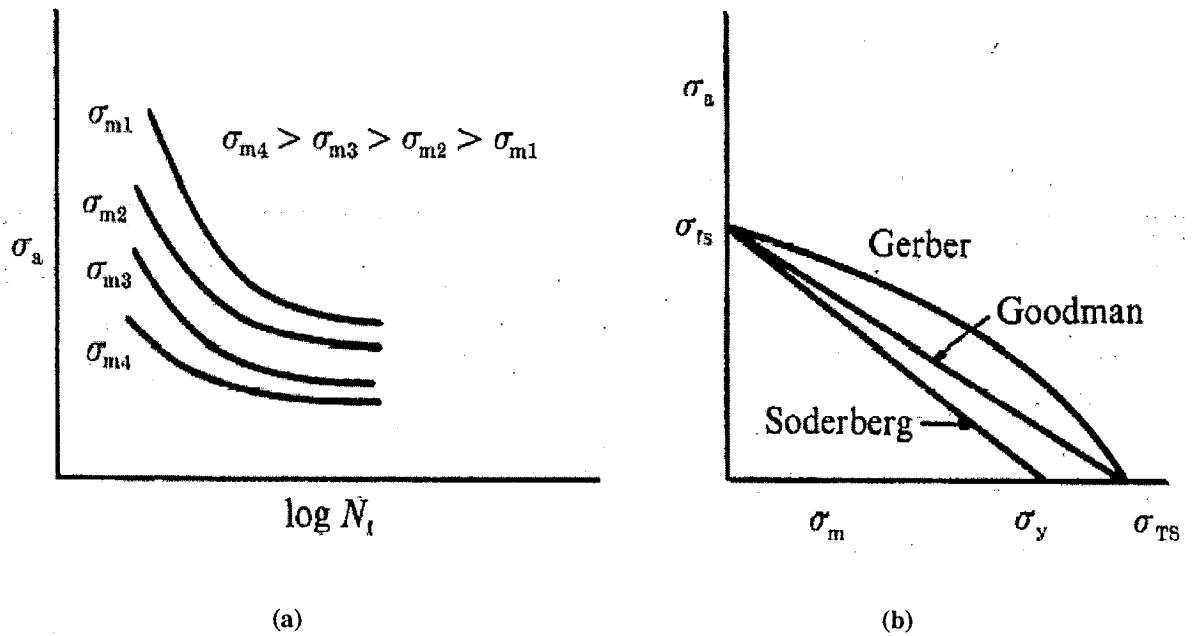


Figure 29 (a) The effects of mean stress; (b) The schematic comparison between different failure criteria. σ_{fs} , σ_y and σ_{TS} are fatigue strength, yield stress and ultimate tensile strength respectively.

The most common failure criteria are Goodman, Modified-Goodman, Soderberg and Gerber. The comparison between these three criteria is shown in Figure 29b and their equations are as follows:

$$\frac{\sigma_a}{\sigma_e} + \frac{\sigma_m}{\sigma_{TS}} = 1 \quad \text{Modified Goodman} \quad (22)$$

$$\frac{\sigma_a}{\sigma_e} + \frac{\sigma_m}{\sigma_y} = 1 \quad \text{Soderberg} \quad (23)$$

$$\left(\frac{\sigma_a}{\sigma_e}\right)^2 + \left(\frac{\sigma_m}{\sigma_{TS}}\right)^2 = 1 \quad \text{Gerber} \quad (24)$$

where $\sigma_a, \sigma_m, \sigma_e, \sigma_y$ and σ_{TS} are alternating stress, mean stress, endurance limit, yield stress and ultimate tensile strength, respectively.

3.6. DIFFERENT AMPLITUDES

In order to handle situations where there are varying amplitude loads, as depicted in Figure 30, a very common approach is the Palmgren-Miner [142] linear damage accumulation rule. If we define $2N_{fi}$ as the number of reversals to failure at i^{th} stress, σ_{ai} , then the partial damage d for each different loading σ_{ai} is

$$d = \frac{2n_i}{2N_{fi}} = \frac{\text{Re versals at } \sigma_{ai}}{\text{Re versals to failure at } \sigma_{ai}} \quad (25)$$

The component is assumed to fail when the total damage becomes equal to 1, or

$$\sum_i \frac{n_i}{N_{fi}} = 1 \quad (26)$$

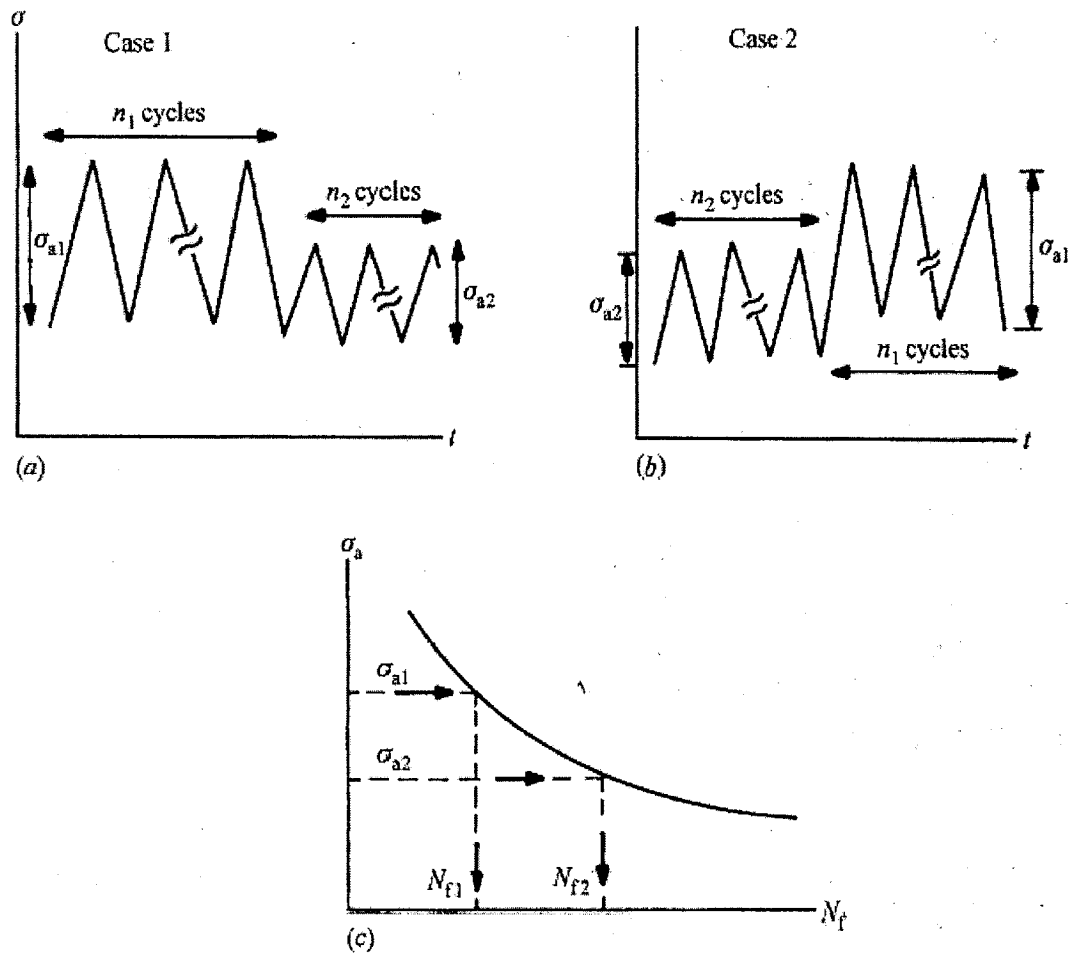


Figure 30 S-N curve in varying amplitude loads.

In the above, it is assumed that the sequence in which the loads are applied has no influence on the lifetime of the component. However, the sequence of load application can have a large influence on the lifetime of the component. Consider a sequence of two different cyclic loads, σ_{a1} and σ_{a2} . Let $\sigma_{a1} > \sigma_{a2}$.

Case 1: Apply σ_{a1} then σ_{a2} . In this case, the total damage is $\sum_i \frac{n_i}{N_f}$. During the first loading (σ_{a1}) numerous microcracks can be initiated, which can be further propagated by the second loading (σ_{a2}). Hence the component may fail even if the total damage is less than one.

Case 2: Apply σ_{a2} then σ_{a1} . In this case also, the total damage is $\sum_i \frac{n_i}{N_f}$. The first loading (σ_{a2}) is not high enough to cause any microcracks, but it is high enough to strain harden the material. Then in the second loading (σ_{a1}), since the material has been hardened it is more difficult to initiate any damage in the material. Hence even if the total damage may be more than one, the component may not fail.

The life prediction under time varying loads and the concept of cumulative damage is described in this chapter. The next chapter will discuss the interaction effect of creep and fatigue on the life of structural components. The different design approaches will be evaluated and the three suggested models will be explained.

CHAPTER 4

CREEP-FATIGUE INTERACTION AND CONSTITUTIVE MODELS

In the previous chapter the life prediction under time varying loads and the concept of cumulative damage was described. This chapter will discuss the interaction effect of creep and fatigue on the life of structural components. The different design approaches are evaluated and the three suggested models are explained.

4.1. INTRODUCTION

The working temperature of a jet engine is limited by the temperatures that its component materials can tolerate, and so there is a continuing requirement for the development of jet-engine materials which can operate at increasingly higher temperatures. Nickel superalloys have been established as disc and blade materials as they meet the requirements for such components. The combination of high temperatures and high stresses in blades make them susceptible to creep, and the interactions of creep and fatigue can seriously affect components' life. In addition, mixed-mode loading produces stress-states which may be closer to those actually applied in service than those applied using simpler loading techniques.

In components which operate at high temperatures, changes in conditions at the beginning and end of operation result in transient temperature gradients. If these transients are repeated, the differential thermal expansion during each transient results in a thermally induced cyclic stress. The extent of the resulting fatigue damage depends on the nature and frequency of the transient, the thermal gradient in the component, and the material properties. Components which are subject to thermally induced stresses generally operate within the creep range so that damage to both fatigue and creep have to be taken into account. Gas turbine blade and disks are particularly subject to severe thermal gradients during start-ups. Under fast starting conditions from relatively low temperatures, severe thermal stresses can result. During steady operation between start-stops, stress relaxation as well as creep processes operate under centrifugal or pressure stresses.

In view of the importance of combined creep and fatigue damage with respect to component reliability, many attempts have been made to develop damage rules that will help in design as well as in component life prediction under creep-fatigue conditions. Several reviews of this subject are available in [143-149]. In developing these damage rules, four types of laboratory tests have been utilized:

- Strain-controlled tests with hold periods at constant stress or strain
- Creep tests under cyclic stress or strain
- Interspersed creep and fatigue tests
- Strain-controlled tests under a thermal condition

Type 4 tests, generally are known as thermo-mechanical fatigue tests. Because the strain-controlled fatigue test (type 1) is the most common, it is described in detail in the following.

4.2. HOLD-TIME EFFECTS IN STRAIN-CONTROLLED FATIGUE

The principal method of studying creep-fatigue interactions has been to conduct strain-controlled fatigue tests with variable frequencies with and without a holding period (hold time) during some portion of the test. The lower frequencies and the hold times can allow creep to take place. In pure fatigue tests, at higher frequencies and short hold times, the fatigue mode dominates and failures start near the surface and propagate transgranularly. As the hold time is increased, or the frequency decreases, the creep component begins to play a role with increasing creep-fatigue interaction. In this region, fractures show a mixed mode involving both fatigue cracking and creep cavitations. A good systematic study of hold-time effects has been carried out by Ellison and Patterson at 565 °C (1050°F), [150]. Their tests included either constant-strain or constant-load hold periods in tension or compression. The resulting data are shown in Figure 31, [150]. The hold time (in minutes) during the tensile/compressive portion of the cycle is also shown on the figure. These data show that the addition of tensile hold periods dramatically reduced the life of the material compared with results of continuous cycling tests, with the longer hold periods leading to shorter lives and creep-dominated failures. Compressive holds offset the detrimental effect of tensile holds, and, in the

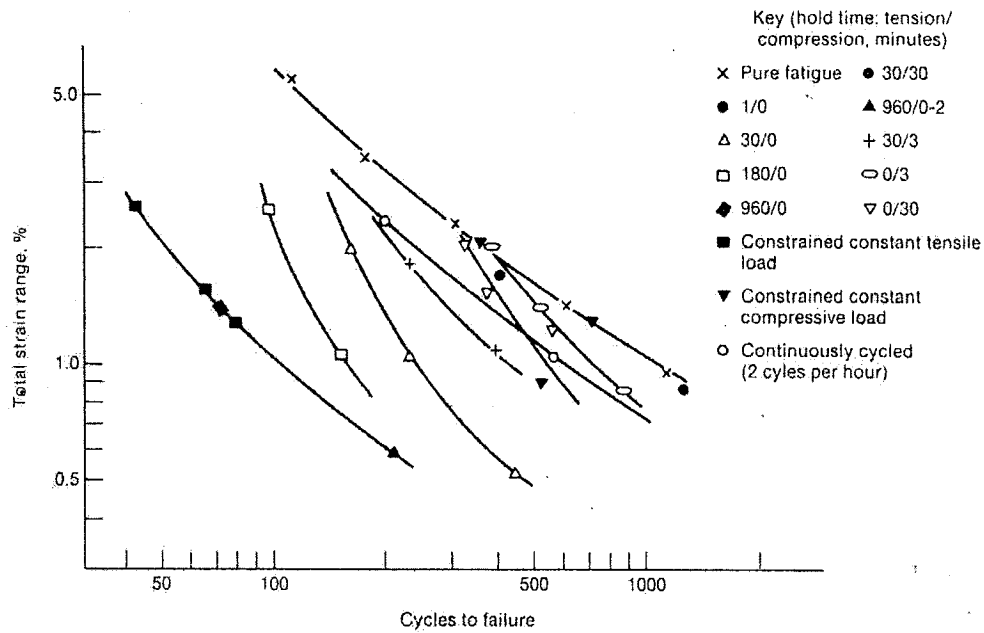


Figure 31 Effects of hold time and tensile vs compressive hold on cyclic endurance life of 1Cr-Mo-V rotor steel at 565 °C [150].

limiting case of equal-duration tensile and compressive holds, the fatigue curve approaches that of the pure fatigue case. Long-term high-strain fatigue data have been obtained for forged 1Cr-1Mo-V4V rotor steel by Thomas and Dawson, [151]. Their results show that the effect of hold time on fatigue life is a function of the type of strain cycle employed, the strain range, and the test temperature. They compared cyclic lives under two types of strain cycles:

the laboratory-type cycle, in which the hold time is normally imposed at the maximum strain in the tensile cycle; and a type II cycle in which the hold time is imposed at the zero strain. Many studies have been carried out on different types of steels, and nickel-base alloys under a variety of test conditions. Hold times and reduced frequencies have been reported to be detrimental. For each material, there is controversy regarding

whether a tensile hold or a compressive hold is detrimental. These controversies seem to arise mainly because data obtained under different test and/or material conditions give different results. The effect of hold time seems to depend on a variety of factors including type of cycle, strain range, temperature, environment, and material ductility. Frequently, test conditions employed in the laboratory seem to be irrelevant to actual conditions existing in a component.

4.3. EFFECT OF RUPTURE DUCTILITY

As the frequency is decreased or as the hold time is increased, the effect of rupture ductility becomes more pronounced, as illustrated by the work of Kadoya et al, [152]. The fatigue life of the low-ductility rotor steel is much more adversely affected by hold time than that of the high-ductility rotor steel. Endurance data for several ferritic steels, in relation to the range of rupture ductility, are illustrated in Figure 32, from the work of Miller et al [153]. The lower the ductility, the lower the creep-fatigue endurance. In addition, long hold periods, small strain ranges, and low ductility support creep-fatigue interaction failures.

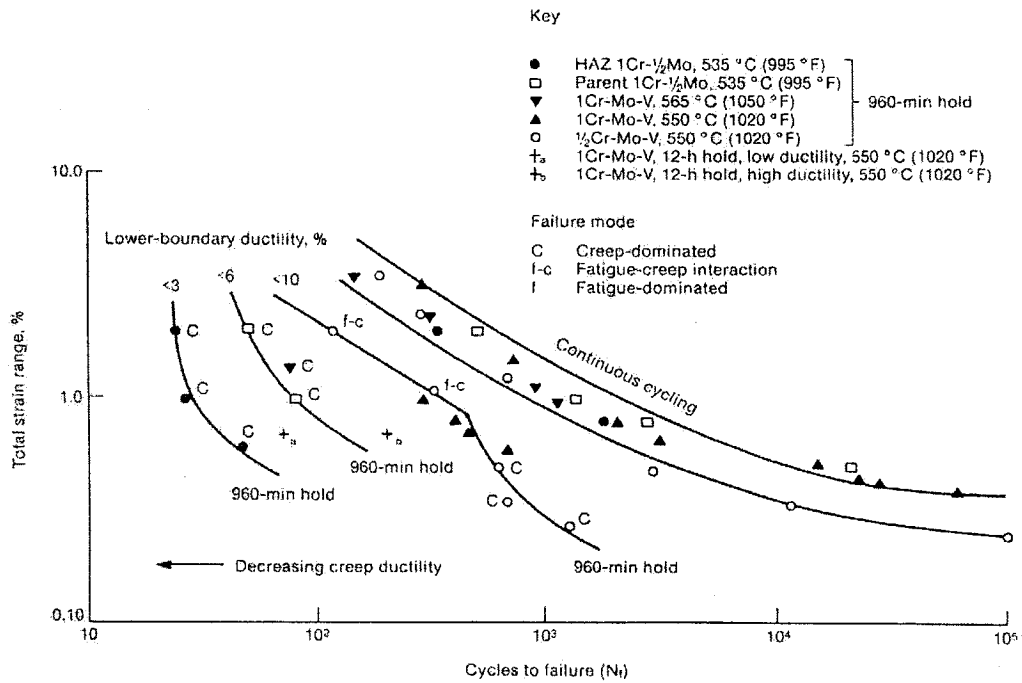


Figure 32 Effect of ductility on endurance of ferritic steels [153].

4.4. EFFECTS OF ENVIRONMENT

The possible roles that can be played by environment in affecting fatigue life are too numerous to describe. The more important ones include formation of oxide notches, grain-boundary changes, increase of net section stress, corrosion-product wedging, and shielding. The first four are fairly obvious and can cause reductions in fatigue life. The last effect, shielding, is described as a net reduction in the effective strain range or stress-intensity range due to corrosion products which in some instances can result in decreased crack growth and increased life.

4.5. DAMAGE RULES AND LIFE PREDICTION

In general, creep-fatigue design considerations are intended to prevent crack initiation, where crack initiation may be defined arbitrarily as the presence of cracks which can be detected visually, say 1 mm in size. The difference between crack initiation and failure life in a small specimen is often a small proportion of the total life, and it can be argued that the failure endurance of a small specimen corresponds to the endurance at crack initiation in a large component. Several damage rules have been suggested for estimating the cumulative damage under creep-fatigue conditions. Interest has tended to focus on four basic types of approaches:

- The damage-summation method
- The frequency-modified strain-range method
- The strain-range-partitioning method
- The ductility-exhaustion method.

In addition to these, several other approaches have also been applied. The frequency modification (FM) approach is essentially a modification of the Coffin-Manson relationship for pure fatigue by incorporating a frequency term [154]. The strain-range partitioning (SRP) approach involves partitioning of the total inelastic strain range into four possible components depending on the direction of straining (tension or compression) and the type of inelastic strain accumulated (creep or time-independent plasticity) [155-159]. The Ostergren's damage function has been proposed by Ostergren for predicting low-cycle fatigue at elevated temperatures [160, 161]. Since the linear

damage summation is the most common one and also it is being used in this study, it will be explained in detail.

Linear Damage Summation

The most common approach is based on linear superposition of fatigue and creep damage. Indeed, the mainstay of the present design procedures is the linear life-fraction rule, which forms the basis of the ASME Boiler and Pressure Vessel Code, Section III, Code Case N-47 [162]. This approach combines the damage summations of Robinson for creep [163] and of Miner for fatigue [164] as follows [165]:

$$\sum \frac{N}{N_f} + \sum \frac{t}{t_r} = D \quad (27)$$

where N/N_f is the cyclic portion of the life fraction, in which N is the number of cycles at a given strain range and N_f is the pure fatigue life at that strain range. The time-dependent creep-life fraction is t/t_r where t is the time at a given stress and temperature, and t_r is the time to rupture at that stress and temperature. D is the cumulative damage index. Failure is presumed to occur when $D = 1$. If Equation (27) were obeyed, a straight line of the type shown in Figure 33 between the fatigue- and creep-life fractions would be expected.

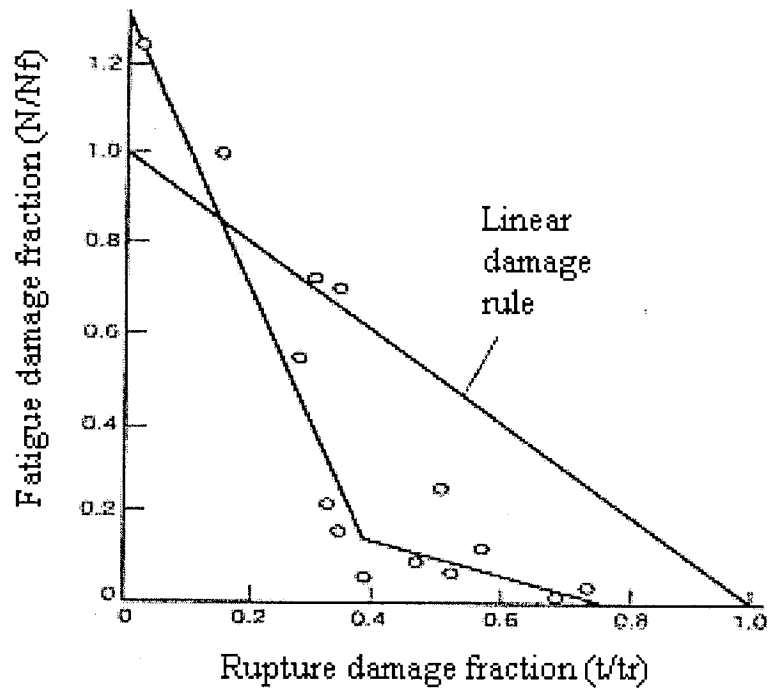


Figure 33 Creep-rupture/low-cycle-fatigue damage interaction curve for 1Cr-Mo-V rotor steel at 540 °C [166].

The life-fraction rule has no mechanistic basis. Its applicability is, therefore, material-dependent. Contrary to experience, it also assumes that tensile and compressive hold periods are equally damaging. The strain softening behavior, which has been seen in many steels, and the effect of prior plasticity on subsequent creep are not taken into account. Uses of virgin-material rupture life to compute creep-life fractions are, therefore, inaccurate. In spite of these limitations, the damage-summation method is very popular because it is easy to use and requires only standard S-N curves and stress-rupture curves.

4.6. EVALUATION OF LIFE-PREDICTION METHODS

The relative qualities of one or more of the damage rules described so far in predicting the lives of specific materials have been assessed by a number of investigators. With respect to Cr-Mo-V rotor steels, Leven compared the linear-damage (LD), frequency-modified strain-range (FM), and strain-range-partitioning (SRP) approaches and concluded that all of them could predict life within a factor of 2 [167]. Similar conclusions were reached by Kuwabara and Nitta [168] and by Batte [149]. Batte has claimed, however, that in the low strain ranges the LD approach is better than the others. Curran and Wundt reported that the LD approach gave non-conservative predictions [166]. Melton compared the FM and SRP approaches and the Ostergren damage function and found the data to be best described by the FM approach [167]. Bisego, Fossati, and Ragazzoni claimed better fit of data to the SRP approach than to the LD approach [168].

There are divergent opinions regarding which damage approach provides the best basis for life prediction. It is quite clear that a number of variables, such as test temperature, strain range, frequency, time and type of hold, waveform, ductility of the material, and damage characteristics, affect the fatigue life. The conclusions drawn in any investigation may therefore apply only to the envelope of material and test conditions used in that study. The validity of any damage approach has to be examined with reference to the material and service conditions relevant to a specific application.

One of the major problems in evaluating the applicability of different life-prediction methods is that in many cases it is necessary to use all the available data in deriving the life-prediction method and thus it is possible to examine only the accuracy with which a given method describes the data. Results from most studies show that even the best of the available methods can predict life only to within a factor of 2 to 3. Some of the cited reasons for these inaccuracies are: failure of the methods to model changing stress-relaxation and creep characteristics caused by strain softening or hardening, use of monotonic creep data instead of cyclic creep data, and lack of sufficiently extended-duration test data. None of the damage rules available today are all involving empirical constants that are material-dependent and difficult to evaluate. Extrapolation of the rules to materials and conditions outside the envelope covered by the specific investigation often results in unsuccessful life predictions. For application to service components, the stress-strain variation for each type of transient and its time dependence must be known with accuracy.

4.7. FAILURE-MECHANISM MAPS

Based on a review of all the available low-cycle-fatigue data, Miller et al have concluded that most of the failures reported are either predominantly fatigue- or creep-controlled and that the region of interaction between the two mechanisms is rather small [153]. The fatigue failures are characterized by trans-granular fracture, whereas the creep failures are characterized by inter-granular fracture. Mixed-mode fractures, indicative of creep-fatigue interaction, have been observed only over a narrow range of test conditions. In many laboratory tests, high strain ranges and short hold times are employed in order to

get quick results. These failures have tended to be fatigue-dominated. Service conditions, on the other hand, involve long hold times (low frequencies) and small strain ranges, which are conducive to creep. Based on these considerations, the various failure regions can be defined in the form of a fracture map, as shown in Figure 34 [169]. Small strain ranges and long hold times are found to promote creep damage, whereas large strain ranges and short hold times promote fatigue damage.

4.8. THERMAL FATIGUE

Most low-cycle-fatigue problems in high-temperature machinery involve thermal as well as mechanical loadings. In other words, the material is subjected to cyclic temperature simultaneously with cyclic stress. Analysis of these loadings and consideration of the attendant fatigue damage become very complex, and gross simplifications are often introduced. In the past, thermal fatigue traditionally has been treated as being synonymous with isothermal low-cycle fatigue at the maximum temperature of the thermal cycle. Life-prediction techniques also have evolved from studies on low-cycle-fatigue. More recently, advances in finite-element analysis and in servo-hydraulic test systems have made it possible to analyze complex thermal cycles and to conduct thermo-mechanical fatigue (TMF) tests under controlled conditions. The assumed equivalence of isothermal LCF tests and TMF tests has been brought into question as a result of a number of studies. It has been shown that for the same total strain range, the TMF test can be more-damaging under certain conditions than the pure LCF test.

Spera has defined thermal fatigue as-"the gradual deterioration and eventual cracking of a material by alternate heating and cooling during which free thermal expansion is partially or fully constrained" [170]. Constraint of thermal expansion causes a thermal stress which may eventually initiate and propagate fatigue cracks. Because thermal cycles usually result in appreciable inelastic strains and cause failure in 10^4 to 10^5 cycles, thermal fatigue may be viewed as a form of low-cycle fatigue. Constraint of free thermal expansion and contraction is an essential ingredient of thermal-fatigue in damage. In a typical laboratory test, a uniaxial specimen - usually a tubular or hourglass-shape specimen - is heated uniformly across its test section while constraining forces are applied through an end grip. This technique is referred to as thermo-mechanical fatigue (TMF) testing. Internal constraints also can be present in laboratory tests such as those using

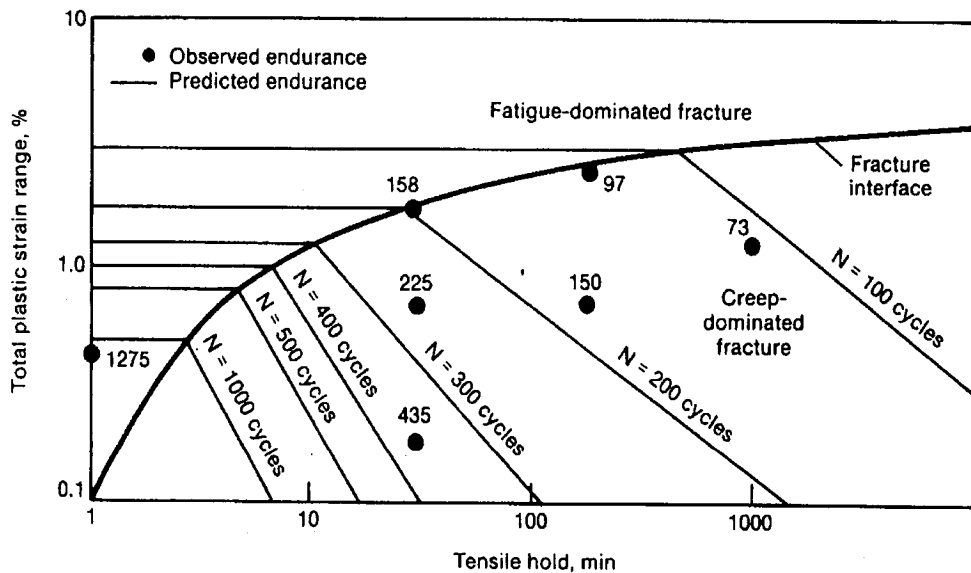


Figure 34 Creep-fatigue failure-mechanism map for 1Cr-Mo-V steel at 565 °C [169].

tapered disk specimens. Such tests are known as thermal stress fatigue (TSF) tests. In the TMF test, the temperature is changed from a maximum to a minimum value concurrently with an independent variation of the strain from a minimum to a maximum value. Spera and Cox have developed a computer program called TF LIFE which can be used to predict the thermal fatigue lives of metals and components [171]. This program is used as a subroutine with a main program supplied by the user. The main program calculates input cycles of temperature and total strain for TF LIFE, which then calculates stress cycle, creep and plastic strain damage, and cyclic life. The life-prediction model uses the linear damage-summation method for estimating the damage caused by creep and fatigue. The creep damage is calculated using modified versions of the life-fraction rule and the universal slopes relationship. Thermo-mechanical fatigue (TMF) testing simulates many of the features of the general fatigue problem, yet retains the relative simplicity and ease of data gathering and interpretation associated with axial strain cycling of smooth laboratory specimens. In these tests, the temperature, strain, and stress can be measured directly at any point within the cycle. Furthermore, any two of these variables can be controlled independent of time. There is now sufficient evidence to show that the fatigue-endurance curves obtained in TMF tests can be quite different from those obtained in isothermal LCF tests. Results reported by Thomas, Bressers, and Raynor [172] on Inconel 738 LC indicate that TMF testing at temperatures from 500 to 850 °C (930 to 1560 °F) was more damaging than isothermal tests at 850 °C, although not by a significant degree.

Based on the results of an extensive study of many materials, Kuwabara, Nitta, and Kitamura [173] have classified them into four groups according to their relative lives in IP cycles (maximum strain at maximum temperature) and OP cycles (maximum strain at minimum temperature), as follows:

- Type I-materials for which IP life is shorter than OP life at lower strain ranges
- Type O-materials for which OP life is shorter than IP life at lower strain ranges
- Type E-materials for which IP and OP lives are nearly equal
- Type E'-materials for which IP life is shorter at higher strain ranges but nearly equal to OP life at lower strain ranges.

A comprehensive study of the TMF behavior of gas-turbine blade alloy Inconel 738 and vane alloy GTD 111 has been concluded recently [172-175]. The data show that the type of cycle, peak temperature, frequency, and hold time affect the lives of the materials and that for a given strain range the life can vary by as much as two orders of magnitude. It was also noted that the maximum tensile stress during a given cycle was a better index than strain range for ranking the behavior under the various conditions. The problems in trying to develop a universal method for life prediction for all materials and components have been reviewed by Russell [174], who points out the need for developing specific techniques focused on specific material and applications.

4.9. MODELS OF CREEP-FATIGUE INTERACTION

4.9.1. Introduction

Advanced gas turbine engines which make use of hot section airfoil cooling present a range of design problems, as the blades operate in a damaging environment of high temperatures, centrifugal and gas pressure forces and thermal cycling. These conditions combine at every point in the blade to create an interaction between creep and thermo-mechanical fatigue damage.

As the blades operate at metal temperatures in excess of $0.4 T_{\text{melt}}$ in Kelvin, creep rupture is clearly a possible failure mode. Also, as the engine cycles through start-up and shut-down with each flight, the transient thermal and body loading stresses cause fatigue damage, which can lead to ultimate failure. The problem becomes one of predicting the relative amounts of creep and fatigue damage at each point in the blade at each moment of the cycle, which in turn depends upon knowing the stress and temperature conditions at each instant and at spatial point. At start-up, the thermal load was applied to the blade, resulting in a transient thermal stress response. These stresses often reached a maximum value σ_{max} at some point in the transient before achieving a lower steady-state condition. It is necessary therefore to record this maximum stress value at each point over the blade and use it in the fatigue life calculation.

4.9.2. Model 1

The fluctuating stress can be considered as a varying stress in fatigue-creep model. Since the fluctuating stress is a combination of alternating and mean stresses, it can be assumed that the part representing the static load can cause creep at elevated temperatures, whereas the alternating part is responsible for fatigue damage. To find the lifetime, the total damage will be found by the following model:

4.9.2.1. Fatigue Damage Prediction

The number of cycles to failure, N_f , can be calculated from the strain range $\Delta\varepsilon$ using the method of universal slopes. This method has the advantage of using material data obtainable from simple tensile tests. The equation combines the Coffin-Manson law given by

$$\frac{\Delta\varepsilon_p}{2} = \varepsilon_f' (2N_f)^c \quad (28)$$

where

$\Delta\varepsilon_p$: plastic strain range

ε_f' : fatigue ductility coefficient, which is some fraction (0.35 to 1) of the true

fracture strain measured in the tension test, and equals to $\text{Ln}\left(\frac{100}{100 - \%RA}\right)$,

RA is area reduction at break

c : fatigue ductility exponent, ranges from about -0.5 to -0.7

N_f : number of reversals (each cycle equals 2 reversals)

and the Basquin law given by

$$\frac{\Delta \epsilon_e}{2} = \frac{\sigma_f'}{E} (2N_f)^b \quad (29)$$

where

$\Delta \epsilon_e$: elastic strain range

σ_f' : fatigue strength coefficient, which is approximated by the true fracture stress, $\approx S_{UT} + 50$ in ksi

b : fatigue strength exponent, which ranges from about -0.06 to -0.14

E : Young's modulus of elasticity

into the form:

$$\frac{\Delta \epsilon_{tot}}{2} = \frac{\sigma_f'}{E} (2N_f)^b + \epsilon_f' (2N_f)^c \quad (30)$$

The total strain range, $\Delta \epsilon_{tot}$, can be found by finite element analysis at each integration point in the model, and the coefficients and the exponents can be found by some fatigue tests on the material. For instance the values for Steel 4340 are

$$\epsilon_f' = 0.58, c = -0.57, \sigma_f' / E = 0.0062, b = -0.09 \quad (31)$$

Using Equation (30) provides us the value of N_f . Once N_f is found, the fatigue damage parameter, D_f , is calculated as

$$D_f = \frac{n}{N_f} = \frac{t}{t_m N_f} \quad (32)$$

where:

n : number of cycles completed

t : the total analysis time

t_m : flight duration (mission time)

4.9.2.2. Creep Damage Prediction

After the initial transient at start-up, the blade metal temperatures and stresses approach a steady-state condition. However, as these temperatures are typically greater than 40% of T_{melt} in Kelvin, creep occurs, resulting in stress redistribution. It is therefore important to model the creep process throughout the life of the component. To find the creep damage, it is needed to find the rupture time. For this purpose the Larson-Miller [176] relation can be used. Starting with Norton power law

$$\dot{\epsilon} = \frac{\epsilon}{t_R} = A_1 \exp\left(\frac{-B_1}{T}\right) \quad (33)$$

From that the rupture time, t_R , is determined as

$$t_R = A_2 \exp\left(\frac{B_2}{T}\right) \quad (34)$$

Taking logarithms on both sides

$$\text{Ln } t_R = \text{Ln } A_2 + \frac{B_2}{T} = f(\sigma, T) \quad (35)$$

Assuming that $\text{Ln } A_2$ is a true constant and that B_2 varies with stress, the equation can be rearranged to arrive at

$$B_2 = T (\text{Ln } t_R - \text{Ln } A_2) = T (C_1 + \text{Ln } t_R) \quad (36)$$

From the pure creep tests for each material, C can be found. For instance for Steel 4340, it equals to 16.65. The suggested value from the tests is $C_1 = 20$. Consequently, from Equation (36)

$$P = T(20 + \text{Ln } t_R) = f(\sigma, T) = b_0 + b_1(\text{Ln } \sigma) + b_2(\text{Ln } \sigma)^2 + b_3(\text{Ln } \sigma)^3 \quad (37)$$

Denoting $Y = \text{Ln } t_R$, and $X = \text{Ln } \sigma$, we have

$$Y = \frac{1}{T + 460} (b_0 + b_1 X + b_2 X^2 + b_3 X^3) \quad (38)$$

where

t_R : rupture time in hours

T : temperature in deg. F

σ : Von-Mises effective stress in ksi

b_0, b_1, b_2, b_3 : material constants

Once t_R is found, the creep damage parameter, D_c , is calculated according to Robinson's rule:

$$D_c = \sum_{i=1}^N \left(\frac{\Delta t}{t_R} \right)_i \quad (39)$$

where

Δt : spend time in hours

t_R : rupture time in hours

i : number of load case

The total damage parameter is:

$$D_{tot} = D_c + D_f = \sum_{i=1}^N \left(\frac{N}{N_f} + \frac{\Delta t}{t_R} \right)_i \quad (40)$$

The total damage parameter $D_{tot} \geq 1$ results in failure.

4.9.3. Model 2

Assuming that the creep behavior is controlled by the mean stress (σ_m) and that the fatigue behavior is controlled by the stress amplitude (σ_a), the two processes combine linearly to produce failure. This approach is similar to the development of the Goodman diagram except that instead of an intercept of ultimate stress (σ_u) on the σ_m axis, the intercept used is the creep-limited static stress (σ_{cr}) as shown in Figure 35. The creep-limited static stress corresponds either to the design limit on creep strain at the design

life or to creep rupture at the design life, depending on which is the governing failure mode. The linear failure prediction rule then may be stated as:

Failure is predicted to occur under combined isothermal creep and fatigue if

$$\frac{\sigma_a}{S_f} + \frac{\sigma_m}{\sigma_{cr}} \geq 1 \quad (41)$$

where

σ_a : alternating stress

σ_m : mean stress

σ_{cr} : creep strength (creep stress for corresponding time to rupture)

S_f : fatigue strength

An elliptic relationship is also shown in Figure 35.

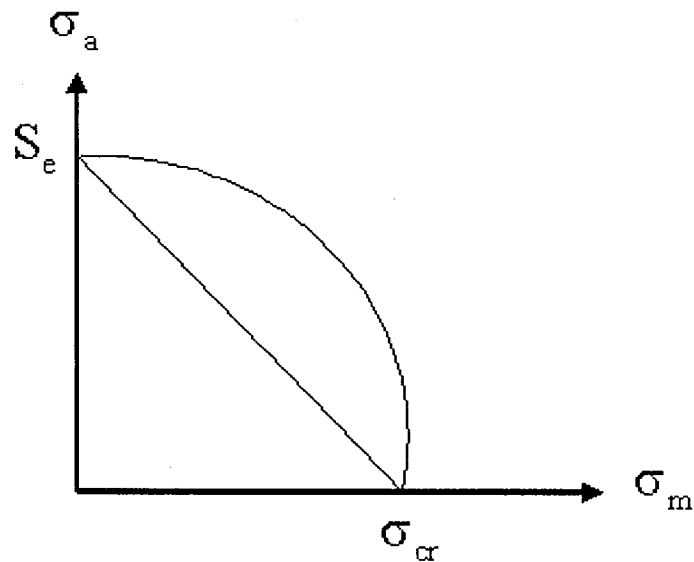


Figure 35 Failure prediction diagram for combined creep and fatigue under constant temperature conditions.

Failure is predicted to occur under combined isothermal creep and fatigue if

$$\left(\frac{\sigma_a}{S_f}\right)^2 + \left(\frac{\sigma_m}{\sigma_{cr}}\right)^2 \geq 1 \quad (42)$$

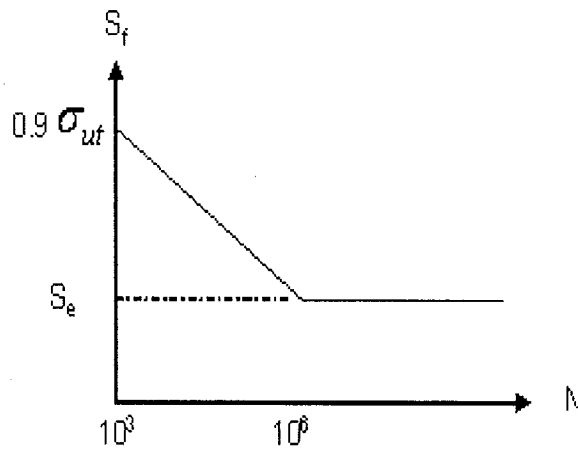


Figure 36 Failure prediction diagram for combined creep and fatigue under constant temperature conditions.

From Equation (41) σ_a , σ_m , and σ_{cr} are known, then S_f can be found. After finding S_f on the base of the following figure, we note that

If $S_f > 0.9 \sigma_{ut}$, then $N < 10^3$

If $0.9 \sigma_{ut} > S_f > S_e$, then $N = N_{\text{diagram}}$

If $S_f < S_e$, then $N \geq 10^6$ cycles (43)

4.9.4. Model 3

4.9.4.1. Fatigue Damage

It is known that in case of pure fatigue, the damage can be defined as

$$D_f = \sum \frac{N_i}{N_{f_i}} \quad (44)$$

where

N_i : number of cycles at stress σ_i

N_{f_i} : number of cycles to failure at stress σ_i

If the process is at constant stress, σ , and isothermal condition, T,

$$D_f = \frac{N}{N_f} \quad (45)$$

where

N : number of cycles at stress σ and temperature T

N_f : number of cycles to failure at stress σ and temperature T

4.9.4.2. Creep Damage

The creep damage under static load can be defined as

$$D_c = \sum \frac{t_i}{t_{R_i}} \quad (46)$$

where

t_i : time spend at stress σ_i and temperature T_i

t_{R_i} : rupture time at stress σ_i and temperature T_i

and in case of having hold time for each stress σ_i and temperature T_i

$$D_c = \sum \frac{(t_h)_i}{t_{R_i}} \quad (47)$$

where $(t_h)_i$ is the hold time at each temperature T_i .

If the process is at constant stress, σ , and isothermal condition, T ,

$$D_c = \frac{Nt_h}{t_R} \quad (48)$$

where

N : number of cycles with hold time at stress σ and temperature T

t_h : hold time at stress σ and temperature T

t_R : rupture time at stress σ and temperature T

4.9.4.3. Creep-Fatigue Damage

In creep-fatigue interaction the total damage is the summation of fatigue damage and creep damage

$$D_t = D_f + D_c = \frac{N}{N_f} + \frac{Nt_h}{t_R} \quad (49)$$

When $D_t = 1$ the failure occurs and hence

$$D_R = \frac{N_R}{N_f} + \frac{N_R t_h}{t_R} = 1 \quad (50)$$

where D_R is the damage at rupture. From that

$$N_R = N_{SF} \left[\frac{1}{\frac{1}{N_f} + \frac{t_h}{t_R}} \right] \quad (51)$$

In Equation (51) N_{SF} is a safety factor which ranges from 0.1 to 1, t_h is known, t_R can be found from Larson-Miller relationship, Equation (38) or from pure creep tests, and N_f can be found from pure fatigue tests or from Equation (31). Then the number of cycles to failure at creep-fatigue interaction, N_R , can be calculated. Knowing the number of cycles spent in combination of creep and fatigue, the present life status can be found as

$$L_r = 1 - \frac{N}{N_R} \quad (52)$$

where L_r is the remained life. If the remaining number of cycles is needed, it can be easily calculated as

$$N_r = N_R - N \quad (53)$$

where N_r is the remaining number of cycles.

4.10. MECHANICAL TESTING

One of the most important facts in test is the load waveform. The following waveforms are applied:

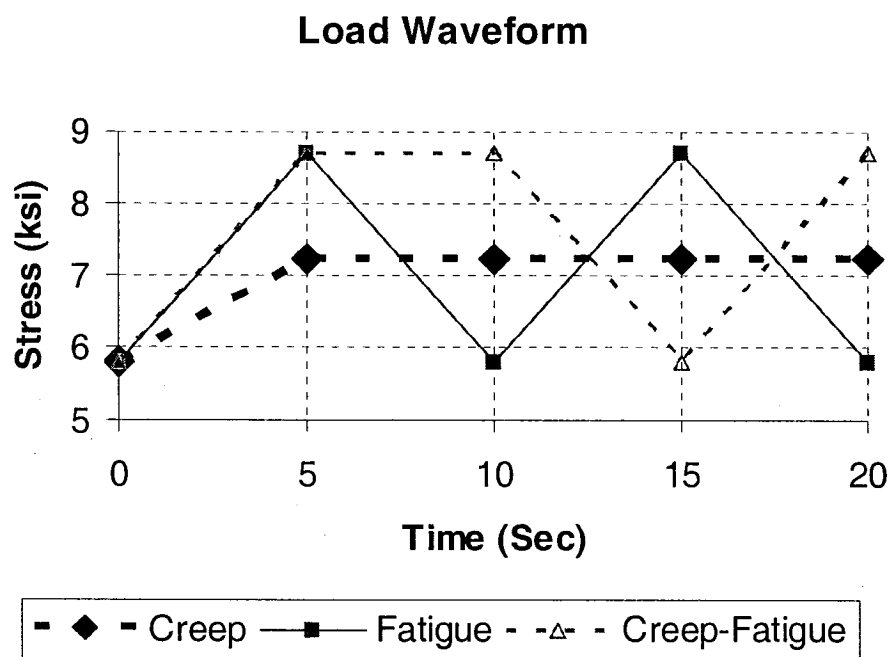


Figure 37 The load waveform in mechanical testing.

4.10.1. Test Schedule for Model 1

The low-cycle fatigue tests will be carried out under closed-loop true temperature control. The tests will be performed between 40.04 MPa (5.81 ksi) and 60.10 MPa (8.71 ksi) for fatigue, and creep-fatigue, but for the latter 5 seconds dwell time will be applied and the test will be done at 800°C. For all tests, the specimens with 228.6 mm (9 in) gauge length and 12.7mm (0.5 in) diameter will be used. For the creep test the average constant stress of 50.07 MPa (7.265 ksi) at 800°C will be applied. The specimen will be heated in a temperature gradient along the gauge length not greater than ± 2 C. Test temperatures varying in the range from 800°C to 1100°C will be applied. Nine specimens will be tested for pure fatigue, pure creep and creep-fatigue interaction, respectively, at different temperatures.

Table 2 Test table for justifying model 1.

Specimen No. B (see notes)	Test temperature (°C)	Test condition (see notes)	Dwell time period (second)
1	25	F	0
2	25	F	0
3	25	F	0
4	800	C	-
5	900	C	-
6	1000	C	-
7	800	CF	5
8	900	CF	5
9	1000	CF	5

Note: C: creep test; F: fatigue test; CF: creep-fatigue test

Table 4 Typical material data from pure creep test.

Case #	T (F)	Design Life (h)	σ_{cr} (ksi)	σ_m (ksi)	σ_a (ksi)	S_f (ksi)	N_{test} (cycle)	$N_{equation}$ (cycle)
1								
2								
n								

the following steps are taken:

1. A test temperature, T, is selected.
2. From the creep test data of the material based on design life, like Table 3, and the selected temperature at step 1, as the working temperature, the corresponding creep-limited static stress, σ_{cr} is selected. For instance the σ_{cr} at 704.44°C (1300 °F) and for 100,000 hour life, is equal to 289.58 MPa (42 ksi).
3. A mean stress, σ_m , and an alternating stress, σ_a , as components of cyclic load are selected.
4. Cyclic load is applied until break and the number of cycles to failure is counted.
5. S_f from Equation (51) is calculated and the number of cycles to failure is found from Equation (43).

4.10.3. Test Schedule for Model 3

From Equation (51), and the following table is constructed.

Table 5 Results of model 3 for creep-fatigue interaction.

Case #	T (F)	σ (ksi)	N_f (cycle)	t_R (Sec)	t_h (Sec)	N_{R-test} (cycle)	$N_{R-equation}$ (cycle)
1							
2							
n							

The procedures are as follows

1. Selecting a temperature, T, between 760-982.22 °C (1400-1800 °F) and a stress, σ , between 206.84- 275.79 MPa (30-40 ksi) for test
2. Selecting a cycle frequency, f, for the fatigue test
3. Running fatigue test and finding number of cycles to failure, N_f
4. Running static isothermal creep test and finding rupture time, t_R
5. Selecting a hold time, t_h , for cyclic creep test
6. Running the cyclic creep test at the same frequency of the fatigue one, and finding the number of cycles to failure, N_R
7. Calculating N_R by Equation (50)
8. Repeating steps 1 to 7 for other samples

Note: In case of using Equations (30) and (50) for fatigue and creep life respectively, steps 3 and 4 can be ignored.

In this chapter different approaches of lifetime prediction in creep-fatigue interaction were discussed and also three suggested constitutive models and their related justification tests for lifetime evaluation were described in details. In next chapter the approximate methods in dynamic analysis of rotating blade in general, and Lagrange-Bhat method specifically will be explained and applied to the rotating gas turbine blade.

CHAPTER 5

APPROXIMATE METHODS IN DYNAMIC ANALYSIS OF ROTATING BLADE

In previous chapter different approaches of lifetime prediction in creep-fatigue interaction were discussed and also three suggested constitutive models and their related justification tests for lifetime evaluation were described in details. Stress analysis under dynamic loading depends strongly on the method used to predict the natural frequencies and the mode shapes. For complex structures, approximate techniques such as Finite Element Methods or the Rayleigh-Ritz methods may give misleading information such as curve veering. Curve veering phenomenon is the strange behavior where the natural frequencies plotted against a structural nondimensional parameter strangely veer away whereas common source suggests that they should meet. Hence curve veering behavior indicates erroneous structural information which may give erroneous response stress information. In this chapter the approximate methods in dynamic analysis of rotating blade in general, and Lagrange-Bhat method specifically will be explained and applied to the rotating gas turbine blade. The curve veering and flattening phenomena also will be discussed.

5.1. LAGRANGE-BHAT METHOD

The equations of vibration can be obtained from the expressions for the kinetic energy $T(z,t)$ and strain energy $U(z,t)$ by using the Lagrangian approach. The equations of motion can be obtained from the energy expressions using Lagrange's equations in the form

$$\frac{\partial}{\partial t} \left(\frac{\partial T}{\partial \dot{q}_j} \right) - \frac{\partial T}{\partial q_j} + \frac{\partial U}{\partial q_j} = f_j(t) \quad j=1,2,\dots,N \quad (54)$$

where q_j is the j th generalized coordinate of the system, which is assumed to have N degrees of freedom. and where f_j is the external force applied at coordinates q_j (for the problem at hand, $f_j = 0$). Here the energies $T(z,t)$ and $U(z,t)$ are the total kinetic energy and strain energy, respectively, in the structure.

In Lagrange-Bhat method, the boundary characteristic orthogonal polynomials, which are orthogonal to each other in the domain of the structure, can be considered as a convenient and complete set of generalized coordinate directions with the magnitudes represented by the generalized coordinates. Bhat [177] used boundary characteristic orthogonal polynomials as generalized coordinate directions to form the Lagrangian, and the Lagrange's equations. In this method, the response $y(z,t)$ is assumed in the form

$$y(z, t) = \sum_{i=1}^N \phi_i(z) q_i(t) \quad (55)$$

where $\Phi_i(z)$ are spatial descriptions of the deflection and $q_i(t)$ are the magnitude of these spatial deflections signifying the generalized coordinates. Using the expressions for the potential and kinetic energies in terms of generalized coordinates, we can write the differential equations using the Lagrange's equations as Equation (54). If the system is under an external force $F(z, t)$, the virtual work done by these forces can be written as

$$W_v = \int_0^l F(z, t) \sum_{i=1}^N \phi_i(z) \partial q_i dz \quad (56)$$

where $\Phi_i(z) \partial q_i$ is a virtual deformation along the q_i coordinate. From this, the generalized force along the q_i coordinate can be written as

$$f_i = \frac{\partial W_v}{\partial q_i} = \int_0^l F(z, t) \phi_i(z) dz \quad (57)$$

Substituting Equation (55) into Equation (54) will give the N number of equations of motion along the N number of generalized coordinates, q_i . Using these equations the natural frequencies, the mode shapes and the response of the structure can be obtained.

Bhat [178] proposed boundary characteristic orthogonal polynomials, as assumed shape functions in the Rayleigh-Ritz method. The construction of these boundary characteristic orthogonal polynomials is described in the following. The simplest polynomial that satisfies at least the geometrical boundary conditions is chosen as the first member of the set and then the higher members of the set are obtained as

$$\Phi_2(z) = (z-B_1) \Phi_1(z) \quad (58)$$

$$\Phi_{n+1}(z) = (z-B_n) \Phi_n(z) - C_n \Phi_{n-1}(z)$$

where

$$B_n = \frac{\int_0^1 z \phi_n^2(z) dx}{\int_0^1 \phi_n^2(z) dx}; \quad C_n = \frac{\int_0^1 z \phi_n(z) \phi_{n-1}(z) dx}{\int_0^1 \phi_{n-1}^2(z) dx} \quad (59)$$

5.2. DYNAMIC ANALYSIS OF ROTATING BLADE

A turbomachine blade, depending on its aspect ratio, can be treated either as a cantilever beam or a cantilever plate mounted on the periphery of a rotating disk at a setting angle. A beam model will represent a turbine blade reasonably well if the blade is slender (i.e. large aspect ratio), is reasonably thick, and only the first few vibrational frequencies and mode shapes are needed accurately. Unfortunately, these conditions are often not met. Many blades in sections of turbomachinery have a small aspect ratio;

efficiency demands thin blades and dynamic response studies require results for many modes, some of which cannot be approximated as beam modes.

Centrifugal forces are set up in the blade due to rotation, which cause in-plane strains, resulting in the stiffening of the blade. Coriolis effects are also present which modify the dynamic behavior. Due to change in structural characteristics with the speed of rotation, the natural frequencies of the structure will change and it is imperative that the speed of operation be away from the natural frequencies for satisfactory operation.

In this section, the dynamics of a rotating blade is studied using Lagrange-Bhat method. The blade is modeled as a rotating beam initially and then as a rotating plate. The setting angle of the blade with respect to plane of rotation and radius of the hub on which the blade is mounted are considered in the formulation. The effects of shear deformation and rotary inertia are also included. The variations of the natural frequencies and mode shapes with the speed of rotation are obtained for several combinations of setting angle and hub radius parameters.

5.3. BLADE MODEL

The cantilever beam, as the model of the rotating blade, is mounted on the periphery of a rotating disc as shown in Figure 38. The xyz coordinate frame is chosen such that x and y axes are in the plane of beam cross-section and are the principal centroidal axes of inertia in that plane. The z -axis is along the beam. XYZ is another

orthogonal Cartesian frame where Z axis is along the beam and XZ plane contains the plane of disc rotation. Origin of both xyz and XYZ coordinate systems are at the root of the beam where it is fixed to the disc. The angle θ between the Y and x axes is the setting or the stagger angle.

5.3.1. Strain Energy

The strain energy, $U(z,t)$, in general may be written as [142],

$$U(z,t) = \frac{1}{2} \int \frac{M^2}{EI_x} dz = \frac{1}{2} \int EI_x \left(\frac{d^2 y}{dz^2} \right)^2 dz \quad (60)$$

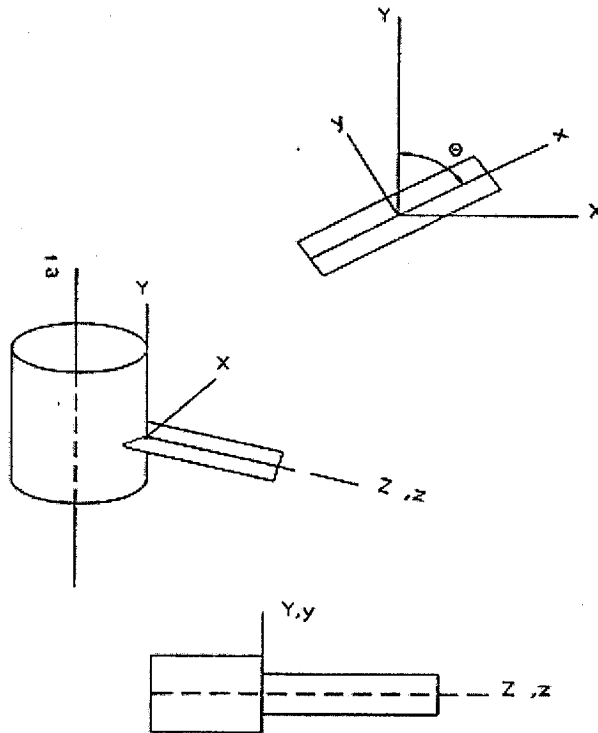


Figure 38 Rotating cantilever beam.

where the integration is carried out along the length of the beam. Let $\bar{z} = z/L$ be the non-dimensional axial length. Substituting this in Equation (60) and integrating along the length of the beam, the expression for strain energy is,

$$U(z, t) = \frac{1}{2L^3} \int_0^1 EI_x \left(\frac{d^2 y}{d\bar{z}^2} \right)^2 d\bar{z} \quad (61)$$

5.3.2. Kinetic Energy

The total kinetic energy of the system is the sum of the kinetic energy due to flexural motion of the beam, T_f and that due to rotation T_r . Since the rotational motion induces centrifugal loads and the consequent energy stored in the beam can be treated as strain energy, some prefer to treat the kinetic energy due to rotation, T_r as strain energy due to rotation.

5.3.2.1. Flexural Kinetic Energy

The total kinetic energy of the blade in flexural vibration can be considered to be made up of two are the translational kinetic energy, T_b and that due to rotation T_r (rotation about a transverse axis, rotary inertia contribution).

For an element dz , the translational kinetic energy dT_b of the mass concentrated at the centroid is given by

$$dT_b(z, t) = \frac{1}{2} m \dot{y}^2 dz \quad (62)$$

where $m = \rho A$.

Hence the total kinetic energy T_b is,

$$T_b(z, t) = \frac{1}{2} m \int_0^L \dot{y}^2 dz \quad (63)$$

The rotational kinetic energy, dT_t , due to rotation of the element about its centroid is,

$$dT_t(z, t) = \frac{\rho I_x dz (\dot{y}')^2}{2} \quad (64)$$

Therefore, the total instantaneous kinetic energy T_t becomes

$$T_t(z, t) = \frac{1}{2} \int_0^L \rho I_x (\dot{y}')^2 dz \quad (65)$$

The combined kinetic energy T_f is the sum of the translational and rotational kinetic energy and can be written from as

$$T_f(z, t) = \frac{1}{2} \int_0^L [\rho A \dot{y}^2 + \rho I_x (\dot{y}')^2] dz \quad (66)$$

5.3.2.2. Kinetic Energy Due to Rotation

Figure 39 shows the blade mounted on the periphery of the rotating disc. For a short element dz , each view shows both the rest position A and the deflected position B, displacements occurring in both η_1z plane (Figure 39a) and ξ_1z plane (Figure 39b). When the blade deflects in the ξ_1z plane, Figure 39b, the line of action of the centrifugal force, dF , on the element dz remains parallel to the z axis. Hence the force component dF_ξ in the ξ_1 is zero and the kinetic energy dT_ξ stored by the element is also zero. Thus,

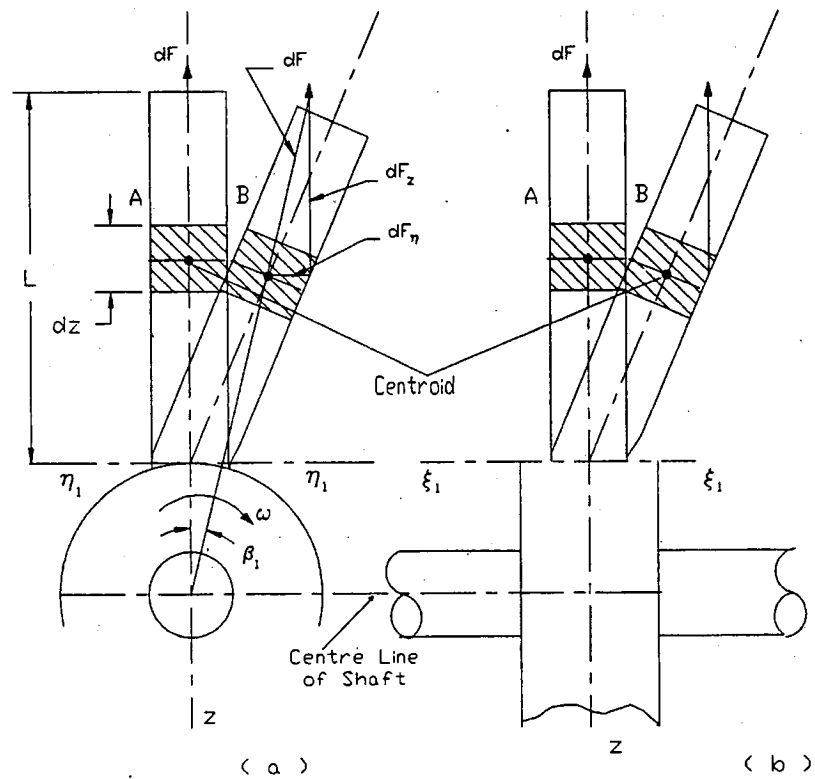


Figure 39 Beam – hub radii assembly.

$$dT_{\xi}(z,t) = 0 \quad (67)$$

With the element dz in the deflected position B, Figure 39a, the force dF can be resolved into two components dF_{η} and dF_z , in the circumferential and radial directions η_1 and z respectively. The circumferential component dF_{η} of the centrifugal force dF is given by,

$$dF_{\eta}(z,t) = dF \sin \beta_1 \quad (68)$$

where,

$$dF(z,t) = m \omega^2 (R+z)dz \quad (69)$$

due to negative gradient of centrifugal force, with increasing z , and

$$\sin \beta_1 = \eta_1/(R+z) \quad (70)$$

In the above equations, R is the disc radius, ω is the angular velocity of rotation of disc and m is the mass of blade per unit length. Similarly, substitution of Equations (69) and (70) into (68) gives,

$$dF_{\eta}(z,t) = m \omega^2 \eta_1 dz \quad (71)$$

Since the η_1 component of the centrifugal force, dF_{η} , increases linearly from zero at the position A, regarded as datum, to a value given by Equation (71) at B, the average force during a displacement η_1 is $dF_{\eta} / 2$. With the force and motion in the same direction, the corresponding gain of the kinetic energy dT_{η} is given by,

$$dT_{\eta}(z, t) = \frac{dF_{\eta}\eta}{2} = \frac{m\omega^2\eta_1^2 dz}{2} \quad (72)$$

and for the entire blade,

$$T_{\eta}(z, t) = \int_0^L \frac{m\omega^2\eta_1^2 dz}{2} \quad (73)$$

The centrifugal force dF acting on the element in the undeflected position A is given by Equation (69). In the deflected position B the force component dF_z in the z direction is,

$$dF_z(z, t) = dF \cos \beta_1 \quad (74)$$

For small displacements, $\cos \beta_1$, approaches unity; the force component in the z direction can, thus, be regarded as constant and is given by Equation (69). The z component of the kinetic energy $dT_z(z, t)$ stored by the element can be written as,

$$dT_z(z, t) = dF_z \Delta = dF \Delta \quad (75)$$

where Δ is the total displacement of the element dz in moving from rest position A to deflected position B. To determine Δ from Figure 40,

$$dz^2 = d\delta^2 + (dz - d\Delta)^2$$

where

$$d\delta = [d\xi_1^2 + d\eta_1^2]^{1/2} \quad (76)$$

represents the increase of total transverse displacement δ . From Equation (76),

$$dz^2 = d\delta^2 + (dz^2 + d\Delta^2 - 2dz d\Delta) \quad (77)$$

Since $d\Delta$ is small, neglecting higher order terms involving $d\Delta$, Equation (77) can be written as,

$$d\Delta = \frac{1}{2} \left(\frac{d\delta}{dz} \right)^2 dz \quad (78)$$

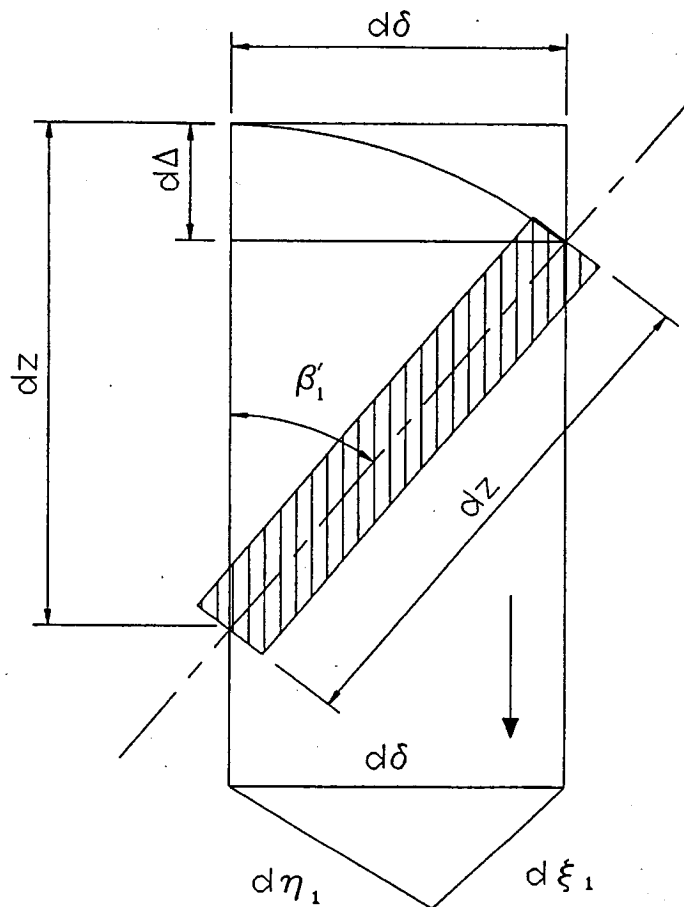


Figure 40 Beam element before and after deflection showing the relative displacement $d\Delta$ of the ends.

Combining Equation (76) and (78),

$$d\Delta = \frac{1}{2} \left[\left(\frac{\partial \xi_1}{\partial z} \right)^2 + \left(\frac{\partial \eta_1}{\partial z} \right)^2 \right] dz \quad (79)$$

and the total displacement Δ , of the element at z , is thus, given by

$$\Delta = \frac{1}{2} \int_0^z \left[\left(\frac{\partial \xi_1}{\partial z} \right)^2 + \left(\frac{\partial \eta_1}{\partial z} \right)^2 \right] dz \quad (80)$$

Assuming small displacements, and making use of Equations (69) and (80), Equation (75) can be rewritten as,

$$dT_z(z, t) = \frac{m\omega^2}{2} (R + z) \left\{ \int_0^z \left[\left(\frac{\partial \xi_1}{\partial z} \right)^2 + \left(\frac{\partial \eta_1}{\partial z} \right)^2 \right] dz \right\} dz \quad (81)$$

Thus, for the entire blade the kinetic energy T_z becomes

$$T_z(z, t) = \frac{\omega^2}{2} \int_0^L \left\{ m(R + z) \int_0^z \left[\left(\frac{\partial \xi_1}{\partial z} \right)^2 + \left(\frac{\partial \eta_1}{\partial z} \right)^2 \right] dz \right\} dz \quad (82)$$

The total kinetic energy due to centrifugal effects is given by,

$$T_r = T_\xi + T_\eta + T_z \quad (83)$$

which can be expressed as,

$$T_r(z, t) = \frac{\omega^2}{2} \int_0^L \left\{ m(R+z) \left[\int_0^z \left[\left(\frac{\partial \xi_1}{\partial z} \right)^2 + \left(\frac{\partial \eta_1}{\partial z} \right)^2 \right] dz \right] + m\eta_1^2 \right\} dz \quad (84)$$

Let,

$$\frac{d}{dz} (F\Delta) = \Delta \left(\frac{dF}{dz} \right) + F \left(\frac{d\Delta}{dz} \right) \quad (85)$$

where Δ is given by Equation (80). Since $\Delta = 0$ at the root ($z = 0$) and $F = 0$ at the free end ($z = L$), integrating this equation with respect to z from 0 to L , the left hand side becomes zero and hence,

$$\int_0^L \Delta \frac{dF}{dz} dz = - \int_0^L F \frac{d\Delta}{dz} dz \quad (86)$$

Using the relationship,

$$\frac{d}{dz} \int_z^L F(z) dz = -F(z) \quad (87)$$

and Equation (69), can be written as,

$$\frac{dF}{dz} = m\omega^2 (R+z) \quad (88)$$

by substituting the values in Equation (85) and integrating between 0 and L gives

$$\begin{aligned} [F\Delta]_0^L &= \frac{\omega^2}{2} \int_0^L \left\{ \left[\left(\frac{d\xi_1}{dz} \right)^2 + \left(\frac{d\eta_1}{dz} \right)^2 \right] \int_z^L [m(R+z)] dz \right\} dz + \\ &\frac{\omega^2}{2} \int_0^L \left\{ m(R+z) \int_0^z \left[\left(\frac{d\xi_1}{dz} \right)^2 + \left(\frac{d\eta_1}{dz} \right)^2 \right] dz \right\} dz \end{aligned} \quad (89)$$

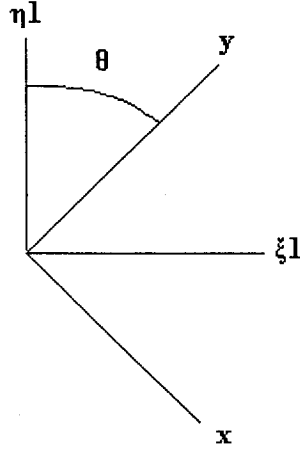


Figure 41 Configuration of two coordinate systems.

The left-hand side of Equation (89) is zero. The second term on the right-hand side is identical with Equation (84) and thus, it follows that

$$T_r(z, t) = -\frac{m\omega^2}{2} \int_0^L \left\{ \left[\left(\frac{d\xi_1}{dz} \right)^2 + \left(\frac{d\eta_1}{dz} \right)^2 \right] \left[\int_z^L [(R+z)] dz \right] - \eta_1^2 \right\} dz \quad (90)$$

From Figure 41 we have

$$\begin{bmatrix} \xi_1 \\ \eta_1 \end{bmatrix} = \begin{bmatrix} \cos\theta & \sin\theta \\ -\sin\theta & \cos\theta \end{bmatrix} \begin{bmatrix} x \\ y \end{bmatrix} \quad (91)$$

Now, using the relationships,

$$\begin{aligned} \eta_1 &= y \cos \theta - x \sin \theta \\ \xi_1 &= y \sin \theta + x \cos \theta \end{aligned} \quad (92)$$

and

$$\frac{d\xi_1}{dz} = \frac{d\xi_1}{dx} \frac{dx}{dz} + \frac{d\xi_1}{dy} \frac{dy}{dz}$$

$$\frac{d\eta_1}{dz} = \frac{d\eta_1}{dx} \frac{dx}{dz} + \frac{d\eta_1}{dy} \frac{dy}{dz} \quad (93)$$

$$\frac{d\xi_1}{dz} = \text{Cos}\theta \frac{dx}{dz} + \text{Sin}\theta \frac{dy}{dz}$$

$$\frac{d\eta_1}{dz} = -\text{Sin}\theta \frac{dx}{dz} + \text{Cos}\theta \frac{dy}{dz} \quad (94)$$

Equation (90), can be written as,

$$T_r(z, t) = \frac{\rho A \omega^2}{2} \int_0^L \left\{ (x^2 \sin^2 \theta - 2xy \sin \theta \cos \theta + y^2 \cos^2 \theta) - \left[\left(\frac{\partial x}{\partial z} \right)^2 + \left(\frac{\partial y}{\partial z} \right)^2 \right] \left[\int_z^L (R+z) dz \right] \right\} dz \quad (95)$$

The in plane deflections x and y are small as compared to the bending deflection z . Hence neglecting coupling of x and y deflections and ignoring higher order terms involving x ,

$$T_r(z, t) = \frac{\rho A \omega^2}{2} \left\{ \int_0^L y^2 \text{Cos}^2 \theta dz - \int_0^L \left(\frac{\partial y}{\partial z} \right)^2 \left(RL + \frac{L^2}{2} - Rz - \frac{z^2}{2} \right) dz \right\} \quad (96)$$

The total kinetic energy of the system in terms of the nondimensional parameter $\bar{z} = z / L$

$$(dz = L d\bar{z}, y' = \frac{dy}{dz} = \frac{1}{L} \frac{dy}{d\bar{z}}, y'' = \frac{1}{L^2} \frac{dy}{d\bar{z}}) \text{ is,}$$

$$T_{\text{total}} = T_f + T_r \quad (97)$$

i.e.

$$T_{\text{total}}(z, t) = \frac{L}{2} \int_0^1 \rho A (\dot{y})^2 d\bar{z} + \frac{1}{2L} \int_0^1 \rho I_x (\dot{y}')^2 d\bar{z} + \frac{\rho A \omega^2}{2} \left[L \int_0^1 y^2 \text{Cos}^2 \theta d\bar{z} - \frac{1}{L} \int_0^1 (y')^2 \left(RL + \frac{L^2}{2} - RL\bar{z} - \frac{L^2 \bar{z}^2}{2} \right) d\bar{z} \right] \quad (98)$$

where a dot represents differentiation with respect to time and (') indicates differentiation with respect to \bar{z} .

Lagrange-Bhat analysis can be applied at this stage to obtain the equations of motions.

Substituting Equation (55) in Equation (98), the total kinetic energy will be

$$T(z, t) = \frac{L}{2} \int_0^1 \rho A \left(\sum_i \dot{\phi}_i \dot{q}_i \right)^2 d\bar{z} + \frac{1}{2L} \int_0^1 \rho I_x \left(\sum_i \dot{\phi}'_i \dot{q}_i \right)^2 d\bar{z} + \frac{\rho A \omega^2}{2} \left[L \int_0^1 \left(\sum_i \dot{\phi}_i \dot{q}_i \right)^2 \text{Cos}^2 \theta d\bar{z} - \frac{1}{L} \int_0^1 \left(\sum_i \dot{\phi}'_i \dot{q}_i \right)^2 \left(RL + \frac{L^2}{2} - RL\bar{z} - \frac{L^2 \bar{z}^2}{2} \right) d\bar{z} \right] \quad (99)$$

and potential energy will be

$$U(z, t) = \frac{EI_x}{2L^3} \int_0^1 \left(\sum_i \phi'_i q_i \right)^2 d\bar{z} \quad (100)$$

Using the substitution parameters $g(\bar{z}) = \bar{R}(1 - \bar{z}) + \frac{1}{2}(1 - \bar{z}^2)$ and $\bar{R} = \frac{R}{L}$, and rearranging

the kinetic and potential energy

$$T(z, t) = \left[\frac{\rho AL}{2} \sum_i \int_0^1 \dot{\phi}_i^2 d\bar{z} + \frac{\rho I_x}{2L} \sum_i \int_0^1 \dot{\phi}'_i^2 d\bar{z} \right] \dot{q}_i^2 + \frac{\rho AL \omega^2}{2} \left[\sum_i \text{Cos}^2 \theta \int_0^1 \dot{\phi}_i^2 d\bar{z} - \sum_i \int_0^1 \dot{\phi}_i^2 g(\bar{z}) d\bar{z} \right] \dot{q}_i^2 \quad (101)$$

$$U(z, t) = \left[\frac{EI_x}{2L^3} \sum_i \int_0^1 \phi_i'^2 d\bar{z} \right] q_i^2 \quad (102)$$

The terms of the Lagrange equation are

$$\frac{\partial \Gamma}{\partial \dot{q}_j} = \left[\rho AL \sum_i \int_0^1 \phi_i^2 d\bar{z} + \frac{\rho I_x}{L} \int_0^1 \phi_i'^2 d\bar{z} \right] \dot{q}_j \quad (103)$$

$$\frac{\partial \Gamma}{\partial q_j} = \rho AL \omega^2 \left[\sum_i \text{Cos}^2 \theta \int_0^1 \phi_i^2 d\bar{z} - \sum_i \int_0^1 \phi_i'^2 g(\bar{z}) d\bar{z} \right] q_j \quad (104)$$

$$\frac{\partial U}{\partial q_j} = \frac{EI_x}{L^3} \left[\sum_i \int_0^1 \phi_i'^2 d\bar{z} \right] q_j \quad (105)$$

Incorporating the following dimensionless parameters,

$$\bar{r}^2 = \frac{I_x}{AL^2}; \lambda = \frac{\rho AL^4}{EI_x}; \eta^2 = \lambda \omega^2 \quad (106)$$

and using Lagrange's equation

$$\left[\int_0^1 \lambda (\phi_i^2 + \bar{r}^2 \phi_i'^2) d\bar{z} \right] \ddot{q}_j + \left\{ \int_0^1 \phi_i'^2 - \eta^2 \text{Cos} \theta [\phi_i^2 - \phi_i'^2 g(\bar{z})] d\bar{z} \right\} q_j = 0 \quad j=1, 2, \dots, N \quad (107)$$

Corresponding to the j^{th} equation, we denote

$$M_{ij} = \int_0^1 \lambda(\phi_i^2 + \bar{r}^2 \phi_i'^2) d\bar{z} \quad (108)$$

$$K_{ij} = \int_0^1 \phi_i''^2 - \eta^2 \text{Cos}\theta [\phi_i^2 - \phi_i'^2 g(\bar{z})] d\bar{z}$$

With $j=1, 2, \dots, N$, we get the complete set of equations which can be expressed in the matrix form as

$$[M]_{N \times N} \{\dot{q}\}_{N \times 1} + [K]_{N \times N} \{q\}_{N \times 1} = \{0\}_{N \times 1} \quad (109)$$

Assuming harmonic motion,

$$\{q\} = \{\bar{q}\} e^{j\Omega t} \quad (110)$$

Equating the determinant of the coefficient matrix to zero, for nontrivial solution, the characteristic equation will be obtained as

$$|K - \Omega^2 M| = 0 \quad (111)$$

In order to study the vibrations of the blade it is modeled as a cantilever beam. The first member of the boundary characteristic orthogonal polynomial set satisfying the clamped-free condition is obtained as follows. Consider the function,

$$\Phi_1(\bar{z}) = b_1 + b_2 \bar{z} + b_3 \bar{z}^2 + b_4 \bar{z}^3 + b_5 \bar{z}^4 \quad (112)$$

The boundary conditions for such a beam are that at $\bar{z} = 0$ the deflection and slope are zero and for $\bar{z} = 1$ the moment and shear force are equal to zero, i.e.

$$\phi_1(0) = \phi_1'(0) = \phi_1''(1) = \phi_1'''(1) = 0 \quad (113)$$

(The prime denotes differentiation with respect to \bar{z}) Substituting the boundary conditions in $\Phi_1(\bar{z})$,

$$\Phi_1(\bar{z}) = b_5 (6\bar{z}^2 - 4\bar{z}^3 + \bar{z}^4) \quad (114)$$

The coefficient b_5 is chosen appropriately so as to normalize $\Phi_1(\bar{z})$ such that,

$$\int_0^1 \Phi_1^2(\bar{z}) d\bar{z} = 1 \quad (115)$$

Therefore, the starting function in the z direction is taken

$$\phi_1(\bar{z}) = \sum_{j=1}^5 b_j \bar{z}^{j-1} \quad (116)$$

where for clamped free beam: $b_1 = b_2 = 0$, $b_3 = 6$, $b_4 = -4$, $b_5 = 1$. Natural frequencies and mode shapes can be obtained by solving this set of equations. A computer algorithm is developed to solve Equation (111) for several parameter combinations of setting angle, hub radius and rotational speeds.

5.4. TEMPERATURE EFFECTS ON NATURAL FREQUENCY

The schematic of the cantilever beam with the length of L and cross section of W by h is shown in Figure 42 as a gas turbine blade. The blade temperature and displacement at hub is T_1, u_1 , and T_2, u_2 respectively.

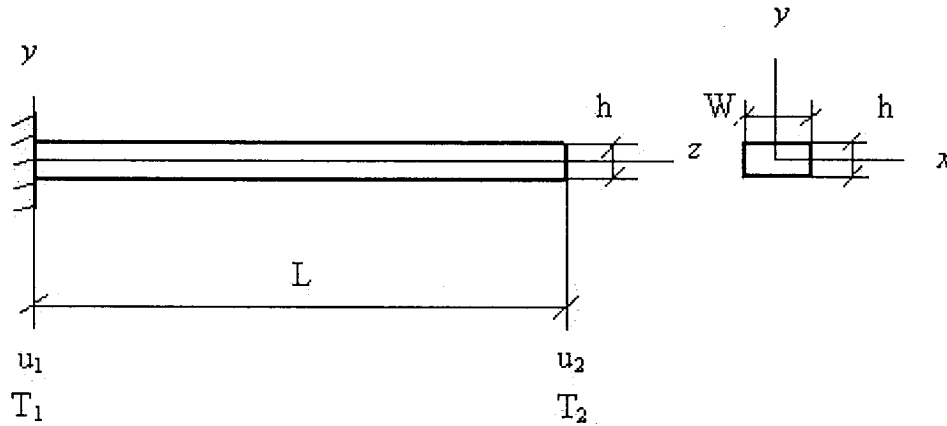


Figure 42 Schematic of the cantilever beam.

If the subscript $T, ()_T$, represents the parameter at thermal environment, then we have:

$$h_T = h(1 + \alpha\Delta T)$$

$$W_T = W(1 + \alpha\Delta T)$$

$$A_T = A(1 + \alpha\Delta T)^2$$

$$L_T = L[1 + (\alpha/2)\Delta T] \quad (\text{see Appendix E}) \quad (117)$$

Taking the temperature as a function of the length of the blade

$$T = az + b = T_1 + (T_2 - T_1)z/L \quad (118)$$

And the temperature difference which is important in parameters at thermal environment

$$\Delta T = T - T_{\text{ref}} = T_1 + (T_2 - T_1) z / L - T_{\text{ref}} \quad (119)$$

where T_{ref} is the atmospheric temperature as reference temperature in which there is no change with length of the blade.

Taking the displacement as a function of the length of the blade

$$u(z, t) = C_1 z + C_2 = (1 - z / L_T) u_1(t) + (z / L_T) u_2(t) \quad (120)$$

The modulus of elasticity can be considered as a function of temperature.

$$E(T) = E(T_0) - (dE/dT) \Delta T = E(T_0) - (dE/dT) [T_1 + (T_2 - T_1) z / L] \quad (121)$$

Taking: $a = E(T_0)$, $b = - (dE/dT) T_1$, $d = a + b$, $c = - (dE/dT) (T_2 - T_1)$,

$$E(T) = E(z) = d + c z / L \quad (122)$$

For instance for the steel with the 64.447% Fe: $a = 216.7$, $b = -0.059$, $c = -0.059(T_2 - T_1)$; [ASM, Vol. 2, pp. 641].

5.4.1. Longitudinal Vibrations

From mechanics of materials, the potential energy or the strain energy is

$$U(z, t) = \frac{1}{2} \int_0^{L_T} E(z) A_T \left[\frac{\partial u(z)}{\partial z} \right]^2 dz \quad (123)$$

Taking into consideration all the parameters in the integral and substituting them

$$U(z, t) = \frac{1}{2} \int_0^{L_T} \left(d + \frac{cz}{L} \right) A (1 + \alpha \Delta T)^2 \frac{1}{L^2 \left(1 + \frac{\alpha}{2} \Delta T \right)^2} (u_1^2 + u_2^2 - 2u_1 u_2) dz \quad (124)$$

Assuming $u_1 = 0$, and neglecting the small amounts

$$\begin{aligned} U(z, t) &= \frac{A}{2L^2} (1 + \alpha \Delta T)^2 \frac{1}{\left(1 + \frac{\alpha}{2} \Delta T \right)^2} \int_0^{L_T} \left(d + \frac{cz}{L} \right) u_2^2 dz \\ &= \frac{A u_2^2}{2L^2} \frac{(1 + \alpha \Delta T)^2}{\left(1 + \frac{\alpha}{2} \Delta T \right)^2} \left(dz + \frac{cz^2}{2L} \right)_0^{L_T} \\ &= \frac{A u_2^2 \left(1 + \frac{\alpha}{2} \Delta T \right)}{4L} \left[2d + c \left(1 + \frac{\alpha}{2} \Delta T \right) \right] \frac{(1 + \alpha \Delta T)^2}{\left(1 + \frac{\alpha}{2} \Delta T \right)^2} \\ U(z, t) &= \frac{A u_2^2 (1 + \alpha \Delta T)^2 (2d + c)}{4L} \end{aligned} \quad (125)$$

The kinetic energy of longitudinal vibration can be defined as

$$T(z, t) = \frac{1}{2} \int_0^{L_T} A_T \rho(z) \left(\frac{\partial u}{\partial t} \right)^2 dz \quad (126)$$

Considering

$$\frac{\partial u}{\partial t} = \left(1 - \frac{z}{L}\right) \dot{u}_1(t) + \frac{z}{L} \dot{u}_2(t) \quad (127)$$

Assuming $u_1 = 0$, and neglecting the small amounts

$$\frac{\partial u}{\partial t} = \frac{z}{L} \dot{u}_2(t) \quad (128)$$

and

$$\rho(z) = \frac{m}{A_T L_T} = \frac{m}{AL(1 + 2\alpha\Delta T + \frac{\alpha}{2}\Delta T)} \quad (129)$$

the kinetic energy will be

$$\begin{aligned} T(z, t) &= \frac{1}{2} \int_0^{L_T} A(1 + \alpha\Delta T)^2 \frac{m}{AL(1 + 2\alpha\Delta T + \frac{\alpha}{2}\Delta T)} \left(\frac{z \dot{u}_2}{L} \right)^2 dz \\ &= \frac{m \dot{u}_2^2}{2AL^3} \int_0^{L_T} \frac{z^2}{(1 + 2\alpha\Delta T + \frac{\alpha}{2}\Delta T)} dz \end{aligned} \quad (130)$$

Integrating, applying the limits, and neglecting the small values

$$T(z, t) = \frac{m\dot{u}_2^2}{6A} \left(\frac{1 + \frac{3\alpha}{2}\Delta T}{1 + 2\alpha\Delta T + \frac{\alpha}{2}\Delta T} \right) \quad (131)$$

Using Lagrangian to find the differential equation of motion, reminding

$$\frac{\partial}{\partial t} \left(\frac{\partial T}{\partial \dot{u}_i} \right) - \frac{\partial T}{\partial u_i} + \frac{\partial U}{\partial u_i} = f_i(t) \quad i = 1, 2 \quad (132)$$

Taking the substituting parameter $H = \left(\frac{1 + \frac{3\alpha}{2}\Delta T}{1 + 2\alpha\Delta T + \frac{\alpha}{2}\Delta T} \right)$ and $N = (1 + \alpha\Delta T)^2(2d + c)$, in

our case the Lagrange equation would be

$$\frac{m}{3A} H\ddot{u}_2 - \frac{AN}{2L} u_2 = 0 \quad (133)$$

Reordering the above equation

$$\ddot{u}_2 - \frac{3A^2N}{2mLH} u_2 = 0 \quad (134)$$

From this eigenvalue problem, the natural frequency would be

$$\omega_n^2 = \frac{3A^2N}{2mLH} \quad (135)$$

If the blade is isothermal $T_1 = T_2 = T_i$, then $c = 0$, and neglecting the small amounts

$$\omega_n^2 = \frac{3A^2(1+2\alpha\Delta T_i)}{mL}(216.7 - 0.059T_i) \quad (136)$$

Plotting the above equation gives the change of natural frequency versus temperature.

5.4.2. Transverse Vibrations

Following the same algorithm for the transverse vibration, the potential energy would be

$$U_T(z, t) = \frac{1}{2} \int_0^L \frac{E_T I_T}{2L_T^3} \left[\frac{\partial^2 y(z)}{\partial z^2} \right]^2 dz = LEI \int_0^L \frac{(d + c\bar{z}) \left(\frac{1}{12} bh^3 \right) (1 + \alpha\Delta T)^4}{2L^3 \left(1 + \frac{\alpha}{2} \Delta T \right)^3} y''^2 d\bar{z} \quad (137)$$

Simplifying this equation and neglecting the small amounts

$$U_T(z, t) = \frac{EI}{2L^2} \int_0^L (d + c\bar{z})(1 + \alpha\Delta T)^4 y''^2 d\bar{z} \approx \frac{EI}{2L^2} \int_0^L (d + c\bar{z})(1 + \alpha\Delta T)^4 y''^2 d\bar{z} \quad (138)$$

because the upper limit, $\alpha\Delta T/L$, is from the order of $e-8$ and is almost negligible. There is no kinetic energy in transverse vibration due to thermal environment and the only effect is the potential energy. To consider the effect of temperature in gas turbine blade dynamic analysis, it's enough to add this potential term to all previous potential terms.

5.5. DYNAMIC OF ROTARY BLADE AT HIGH TEMPERATURE

Referring to Equation (100) and taking into account the potential energy due to thermal environment, Equation (138), we have

$$L_1 = T_{\text{tot}}(z,t) - U_{\text{tot}}(z,t) \quad (139)$$

where $U_{\text{total}} = U_{\text{strain}} + U_{\text{thermal}}$. Assuming harmonic motion,

$$U_{\text{tot}}(z,t) = \frac{1}{2L^3} \int_0^1 EI_x y''^2 d\bar{z} + \frac{EI}{2L^2} \int_0^1 (d + c\bar{z})(1 + \alpha\Delta T)^4 y''^2 d\bar{z} \quad (140)$$

Incorporating the following nomenclature,

$$E(\bar{z}) = L(d + c\bar{z})(1 + \alpha\Delta T)^4 \quad (141)$$

and Equation (142)

$$\frac{\partial U}{\partial q_j} = \frac{EI_x}{L^3} \left[\sum_i \int_0^1 [1 + E(\bar{z})] \phi_i''^2 d\bar{z} \right] q_j \quad (142)$$

the Lagrange equation is

$$\left[\int_0^1 \lambda(\phi_i'^2 + \bar{r}^2 \phi_i''^2) d\bar{z} \right] \ddot{q}_j + \left\{ \int_0^1 [1 + E(\bar{z})] \phi_i''^2 - \eta^2 \text{Cos}\theta [\phi_i'^2 - \phi_i''^2 g(\bar{z})] d\bar{z} \right\} q_j = 0 \quad (143)$$

Corresponding to the j^{th} equation, we denote

$$\begin{aligned} M_{ij} &= \int_0^1 \lambda(\phi_i^2 + \bar{r}^2 \phi_i'^2) d\bar{z} \\ K_{ij} &= \int_0^1 [1 + E(\bar{z})] \phi_i''^2 - \eta^2 \text{Cos}\theta [\phi_i^2 - \phi_i'^2 g(\bar{z})] d\bar{z} \end{aligned} \quad (144)$$

With $j=1, 2, \dots, N$, we get the complete set of equations which can be expressed in the matrix form as

$$[M]_{N \times N} \{\ddot{q}\}_{N \times 1} + [K]_{N \times N} \{q\}_{N \times 1} = \{0\}_{N \times 1} \quad (145)$$

Assuming harmonic motion,

$$\{q\} = \{\bar{q}\} e^{j\Omega t} \quad (146)$$

Equating the determinant of the coefficient matrix to zero, for nontrivial solution, the characteristic equation will be obtained as

$$|K - \Omega^2 M| = 0 \quad (147)$$

5.6. CURVE VEERING

The plots of variation of eigenvalues or natural frequencies of vibrating structures with respect to a non-dimensional system parameter often cross each other or abruptly veer away avoiding the crossing. This phenomenon is termed as curve veering and has been

observed both in approximate solutions as well as in exact solutions associated with the vibration of some vibrating systems. Illustrating a family of loci is one way to present the dependence of eigenvalue on a system parameter. The curve veering mainly has been observed in approximate solutions. In the present study also due to application of approximate method, curve veering has been observed in both thermal and non-thermal rotating blade (Figure 43 and Figure 44), but as was shown by Sabour et al [93] it will be vanished when a larger number of terms are used in the investigation. Here again the curve veering may be shifted to the still higher natural frequencies. In the present study, a rotating cantilever blade is considered from the point of view of curve veering when its natural frequencies are plotted against the rotational speed. The shifting behavior of curve veering from lower order natural frequencies to higher order natural frequencies while increasing the number of assumed shape functions is examined. The results of the study indicate that the number of terms used in the Lagrange-Bhat method should be sufficiently large in order to avoid the pseudo curve veering behavior in the frequency range of interest. However, when the natural modes were identified before and after the apparent curve veering points, the veered curve did not change the mode shape, indicating that it may not be the true curve veering. All modes, before and after the crossing point had the same number of nodes. In following figures: $\omega_b = \frac{\omega}{\omega_n}$.

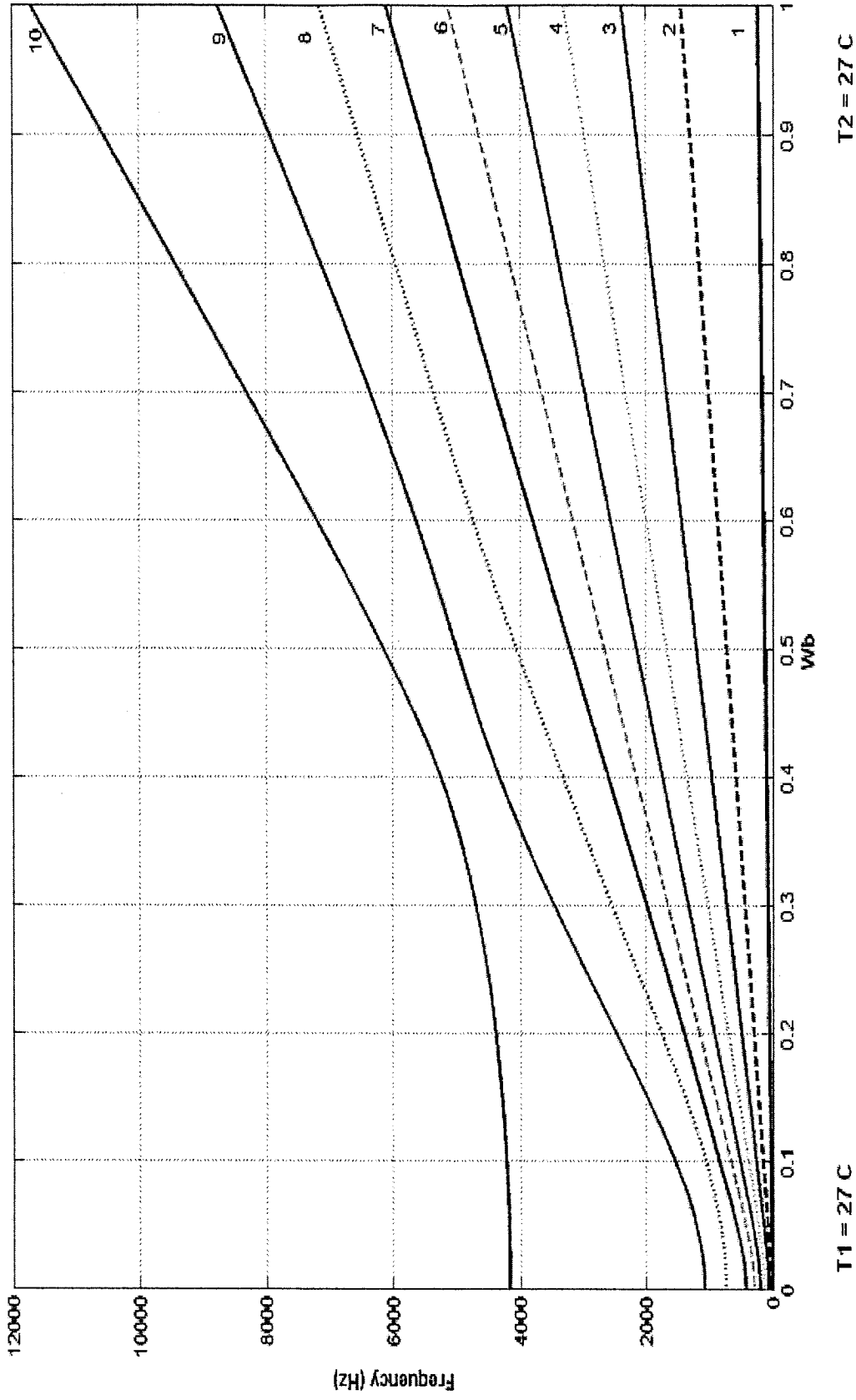


Figure 43 Curve veering in nonthermal rotating blade, $\Delta T=0^\circ\text{C}$.

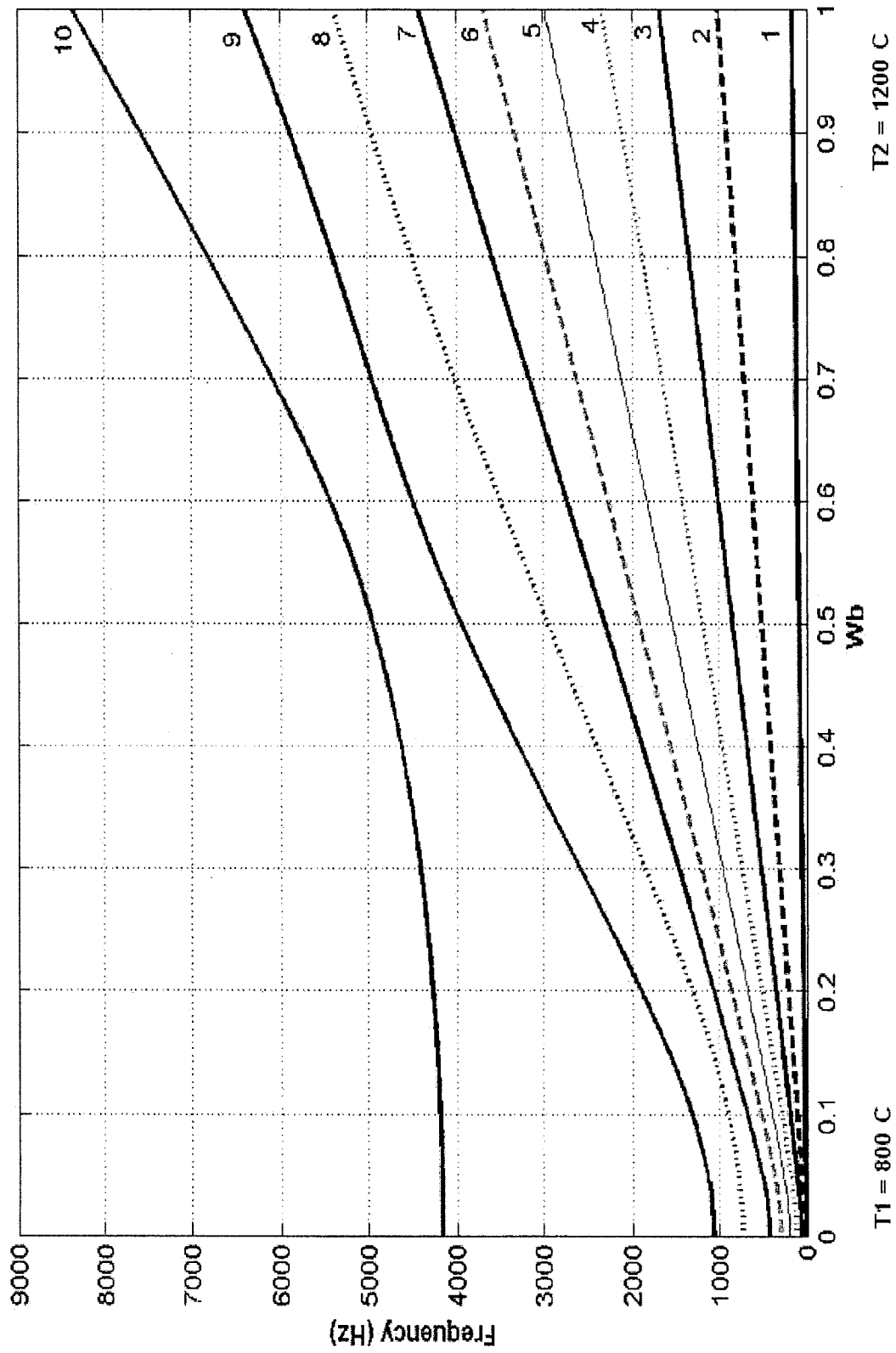


Figure 44 Curve veering in thermal rotating blade, $\Delta T=400^{\circ}C$.

5.7. FLATTENING

By increasing the angular speed of the blade, it will be stiffer and due to that, the deflection of the blade will be reduced and the frequency of the response will be increased. This behavior is seen in both thermal and non-thermal blades, although at thermal case in comparison with the non-thermal blade, higher deflections and lower frequencies are seen. In both cases, the flattening phenomenon can be depicted if the nondimensional deflection is plotted versus non-dimensional blade length (Figure 45 and Figure 46) which has a very good agreement with the Bhat [87] results for the rotating cantilever beam. The higher deflections and lower frequencies in thermal environment, due to reduction of Young modulus of elasticity are quite reasonable.

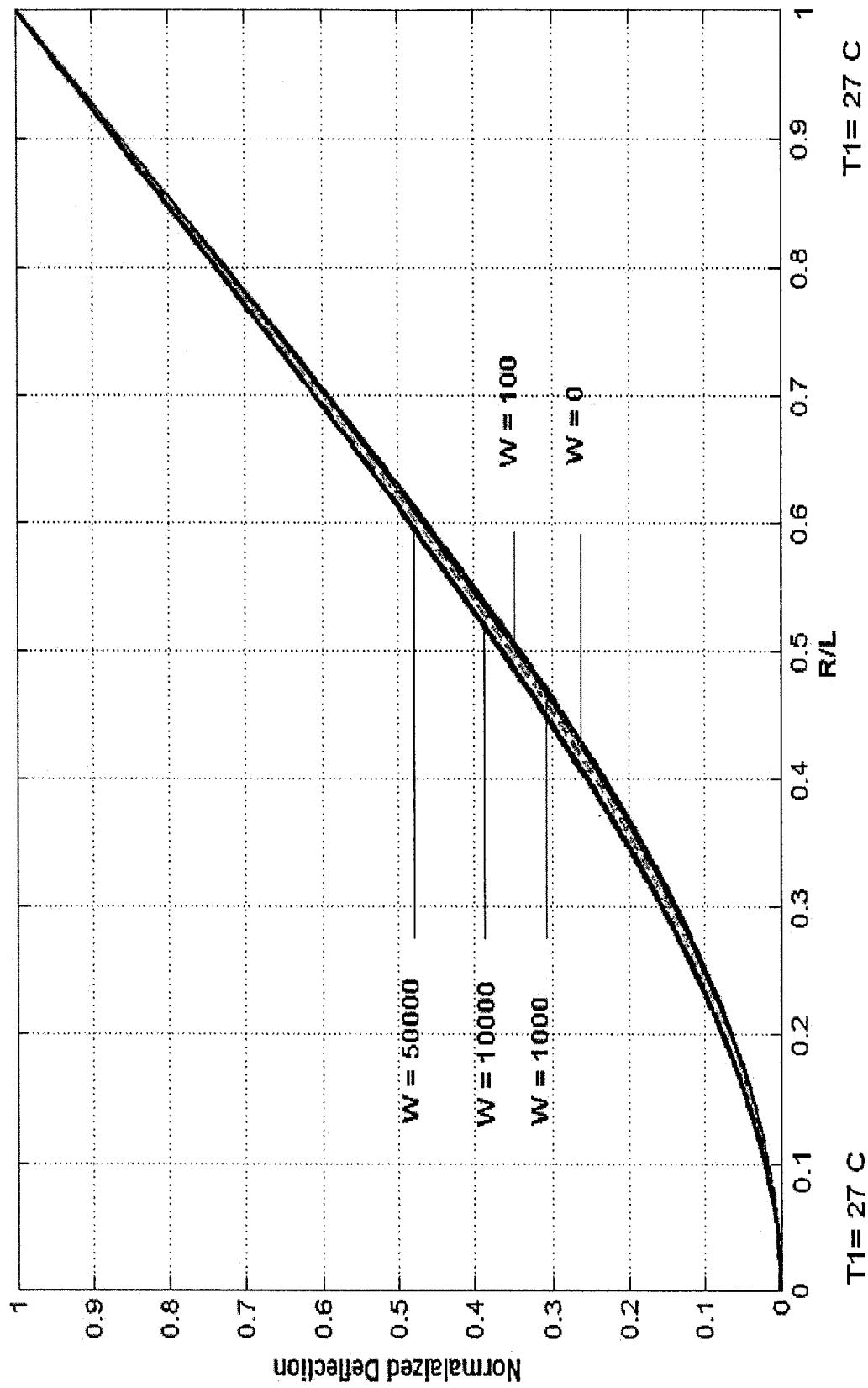
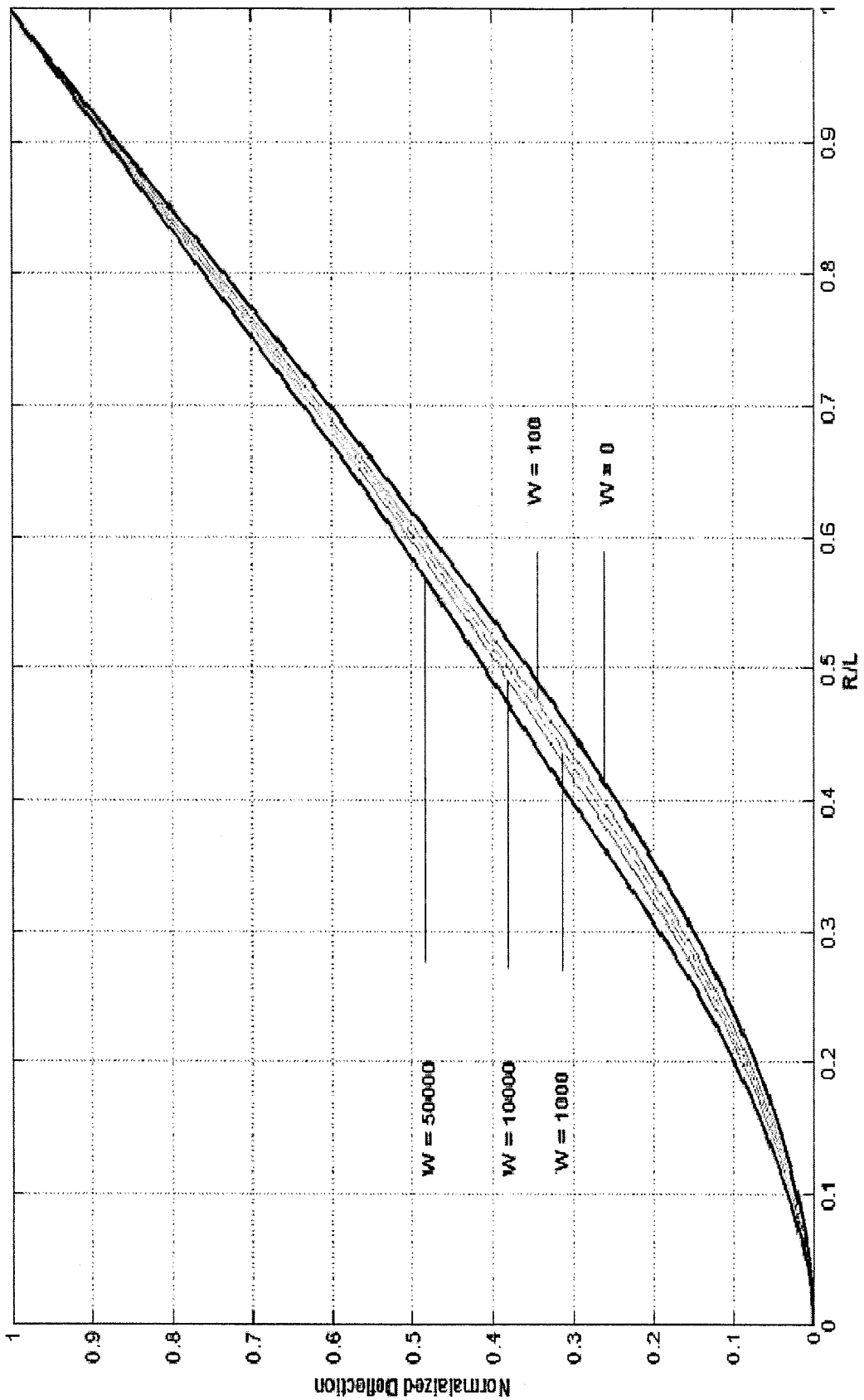


Figure 45 Flattening in nonthermal rotating blade, $\Delta T = 0^\circ\text{C}$.



$T_2 = 1200\text{ C}$

$T_1 = 800\text{ C}$

Figure 46 Flattening in thermal rotating blade, $\Delta T = 400^\circ\text{C}$.

In this chapter, the Lagrange-Bhat method has been explained and used to analyse the dynamics of the rotating cantilever blade in both non-thermal and thermal environments. The curve veering and flattening phenomena also were discussed. In next chapter the scale model idea will be described and the thermal scaling model will be used as first time in this thesis, and will be justified by FEM. The theory and application of dimensional and dynamic analyses also will be presented.

CHAPTER 6

EXPERIMENTAL INVESTIGATION ON SCALED MODELS, **INCLUDING TEMPERATURE SCALING**

In previous chapter, the Lagrange-Bhat method has been explained and used to analyze the dynamics of the rotating cantilever blade. The curve veering and flattening phenomena also were discussed. In this chapter the scale model idea will be described and the thermal scaling model will be used in this thesis, and will be justified by FEM. The theory and application of dimensional analyses also will be presented. The justification of the suggested models and the thermal scaling will be discussed too.

6.1. THEORETICAL ANALYSIS

The requirement of static equilibrium is essentially obvious. It is the one aspect of structural behavior in which the engineer may place complete confidence. Of course, if dynamic behavior is to be investigated, it is necessary to consider the problem in terms of the laws of motion. The requirement of compatibility of deformations is a little more difficult to take into account. It is particularly difficult to visualize what happens to the strains in the vicinity of a discontinuity, say, due to the presence of a crack or under a point load. In one-dimensional problems it is usual to consider discrete deformations, for example, the total axial extension in a tie or the rotation at the end of a beam. The distribution of strains across the sections are generally assumed to take some simple

forms: the best known of these is that plane sections remain plane. Depending on whether the structure is stiff or flexible, the overall behavior is examined in terms of the small deflection theory or the large deflection theory. The stress-strain relationships for the materials of the structure must be taken into account, when relating the changes in geometry, due to the structural actions. In the analysis of one-dimensional structures, attention is again focused on the overall behavior in terms of load-deflection or moment-curvature relationships in which the stress-strain relationship has been assumed or is implicit in the formulation of the force-deformation relationships. The shape of the force-deformation curve will determine whether the structural behavior will be linear or non-linear, or whether the mode of failure will be of a brittle or ductile character. Some of the assumptions introduced to facilitate the theoretical analysis of skeletal structures may also be introduced to advantage in the planning of model analysis methods. This is particularly the case for models used to simulate the behavior of elastic prototype structures which are assumed to be composed of homogeneous, isotropic materials complying with Hooke's Law and never stressed beyond their limits of proportionality.

6.1.1. Non-linear Elastic Behavior

Elastic models may simulate overall non-linear elastic behavior although the materials have linear stress-strain characteristics. This happens when the deflections are such that stresses, strains, and reactions are no longer directly proportional to the applied loads, that is, the deformations affect the actions of the applied loads. Non-linear behavior in skeletal structures may develop due to large deflections, changes in boundary conditions or as a result of stability. The principle of superposition is not valid where non-

linear behavior exists and indirect model analysis cannot be used. Therefore, in the general case, in order to reproduce a prescribed state of deformation of the prototype it should be $\epsilon_p = \epsilon_m$ and $\nu_p = \nu_m$. Also, the ratio of the stresses will be the same as the ratio of the Young's Modulus of Elasticity for the prototype and model materials.

6.1.2. Linear Elastic Behavior

If the overall behavior of a skeletal structure is linear, the similarity requirements may be simplified. Since the principle of superposition is valid for linear behavior, indirect as well as direct model methods may be used. By using the model to predict overall behavior it is permissible to use different shapes of cross-sections of the members of the model and the prototype provided the ratios of their gross axial, flexural, shear and torsional rigidities are correctly reproduced to scale.

6.1.3. Characteristics of Observations

Observations have two general characteristics, qualitative and quantitative. The qualitative aspect of an observation serves to identify the characteristics of behavior so that the phenomenon may be accurately described or at least identified sufficiently to distinguish it from any other phenomenon. In addition, a quantitative indication of the phenomenon is essential to indicate the extent or degree of the occurrence and to assist in distinguishing it from qualitatively similar occurrences of different magnitude. In order to maintain an effective and accurate record of an observation so as to make predictions from it, or to convey accurately information concerning it to someone else, standards of

description are necessary. The qualitative characteristics of the observation may be described in terms of standardized operations which identify classes of quantities such as length (L), force (F), or time (T). These qualitative characteristics are called the dimensions of the quantity observed.

6.1.4. Scale Model In Creep-Fatigue

The creep-fatigue phenomenon involves the following parametric relation (Appendix F):

$$f(l, M, I, \rho, E, t, \omega, \sigma, \varepsilon, T, F, \Delta, \delta, \alpha, a) = 0 \quad (148)$$

The dimensions of the parameters involved are given in Table 6 (Appendix F). The For exact modeling one very difficult scaling law relating to the modulus of elasticity and densities of the model and prototype must be satisfied. If the modulus of elasticity of the model material is the same as the prototype material, then the model material density must be:

$$\rho_m = \lambda_L \rho_p \quad (149)$$

For any reasonable value of λ_L , the model density requirement is impossible to satisfy because of material unavailability, and make it extremely difficult to choose the respective λ -factor.

Table 6 Parameters involved in modeling.

	Symbol	Measured Quantity	Dimension
1	l	Characteristic Length	L
2	I	Moment of Inertia	L ⁴
3	ρ	Density	ML ⁻³
4	E	Modulus of Elasticity	ML ⁻¹ T ⁻²
5	t	Characteristic Time	T
6	ω	Characteristic Frequency	T ⁻¹
7	σ	Stress	ML ⁻¹ T ⁻²
8	ε	Strain	-----
9	T	Temperature	θ
10	F	Force	MLT ⁻²
11	Δ	Elongation	L
12	δ	Deflection	L
13	α	Thermal Expansion Coefficient	θ ⁻¹
14	M	Mass	M
15	a	Characteristic Acceleration of Vibration	LT ⁻²

extraction of nondimensional Π-numbers is explained in Appendix F. The Π-numbers are:

$$(1) \Rightarrow \Pi_1 = \left(\frac{at^2}{L}\right)_p = \left(\frac{at^2}{L}\right)_m \Rightarrow \lambda_t = \lambda_L^{1/2}$$

$$(2) \Rightarrow \Pi_2 = \left(\frac{Et^2}{\rho L^2}\right)_p = \left(\frac{Et^2}{\rho L^2}\right)_m \Rightarrow \lambda_E = \frac{\lambda_\rho \lambda_L^2}{\lambda_t^2} = \lambda_\rho \lambda_L$$

$$(3) \Rightarrow \Pi_3 = \left(\frac{Et^2}{\rho L^2} \right)_p = \left(\frac{\sigma t^2}{\rho L^2} \right)_m \Rightarrow \lambda_\sigma = \lambda_\rho \lambda_L$$

$$(4) \Rightarrow \Pi_4 = \left(\frac{I}{\Delta \delta L^2} \right)_p = \left(\frac{I}{\Delta \delta L^2} \right)_m \Rightarrow \lambda_I = (\lambda_L)^4$$

$$(5) \Rightarrow \Pi_5 = \left(\frac{Ft^2}{\rho L^4} \right)_p = \left(\frac{Ft^2}{\rho L^4} \right)_m \Rightarrow \lambda_F = \lambda_\rho (\lambda_L)^3$$

$$(6) \Rightarrow \Pi_6 = \left(\frac{\delta}{L} \right)_p = \left(\frac{\delta}{L} \right)_m \Rightarrow \lambda_\delta = \lambda_L$$

$$(7) \Rightarrow \Pi_7 = \left(\frac{\Delta}{L} \right)_p = \left(\frac{\Delta}{L} \right)_m \Rightarrow \lambda_\Delta = \lambda_L$$

$$(8) \Rightarrow \Pi_8 = (\omega t)_p = (\omega t)_m \Rightarrow \lambda_\omega = (\lambda_L)^{-1/2}$$

$$(9) \Rightarrow \Pi_9 = (\varepsilon)_p = (\varepsilon)_m \Rightarrow \lambda_\varepsilon = 1$$

$$(10) \Rightarrow \Pi_{10} = \left(\frac{E}{\sigma} \right)_p = \left(\frac{E}{\sigma} \right)_m \Rightarrow \lambda_E = \lambda_\sigma = \lambda_\rho \lambda_L$$

$$(11) \Rightarrow \Pi_{11} = \left(\frac{\rho A \omega^2}{T \alpha E} \right)_p = \left(\frac{\rho A \omega^2}{T \alpha E} \right)_m \Rightarrow \lambda_{\Delta T} \lambda_\alpha \lambda_E = \lambda_\rho \lambda_A \lambda_\omega^2 \Rightarrow \lambda_{\Delta T} = \frac{\lambda_\rho \lambda_A \lambda_\omega^2}{\lambda_\alpha \lambda_E}$$

$$\text{also we have } (\varepsilon_T)_p = (\varepsilon_T)_m \Rightarrow \lambda_{\Delta T} = \lambda_T = \lambda_k^{-1} = \frac{\lambda_\rho \lambda_A \lambda_\omega^2}{\lambda_\alpha \lambda_E} \quad (150)$$

Since all the events must be modeled on unified time scale, meaningful model results are expected only if all frequency scale factors $(\lambda_\omega, \lambda_{\omega_n})$ have the same value. The time scale is unified with

$$\lambda_\omega = \lambda_{\omega_n} = (\lambda_L)^{-1/2} \quad (151)$$

where

$$\omega_n = \sqrt{\frac{K}{m}} = \sqrt{\frac{AE}{L\rho L^3}} = k_1 \sqrt{\frac{EI}{A\rho L^4}} \quad (152)$$

Taking λ_c , cross-section length factor, dimensionally we have $\Rightarrow I = k_2 (\lambda_c)^4$

$$\lambda_\omega = \lambda_{\omega_n} = (\lambda_L)^{-1/2} = \sqrt{\frac{\lambda_E \lambda_c^4}{\lambda_\rho \lambda_c^2 \lambda_L^4}} \Rightarrow \frac{\lambda_c}{\lambda_L^2} \sqrt{\frac{\lambda_E}{\lambda_\rho}} \Rightarrow \lambda_c = (\lambda_L)^{3/2} \sqrt{\frac{\lambda_\rho}{\lambda_E}} \quad (153)$$

This result is distortion in cross section, but will give free choice to material. Limitation with this is that we only get correct scaling for bending natural frequency, because we are scaling frequencies using bending frequency expression. When the structure does not have gravitational force, it is acceptable to neglect acceleration.

For any vibrating structure simulation:

$$\left(\frac{\rho \omega^2 L^2}{E}\right)_p = \left(\frac{\rho \omega^2 L^2}{E}\right)_m \quad (154)$$

$$(v)_p = (v)_m \quad (155)$$

Equation (155) can be neglected if $\dot{\epsilon}$ is not high, and otherwise we should select the same material.

$$\text{(Equation 154)} \Rightarrow \lambda_\omega = \frac{1}{\lambda_L} \sqrt{\frac{\lambda_E}{\lambda_\rho}} \Rightarrow \text{Time scale} = \lambda_t = (\lambda_\omega)^{-1} = \lambda_L \sqrt{\frac{\lambda_\rho}{\lambda_E}} \quad (156)$$

Using this scale in other equations:

$$(1) \Rightarrow \lambda_a = \frac{\lambda_L}{\lambda_i^2} = \frac{\lambda_L \lambda_E}{\lambda_L^2 \lambda_\rho} \Rightarrow \text{Acceleration scale} = \lambda_a = \frac{\lambda_E}{\lambda_\rho \lambda_L} \quad (157)$$

$$(3) \Rightarrow \lambda_\sigma = \frac{\lambda_L^2 \lambda_\rho}{\lambda_i^2} \Rightarrow \text{Stress scale} = \lambda_\sigma = \lambda_E \quad (158)$$

$$(5) \Rightarrow \lambda_F = \lambda_L^3 \lambda_\rho \Rightarrow \text{Force scale} = \lambda_F = \lambda_E \lambda_L^2 \quad (159)$$

$$(11) \Rightarrow \lambda_{\Delta T} \lambda_\alpha \lambda_E = \lambda_\rho \lambda_A \lambda_\omega^2 \Rightarrow \text{Temperature scale} = \lambda_{\Delta T} = \frac{\lambda_\rho \lambda_A \lambda_\omega^2}{\lambda_\alpha \lambda_E} \quad (160)$$

This is a distortion or relaxation because $\lambda_a=1$ or $(a)_p = (a)_m$.

6.2. SCALE MODEL OF CANTILEVER BEAM IN CREEP-FATIGUE

6.2.1. Frequency Scaling

- a) Same material, and different dimensions from [179]. Table 7 shows the information of two different materials selected for scale model test.

Table 7 Parameters involved in modeling.

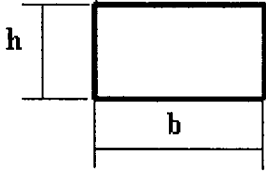
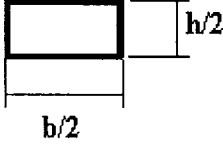
Parameters	Prototype	Model
Length	1 m	0.5 m
Dimension	38.17 x 6.38 cm	19.085 x 3.19 cm
Material	Steel	Aluminum
Modulus of Elasticity	2.05e11 N/m ²	69e9 N/m ²
Density	7870 kg/m ³	2700 kg/m ³
Poisson's Ratio	0.29	0.3
Thermal Expansion Coefficient	12e-6 m/m°C	23e-6 m/m°C
Cross Section		

Table 8 Parameters involved in modeling.

Sr. No.	Model ω_n (Hz)		Prototype ω_n (Hz)		Prototype ω_n (Hz)	
	(ANSYS)		(Predicted)		(ANSYS)	
	Present	ref. [178]	Present	ref. [178]	Present	ref. [178]
1	10.4196	10.42	5.25978	5.259986	5.2598	5.26
2	65.2981	65.298	32.9623	32.96225	32.962	32.962
3	182.818	182.82	92.2860	92.28702	92.288	92.289
4	358.217	358.22	180.827	180.8284	180.83	180.83
5	592.093		298.886		298.89	

with the above data we have: $\lambda_l=2$, $\lambda_E=2.89855$, $\lambda_p=2.88889$, Length scale factor = 2 →

$$\lambda_\omega = \frac{1}{\lambda_L} \sqrt{\frac{\lambda_E}{\lambda_p}} = 0.5008354, \text{ the results of predicted natural frequencies and the one}$$

calculated by FEM are tabulated in Table 8.

b) Different materials and half size.

Table 9 shows the information of two different materials selected for scale model test.

With the above data we have: $\lambda_l=2$, $\lambda_E=2.89855$, $\lambda_p=2.88889$ and Length scale factor = 2

$$\rightarrow \lambda_\omega = \frac{1}{\lambda_L} \sqrt{\frac{\lambda_E}{\lambda_p}} = 0.5008354. \text{ The results of predicted natural frequencies and the one}$$

calculated by FEM are tabulated in Table 10.

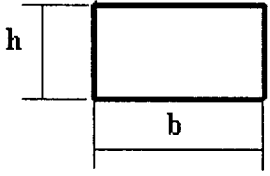
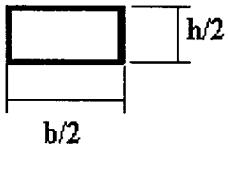
Note: The change of length in general (length scale) should be considered in area (A) and moment of inertia (I) as well.

6.2.2. Amplitude Scaling

Figure 47 and Figure 48 show the amplitudes of outputs due to harmonic input force.

We have $\lambda_F = \lambda_E \lambda_L^2 = 11.59$. In order to get the output of the model, the applied force on model should be 8.625 N, instead of 100 N for the prototype. By Equation (149) $\lambda_\delta = \lambda_L=2$. As the figures show, the maximum amplitude of the prototype by ANSYS is 4.51 mm and the predicted maximum amplitude of the prototype is $2 * 2.4 = 4.8$ mm. The small error is due to the fact that number of substeps taken in harmonic analysis is not exact and if we increase number of substeps we will get exact predicted value.

Table 9 Parameters involved in modeling.

Parameters	Prototype	Model
Length	1 m	0.5 m
Material	Steel	Aluminum
Modulus of Elasticity	2e11 N/m ²	69e9 N/m ²
Density	7800 kg/m ³	2700 kg/m ³
Poisson's Ratio	0.3	0.3
Thermal Expansion Coefficient	12e-6 m/m°C	23e-6 m/m°C
Cross Section		

6.2.3. Acceleration Scaling

Figure 49 and Figure 50 show the accelerations of outputs due to harmonic input force.

We have $\lambda_F = \lambda_E \lambda_L^2 = 11.59$. In order to get the output of the model, the applied force on model should be 8.625 N, instead of 100 N for the prototype. By Equation (149)

$\lambda_a = \frac{\lambda_E}{\lambda_\rho \lambda_L} = 0.50167$. As the figures show, the first maximum acceleration of the

prototype by ANSYS is 41981.7 g and the predicted maximum acceleration of the

prototype is $0.50167 * 95774.2 = 48047.04$ g. The second maximum acceleration of the

prototype by ANSYS is 140615 g and the predicted maximum acceleration is equal to

Table 10 Parameters involved in modeling.

Sr. No.	Model ω_n (Hz) (ANSYS)	Prototype ω_n (Hz) (Predicted)	Prototype ω_n (Hz) (ANSYS)
1	16.332	8.1796	8.1645
2	102.34	51.255	51.160
3	286.50	143.49	143.22
4	561.29	281.11	280.60
5	927.63	464.59	463.74
6	1385.4	693.86	692.58
7	1934.6	968.92	967.16
8	2528.3	1266.3	1264.1
9	2575.6	1289.9	1287.6
10	3308.5	1657.0	1654.0

$0.50167 * 281181.21 = 141060.18$ g. The small error is due to the fact that number of substeps taken in harmonic analysis is not exact if we increase number of substeps we will get exact predicted value.

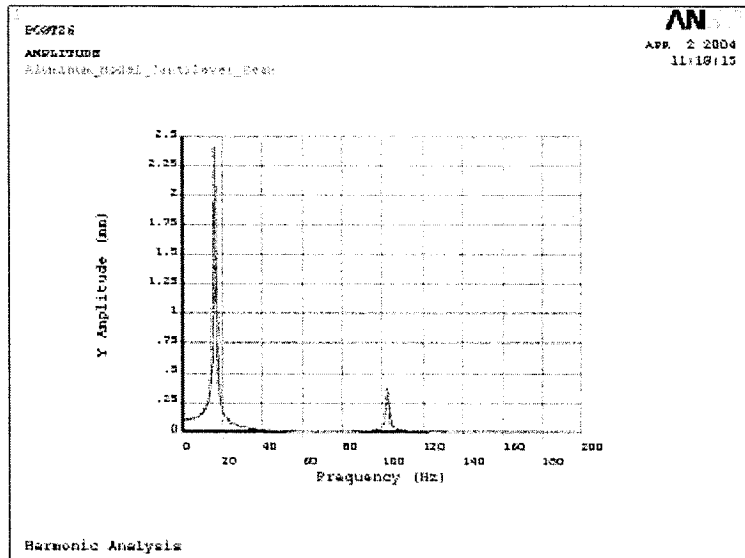


Figure 47 Amplitude vs. frequency of the 0.5 meter model.

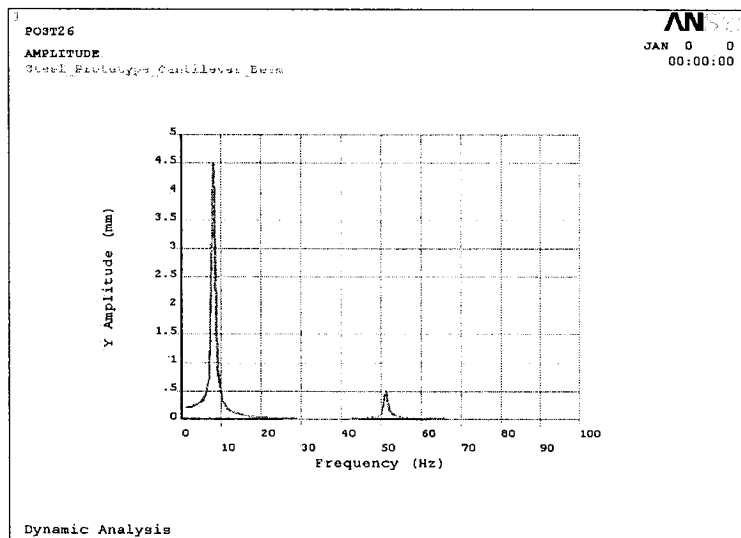


Figure 48 Amplitude vs. frequency of the 1 meter prototype.

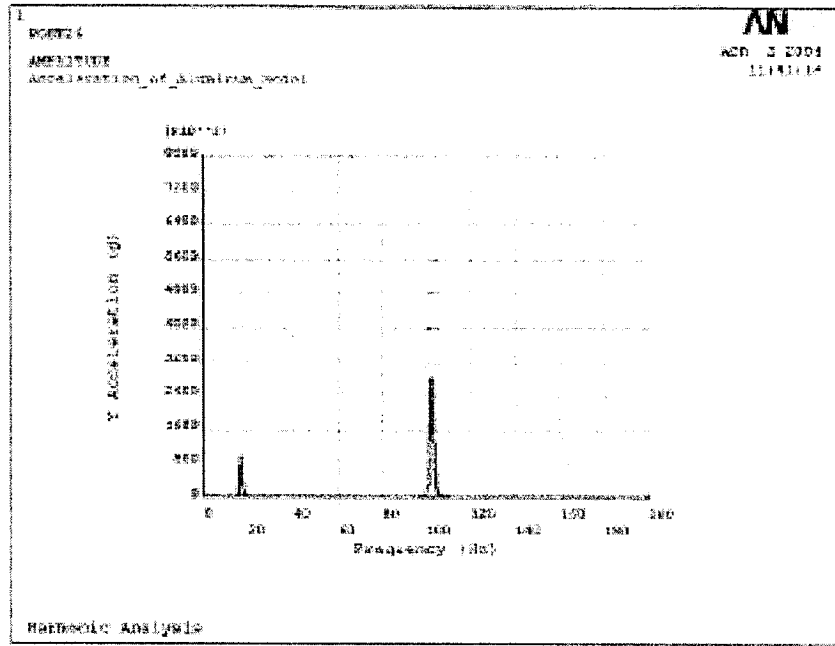


Figure 49 Acceleration vs. frequency of the 0.5 meter model.

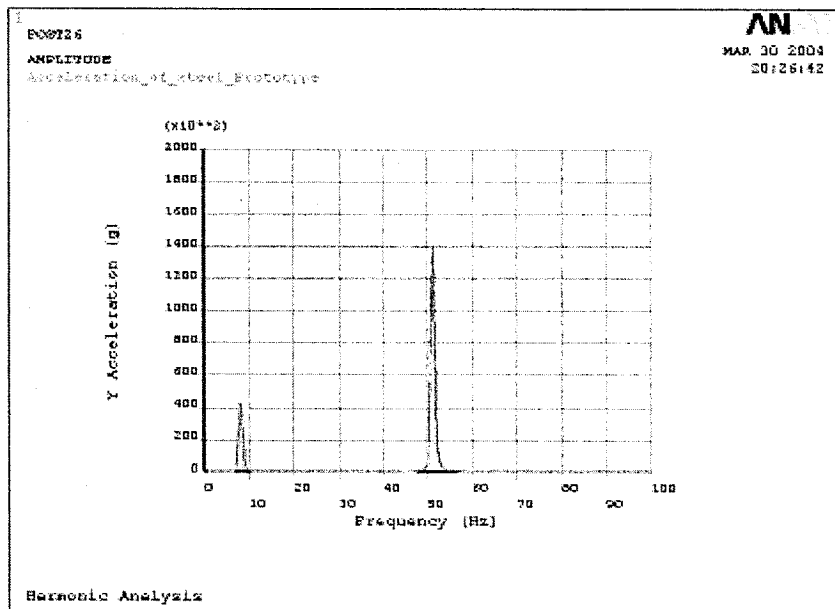


Figure 50 Acceleration vs. frequency of the 1 meter prototype.

6.2.4. Stress Scaling

Figure 51 and Figure 52 show the direct and bending stresses of outputs due to harmonic input force.

We have $\lambda_F = \lambda_E \lambda_L^2 = 11.59$. In order to get the output of the model, the applied force on model should be 8.625 N, instead of 100 N which is for prototype.

By Equation (160) $\lambda_\sigma = \lambda_E = 2.89855$. As the figures show, the maximum stress of the prototype by ANSYS is $0.6e9$ Pa and the predicted maximum stress of the prototype is $2.89855 * 0.206e9 = 0.597e9$ pa.

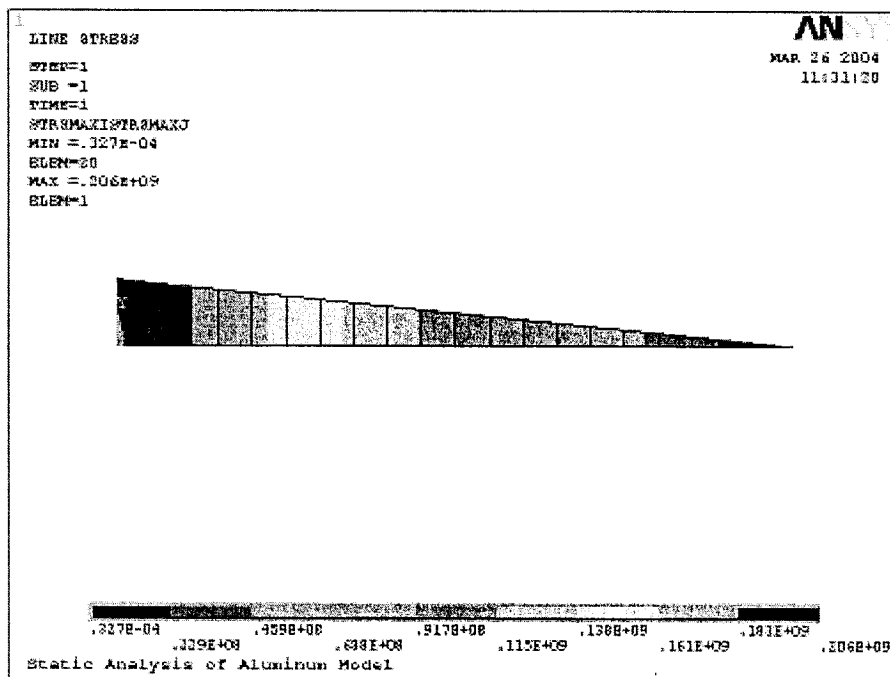


Figure 51 Stress vs. length of the 0.5 meter model.

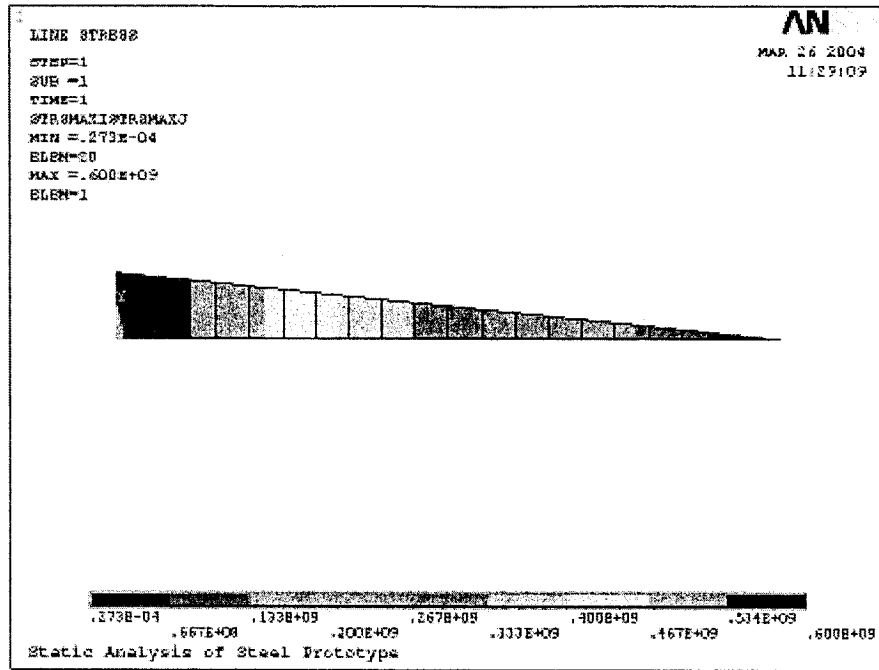


Figure 52 Stress vs. length of the 1 meter prototype.

6.2.5. Strain Scaling

Figure 53 and Figure 54 show the elastic bending strains of outputs due to harmonic input force.

We have $\lambda_F = \lambda_E \lambda_L^2 = 11.59$. Then to get the output of the model, the applied force on model should be 8.625 N, instead of 100 N which is for prototype.

By Equation (149) $\lambda_e = 1$. As the figures show, the maximum strain of the prototype by ANSYS is 0.003001 and the predicted maximum stress of the prototype is $1 * 0.002991 = 0.002991$.

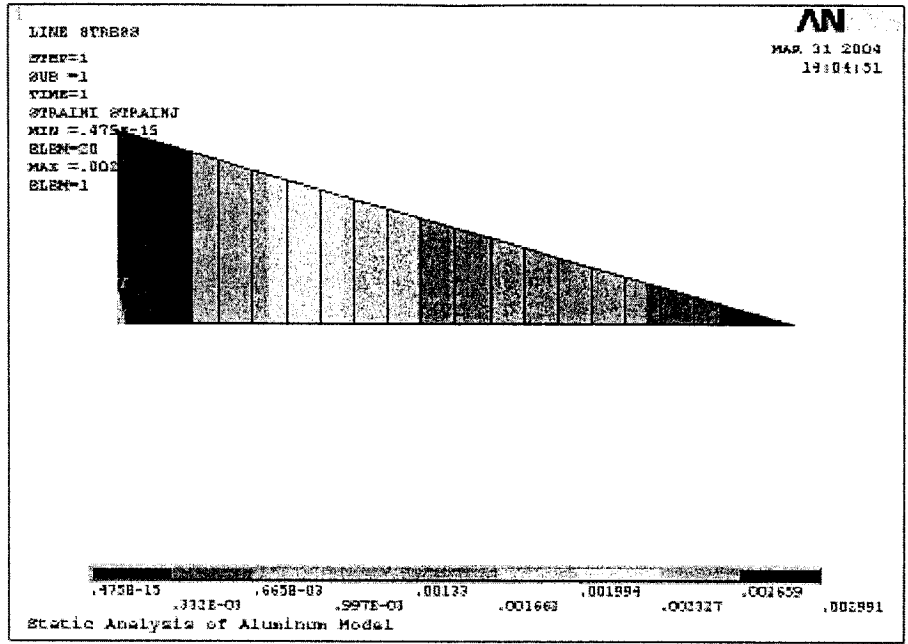


Figure 53 Strain vs. length of the 0.5 meter model.

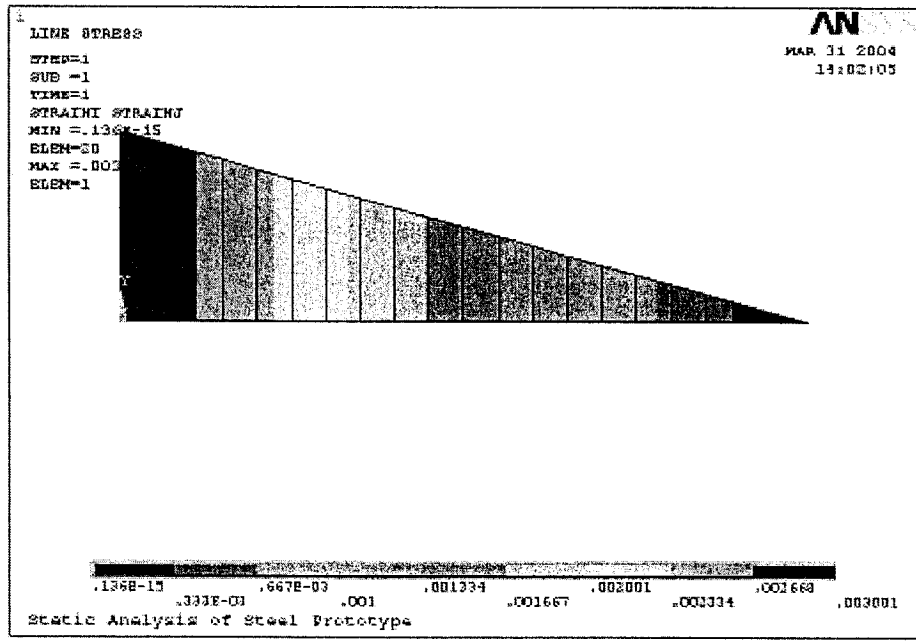


Figure 54 Strain vs. length of the 1 meter prototype.

6.2.6. Temperature effect

From Equation (160) we have $\lambda_{\Delta T} = \frac{\lambda_{\rho} \lambda_A \lambda_{\omega}^2}{\lambda_{\alpha} \lambda_E}$. By taking this scale factor into

consideration for applying the temperature on prototype and model we will investigate the stresses, strains and elongations in prototype and model.

6.2.6.1. Strain Scaling

Figure 55 and Figure 56 show the thermal strains of outputs due to temperature input load.

We have $\lambda_{\Delta T} = \frac{\lambda_{\rho} \lambda_A \lambda_{\omega}^2}{\lambda_{\alpha} \lambda_E} = 1.917$. Then to get the output of the model, the applied

temperature on model should be 312.12K, while the applied temperature on prototype is 348K, and the reference temperature for both is 273K.

Logically we should have $\lambda_{\epsilon} = 1$. As the figures show, the maximum strain of the prototype by ANSYS is 0.9e-3 and the predicted maximum stress of the prototype is $1 * 0.9e-3 = 0.9e-3$.

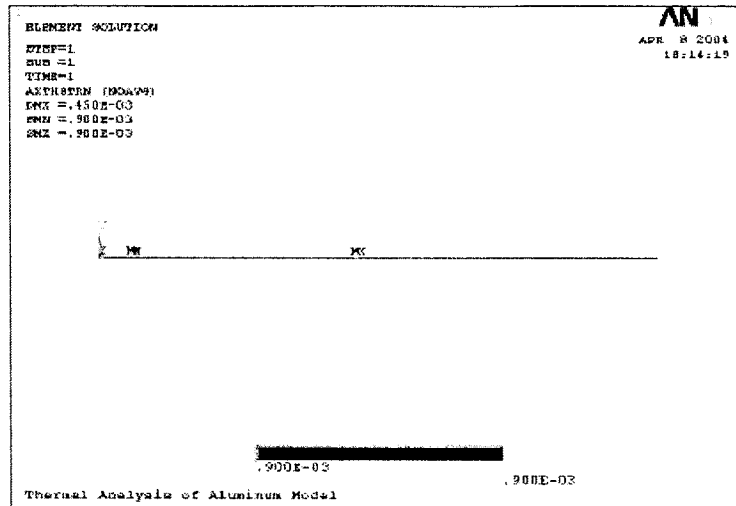


Figure 55 Strain vs. length of the 0.5 meter model.

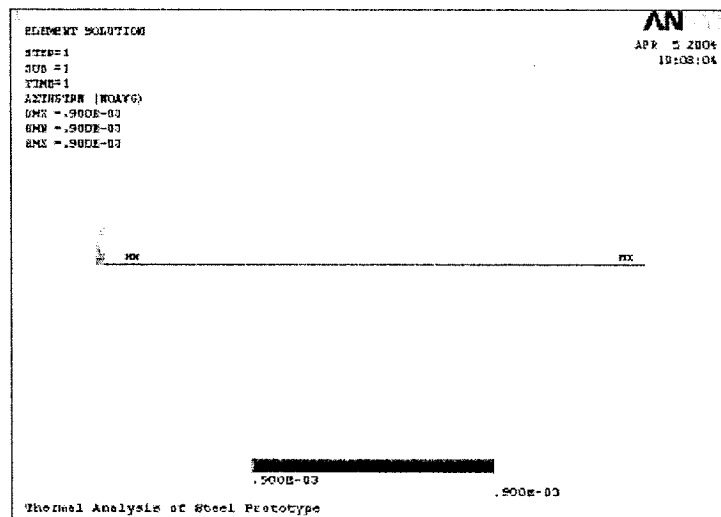


Figure 56 Strain vs. length of the 1 meter prototype.

6.2.6.2. Displacement Scaling

Figure 57 and Figure 58 show the axial elongation due to thermal strain.

We have $\lambda_{\Delta T} = \frac{\lambda_p \lambda_A \lambda^2_{\omega}}{\lambda_{\alpha} \lambda_E} = 1.917$. Then to get the output of the model, the applied

temperature on model should be 312.12K, while the applied temperature on prototype is 348K 8.625 N, and the reference temperature for both is 273K.

By Equation (149), $\lambda_\delta = \lambda_L=2$. As the figures show, the maximum displacement of the prototype by ANSYS is $0.9e-3$ mm and the predicted maximum amplitude of the prototype is $2 * 0.45e-3 = 0.9e-3$ mm.

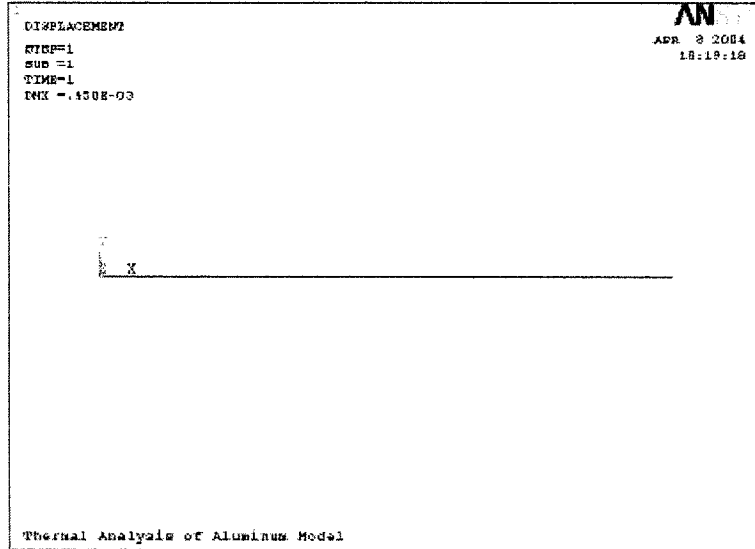


Figure 57 Displacement vs. length of the 0.5 meter model.

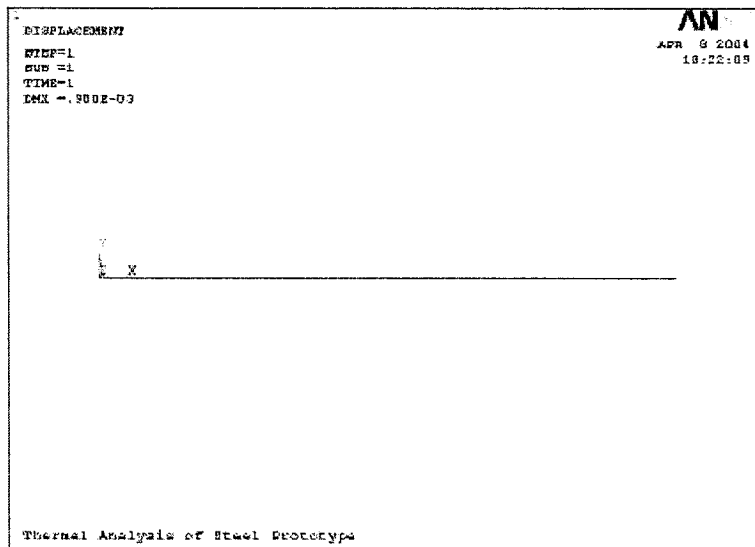


Figure 58 Displacement vs. length of the 1 meter prototype.

6.3. SCALE MODEL OF GAS TURBINE BLADE IN CREEP-FATIGUE

Table 11 Parameters involved in modeling.

Parameters	Prototype	Model
Length	0.328 m	0.164 m
Material	Steel	Aluminum
Modulus of Elasticity	2e11 N/m ²	69e9 N/m ²
Density	7800 kg/m ³	2700 kg/m ³
Poisson's Ratio	0.3	0.3
Thermal Expansion Coefficient	12e-6 m/m°C	23e-6 m/m°C
Cross Section		

whit the above data we have:

$$\lambda_l=2, \lambda_E=2.89855, \lambda_\rho=2.88889$$

$$\text{Length scale factor} = 2 \rightarrow \lambda_\omega = \frac{1}{\lambda_L} \sqrt{\frac{\lambda_E}{\lambda_\rho}} = 0.5008354$$

It must be noted that the change of length in general (length scale) should be considered in area (A) and moment of inertia (I) as well.

6.3.1. Natural Frequencies Scaling

Table 12 presents the natural frequencies of first 10 modes of the model, and the prototype by ANSYS and also the predicted values for the prototype. As expected, the ANSYS values conform that the natural frequencies of model is = natural frequencies of model * natural frequency scale factor.

Table 12 Parameters involved in modeling.

Sr. No.	Model ω_n (Hz) (ANSYS)	Prototype ω_n (Hz) (Predicted)	Prototype ω_n (Hz) (ANSYS)
1	51.536	102.90	102.90
2	212.09	423.47	423.48
3	223.11	445.48	445.48
4	491.09	980.54	980.55
5	528.41	1055.1	1055.1
6	907.37	1811.7	1811.7
7	1347.2	2689.9	2689.9
8	1468.2	2931.5	2931.5
9	1603.6	3201.8	3201.8
10	2174.6	4341.9	4342.0

6.3.2. Stress Scaling

Figure 59 and Figure 60 show the stress of outputs due to rotary speed input.

We have $\lambda_\omega = \frac{1}{\lambda_L} \sqrt{\frac{\lambda_E}{\lambda_\rho}} = 0.5008354$. Then to get the output of the model, the applied

rotary speed on model should be $314.159265 / 0.5008354 = 627.270988$ rpm.

By Equation (149), $\lambda_\sigma = \lambda_E = 2.89855$. As the figures show, the maximum stress of the prototype by ANSYS is $0.767e8$ Pa and the predicted maximum amplitude of the prototype is $0.265e8 * 2.89855 = 0.768e8$ pa.

The small error is due to the fact that number of substeps taken in Harmonic analysis is not exact if we increase number of substeps we will get exact predicted value.

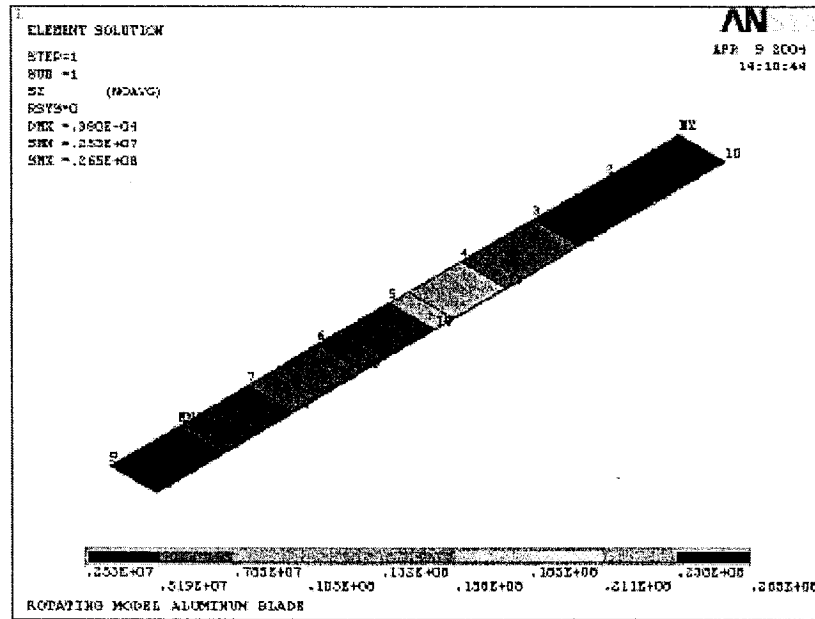


Figure 59 Stress vs. length of the 0.164 meter model.

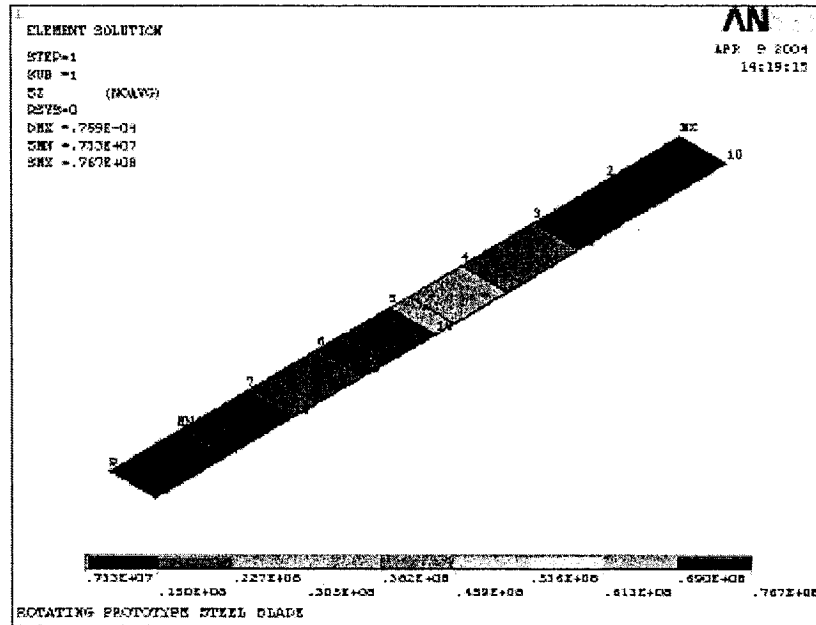


Figure 60 Stress vs. length of the 0.328 meter prototype.

6.3.3. Strain Scaling

Figure 61 and Figure 62 show the elastic strains of outputs due to rotary speed input load.

We have $\lambda_{\omega} = \frac{1}{\lambda_L} \sqrt{\frac{\lambda_E}{\lambda_{\rho}}} = 0.5008354$. Then to get the output of the model, the applied

rotary speed on model should be $314.159265 / 0.5008354 = 627.270988$ rpm.

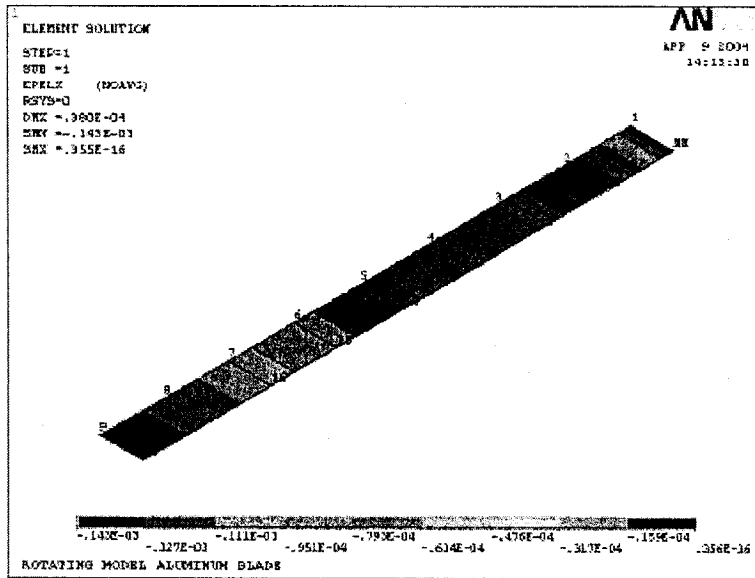


Figure 61 Strain vs. length of the 0.164 meter model.

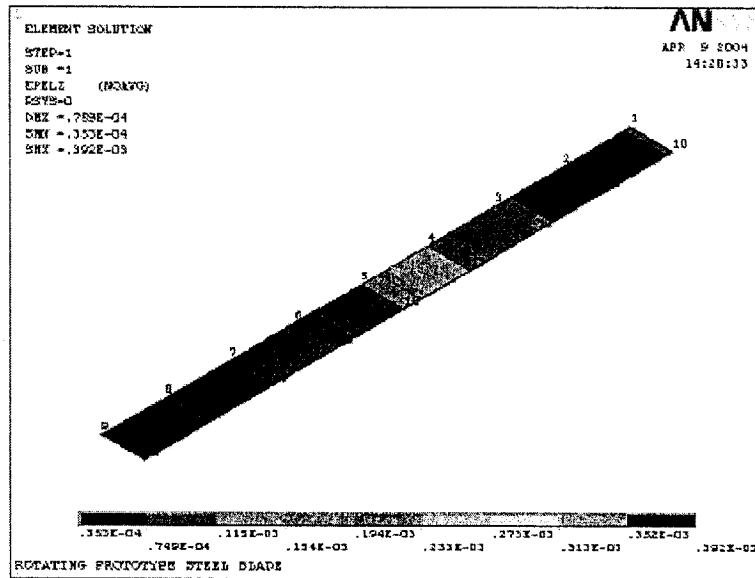


Figure 62 Strain vs. length of the 0.328 meter prototype.

By Equation (149), $\lambda_c = 1$. As the figures show, the maximum strain of the prototype by ANSYS is $0.392e-3$ and the predicted maximum stress of the prototype is $1 * 0.392e-3 = 0.392e-3$.

6.3.4. Displacement Scaling

By Equation (149), $\lambda_s = \lambda_L = 2$. As the figures show, the maximum displacement of the prototype by ANSYS is $0.759e-4$ mm and the predicted maximum amplitude of the prototype is $2 * 0.380e-4 = 0.760e-4$ mm. As Figure 63 and Figure 64 show, the displacement of prototype is twice of the model displacement.

6.3.5. Temperature Effect

From Equation (160) we have $\lambda_{\Delta T} = \frac{\lambda_\rho \lambda_A \lambda_\omega^2}{\lambda_\alpha \lambda_E}$. By taking this scale factor into

consideration for applying the temperature on prototype and model and keeping the scale

factor for angular speed as $\lambda_\omega = \frac{1}{\lambda_L} \sqrt{\frac{\lambda_E}{\lambda_\rho}} = 0.5008354$, we will investigate the stresses,

strains and elongations in prototype and model

6.3.5.1. Stress Scaling

Figure 65 and Figure 66 show the principal stresses, and Figure 67 and Figure 68 show

the Von-Mises stresses of outputs due to rotary speed input. We have $\lambda_\omega = \frac{1}{\lambda_L} \sqrt{\frac{\lambda_E}{\lambda_\rho}} =$

0.5008354. Then to get the output of the model, the applied rotary speed on model should

be $314.159265 / 0.5008354 = 627.270988$ rpm. By Equation (149), $\lambda_\sigma = \lambda_\varepsilon = 2.89855$.

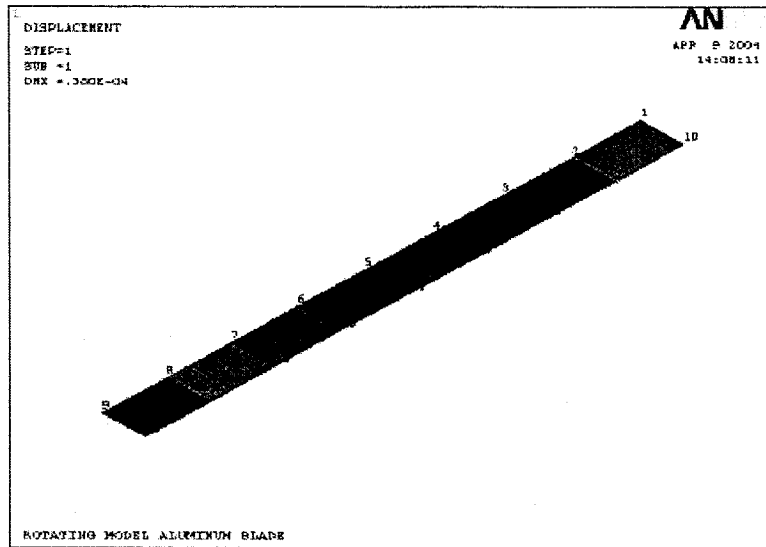


Figure 63 Displacement vs. length of the 0.168 meter model.

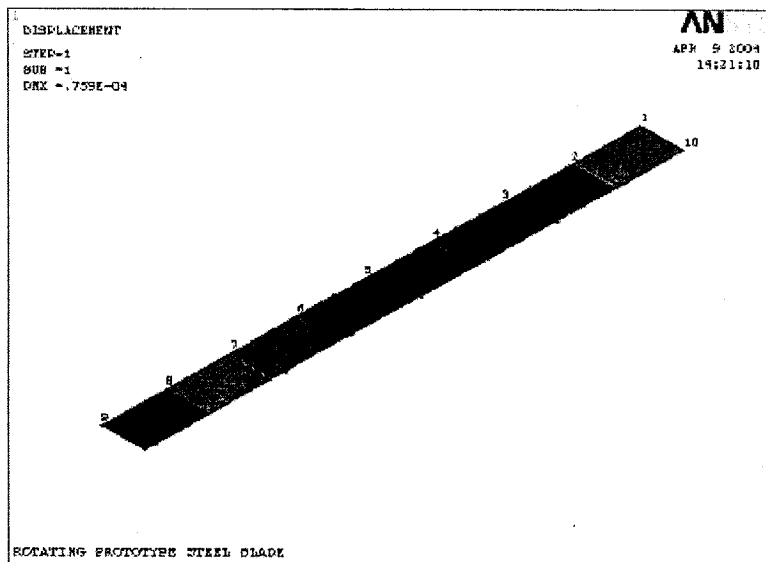


Figure 64 Strain vs. length of the 0.328 meter prototype.

As the figures show, the principle stress of the prototype by ANSYS is $0.767e8$ Pa and the predicted one of the prototype is $0.265e8 * 2.89855 = 0.768e8$ pa. Also the Von-Mises stress of the prototype by ANSYS is $0.796e8$ Pa and the predicted one of the prototype is $0.275e8 * 2.89855 = 0.797e8$ pa.

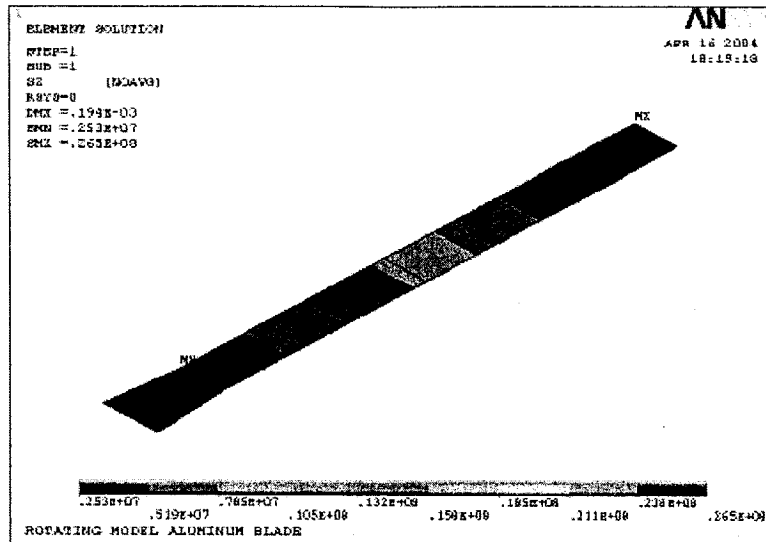


Figure 65 Principle stress vs. length of the 0.164 meter model.

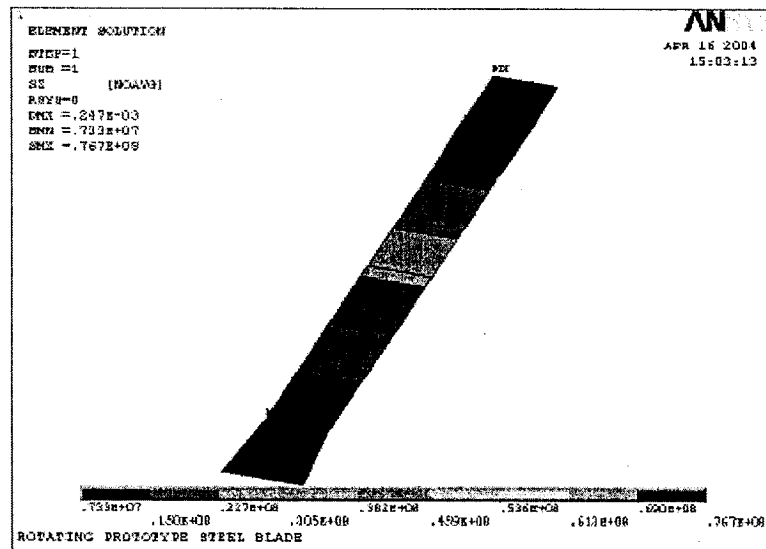


Figure 66 Principle stress vs. length of the 0.328 meter prototype.

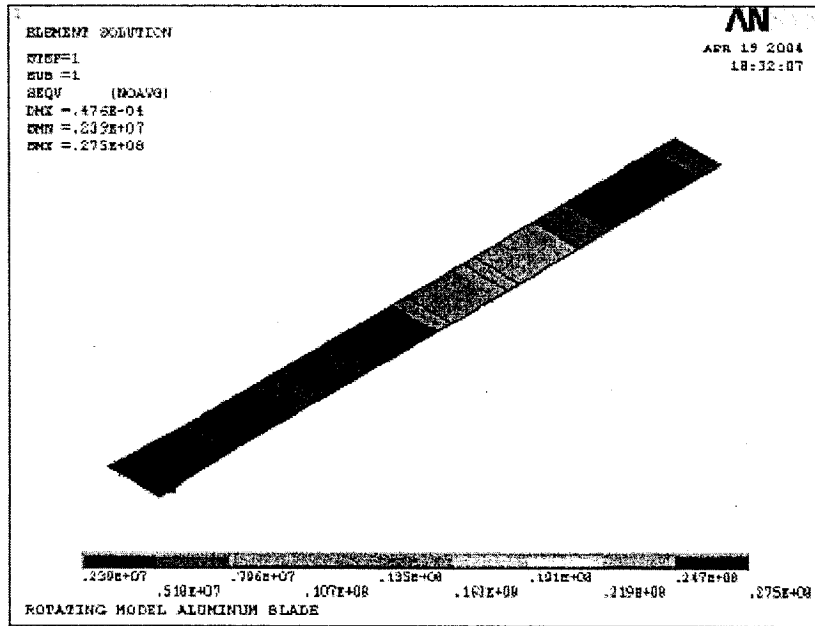


Figure 67 Von-Mises stress vs. length of the 0.164 meter model.

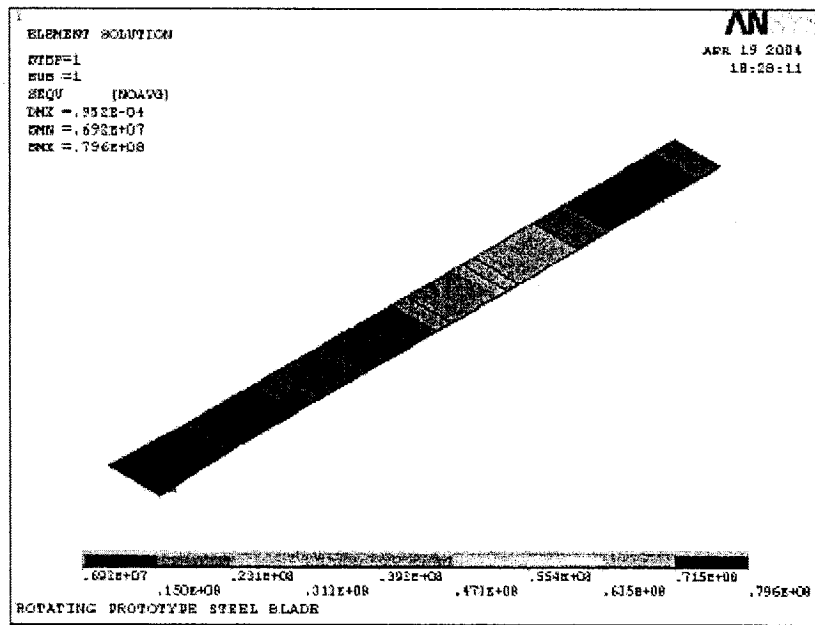


Figure 68 Von-Mises stress vs. length of the 0.328 meter prototype.

6.3.5.2. Force Scaling

Figure 69 and Figure 70 show the axial forces of the model and prototype respectively. We followed the scale factors for length, cross sectional area, Modulus of elasticity, and density, and as the figures show the force scale matches, which is conformation of the “Pi”’s. By Equation (149) we have $\lambda_F = \lambda_E \lambda_L^2 = 11.59$. The force of the prototype by ANSYS is 3330 N and the predicted one of the prototype is $287.215 * 11.59 = 3328.82$ N.

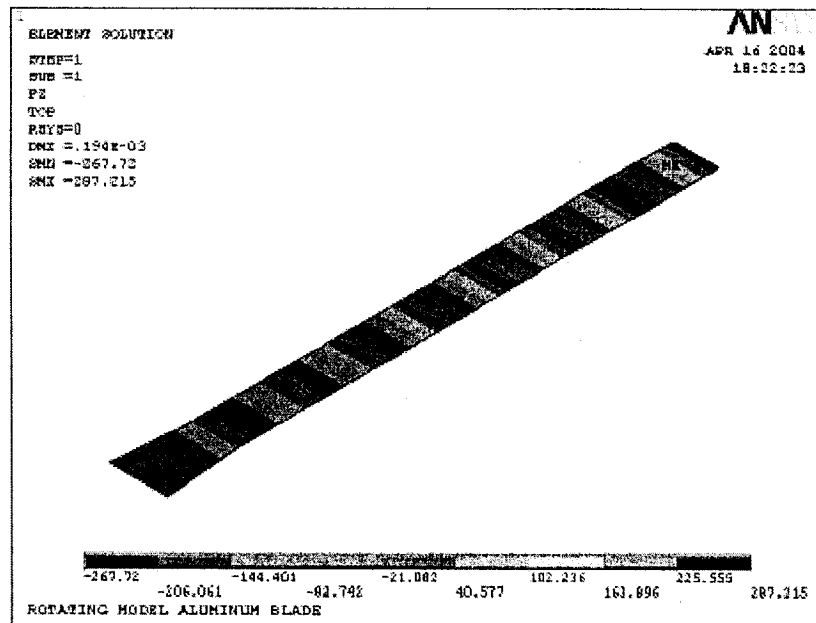


Figure 69 Force vs. length of the 0.164 meter model.

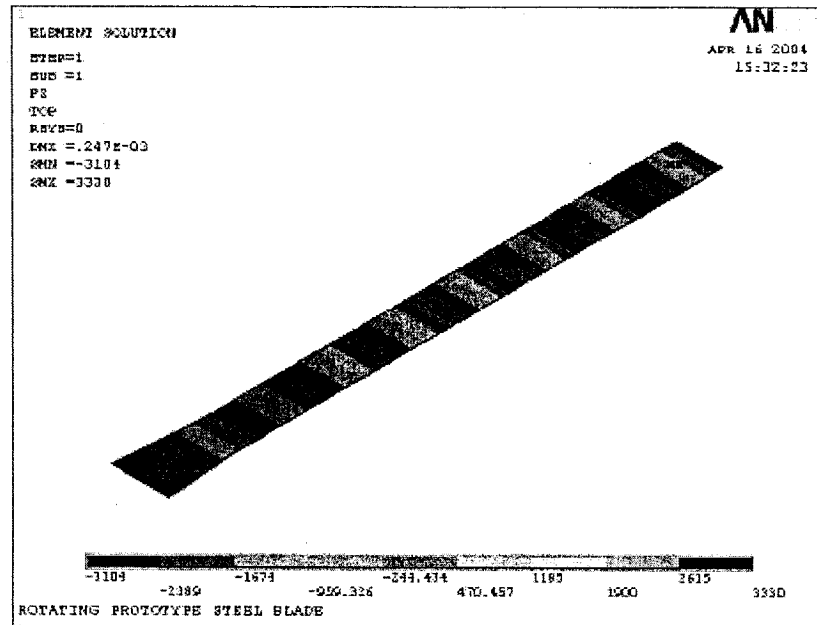


Figure 70 Force length of the 0.328 meter prototype.

6.3.5.3. Strain Scaling

Figure 71 to Figure 76 show the Von-Mises, elastic and thermal strains of outputs due to temperature and angular speed input load.

We have $\lambda_{\Delta T} = \frac{\lambda_{\rho} \lambda_A \lambda_{\omega}^2}{\lambda_{\alpha} \lambda_E} = 1.917$. Then to get the output of the model, the applied

temperature on model should be 312.12K, while the applied temperature on prototype is 348K, and the reference temperature for both is 273K.

Logically we should have $\lambda_{\epsilon} = 1$. As the figures show, all the strains of the 0.168 m Aluminum model and the 0.328 m Steel prototype are identical.

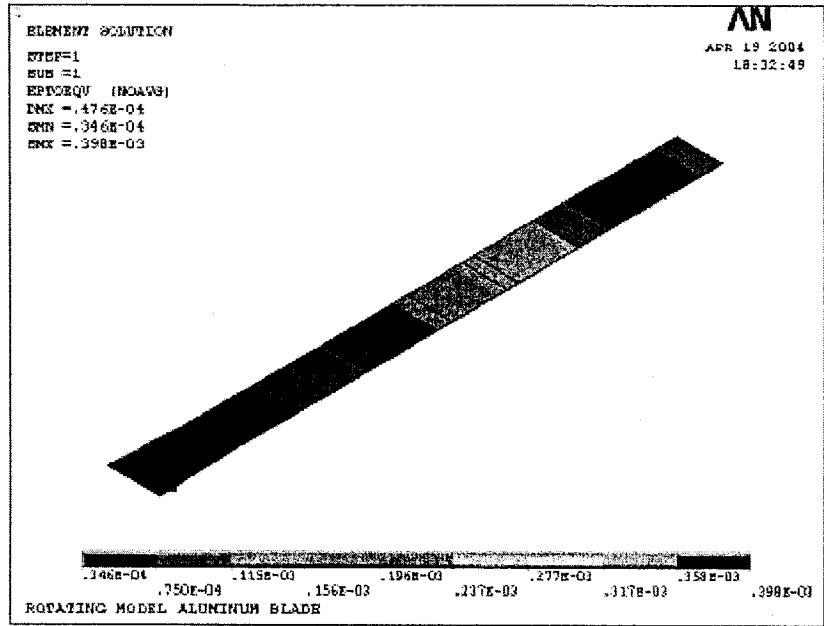


Figure 71 Von-Mises strain vs. length of the 0.164 meter model.

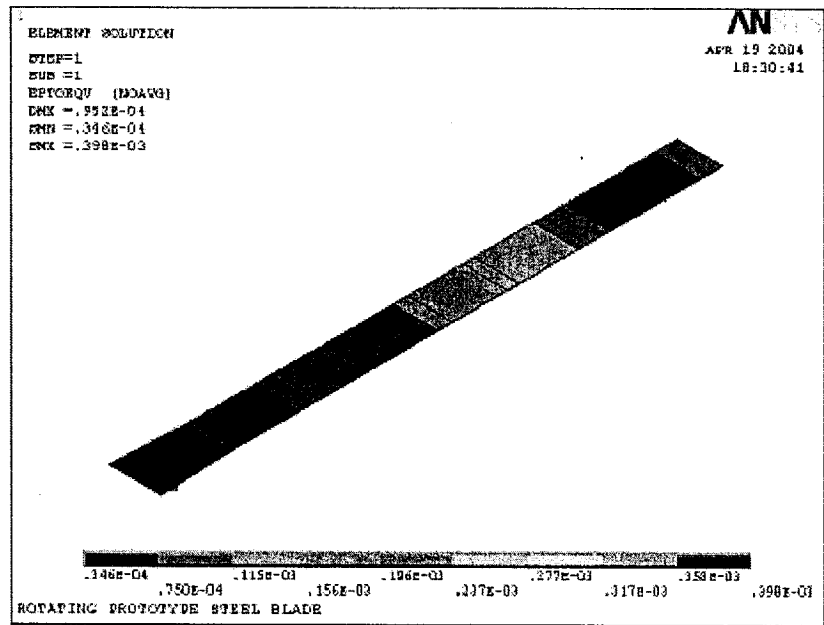


Figure 72 Von-Mises strain vs. length of the 0.328 meter prototype.

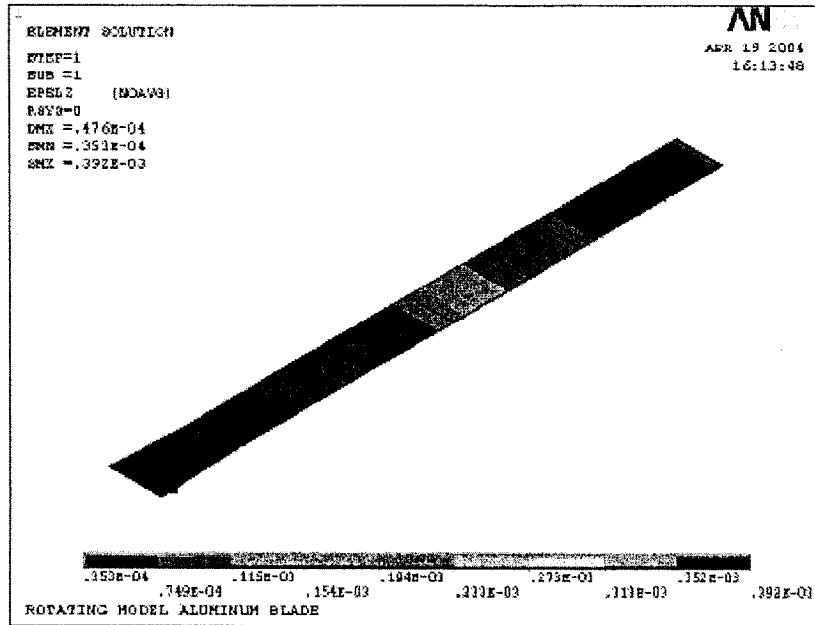


Figure 73 Elastic strain vs. length of the 0.164 meter model.

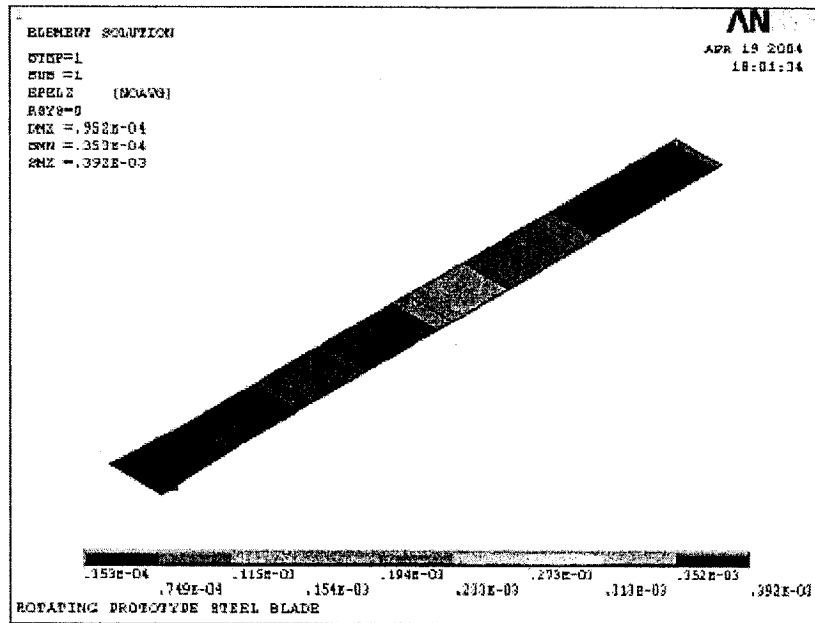


Figure 74 Elastic strain vs. length of the 0.328 meter prototype.

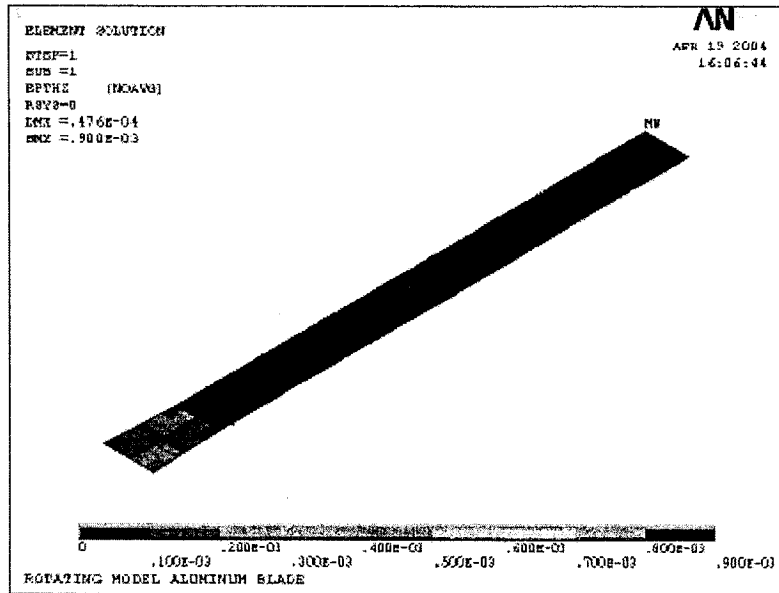


Figure 75 Thermal strain vs. length of the 0.164 meter model.

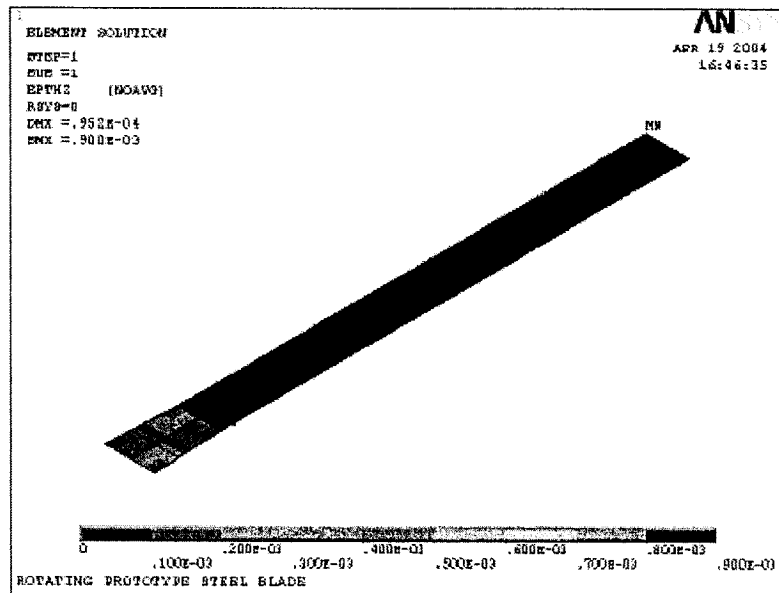


Figure 76 Thermal strain vs. length of the 0.328 meter prototype.

6.3.5.4. Displacement Scaling

Figure 77 and Figure 78 show the axial elongation due to thermal and angular speed loads. By Equation (149), $\lambda_\delta = \lambda_L = 2$. As the figures show, the maximum displacement of

the prototype by ANSYS is $0.944e-4$ mm and the predicted maximum amplitude of the prototype is $2 * 0.472e-4 = 0.944e-4$ mm.

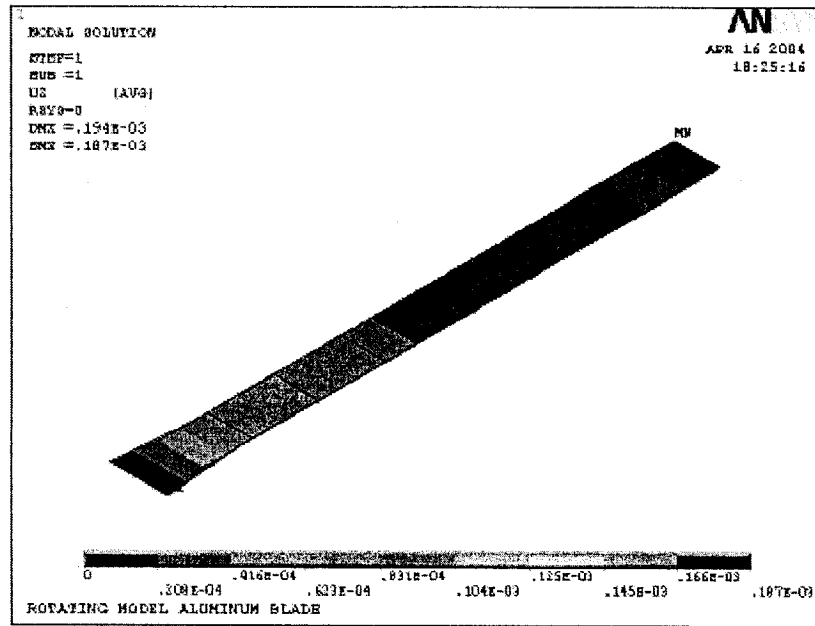


Figure 77 Displacement vs. length of the 0.168 meter model.

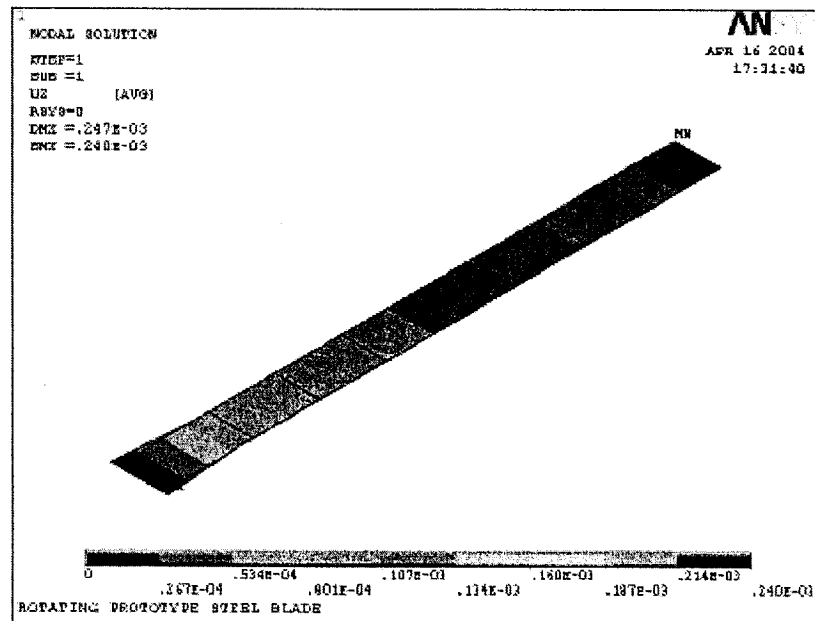


Figure 78 Displacement vs. length of the 0.328 meter prototype.

6.4. TEST ANALYSIS

6.4.1. Accelerated Testing

Frequently high-temperature strength data are needed for conditions for which there is no experimental information. This is particularly true of long-time creep and stress-rupture data, where it is quite possible to find that the creep strength to give 1 percent deformation in 100,000 h (11.4 years) is required, although the alloy has been in existence for only 2 years.

Obviously, in such situations extrapolation of the data to long times is required. Reliable extrapolation of creep, creep-fatigue, and stress-rupture curves to longer times can be made only when it is certain that no structural changes occur in the region of extrapolation which would produce a change in the slope of the curve. Since structural changes generally occur at shorter times for higher temperatures, one way of checking on this point is to-examine the log-stress-log-rupture life plot at a temperature several hundred degrees above the required temperature. For example, if in 1,000 h no change in slope occurs in the curve at about 100°C above the required temperature, extrapolation of the lower temperature curve as a straight line to 10,000 h is probably safe and extrapolation even to 100,000 h may be possible.

Certain useful techniques have been developed for approximating long-term behavior based on a series of short-term tests. For instance the data from creep testing may be cross plotted in a variety of different ways. The basic variables involved are

stress, strain, time, temperature, and perhaps strain rate. Any two of these basic variables may be selected as plotting coordinates, with the remaining variables to be treated as parametric constants for a given curve.

One of the commonly used methods for extrapolating short-time creep and creep-fatigue data to long-term applications is the thermal acceleration method. Creep testing guidelines usually dictate that test periods of less than 1 percent of the expected life are not deemed to give significant results. Tests extending to at least 10 percent of the expected life are preferred where feasible.

Thermal Acceleration Method

The thermal acceleration method involves laboratory testing at temperatures much higher than the actual service temperature expected. As shown in Figure 79 the data are plotted as stress versus time for a family of constant temperatures where the creep strain produced is constant for the whole plot. It may be noted that stress rupture data may also be plotted in this way. As an aid in extrapolation of stress-rupture data several time-temperature parameters have been proposed for trading off temperature for time. The basic idea of these parameters is that they permit the prediction of long-time rupture behavior from the results of shorter time tests at higher temperatures at the same stress.

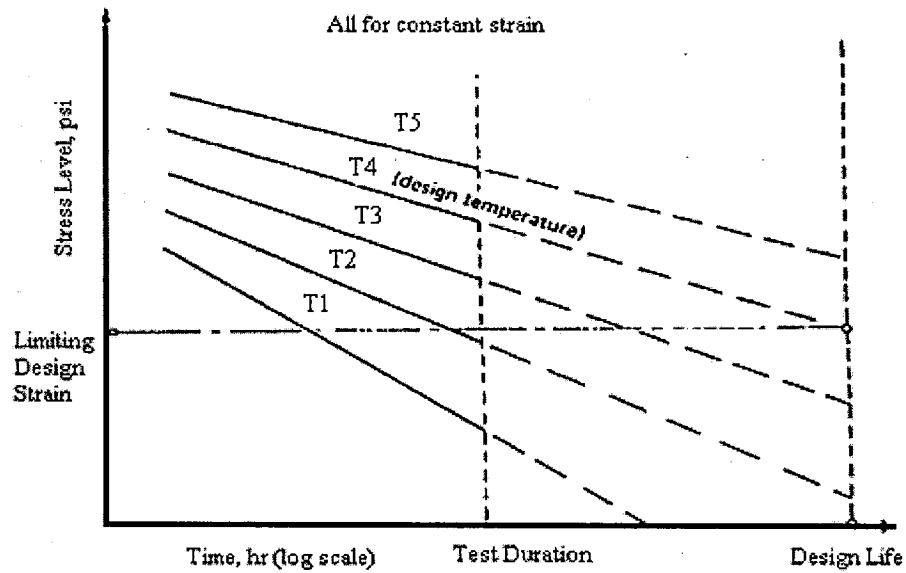


Figure 79 Thermal acceleration method of creep testing.

In our tests, we did both upscale and subscale temperature tests. Indeed to justify the scale model theory and specifically the thermal scaling, the subscale temperature has been used for model in comparison with the prototype. On the other hand to run the creep and creep-fatigue a test in a shorter time than the reality, tests at the upscale temperature have been carried out.

More or less the same upscale force has been applied for the fatigue test to take shorter time than the real case. In case of applying the real normal load, it may take about 6 months.

6.4.2. Experimental Procedure

I) CREEP-FATIGUE INTERACTION TESTS

I.1. Material and Specimen

Materials for creep-fatigue tests were Steel 4340. The material and its chemical, physical, and mechanical properties are listed in Table 13, Table 14, and Table 15 respectively.

Table 13 Chemical properties of steel 4340.

C	MN	P	S	Si	Cu	Ni	Cr	Mo	Al	V	N	Cb	Sn
0.4	0.75	0.008	0.029	0.26	0.03	1.72	0.87	0.23	0.021	0.001	0.0055	0.002	0.001

Table 14 Physical properties of steel 4340.

%A	T _{melt} (°C)	ρ (kg/m ³)	α (μm/m°C)	%ΔL	ν
36-43	1426.67	7.85e3	13.7	13.2	0.29

Table 15 Mechanical properties of steel 4340.

S _y (Mpa)	E (Gpa)	S _{ut} (Mpa)	BHN
710	195-205	825-1110	248

Figure 80 shows the geometry of a specimen used for the creep-fatigue tests.

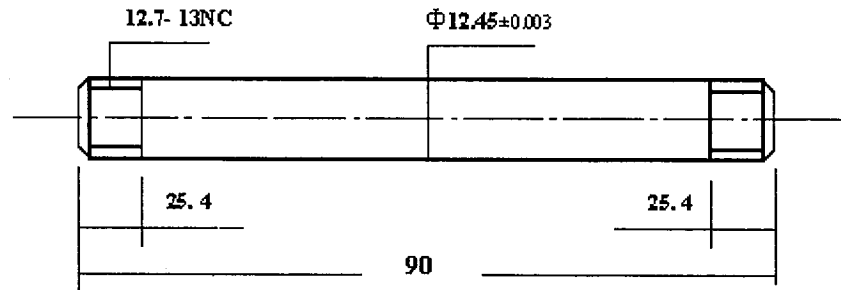


Figure 80 Geometry of fatigue, creep, and creep-fatigue specimen, steel 4340 (dimension in mm).

I.2. Apparatus and Test Conditions

The apparatus used in this study was Gleeble-3500 (Figure 81), a controlled electro-hydraulic thermal-fatigue testing machine with high-precision conduction heating and air-cooling functions [180].

For axial displacement measurement, Fastar-SP100 sensor from Data Instruments was used which is based on inductance variation. Temperature was measured by 0.2 mm diameter thermo-couples welded at the middle and both ends of the specimen. The temperature difference within the gage length was not greater than $\pm 2^\circ\text{C}$ to the set temperature throughout the duration of a test. In the creep-fatigue tests, force was computer-controlled by the same triangular waveform cycling. The same temperature was used for creep, and creep-fatigue tests, using the output of the thermocouple. The following waveforms shown in Figure 82 were applied in the tests.

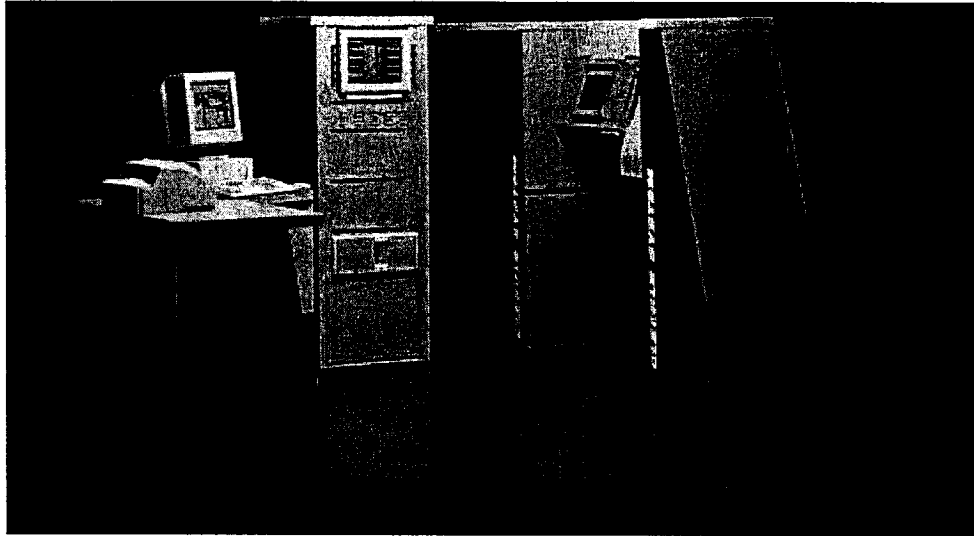


Figure 81 Gleeble-3500 for different creep, fatigue and creep-fatigue tests.

The tests were in two main categories:

- Thermal Scaling
- Creep-Fatigue Interaction

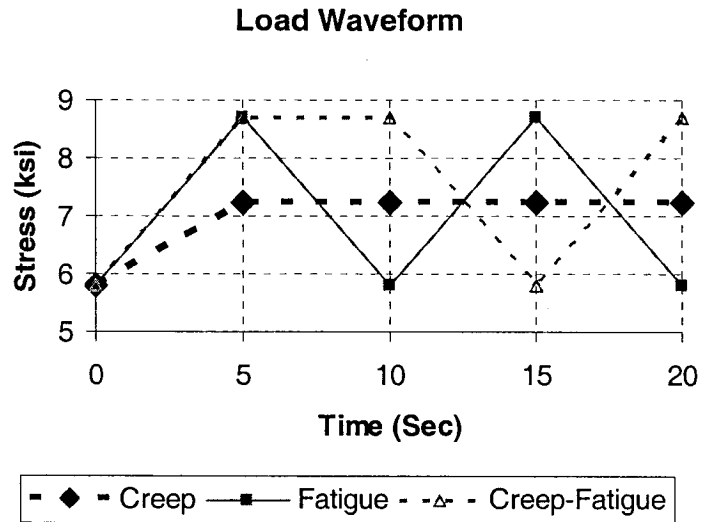


Figure 82 Load waveform for creep, fatigue, and creep-fatigue tests.

and were done using the testing facilities at the National Research Council (NRC), at Boucherville, Quebec.

I.3. Creep

I.3.1. Model Results

In order to use the Larson-Miller relation, the constant “C” should be found.

$$P = T_1(C + \text{Ln } t_{R1}) = T_2(C + \text{Ln } t_{R2}) \quad (161)$$

From the following test results (Table 16), the average value of three last tests for C was found as 16.65.

Table 16 Creep test results for steel 4340.

Test #	T (°C)	T (K)	t _R (sec)
1	800	1073.15	3645
2	850	1123.15	1205
3	853	1126.15	1125
4	875	1148.15	715

From Equation (37) of chapter 4

$$P = T_1(C + \text{Ln } t_{R1}) = b_0 + b_1(\text{Ln } \sigma) \quad (162)$$

Substituting the data from the test, for instance from the second row of the Table 16, and taking into consideration that the test stress was equal to 50.09 MPa (7265 Psi)

$$P = 11205[16.65 + \text{Ln } (1205)] = b_0 + b_1 \text{Ln}(7265) \quad (163)$$

Taking $b_0 = 10000$, then we have $b_1 = 1874.785$. Now for our case study which is at 800 °C to find the rupture time, either Equation (35), or Equation (37) of chapter 4 can be used. Using Equation (37)

$$P = 1073.15[16.65 + \text{Ln } t_R] = 10000 + 1874.785 \text{Ln}(7265) \quad (164)$$

From this we have:

$$t_R = 3691.449 \text{ sec}$$

(165)

1.3.2. Test Results

It includes 4 tests on a 90 mm long of a 12.7 mm diameter Steel 4340 which was cleaned and annealed at 248 BHN. For creep test the following waveform shown in Figure 83 has been applied. Indeed we could just apply the temperature and the force of 6.31KN which is equal to stress of 50.09 MPa (7265 Psi).

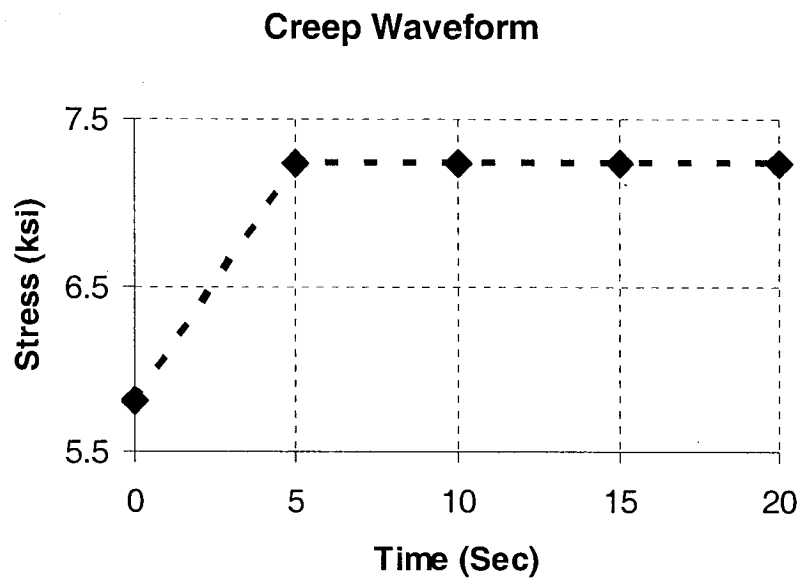


Figure 83 Stress waveform for creep tests.

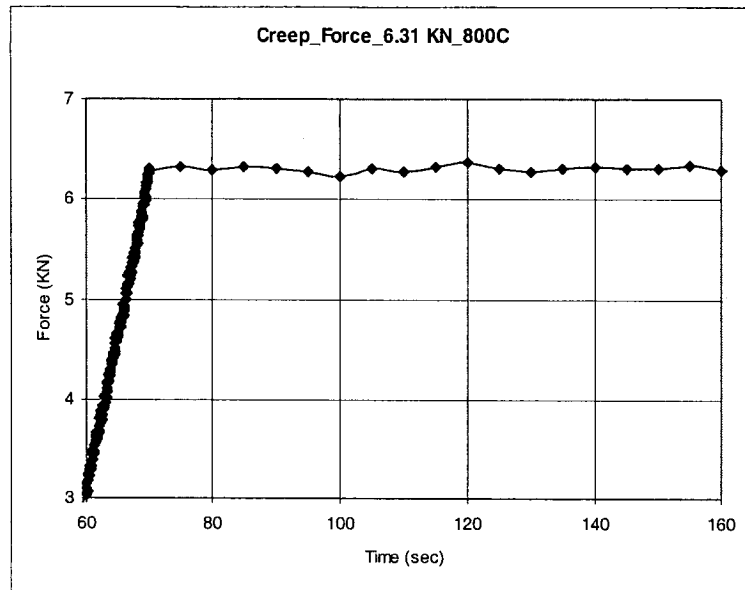


Figure 84 Force waveform for creep tests.

Due to these conditions we had

$$t_R = 3645 \text{ sec} \quad (166)$$

The following figures show the effect of temperature on creep strain.

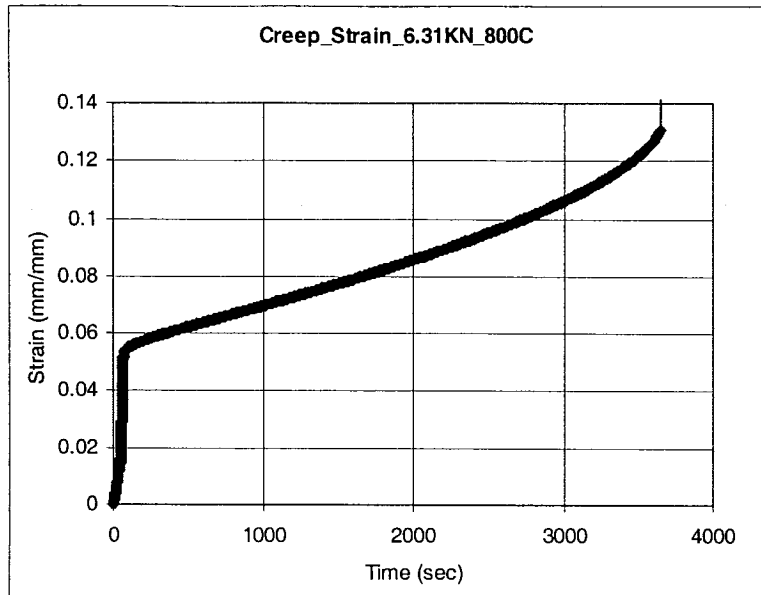


Figure 85 Creep strain vs. time at 800°C in creep test.

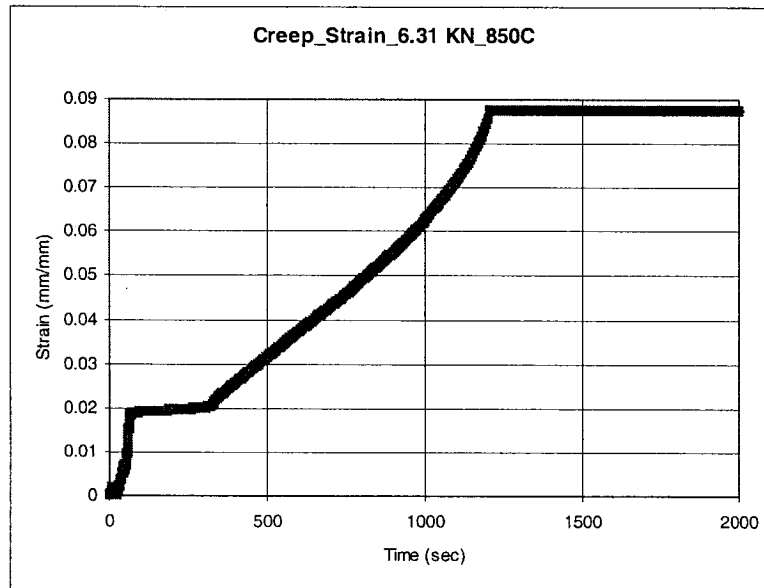


Figure 86 Creep strain vs. time at 850°C in creep test.

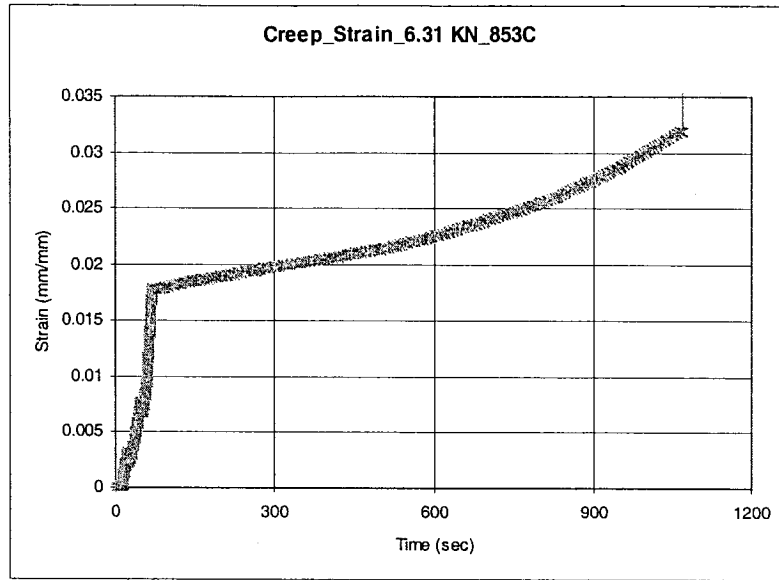


Figure 87 Creep strain vs. time at 853°C in creep test.

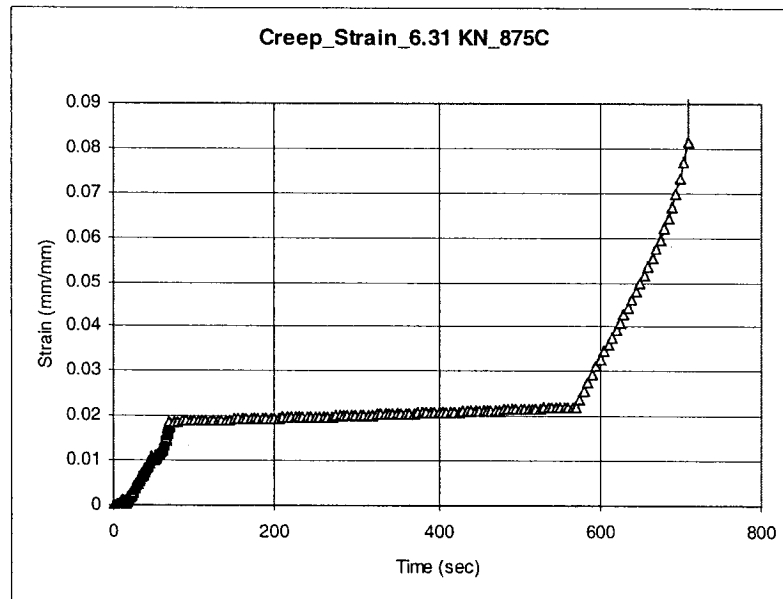


Figure 88 Creep strain vs. time at 875°C in creep test.

I.4. Fatigue

I.4.1. Model Results

The universal slope which is the combination of Coffin-Manson law (for plastic strain) and Basquin law (for elastic strain) has been used.

$$\frac{\Delta\varepsilon}{2} = \varepsilon_f' (2N_f)^c + \varepsilon_f (2N_f)^b \quad (167)$$

where:

$\Delta\varepsilon$: total strain range (in)

ε_f' : fatigue ductility coefficient, equals $\text{Ln}\left(\frac{100}{100 - \%RA}\right)$, which %RA is

reduction area in percentage

ε_f : fatigue strength coefficient, approximately equals S_{ut} / E

b : fatigue strength exponent, material dependent constants

c : fatigue ductility exponent, material dependent constants

S_{ut} : ultimate tensile stress (Psi)

E : Young's modulus of elasticity (Psi)

$2N_f$: number of reversals (2 reversals equals one cycle)

Since many tests are needed to find the constants, the suggested values in ASM handbook V.II for Steel 4340 have been used. Consequently,

$$\frac{\Delta\varepsilon}{2} = 0.58(2N_f)^{-0.57} + 0.0062(2N_f)^{-0.09} \quad (168)$$

Total strain was found from the test, which was 1.639915 mm = 0.0645636 in, and hence

$$0.0322818 = 0.58(2N_f)^{-0.57} + 0.0062(2N_f)^{-0.09} \quad (169)$$

From Equation (30), the number of reversals ($2N_f$) will be obtained as

$$2N_f = 190.8691 \text{ cycles} \quad (170)$$

1.4.2. Test Results

The cyclic load was applied on a sample of 12.7 mm diameter 90 mm long Steel 4340 until break down. The minimum stress was 40.04 MPa (5.81 ksi) and the maximum stress was 60.10 MPa (8.72 ksi). Practically we could apply force between 5.07 KN to 7.61 KN.

Fatigue Waveform

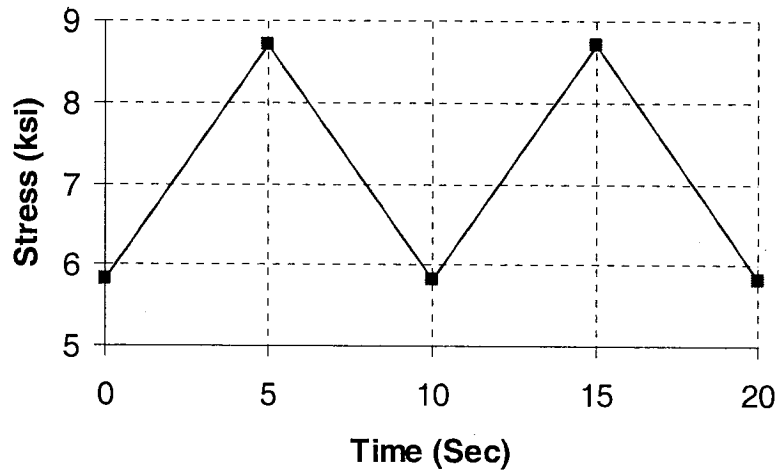


Figure 89 Stress waveform for fatigue test.

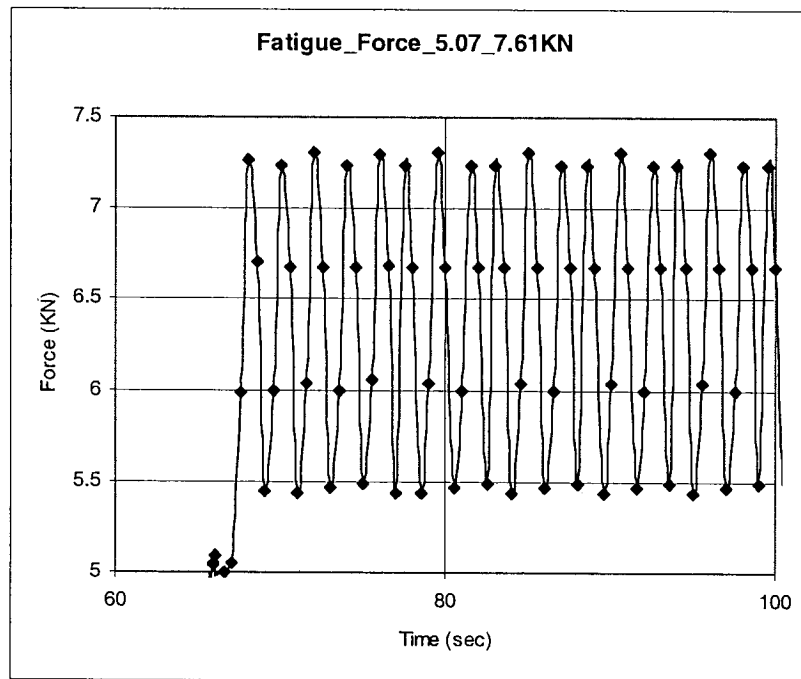


Figure 90 Force waveform for fatigue test.

The total spend time was 2019.5 seconds and each cycle was 10 seconds, but it took 66 seconds preliminary time to start the cyclic load. Then if we take the net time for the cyclic load, the number of reversals is obtained as

$$2N_f = (2019.5 - 66) / 10 = 195.35 \text{ cycles} \quad (171)$$

and if we take the total spend time

$$2N_f = 2019.5 / 10 = 201.95 \text{ cycles} \quad (172)$$

Figure 91 shows the strain vs. time in fatigue test.

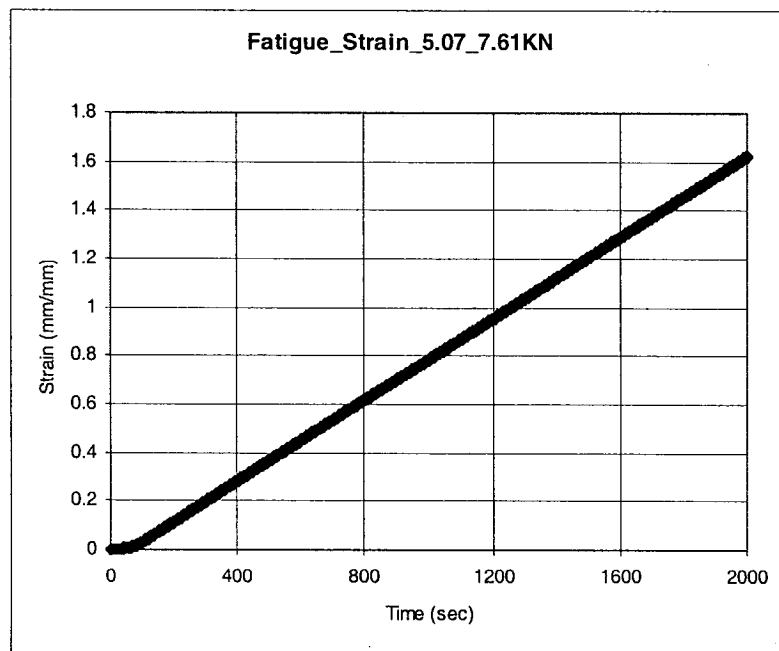


Figure 91 Strain vs. time in fatigue test.

I.5. Creep-Fatigue Interaction

I.5.1. Model 1 Results

I.5.1.1. Test Data

The test data has been used to find the total damage at creep-fatigue interaction. As an example the damage at 50 seconds will be

I. Creep damage: From Equation (46) of chapter 4

$$D_C = 50 / 3645 = 0.01372 \quad (173)$$

II. Fatigue damage: From Equation (45) of chapter 4

$$D_F = 50 / 2019.5 = 0.02476 \quad (174)$$

III. Total damage: From Equation (49) of chapter 4

$$D_T = D_C + D_F = 0.01372 + 0.02476 = \mathbf{0.0384786} \quad (175)$$

I.5.1.2. Calculation

The data from the calculation has been used to find the total damage at creep-fatigue interaction. As an example the damage at 50 seconds will be

I. Creep damage: From Equation (46) of chapter 4

$$D_C = 50 / 3691.449 = 0.0135448 \quad (176)$$

II. Fatigue damage: From Equation (45) of chapter 4

$$D_F = 50 / 190.8691 = 0.02619596 \quad (177)$$

III. Total damage: From Equation (49) of chapter 4

$$D_T = D_C + D_F = 0.0135448 + 0.02619596 = \mathbf{0.0275504} \quad (178)$$

1.5.1.3. Test Results

The cyclic load was applied on a sample of 12.7 mm diameter 90 mm long Steel 4340 until break down. The minimum stress was 40.04 MPa (5.81 ksi) and the maximum stress was 60.10 MPa (8.72 ksi) and the hold time was 5 seconds.

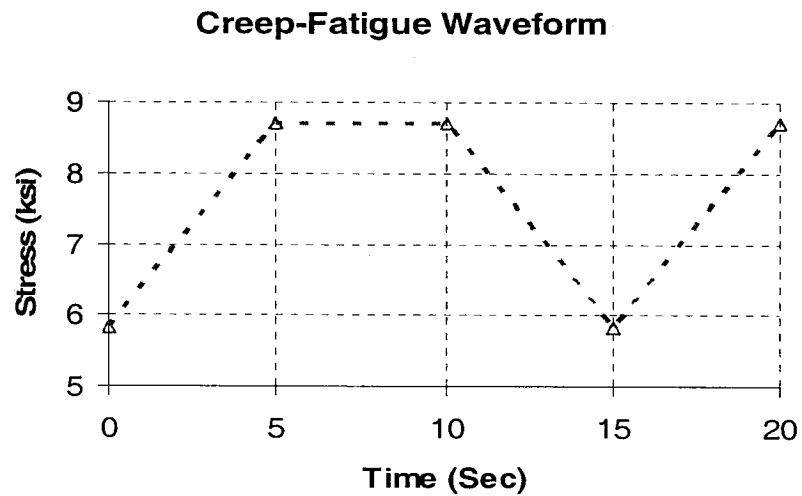


Figure 92 Stress waveform for creep-fatigue test.

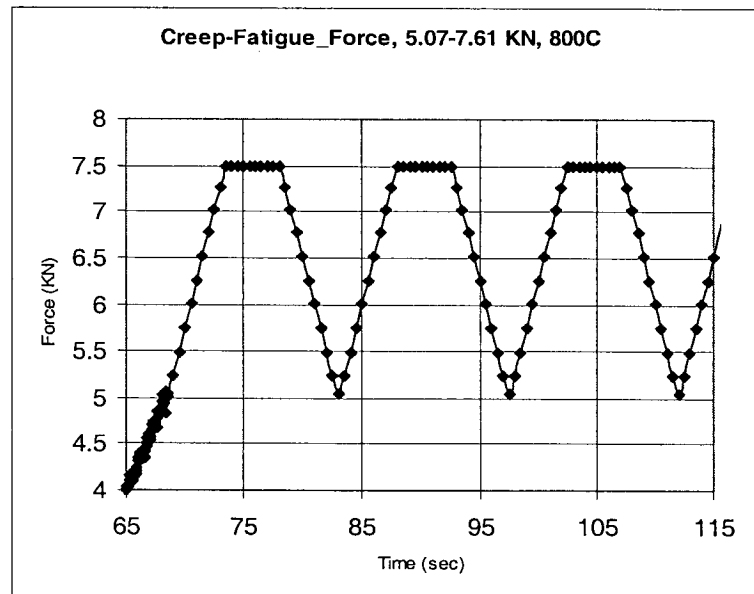


Figure 93 Force waveform for creep-fatigue test.

Indeed we could apply the force and temperature and measure the stress and strain. Practically break down happened after 1254.5 seconds. Then the damage for our case study at 50 seconds is:

$$D_T = 50 / 1254.5 = 0.03986 \quad (179)$$

Figure 94 shows the strain under creep-fatigue interaction.

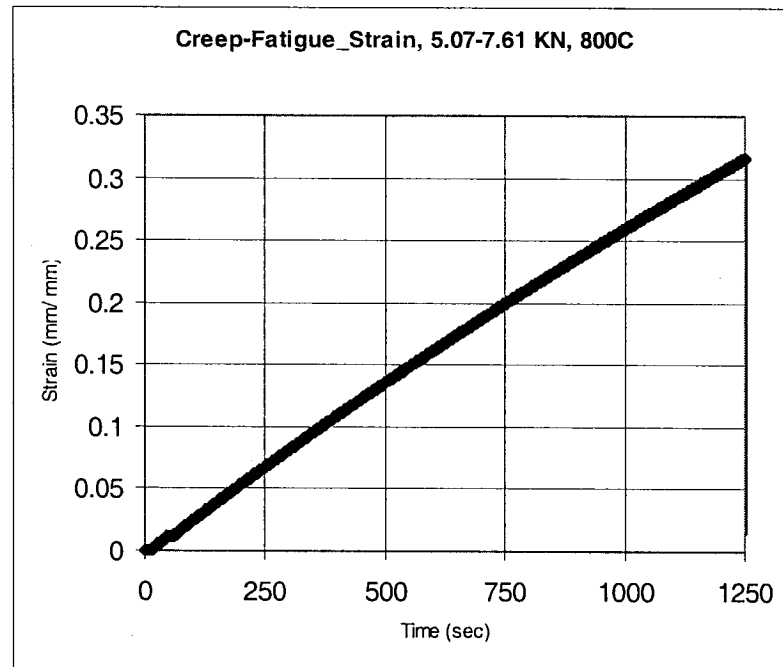


Figure 94 Strain vs. time in creep-fatigue test.

1.5.2. Model 2 Results

Based on the Miners's rule for fatigue failure, we have

$$\frac{\sigma_a}{S_f} + \frac{\sigma_m}{\sigma_{cr}} \geq 1 \quad (180)$$

where

σ_a : alternating stress

σ_m : mean stress

σ_{cr} : creep strength (creep stress for corresponding time to rupture)

S_f : fatigue strength

For the case that was tested we have:

σ_a : 10.03 Mpa

σ_m : 50.07 Mpa

σ_{cr} : for 800°C and 1 hour lifetime is 50.7 Mpa

S_{ut} : 825 Mpa, then $0.9S_{ut} = 742.5$ Mpa

Substituting these values in Equation (41), we have

$$S_f = 807.18 \text{ MPa} \quad (181)$$

which is greater than $0.9S_{ut} = 742.5$ Mpa. Then it can be concluded that:

$$N_f < 10^3 \quad (182)$$

This is reasonable because from the test we have:

$$N_f = \text{Total spend time} / \text{Period of 1 cycle} = 1254.5 / 15 = 83.6 \quad (183)$$

1.5.3. Model 3 Results

From Equation (51) of chapter 4 we have:

$$N_R = N_{SF} \left[\frac{1}{\frac{1}{N_f} + \frac{t_h}{t_R}} \right] \quad (184)$$

where

N_R : number of cycles to failure in creep-fatigue

N_f : number of cycles to failure in fatigue test

N_{SF} : safety factor

t_h : hold time at stress σ and temperature T

t_R : rupture time at stress σ and temperature T

For the case that was tested we have:

N_f : 195.35

N_{SF} : 0.54

t_h : 5 sec

t_R : 3645 sec

Using Equation (51) of chapter 4, we get the number of cycles to break for the steel 4340 as

$$N_R = \mathbf{83.1951} \text{ cycles} \quad (185)$$

The present life status for instance after 50 seconds, which is equivalent to 3.33 cycles, is

$$L_R = 1 - \frac{N}{N_R} = 1 - \frac{3.33}{83.1951} = 0.9599 \quad (186)$$

Test result gives

$$N_R = 1254.5 / 15 = \mathbf{83.6} \text{ cycles} \quad (187)$$

The present life status for instance after 50 seconds, which is equivalent to 3.33 cycles, is

$$L_R = 1 - \frac{N}{N_R} = 1 - \frac{3.33}{83.6} = 0.9601 \quad (188)$$

6.5. FRACTOGRAPHY (SEM)

Although the intent of the present research is mainly mathematical modeling of the creep-fatigue phenomena validated through testing, fractography of the test specimens are presented order to give another dimension to the phenomena. It is not the intent here to discuss them in any detail. The fractography (Scanning Electron Microscopy) of the fracture cross section also has been done and is shown in Figure 95 for aluminium and in Figure 96 for steel. In the case of creep, the fracture is mostly inter-crystalline (intergranular). However, in contrast, the fracture is due to the trans-crystalline (transgranular) failure surface exhibited by room temperature fatigue failures. Creep rupture typically occurs without necking and without warning. In creep-fatigue situation, the fracture is mixed of intergranular and transgranular, which means it is the combination of creep and fatigue phenomena (Figure 97) [181].

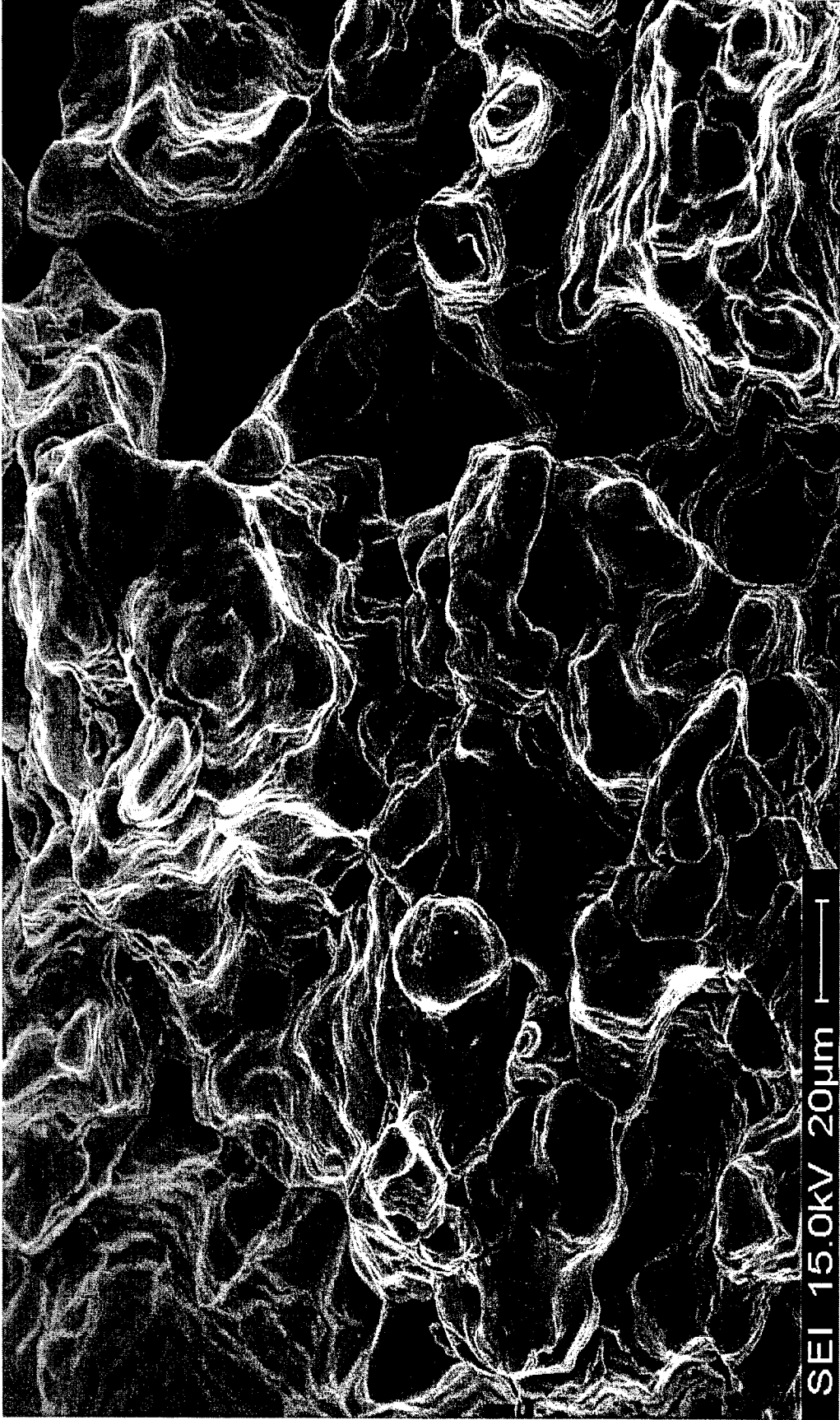


Figure 95 Fractography of Al-2023 at creep condition, 400X.

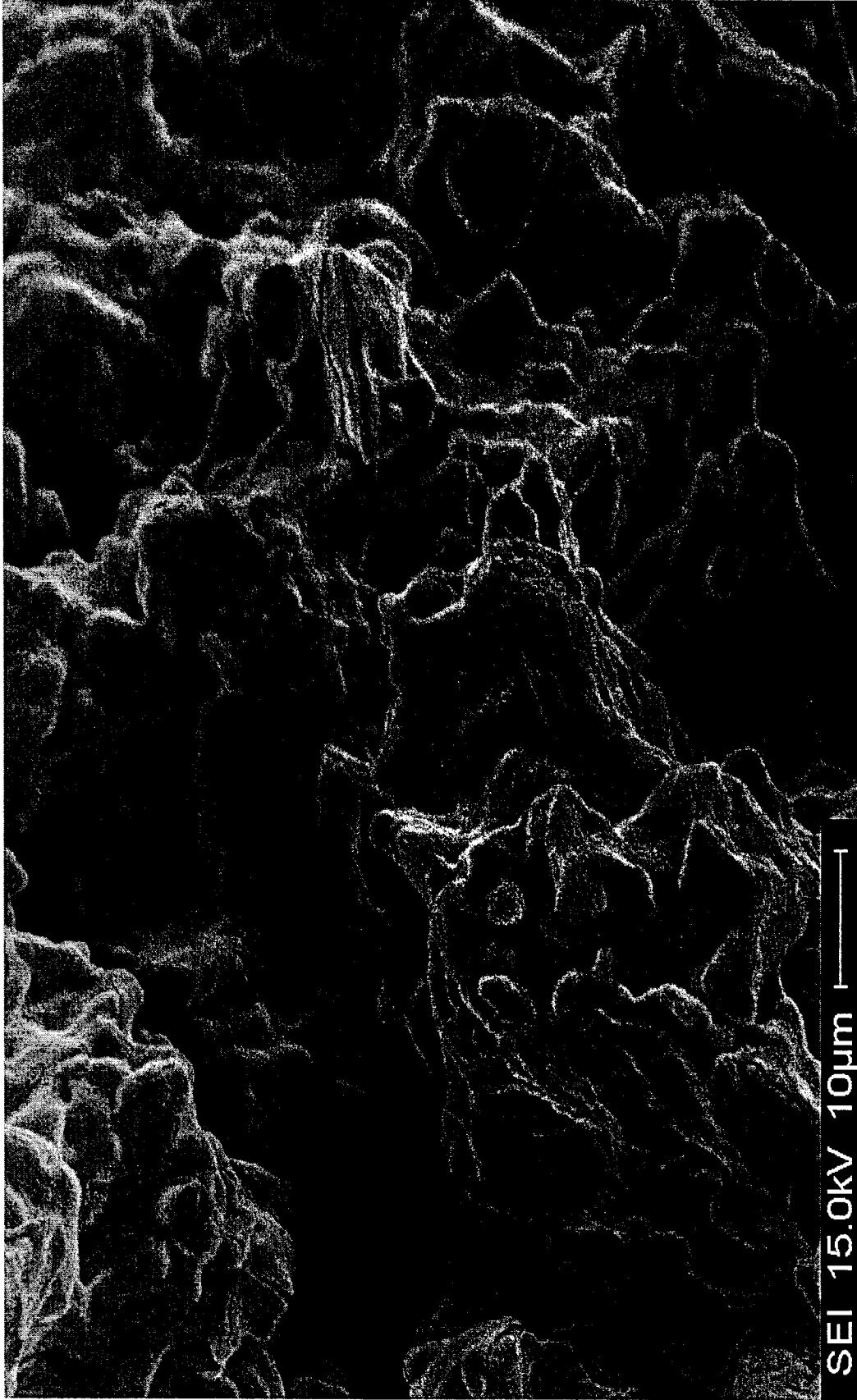


Figure 96 Fractography of St-4340 at creep condition, 1100X.

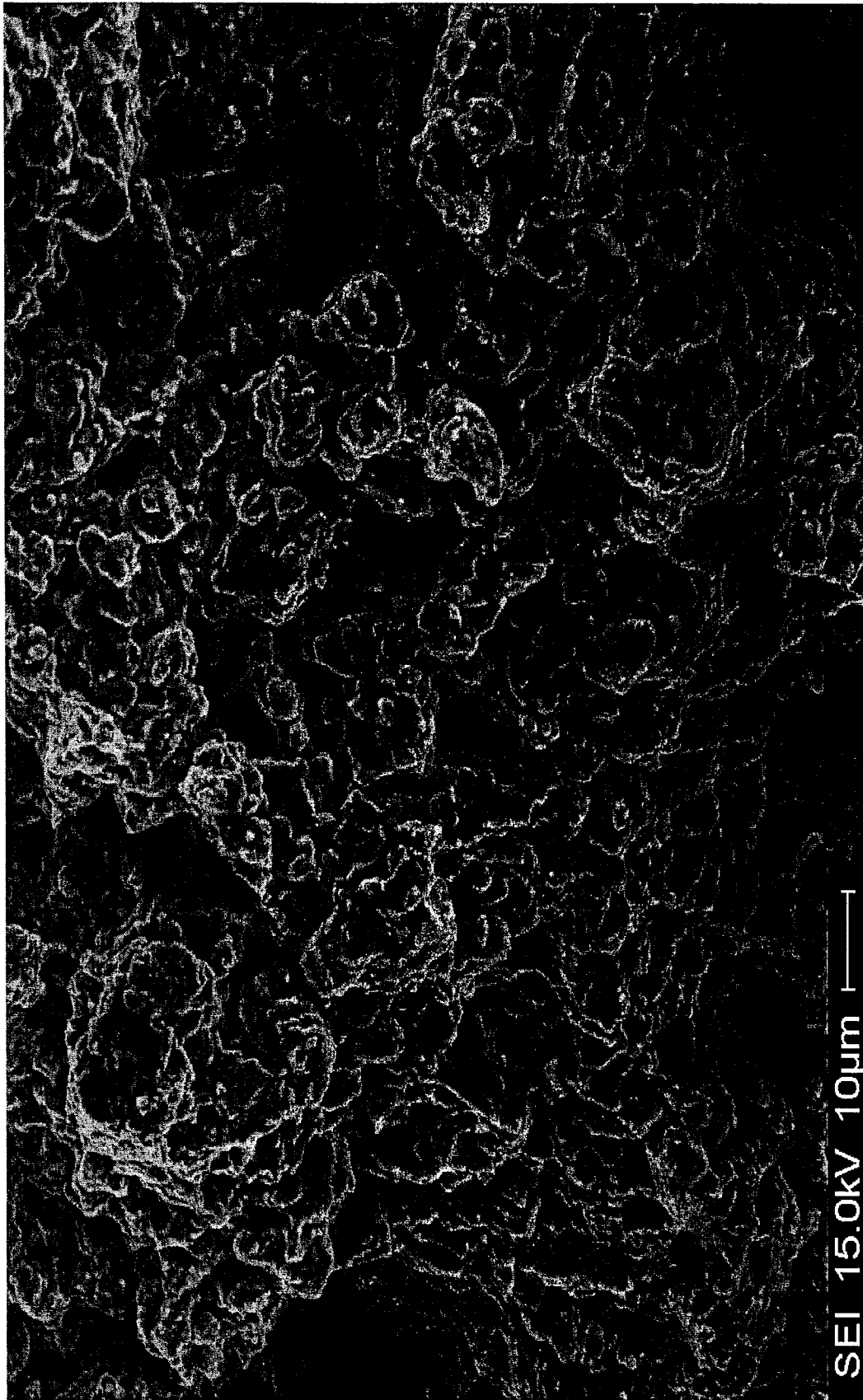


Figure 97 Fractography of St-4340 at creep-fatigue condition, 800X.

II) SCALE MODEL TESTS

The materials used for thermal scaling test were Al 2023 as model and Steel 4340 as prototype. The specifications of the Steel 4340 were mentioned above. The material and its chemical, physical, and mechanical properties of Al 2023 are listed in Table 17, Table 18, and Table 19 respectively.

Table 17 Chemical properties of Al 2023.

MN	SI	CU	Cr	Mg	Ti	Zn	Others
0.3-0.9	0.5	3.8-4.9	0.1	1.2-1.8	0.25	0.15	0.15

Table 18 Physical properties of Al 2023.

ρ (kg/m ³)	α ($\mu\text{m}/\text{m}^\circ\text{C}$)
2.77e3	38.5

Table 19 Mechanical properties of Al 2023.

S_y (Mpa)	E (Gpa)	S_{ut} (Mpa)
344.05-361.29	195-205	473.67-487.46

The geometry of Steel 4340 specimen was shown in Figure 80, and shows the geometry of Al 2023 specimen.

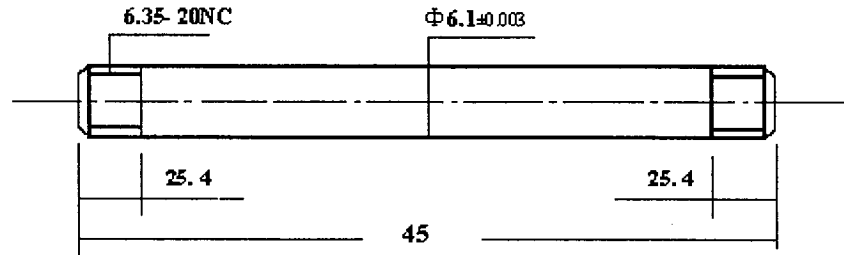


Figure 98 Geometry of fatigue, creep, and creep-fatigue specimen Al 2024 (dimension in mm).

Parameters involved in scale modeling are presented in Table 7. Two kinds of modeling have been done:

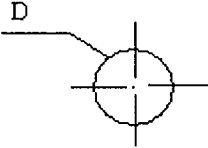
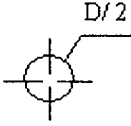
1) Temperature scaling:

In this test, besides the dimensional scaling, the applied temperature was scaled on model, and the total strains of prototype and model have been compared.

2) Temperature-Force scaling

In this test, besides the dimensional scaling, the applied temperature and axial tension force were scaled in the model, and the total strain of prototype and model have been compared.

Table 20 Parameters involved in modeling.

Parameters	Prototype	Model
Length	228.6 mm	114.3 mm
Dimension	12.7 mm diameter	6.35 mm diameter
Material	Steel	Aluminum
Modulus of Elasticity	195e9 N/m ²	72.4e9 N/m ²
Density	7850 kg/m ³	2770 kg/m ³
Poisson's Ratio	0.29	0.3
Thermal Expansion	12 μm / m°K	38.5 μm / m°K
Cross Section		

The following scales have been applied to the model:

$$\lambda_F = \lambda_E \lambda_L^2 = 10.870 \quad (189)$$

$$\lambda_t = (\lambda_\omega)^{-1} = \lambda_L \sqrt{\frac{\lambda_\rho}{\lambda_E}} = 2.05 \quad (190)$$

$$\lambda_{\Delta T} = \frac{\lambda_{\rho} \lambda_A \lambda_{\omega}^2}{\lambda_{\alpha} \lambda_E} = 1.856 \quad (191)$$

$$\Delta T_m = \Delta T_p / \lambda_T \quad (192)$$

The results obtained are presented in Figure 99 to Figure 102.

The total strain is plotted against time in Figure 99. The difference between the total strains of the prototype and the model is about 1% which is very good agreement. It is good to be mentioned that the measured total strain of the model is due to applying the calculated scaled temperature.

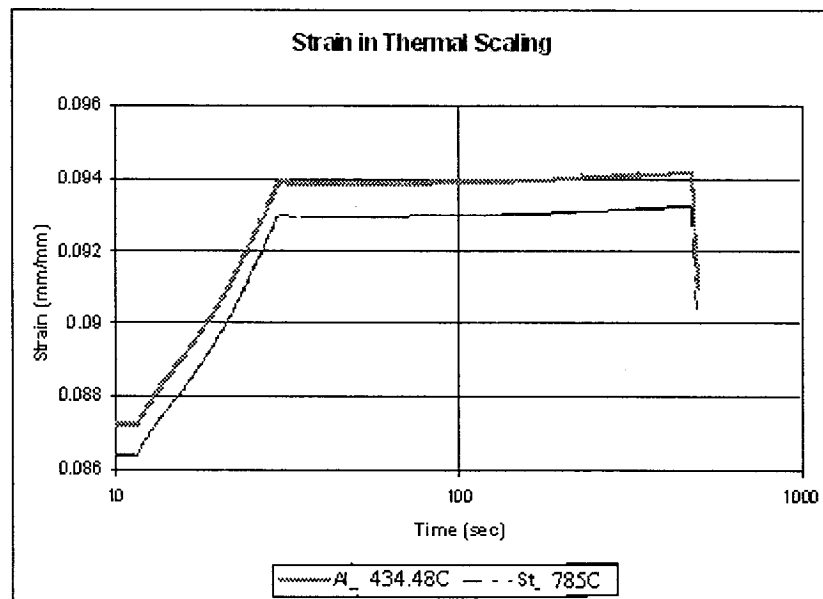


Figure 99 Total strain vs. time in thermal scaling.

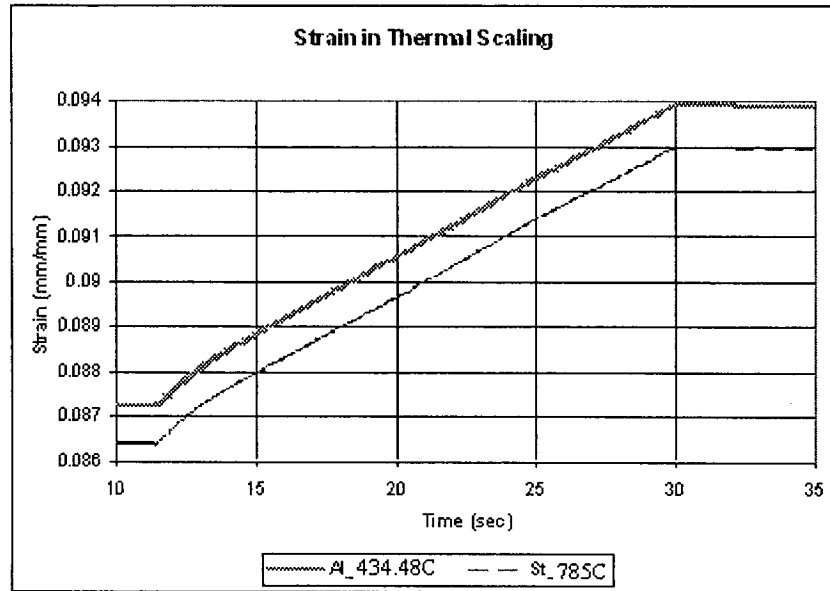


Figure 100 Total strain vs. time in thermal scaling.

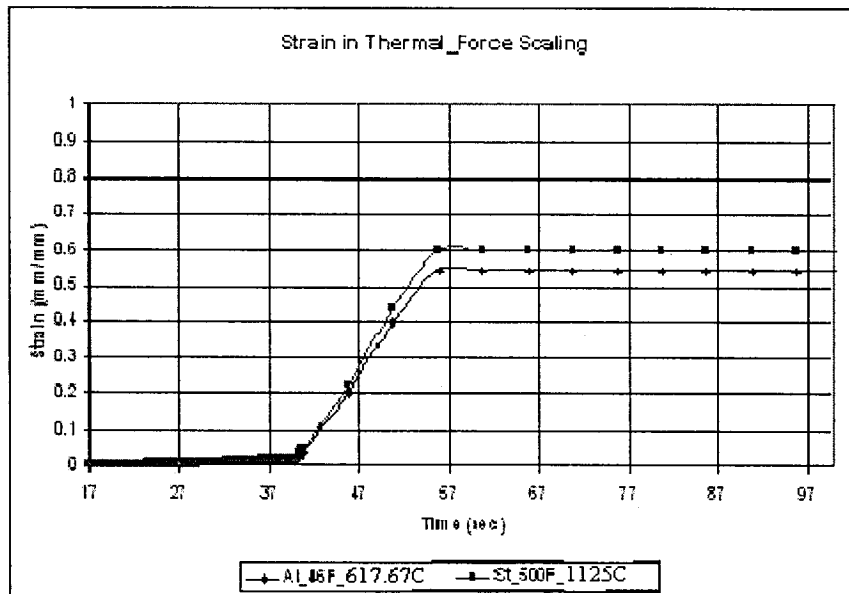


Figure 101 Total strain vs. time in temperature-force scaling.

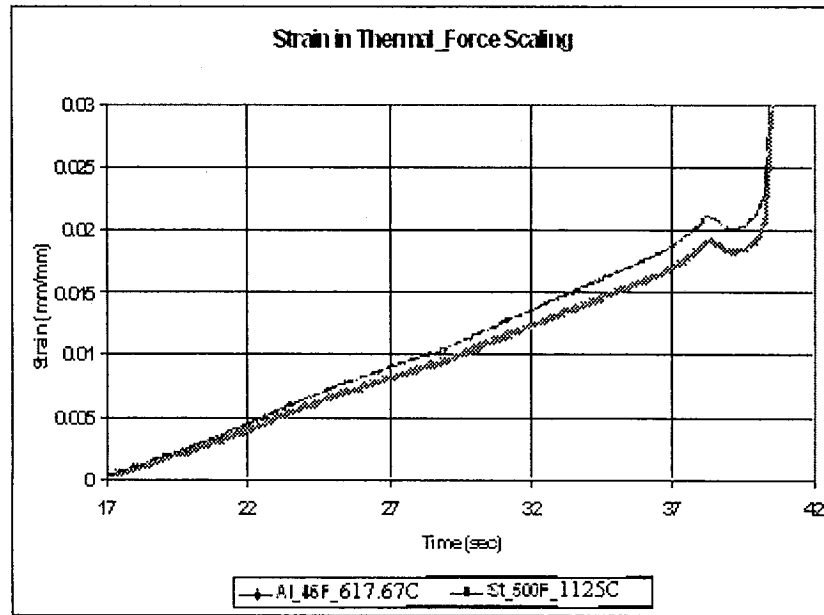


Figure 102 Total strain vs. time in temperature-force scaling.

Figure 102 is the zoom in of Figure 101 which shows the detail of the behavior of the prototype and the model close to the break point. For about half of the lifetime the total strain of both the prototype and the model are almost the same. Although by increasing the time, the difference between the two curves is also increasing, but they face the failure almost at the same time, and the maximum difference of the total strains is about 10%.

III) DISCUSSION AND CONCLUSIONS

a) CREEP-FATIGUE INTERACTION MODELS

Three constitutive models have been suggested. In first model, the main idea is that the total damage can be used for break point of the components, and the damages due to creep and fatigue can be accumulated linearly. In this model, the creep model uses a Norton power law, Larson-Miller and Robinson's rule approach, while the fatigue model combines Miner's rule and the universal slopes method. The damages are calculated separately and the total damage is found by linear summation in order to find the lifetime.

In model 2, the fluctuating stress is considered as a varying stress in fatigue-creep model. Since the fluctuating stress is combination of alternating and mean stress, it can be assumed that the mean part represents the static load which can cause creep at elevated temperatures, whereas the alternating part is responsible for fatigue damage. This model is an extension to Goodman theory, except that instead of an intercept of ultimate stress (σ_u) on the σ_m axis, the intercept used is the creep-limited static stress (σ_{cr}).

In model 3, the approach for this model is that the creep-fatigue interaction can be considered as cyclic fatigue but with the hold time at maximum, minimum, or extreme stresses. This model has two strong points: 1) the required data can be used from pure creep and pure fatigue tests; 2) it has a safety factor (or a weakness factor) that is based on the material information and industrial experiences, between 0-1.

Out of three constitutive models, the first one is the most accurate and reasonable one, although the 3rd one is the easiest one. The main weak point of the second one is that it gives just a range of the lifetime or lifecycle for the low frequency loads, and it cannot be accurate at that region. The weak point of the 3rd one is finding the safety factor accurately.

Although we have not done more tests to find the constants in universal slope equation, and the one from ASM handbook has been used, but for unknown materials many more tests are needed to find those constants. In our case, the final result of the lifetime prediction in creep-fatigue interaction tests and the first constitutive model has quite reasonable and acceptable mach.

b) SCALE MODEL

The thermal scaling test has been done in two cases, with and without force presence. In both cases the agreement of analytical results with those from the test are surprisingly close, which is a big achievement, because in the literature there is no work on thermal scaling except the one which have been done by NASA. In all those investigations NASA has selected both the prototype and the model from the same material, and of course with the same thermal expansion.

In this chapter the theory and application of scale model tests in general, are explained and specially the thermal scaling are described and used for the first time. Also the justification of the three lifetime predictions and the thermal scaling tests are presented. In the next chapter the results and discussion of the thesis on the whole will be presented, and the recommendations for future work will be proposed.

CHAPTER 7

DISCUSSION AND CONCLUSIONS

In previous chapter the theory and application of scale model tests in general, were explained and specially the thermal scaling was described and used for the first time. Also the justification of the three lifetime predictions and the thermal scaling tests were presented. In this chapter the results and discussion of the thesis on the whole are presented, and the recommendations for future work are given.

7.1. GENERAL

The lifetime of gas turbine components in creep-fatigue interactions has been studied in this thesis.

Three suitable models for predicting the lifetime were developed and studied. The finite element technique was used to study the component dynamic behavior. Natural frequencies and mode shapes were obtained. The response and stress due to harmonic and centrifugal loading were also obtained. The analytical results were compared with those obtained from experiments.

The dynamic analysis of the gas turbine blade was first studied using beam characteristic orthogonal polynomials in the Lagrange-Bhat method. The blade was idealized as a cantilever beam due to its low aspect ratio. The variation of the natural frequencies and mode shapes with speed of rotation was obtained.

The frequencies of applied loads also are important because of fatigue phenomenon. In view of the complex shape of the blade, approximate methods such as FEM were used to find the natural frequencies. Using FEM method for natural frequencies causes the phenomenon called curve veering.

Mathematical models for prediction of the operating life of aircraft components, specifically gas turbine blades, which are subjected to creep-fatigue at high temperatures, was proposed. The components were modeled by finite element methods.

The simulation studies on the life-limiting mode of failure, as well as estimating the expected lifetime of the blade, using the proposed models have been carried out.

The finite element method was employed to model the structure. Because of stress redistribution due to the creep process, it was necessary to include a full inelastic creep step in the finite element analysis, as over-conservative creep life predictions usually result when only the initial elastic stresses are considered.

Experimental investigations were carried out in order to validate the theoretical model. In experimental validation, the failure specifications of sample were compared with the result of simulation. The experimentally measured lifetime and the total creep strain of the failed specimens were compared with those predicted using the analytical models.

The main contributions in the thesis are:

1. Innovative failure models in order to obtain the operating life of the blades in high temperature environments of gas turbine engines. These models are mathematically very simple and even more important, they do not need the complicated tests for the materials, and only the pure fatigue and pure creep tests data are enough for life prediction in creep-fatigue environment.
2. Developing finite element methods to study creep-fatigue interaction effects to get meaningful results for industrial applications. Although the commercial FEM software have the ability to analyze the creep and fatigue phenomena individually, none of them have built in program or model for creep-fatigue analysis. The present study provides a good approach to write a comprehensive program for this mixed mode of failure.
3. Analyzing the curve veering and flattening phenomena in rotating blade in thermal environment, using Lagrange-Bhat method and energy equation.
4. Using similitude method (Scale model analysis), and developing thermal scaling method for lifetime prediction for the first time. Although the scale model idea has been used for long time, the thermal scaling idea has been used just by NASA

in which, both the prototype and the model are from the same material. In thermal study the different materials are selected for model and prototype.

7.2. CONCLUSIONS

The conclusions arrived on the basis of the results of this investigation in the different chapters of the thesis are summarized and given below:

- 1) The natural frequencies of a rotating beam increase linearly at higher rotational speeds.
- 2) The beam tries to straighten itself as the rotational speed is increased (the flattening effect).
- 3) Depending on the number of terms used for shape functions, the pseudo curve veering in thermal rotating blade happens at higher modes, and by increasing the number of terms, the curve veering also moves to the still higher modes.
- 4) The blade in a thermal environment has almost the same behavior of non-thermal environment, except that at higher temperatures, the deflections are higher and the natural frequencies are lower.
- 5) The deflections of thermal and non-thermal blade, at standstill are the same, but the deflection of the thermal blade at the tip is more than the nonthermal one.
- 6) The scale model analysis can be used even for dynamic analysis to find the natural frequencies.
- 7) The scale model analysis can be used even for thermal environment.

- 8) The maximum stress occurs at the root of the blade and decreases in value towards the tip.
- 9) The linear summation of creep and fatigue damages in low strains has very good result for creep-fatigue life prediction.
- 10) By acceleration distortion the thermal scaling is applicable to different materials for prototype and model.

7.3. RECOMANDATIONS FOR FUTURE WORK

Some suggestions for possible future work are given below:

1. Pretwist and taper can be incorporated in the formulation of the blade models.
2. The effect of aerodynamic forces on blade response can be investigated.
3. Experimental validation with the inclusion of the blades can be carried out.
4. Modal testing can be carried out to determine the mode shapes of stationary and rotating blade.
4. Combining the study with the other field like smart materials, can be done by future work.
6. Taking the curvature of the beam into consideration in analysis.

REFERENCES

- [1] O. Ryuichi, K. Takayuki, T. Mitsuyoshi, M. Hideki, *Initiation and Growth of Small Cracks in Creep Fatigue of Oxide Dispersion-Strengthened Superalloys at Elevated Temperature*, Japan Society of Mechanical Engineers, Transactions A, Vol. 59, No. 560, pp. 933-938, April 1993.
- [2] J. Ewald, S. Sheng, *The Two Criteria Diagram for Creep Crack Initiation and Its Application to an IP-Turbine*, Materials at High Temperatures, Vol. 15, pp. 323-330, 2003.
- [3] J. Granacher, T. S. Mao, and R. Fischer, *Finite Element Calculation of Creep Crack Initiation on An IP-Turbine Rotor Using the C^* -Parameter*, Materials at High Temperatures, Vol. 15, pp. 331-335, 2003.
- [4] K. Maile, A. Klenk, J. Granacher, G. Schellenberg, M. Tramer, *Creep and Creep Fatigue Crack Behavior of 1Cr- and 9Cr-Steels*, Key Engineering Materials (1013-9826), Vols. 171-174, pp. 85-97, 2000.
- [5] K. Ryoichi, *Creep-Fatigue Crack Growth and Fractography of Metallic Materials in Air and Vacuum at Elevated Temperatures*, Fatigue and Fracture of Engineering Materials and Structures, Vol. 16, No. 6, pp. 619-630, June 1993.
- [6] D.J. Michel, A.W. Thompson, *Elevated Temperature Fatigue Crack Propagation*, Virginia University, Fatigue 87, Vol. 2, pp. 1057-1066, 1987.

- [7] S. Wang, S. Chi, G. Geng, *Investigation on LCF Crack Growth Rate With Controlling Deflection at High Temperature*, Acta Metallurgica Sinica (ISSN 0412-1961), Vol. 20, pp. A83-A91, April 1984.
- [8] K. Sadananda, P. Shahinian, *Creep-Fatigue Crack Growth, Cavities and Cracks in Creep, and Fatigue*. (A82-10048 01-26) London, Applied Science Publishers, pp. 109-195, 1981.
- [9] P. Shahinian, K. Sadananda, *Crack Growth Behavior under Creep-Fatigue Conditions in Alloy 718 (in nickel-chromium stainless steel)*, Proceedings A77-47042, pp. 365-390, New York, ASME, 1976.
- [10] M.F. Geng, *An Idea for Predicting Crack Growth Time to Fracture under Creep-Fatigue Conditions*, Material Science and Engineering A, Vol. 257, Issue 2, pp. 250-255, December 1998.
- [11] S. Marie, C. Delaval, *Fatigue and Creep-Fatigue Crack Growth in 316 Stainless Steel Cracked Plates at 650°C*, International Journal of Pressure Vessels and Piping, Vol. 78, Issue 11-12, pp. 847-857, November 2001.
- [12] A.E. Gemma, *Hold-Time Effect of a Single Overload on Crack Retardation at Elevated Temperature*, Engineering Fracture Mechanics, Vol. 11, No. 4, pp. 763-769, 1979.
- [13] C. R. Brinkman, G. E. Korth and R. R. Hobbins, *Estimates of Creep-Fatigue Interaction in Irradiated and Unirradiated Austenitic Stainless Steels*, Nuclear Technology, Vol. 16, pp. 297-307, 1972.
- [14] K. Yagi, K. Kubo, C. Tanaka, *Effect of Creep Stress on Creep-Fatigue Interaction*

- for SUS 304 Austenitic Steel*, Journal of Japan Society of Materials Science, Vol. 28, pp. 400-406, May 1979.
- [15] E. E. Reis, R. H. Ryder, *Creep-Fatigue Damage in OFHC Coolant Tubes for Plasma Facing Components*, Proceedings of 19th Symposium on Fusion Technology, September 1996.
- [16] R.S. Bellows, J.K. Tien, *Orientation Effects on the Creep-Fatigue Behavior of Single Crystal Ni3Al*, Scripta Metallurgica, Vol. 21, pp. 653-656, May 1987.
- [17] R. Richard-Frandsen, J.K. Tien, *On the Effect of Orientation on Creep-Fatigue Behavior of a Single Crystal Nickel-Base Superalloy*, Scripta Metallurgica (ISSN 0036-9748), Vol. 18, pp. 731-734, July 1984.
- [18] T.V. Duggan and P. Sabin, *The Effect of Geometry on Crack Formation*, *Advances in Research on the Strength and Fracture of Materials*, Proceedings of the Fourth International Conference on Fracture, Vol. 3A (A78-33601 13-23), New York, Pergamon Press, pp. 285-292, 1978.
- [19] I. Berman, A.C. Gangadharan, G.H. Jaisingh, G.D. Gupta, *Effects of Material Parameter Variability on Buckling and Creep Fatigue Interaction at Elevated Temperature*, Transactions, Series J- Journal of Pressure Vessel Technology, Vol. 98, pp. 75-80, February 1976.
- [20] Y. S. Park, S. W. Nam, and S. K. Hwang, *Intergranular Cracking under Creep-Fatigue Deformation in Lamellar TiAl alloy*, Material Letters, Vol. 53, Issue 6, pp. 392-399, April 2002.

- [21] S. Hardt, H. J. Maier, and H. J. Christ, *High-Temperature Fatigue Damage Mechanisms in near- α Titanium alloy IMI834*, International Journal of Fatigue, Vol. 21, Issue 8, pp. 779-789, September 1999.
- [22] I. Salam, A. Tauqir, A. Q. Khan, *Creep-Fatigue Failure of an Aero Engine Turbine Blades*, Engineering Failure Analysis, Vol. 9, pp. 335-347, 2002.
- [23] R. D. W. Bestwick, D. E. Buckthorpe, *Strain Based Creep-Fatigue Design Rules*, Fatigue and Fracture of Engineering Materials and Structures, Vol. 17, No. 17, pp.849-859, 1994.
- [24] S. R. Holdsworth, *A Knowledge Based System for Creep-Fatigue Assessment*, Nuclear Engineering and Design, Vol. 188, pp. 289-301, 1999.
- [25] G. Zhang, B. Richter, *A New Approach to the Numerical Fatigue-Life Prediction of Spot-Welded Structures*, Fatigue and Fracture of Engineering Materials and Structures, Vol. 23, pp. 499-508, 2000.
- [26] J. Lemaitre, A. Plumtree, *Application of Damage Concept to Predict Creep-Fatigue Failure*, Transactions of ASME, Vol. 101, pp. 284-292, July 1979.
- [27] X. Q. shi, Z. P. Wang, W. Zhou, H. L. Pang, and Q. J. Yang, *A New Creep Constitutive Model for Eutectic Solder Alloy*, Journal of Electronic Packaging, Vol. 124, pp. 85-90, 2002.
- [28] D. Rubesa, *Lifetime Prediction and Constitutive Modeling for Creep-Fatigue Interaction*, Gebruder Borntraeger, Berlin, Stuttgart, pp.140, 1996.
- [29] F. Colombo, B. Masserey, E. Mazza, S. holdsworth, *Service-Like Thermo-Mechanical Fatigue Tester for the Lifetime Assessment of Turbine Components*, 9th International Conference on the Mechanical Behavior of Materials, Geneva,

Switzerland, May 2003.

- [30] S. R. Holdsworth, E. Mazza, and A. Jung, *Creep-Fatigue Damage Development During Service-Cycle Thermo-Mechanical Fatigue Tests of 1CrMoV Rotor Steel*, 9th International Conference on the Mechanical Behavior of Materials, Geneva, Switzerland, May 2003.
- [31] E. Charkaluk, A. Constantinescu, *An Energetic Approach in Thermo-Mechanical Fatigue for Silicon Molybdenum Cast Iron*, *Materials at High Temperatures*, Vol. 17, No. 3, pp. 373-380, 2000.
- [32] Q. Yao, J. Qu, and S. X. Wu, *Estimate the Thermo-Mechanical Fatigue Life of Two Chip Scale Packages*, *Journal of Electronic Packaging*, Vol. 121, 1999, pp. 196-201.
- [33] C. Y. Jeong, B. G. Choi, and S. W. Nam, *Normalized life Prediction in Terms of Stress relaxation Behavior under Creep-Fatigue Interaction*, *Materials Letters*, Vol. 49, Issue 1, pp. 20-24, May 2001.
- [34] L. J. Chen, G. Yao, J. F. Tian, Z. G. Wang and H. Y. Zhao, *Fatigue and Creep-Fatigue Behavior of a Nickel-Base Superalloy at 850°C*, *International Journal of Fatigue*, Vol. 20, Issue 7, pp. 543-548, August 1998.
- [35] J. Tong, S. Dalby, J. Byrne, M. B. Henderson, and M. C. Hardy, *Creep, Fatigue and Oxidation in Crack Growth in Advanced Nickel Base Superalloys*, *International Journal of Fatigue*, Vol. 23, Issue 10, pp. 897-902, November 2001.
- [36] L. F. Coffine, *Fatigue at Elevated Temperatures*, ASTM 520, pp. 5-34, 1973.

- [37] E. Aghion, M. Bamberger, A. Berkovits, *Creep-Fatigue-Environment Interaction at the Propagating Crack Tip in MAR- M200Z+Hf Alloy*, Israel Journal of Technology, Vol. 24, No. 1-2, pp. 225-229, 1988.
- [38] M. Okada, M. Tsutsumi, T. Kitamura, R. Ohtani, *Initiation and Growth of Small Cracks in Directionally Solidified MAR-M 247 under Creep-Fatigue*, Fatigue and Fracture of Engineering Materials and Structures, Vol. 21, Issue 6, pp. 751-760, June 1998.
- [39] P.K. Venkiteswaran, D.C. Ferguson, and D.M.R. Taplin, *Combined Creep-Fatigue Behavior of Inconel Alloy X-750, Vibratory Stresses on Turbine Blade, Fatigue at Elevated Temperatures*, Proceedings of the Symposium, (A74-10601 01-17) Philadelphia, Pa., ASTM, pp. 462-472, 1973.
- [40] M. Ohnami, M. Sakane, *A Study on Creep-Fatigue Interaction of a Cobalt-Base Superalloy X-40 at High Temperature - Especially, Effect of Strain Wave Shapes on Creep-Fatigue Interaction*, JSME, Bulletin, Vol. 21, pp. 547-553, Apr. 1978.
- [41] C.W. Koburger, D.J. Duquette, N.S. Stoloff, *Creep-Fatigue Interaction in a Cobalt-Base Aligned Eutectic*, Metallurgical Transactions A - Physical Metallurgy and Materials Science, Vol. 11A, pp. 1107-1115, July 1980.
- [42] A. Plumtree, N-G. Persson, *Creep-Fatigue Interaction in an Austenitic Fe-Ni-Cr Alloy at 600 C*, Advances in Research on the Strength and Fracture of Materials, Proceedings of the Fourth International Conference on Fracture (A78-33601 13-23) New York, Pergamon Press, pp. 821-829, 1978.

- [43] R. Ohtani, T. Kitamura, W. Zhou, *Effect of Internal Creep Microcracks on Fatigue Macrocrack Propagation at High Temperatures*, International Journal of Fatigue, Vol.19, Issue 2, pp. 185, February 1997.
- [44] V. S. Srinivasan, A. Nagesha, M. Valsan, K. Bhanu Sankara Rao, S. L. Mannan and D. H. Sastry, *Effect of Hold-Time on Low Cycle Fatigue Behavior of Nitrogen Bearing 316L Stainless Steel*, International Journal of Pressure Vessels and Piping, Vol. 76, Issue 12, pp. 863-870, October 1999.
- [45] T. Kordisch, H. Nowack, *Life Prediction for the Ti-alloy IMI 834 Under High Temperature Creep-Fatigue Loadings*, Fatigue and Fracture of Engineering Materials and Structures, Vol. 21, Issue 1, pp. 47-63, January 1998.
- [46] O. Masakazu, T. Hiromichi, M. Junnosuke, *Microscopic Aspect and Mechanics of Creep-Fatigue Failure in SiC Whisker Reinforced Aluminum Base Composite at High Temperature*, Materials Science Research International (1341-1683), Vol. 3, No. 1, pp. 56-62, Mar. 1997.
- [47] D. J. Michel, H.H. Smith, *Accelerated Creep-Fatigue Crack Propagation in Thermally Aged Type 316 Stainless Steel*, Acta Metallurgica, Vol. 28, pp. 999-1007, July 1980.
- [48] J. Wareing, B. Tomkins, *Creep-Fatigue Interaction Failure in Type 316 Stainless Steel*, Advances in Research on the Strength and Fracture of Materials, Proceedings of the Fourth International Conference on Fracture, Vol. 4 (A78-33601 13-23) New York, Pergamon Press, pp. 81-86, 1978.
- [49] P. S. Maiya, S. Majumdar, *Elevated-Temperature Low-Cycle Fatigue Behavior of*

- Different Heats of Type 304 Stainless Steel*, Metallurgical Transactions A – Physical Metallurgy and Materials Science, Vol. 8A, pp. 1651-1660, Nov. 1977.
- [50] J. Wareing, *Creep-Fatigue Interaction in Austenitic Stainless Steels*, Metallurgical Transactions A - Physical Metallurgy and Materials Science, Vol. 8A, pp. 711-721, May 1977.
- [51] A. Plumtree, *Creep-Fatigue Interaction in Type 304 Stainless Steel at Elevated Temperatures*, Metal Science, Vol. 11, pp. 425-431, Aug.-September 1977.
- [52] A. Miller, *An Inelastic Constitutive Model for Monotonic, Cyclic, and Creep Deformation. II - Application to Type 304 Stainless Steel*, ASME, Conference on Micromechanical Modeling of Flow and Fracture, ASME, Transactions, Series H - Journal of Engineering Materials and Technology, Vol. 98, pp. 106-112, April 1976.
- [53] S. W. Nam, *Assessment of Damage and Life Prediction of Austenitic Stainless Steel under High Temperature Creep-Fatigue Interaction Condition*, Materials Science and Engineering, A, Vol.322, Issue 1, pp. 64-72, 2002.
- [54] N. Isobe, S. Sakurai, M. Yorikawa, K. Imou, Y. Takahashi, *Life Prediction of 316FR Stainless Steel under Creep-Fatigue Loading With Elastic Follow-up*, The International Journal of Pressure Vessels and Piping, Vol. 77, Issue 13, pp. 817-823, November 2000.
- [55] Y. Takahashi, T. Ogata, K. Take, *Study on Creep-Fatigue Failure Prediction Methods for Type 304 Stainless Steel*, Nuclear Engineering and Design, Vol. 153, Issue 2, pp. 235-244, January 1995.

- [56] R. Hales, *A Quantitative Metallographic Assessment of Structural Degradation of Type 316 Stainless Steel during Creep-Fatigue*, *Fatigue Engineering Material Structures*, Vol.3, Issue 4, pp. 339-356, 1980.
- [57] J. Wareing, *Creep-Fatigue Behavior of Four Casts Type 316 Stainless Steels*, *Fatigue Engineering Material Structures*, Vol. 4, pp. 131-145, 1981.
- [58] C. Jaske, H. Mindlin, J. Perrin, *Combined Low-Cycle Fatigue and Stress Relaxation of Alloy 800 and Type 304 Stainless Steel at Elevated Temperatures*, *ASTM, STP 520*, Vol. 365-376, 1973.
- [59] M. Okazaki, Y. Yamazaki, *Creep-Fatigue Small Crack Propagation in a Single Crystal Ni-Base Superalloy, CMSX-2*, *International Journal of Fatigue*, Vol. 21, Supplement 1, pp. 79-86, September 1999.
- [60] D. Rubesa, *Lifetime Prediction and Constitutive Modeling for Creep-Fatigue Interaction*, pp. 20, Gebruder Borntraeger Berlin, Stuttgart, 1996.
- [61] ASME Boiler and Pressure Vessel Code, Section III, Code Case N-47, 1974.
- [62] E. L. Robinson, *Effect of Temperature Variation on the Creep Strength of Steel*, *Transaction ASME*, Vol. 160, pp. 253-259, 1938.
- [63] M. A. Miner, *Cumulative Damage in Fatigue*, *Journal of Applied Mechanics*, Vol. 12, No. 3, pp. A159-A167, 1945.
- [64] L. F. Coffin, *Prediction Parameters and Their Application to High Temperature Low Cycle Fatigue*, *Proceedings of Second International Conference on Fracture*, Brighton, London, Chapman Hall, pp. 643-654, 1969.
- [65] S. S. Manson, *Fatigue at Elevated Temperatures*, *STP 520*, ASTM, Philadelphia, pp. 744-782, 1973.

- [66] S. S. Manson, G. R. Halford, and A. C. Nachtigall, *Advances In Design, for Elevated Temperature Environments*, ASME National Congress on Pressure Vessels and Piping, pp. 17, 1975.
- [67] S. S. Manson, G. R. Halford, and M. H. Hirschberg, *Creep-Fatigue Analysis by Strainrange Partitioning*, NASA Report TMX-67838, NASA, 1971.
- [68] G. R. Halford, M. H. Hirschberg, and S. S. Manson, *Fatigue at Elevated Temperatures*, STP 520, American Society for Testing and Materials, Philadelphia, pp. 659, 1973.
- [69] G. R. Halford, J. F. Saltsman, and M. H. Hirschberg, *Fatigue at Elevated Temperature*, NASA Technical Note 73737, NASA, 1977.
- [70] W. J. Ostergren, *A Damage Function and Associated Failure Equations for Predicting Hold time and Frequency Effects in Elevated Temperature Low Cycle Fatigue*, ASTM, Journal of Test Evaluation, Vol. 4, No. 5, pp. 327-339, 1976.
- [71] W. J. Ostergren, *Correlation of Hold Time Effects in Elevated Temperature Fatigue Using a Frequency Modified Damage Function*, ASME-MPC Symposium on Creep-Fatigue Interaction, MPC-3, Metal Properties Council, New York, pp. 179, 1976.
- [72] M. M. Leven, *Evaluation of Three Design Method in Cr-Mo-V rotor steels* Experimental mechanic, Vol. 353, September 1973.
- [73] K. Kuwabara and A. Nitta, *Estimation of Thermal Fatigue Damage in Steam Turbine Rotors*, Report 277001, Central Research Institute for the Electric Power Industry (Japan), July 1977.
- [74] A. D. Batte, *Creep-Fatigue Life Predictions, in Fatigue at High Temperature*,

- R. P. Skelton, Edited, Applied Science Publishers, London, 1983.
- [75] R. M. Curran and B. M. Wundt, *Interpretive Report on Notched and Un-notched Creep-Fatigue Interspersion Tests in CrMo, 2 ¼ Cr-1Mo and Type 304 Stainless Steel*, publication MPC-8, ASME, pp. 218-314, 1982.
- [76] K. N. Melton, *Strain Wave Shape and Frequency effects on the High Temperature Low Cycle Fatigue Behavior of 1CrMOV Ferritic Steel*, Material Science Engineering, pp. 21-28, 1982.
- [77] V. Bisego, C. Fossati, and S. Ragazzoni, *An Energy Based Criterion for Low Cycle Fatigue Damage Evaluation*, Educational Book No. H 00217, PVP Vol. 60, ASME, New York, 1982.
- [78] G. B. Warburton, *The Vibration of Rectangular Plates*, Proceedings of the Institution of Engineers Series A, No. 168, pp. 371-384, 1954.
- [79] R. W. Claassen and C. J. Thorne, *Vibration of Rectangular Plate*, Journal of Aerospace Science, No. 29, pp. 1300-1305, 1962.
- [80] N. J. Huffington, *On the Occurrence of Nodal Patterns of Nonparallel Form in Rectangular Orthographic Plates*, Journal of Applied Mechanics, Transaction of ASME, No. 29, pp. 459-461, 1961.
- [81] G. S. Schajer, *The Vibration of a Rotating Circular String Subject to a Fixed Elastic Restraint*, Journal of Sound and Vibration, No. 92, Issue 1, pp. 11-19, 1984.
- [82] N. C. Perkins and C. D. Mote, *Comments on Curve Veering in Eigenvalue Problems*, Journal of Sound and Vibration, No. 106, Issue 3, pp. 451-463, 1986.

- [83] R. B. Bhat, *Curve Veering: Inherent Behavior of Some Vibrating Systems*, Journal of Shock and Vibration, No. 7, pp. 1-9, 2000.
- [84] W. Carnegie, *Vibration of Rotating Cantilever Blading*, Journal of Mechanical Engineering Science, No. 1, Issue 3, pp. 235-240, 1959.
- [85] A. W. Leissa, *On a Curve Veering Aberration*, Journal of Applied Mathematics and Physics (ZAMP), No. 25, pp. 99-110, 1974.
- [86] S. Chonan, *Vibration and Stability of Annular Plates under Conservative Loads*, Journal of Sound and Vibration, No. 80, Issue 3, pp. 413-420, 1982.
- [87] R. B. Bhat, *Transverse Vibrations of a Rotating Uniform Cantilever Beam With tip Mass Using Beam Characteristic Orthogonal Polynomials in Rayleigh-Ritz Method*, Journal of Sound and Vibration, No. 104, Issue 3, pp. 493-499, 1985.
- [88] J. T. S. Wang, D. Shaw, and O. Mahrenholtz, *Vibration of Rotating Rectangular Plates*, Journal of Sound and Vibration, No. 112, Issue 3, pp. 455-468, 1987.
- [89] C. K. Rao, *Frequency Analysis of Clamped-Clamped Uniform Beams With Intermediate Elastic Supports*, Journal of Sound and Vibration, No. 133, pp. 502-509, 1989.
- [90] C. K. Rao, *Frequency Analysis of Two-Span Uniform Bernoulli-Euler Beams*, Journal of Sound and Vibration, No. 137, Issue 1, pp. 144-150, 1989.
- [91] C. Pierre, *Mode Localization and Eigenvalue Loci Veering Phenomena in Disordered Structures*, Journal of Sound and Vibration, No. 126, Issue 3, pp. 485-502, 1988.
- [92] R. R. Swamy and R. A. Marcus, *Perturbative Examination of Avoided Crossings*, Journal of Chemical Physics, No. 74, Issue 2, pp. 1379-1384, 1981.

- [93] M. H. Sabour, R. B. Bhat and H. Moustapha, *Pseudo Curve Veering in Rotating Structures using the Rayleigh-Ritz Method*, CSME Forum May 21-24, Queen's University, Kingston, ON, 2002.
- [94] J. Dieterich, *Scale Models in Engineering fundamentals and applications*, Pergamon Press, pp.35, 1977.
- [95] W. K. Chen., *Algebraic theory of dimensional analysis*, Journal of the Franklin Institute, Vol. 292, No. 6, pp. 403-422, December 1971.
- [96] T. J. Higgins, *Electroanalogic Methods*, Applied Mechanics Reviews, Vol. 10, No. 8, pp. 331-335, August 1957.
- [97] E. O. Macagno, *Historical-Critical Review of Dimensional Analysis*, Journal of the Franklin Institute, Vol. 292, No. 6, pp. 391-402, December 1971.
- [98] E. Buckingham, *Physically Similar Systems; Illustrations of Use of Dimensional Equations*, Physical Review, Vol. 4, No. 4, pp. 345-376, June 1914.
- [99] J. W. Rayleigh, *The Principle of Similitude*, Nature, Vol. 95, No. 2389, pp. 66-68, March 1915.
- [100] W. E Baker, P. S. Westine, F. T. Dodge, *Similarity Methods in Engineering Dynamics, Theory and Practice of Scale Modeling*, Hayden Book Company, Inc., Rochelle Park, New Jersey, pp. 325,1973.
- [101] J. N. Mansfield, J. McGregor, *Contractual Acceptance Tests of Model Turbines*, Proceedings of Symposium on Model testing of Hydraulic Machinery and Associated Structures, Vol. 182, Part 3M, pp. 28-31, 1967-68.

- [102] I. S. Paterson, G. Campbell, *Pump Intake Design Investigations*, Proceedings of Symposium on Model testing of Hydraulic Machinery and associated Structures, Vol. 182, Part 3M, pp. 1-10, 1967-68.
- [103] I. S. Paterson, T. A. McConnell, *Integrated Design of Pump and Adjacent System*, Proceedings of Symposium on Model testing of Hydraulic Machinery and Associated Structures, Vol. 182, Part 3M, pp. 11-19, 1967-68.
- [104] R. K. Duggins, *Hydraulic Stability of a Model Hydroelectric Installation*, Proceedings of Symposium on Model testing of Hydraulic Machinery and Associated Structures, Vol. 182, Part 3M, pp. 20-27, 1967-68.
- [105] R. A. Nixon, E. A. Spencer, *Model Testing of High Head Pumps*, Proceedings of Symposium on Model testing of Hydraulic Machinery and Associated Structures, Vol. 182, Part 3M, pp. 32-41, 1967-68.
- [106] T. Ward, *Thermodynamic Scale Effects on Pump Suction Performance*, Proceedings of Symposium on Model testing of Hydraulic Machinery and Associated Structures, Vol. 182, Part 3M, pp. 42-47, 1967-68.
- [107] D. Vasallos, *Physical Modeling and Similitude of Marine Structures*, Ocean Engineering, Vol. 26, pp. 111-123, August 1998.
- [108] H. N. Abramson, *Some Modern Developments in the Application of Scale-Models in Dynamic Testing*, Colloquium on Use of Models and Scaling in Shock and Vibration, ASME Winter Annual Meeting , pp. 1-15, ASME, New York, November 1963.
- [109] J. Andrews, J. W. Church, *A Model for the Simulation of Wave Impact Loads and Resulting Transient Vibration of a Naval Vessel*, Colloquium on Use of Models

- and Scaling in Shock and Vibration, ASME Winter Annual Meeting , pp. 16-28, ASME, New York, November 1963.
- [110] *Wind Tunnel Studies of Buildings and Structures*, American Society of Civil Engineers Manuals and Reports on Engineering Practice No. 67, 1999.
- [111] R. L. Wardlaw, C. A. Ponder, *An Example of the Use of Wind Tunnels for Investigating the Aerodynamic stability of Bridges*, Quarterly Bulletin Division of Mechanical Engineering and the National Aeronautical Establishment, Report No. DME/NAE 3, pp. 13-34, July-September 1969.
- [112] National Research Council of Canada Quarterly Bulletin of the Division of Mechanical Engineering and the National Aeronautical Establishment, January 1 to March 31 1970.
- [113] A. A. Regier, *The Use of Scaled Dynamic Models in Several Aerospace Vehicle Studies*, Colloquium on Use of Models and Scaling in Shock and Vibration, ASME Winter Annual Meeting , pp. 34-50, ASME, New York, November 1963.
- [114] G. W. Brooks, *The Application of Models to Helicopter Vibration and Flutter Research*, Proceeding of Ninth Annual Forum, American Helicopter Society, Washington, D.C., May 1953.
- [115] J. L. Sewall, R. W. Herr, and W. B. Igoe, *Flutter Investigation of a True-Speed Dynamic Model with Various Tip-Tank Configurations*, NASA TN D-178, March 1960.
- [116] H. L. Runyan, H. G. Morgan, and J. S. Mixson, *Role of Dynamic Models in Launch Vehicle Development*, Experimental Techniques in Shock and Vibration, ASME, New York, pp. 55-69, November 1962.

- [117] J. Ferritto, *Dynamic test of Model Concrete*, Dynamic Modeling of Concrete Structures, SP73-2, Publication SP-73 American Concrete Institute Detroit, pp. 23-33, 1982.
- [118] R. W. Clough, *Earthquake Simulator Research on Arch Dam Models*, Dynamic Modeling of Concrete Structures, Publication SP-73-5, American Concrete Institute, Detroit, pp. 83-105, 1982.
- [119] D. P. Abrams, *Behavior of Small Scale Reinforced Concrete Model Structures*, Dynamic Modeling of Concrete Structures, SP73-4, Publication SP-73 American Concrete Institute Detroit, pp. 65-82, 1982.
- [120] K. Takanashi, K. Ohi, *Response observation of scaled model structures to strong earthquakes*, Journal of Constructional Steel Research, Volume 13, Issues 2-3, pp. 189-210, 1989.
- [121] W. G. Godden, *Seismic Modeling of Long-Span Bridges*, Dynamic Modeling of Concrete Structures, SP73-6, Publication SP-73 American Concrete Institute Detroit, pp. 107-123, 1982.
- [122] T. Ward, *Thermodynamic Scale Effects on Pump Suction Performance*, proceeding of Symposium at Model Testing of Hydraulic Machinery and Associated Structures, Vol. 182, part 3M, 1967-68.
- [123] H. N. Abramson, G. E. Nevill, *Some Modern Developments in the Application of Scale-Models in Dynamic Testing*, Colloquium on Use of Models and Scaling in Shock and Vibration, ASME Winter Annual Meeting, pp. 1-15, ASME, New York, November 1963.

- [124] S. K. Clark, R. N. Dodge, J. I. Lackey, and G. H. Nybakken, *Structural Modeling of Aircraft Tires*, Journal of Aircraft, Vol. 9, No. 2, pp. 162-167, February 1972.
- [125] A. A. Ezra, *Scaling Laws and Similitude Requirements for Valid Scale Model Work*, Colloquium on Use of Models and Scaling in Shock and Vibration, ASME Winter Annual Meeting, pp. 57-64, ASME, New York, November 1963.
- [126] S. Katzoff, *Similitude in Thermal Models of Spacecraft*, NASA Technical Note D-1631, April 1963.
- [127] J. William, J. O'Sullivan, *Theory of Aircraft Structural Models subject to Aerodynamic Heating and External Loads*, NASA Technical Note 4115, Washington, April 1963.
- [128] J. Callister, D. William, *Material Science and Engineering*, an Introduction, third edition, pp. 226, 1985.
- [129] E. N. C. Andrade, *Creep and Recovery*; Process Research Society London, Vol. 90A, pp. 329-342, 1914.
- [130] F. Garofalo, *Properties of Crystalline Solids*, ASTM Specific Technical Publication, Vol. 283, pp. 82, 1960.
- [131] J. Callister, D. William, *Material Science and Engineering*, an introduction, third edition, pp.227, 1985.
- [132] Z. W. Rosenhain and D. Ewen, *Fracture at Elevated Temperature*, Journal of Insta Metallica, Vol. 10, pp. 119, 1913.
- [133] Z. Jeffries, Transaction of Metallurgy Society, AIME, Vol. 60, pp. 474-576, 1919.
- [134] G. E. Dieter, *Mechanical metallurgy*, McGraw-Hill, second edition, pp. 482, 1976.

- [135] R. F. Gill and R. M. Goldhoff, *crack growth in creep and the effect of cyclic loading on growth in creep-fatigue*, *Metalurgy Engineering Quality*, Vol. 10, pp. 30-39, August 1970.
- [136] F. R. Larson and J. Miller, *A Time-Temperature Relationship for Rupture and Creep Stresses*, *Transaction of ASME*, Vol. 74, pp. 765-771, 1952.
- [137] ANSYS Inc. Theory Reference, Version 6, 2003.
- [138] P. C. Paris, F. Erdogan, *A Critical Analysis of Crack Propagation Laws*, *Transaction of ASME*, Vol. 85, pp. 528-534, 1965.
- [139] V. T. Troshchenko, A. V. Prokopenko, *Fatigue Strength of Gas Turbine Compressor Blades*, *Engineering Failure Analysis*, Vol. 7, pp. 209-220, 2000.
- [140] O. H. Basquin, *The Exponential Law of Endurance Tests*, *ASTM Proceedings*, Vol. 10, pp. 230, 1910.
- [141] J. Coffin, S. S. Manson, *Fatigue at Elevated Temperatures*, STP 520, ASTM, Philadelphia, pp. 744-782, 1973.
- [142] J. E. Shigley, C. R. Mischke, *Mechanical Engineering Design*, Sixth edition, pp. 416, 2003.
- [143] C. E. Jaske and N. D. Frey, *High Cycle Fatigue of 2 1/4Cr-1Mo Steel at Elevated Temperature*, Paper C46/80, *Proceedings of the Fourth International Conference on Pressure Vessel Technology*, Institute of Mechanical Engineers, London, pp. 350, 1980.
- [144] R. H. King and A. Smith, *Thermal Fatigue Processes and Testing Techniques*, IOM/ISI Conference on Thermal and High Strain Fatigue, London, pp. 364-376, 1967.

- [145] E. G. Ellison, *A Review of the Interaction of Creep and Fatigue*, Mechanical Engineering Science, Vol. 11, pp. 318-339, 1969.
- [146] B. Tomkins and J. Wareing, *Elevated Temperature Fatigue Interactions in Engineering Materials*, Metallurgical Science, Vol II, pp. 416-424, 1977.
- [147] E. M. Wundt and E. Krempl, *Hold Time Effects in High Temperature Low Cycle Fatigue-A Literature Survey and Interpretive Report*, STP 489, ASTM, Philadelphia, 1971.
- [148] L. F. Coffin, *Fatigue at High Temperature-Prediction and Interpretation*, Proceeding of the Institution of Mechanical Engineers, Vol 188, 1974, p 109-127.
- [149] A. D. Batte, *Creep-Fatigue Life Predictions, in Fatigue at High Temperature*, R. P. Skelton, Edited, Applied Science Publishers, London, 1983.
- [150] E. G. Ellison and A. J. F. Patterson. Proceeding of the Institution of Mechanical Engineers, Vol. 190, pp. 321-350, 1976.
- [151] G. Thomas and R. A. T. Dawson, *The Effect of Dwell Period and Cycle Type on High Strain Fatigue Properties of 1CrMoV Rotor Forgings at 500-550 °C*, Proceedings of the International Conference on Engineering Aspects of Creep, Vol. I, Mechanical Engineering Publishers, London, pp. 167- 175, 1980.
- [152] Y. Kadoya et al, *Creep Fatigue Life Prediction of Turbine Rotors*, Life Assessment and Improvement of Turbogenerator Rotors for Fossil Plants, New Yourk, pp. 3.101-3.114, 1985.
- [153] D. A. Miller, R. H. Priest, and E. G. Ellison, *A Review of Material Response and Life Prediction Techniques under Fatigue-Creep Loading Conditions*, High Temperature Material Processing, Vol. 6, No.3 and 4, P 115-194, 1984.

- [154] L. F. Coffin, *Prediction Parameters and Their Application to High Temperature Low Cycle Fatigue*, Proceedings of Second International Conference on Fracture, Brighton, London, Chapman Hall, pp. 643-654, 1969.
- [155] S. S. Manson, *Fatigue at Elevated Temperatures*, STP 520, ASTM, Philadelphia, pp. 744-782, 1973.
- [156] S. S. Manson, G. R. Halford, and A. C. Nachtigall, Advances In Design, for Elevated Temperature Environments, ASME National Congress on Pressure Vessels and Piping, pp. 17, 1975.
- [157] S. S. Manson, G. R. Halford, and A. C. Nachtigall, NASA Report TMX-67838, NASA, 1971.
- [158] G. R. Halford, M. H. Hirschberg, and S. S. Manson, *Fatigue at Elevated Temperatures*, STP 520, ASTM, Philadelphia, p 659, 1973.
- [159] G. R. Halford, J. F. Saltsman, and M. H. Hirschberg, NASA Technical Note 73737, NASA, 1977.
- [160] W. J. Ostergren, *A Damage Function and Associated Failure Equations for Predicting Hold time and Frequency Effects in Elevated Temperature Low Cycle Fatigue*, ASTM, Journal of Test Evaluation, Vol. 4, No. 5, pp. 327-339, 1976.
- [161] W. J. Ostergren, *Correlation of Hold Time Effects in Elevated Temperature Fatigue Using a Frequency Modified Damage Function*, ASME-MPC Symposium on reep-Fatigue Interaction, MPC-3, Metal Properties Council, New York, pp. 179, 1976.
- [162] ASME Boiler and Pressure Vessel Code, Section III, Code Case N-47, 1974.

- [163] E. L. Robinson, *Effect of Temperature Variation on the Creep Strength of Steel*, Transaction ASME, Vol. 160, pp. 253-259, 1938.
- [164] M. A. Miner, *Cumulative Damage in Fatigue*, Journal of Applied Mechanics, Vol. 12, No. 3, pp. A159-A167, 1945.
- [165] S. Taira, *Creep in Structures*, Academic Press, pp. 96-124, 1962.
- [166] R. M. Curran and B. M. Wundt, *Interpretive Report on Notched and Un-notched Creep-Fatigue Interspersion Tests in CrMo, 2 1/4 Cr-1Mo and Type 304 Stainless Steel*, publication MPC-8, ASME, pp. 218-314, 1977.
- [167] K. N. Melton, *Strain Wave Shape and Frequency effects on the High Temperature Low Cycle Fatigue Behavior of 1CrMOV Ferritic Steel*, Material Science Engineering, pp. 21-28, 1982.
- [168] V. Bisego, C. Fossati, and S. Ragazzoni, *An Energy Based Criterion for Low Cycle Fatigue Damage Evaluation, Material Behavior at Elevated Temperatures and Component Analysis*, Educational Book No. H 00217, PVP, Vol. 60, ASME, New York, pp. 175, 1982.
- [169] D. A. Miller, *A Creep-Fatigue Failure Mechanism Map for 1Cr-Mo-V at 565°C*, Material Science Engineering, Vol. 54, pp. 273-278, 1982.
- [170] D. A. Spera, *What Is Thermal Fatigue?* Thermal Fatigue of Materials and Components, D. A. Spera and D. Mowbray, Edited STP 612, ASTM, Philadelphia, pp. 3-9, 1976.
- [171] D. A. Spera and E. C. Cox, *Description of a Computerized Method for Predicting Thermal Fatigue Life of Materials*, Thermal Fatigue of Materials and Components, STP 612, ASTM, Philadelphia, pp. 69-85, 1976.

- [172] G. B. Thomas, J. Bressers, and D. Raynor, *Low Cycle Fatigue and Life Prediction Methods*, High Temperature Alloys for Gas Turbines, R. Brunetaud, Edited, D. Riedel Publishing Co., Dordrecht, Netherlands, pp. 291-317, 1982.
- [173] A. Nitta, and T. Kitamura, *Thermal Mechanical Fatigue Life Prediction in High Temperature Component Materials for Power Plants*, Advances in Life Prediction, D.A. Woodford and R. Whitehead, Ed., ASME, New York, pp. 131-141, 1985.
- [174] E. S. Russell, *Practical Life Prediction Methods for Thermo-Mechanical Fatigue of Gas Turbine Buckets*, Life prediction for High Temperature Gas Turbine Materials (conference proceedings), V. Weiss and W. T. Bakker, Edited, Report AP 4477, Electrical Power Research Institute, Palo Alto, CA, pp. 3.1-3.17, 1985.
- [175] G. T. Embley and E. S. Russell, *Thermal Mechanical Fatigue of Gas Turbine Bucket Alloys*, First Parsons International Turbine Conference, Dublin, Ireland, pp. 157-164, June 1984.
- [176] F. R. Larson, J. Miller, *A Time-Temperature Relationship for Rupture and Creep Stress*, Transaction of the ASME, pp. 765-775, July 1952.
- [177] R. B. Bhat, *Lagrange-Bhat Method to Analyze Vibration of Structures Using Boundary Characteristic Orthogonal Polynomials*, Cairo University, Proceeding of Conference on Mechanical Design and Production Cairo, Egypt, pp. 230-237, January 2004.
- [178] R. B. Bhat, *Plate Deflections Using Orthogonal Polynomials*, Journal of Engineering Mechanics, Transactions ASCE, Vol.111, pp. 1301-1309, 1985.

- [179] A. Jha, *Dynamic Testing of Structures Using Scale Models*, Master Thesis, pp. 60, August 2004.
- [180] Dynamic Systems, Inc. P.O. Box 1234, Poestenkill NY, 12140
- [181] ASM Handbook Vol. 12, Fractography, Hardcover 9th edition, Asm Intl; ISBN: 0871700182, pp. 567, November 1989

APPENDIX

Appendix A

Typical Material Data From Tests

This is the typical material data for creep strain equal to 0.005.

T (°F)	1300	1400	1500	1600	1700	1800	1900	2000
Time (h)	Stress (ksi)							
0.1	120.	110.	96.0	80.0	64.5	48.5	35.0	25.0
10	90.0	77.0	60.0	44.5	30.0	18.6	10.3	5.70
20	86.0	72.0	57.0	40.5	27.0	15.0	8.20	4.30
50	80.5	67.0	51.5	36.0	22.5	12.0	6.20	3.00
100	78.0	62.5	48.0	32.0	19.0	10.0	4.85	2.30
200	74.5	60.0	44.5	28.5	16.5	8.30	3.85	1.70
500	69.5	56.0	39.0	23.8	13.0	6.60	2.80	1.18
1000	66.5	52.5	35.5	21.0	11.0	5.50	2.20	0.92
2000	63.0	49.8	32.0	18.5	9.25	4.60	1.72	0.70
5000	59.8	46.0	28.0	15.5	7.00	3.65	1.25	0.48
10000	56.0	43.5	25.0	13.5	6.40	3.00	1.00	0.36
100000	42.0	31.0	17.0	8.50	3.60	1.50	0.43	0.15

Appendix B

The Procedure of Tabular Material Format Creep Calculations

If σ_{ij} , T_{ij} are the stress and temperature at the time interval i and station j , the program calculations steps for the rupture life are as follows:

1. Calculates σ_{i1} to σ_{iL} .
2. Interpolates to get the corresponding time t_{ij} for strain conditions of 0.5%, 1 %, 2.0%,... and stress rupture for all σ_{ij} and T_{ij} . These two procedures will be repeated for all the strain conditions, i.e. 0.5%, 1 %,2%,.. ..to stress rupture for all σ_{ij} , T_{ij} .
3. Plots creep strain ϵ versus time t for all σ_{ij} , T_{ij} .
4. For each station j , obtain ϵ_1 for time interval t_1 uses σ_1 , T_1 , t_1 and curve1 in Figure 19.
5. For each station j , obtains t_{el} (equivalent time) for time interval t_2 using σ_2 , T_2 , ϵ_1 and curve 2 in figure 2
6. With $t=t_2 + t_{el}$, σ_2 , T_2 , ϵ_1 and curve 2 in figure 2 :
7. Repeats steps 5 and 6 for the remaining time intervals of the mission and subsequent ones.
8. At the end of each mission, k , calculates the blade elongation
9. If $\epsilon_{jk} > \text{creep strain limit}$ or $\Delta_{lk} > \text{creep elongation limit}$ or $k = \text{specified number of missions}$, program will stop and a message is .printed to indicate that strain or elongation limit has been reached

Appendix C

Arguments

These are the command line arguments that must be entered for running the macro.

ARG1 : Number of missions

ARG2 : Material deterioration (temperature)

ARG3 : Creep option 1(on) or 0(off)

ARG4 : Nonlinear geometry 1(on) or 0(off)

ARG5 : Geometry filename

ARG6 : Geometry file extension

ARG7 : Load filename

ARG8 : Load file extension

ARG9 : Creep strain limit (in/in)

ARG10: Material properties filename

ARG11: Material properties extension

ARG12: Creep constant filename

ARG13: Creep constant extension

ARG14: Creep ratio

And following input files:

Geometry file

The geometry file contains 4 columns that must be separated by space. The columns are X, Y, Z, and the cross sectional area respectively. The blade is along “y” direction.

<u>X</u>	<u>Y</u>	<u>Z</u>	<u>Area</u>
0.000	3.2809800	0.000	0.0961
0.000	3.8492016	0.000	0.0731
0.000	4.1333124	0.000	0.0642
0.000	4.2280160	0.000	0.0617
0.000	4.3227196	0.000	0.0593
0.000	4.4174232	0.000	0.0573
0.000	4.5121268	0.000	0.0554
0.000	4.6068304	0.000	0.0537
0.000	4.7015340	0.000	0.0522
0.000	4.7962376	0.000	0.0510
0.000	4.8909412	0.000	0.0500
0.000	5.2697556	0.000	0.0477
0.000	5.6485700	0.000	0.0488
0.000	5.9000000	0.000	0.2194

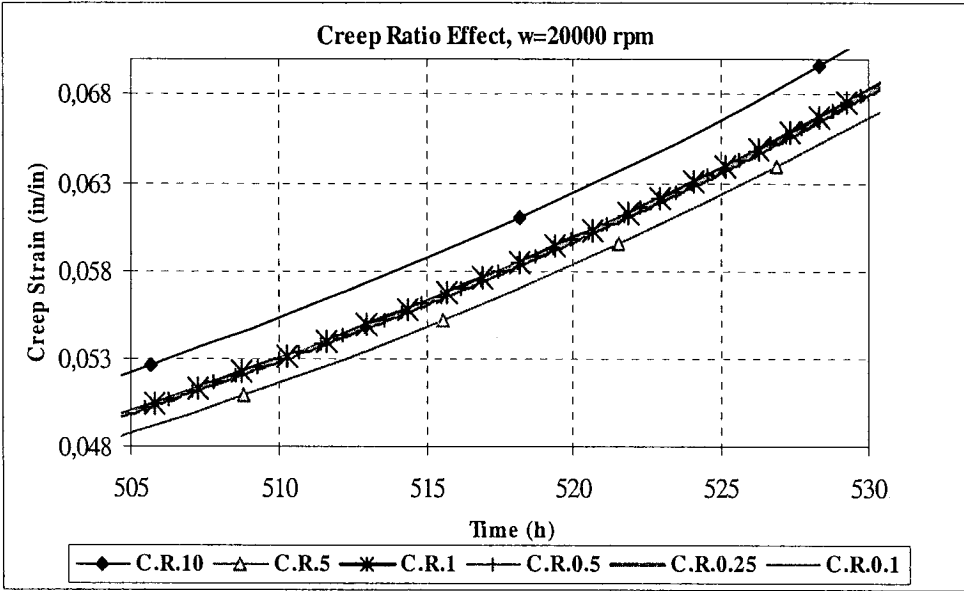
Load file

The first column of load file is the cumulative time in seconds, the second column is the angular speed in rpm, the third column is the T_4 at each time, the fourth column is minimum and maximum T_4 , and from the fifth column and after that are the minimum and maximum blade temperatures of the nodes (it starts from the first node, at the hub).

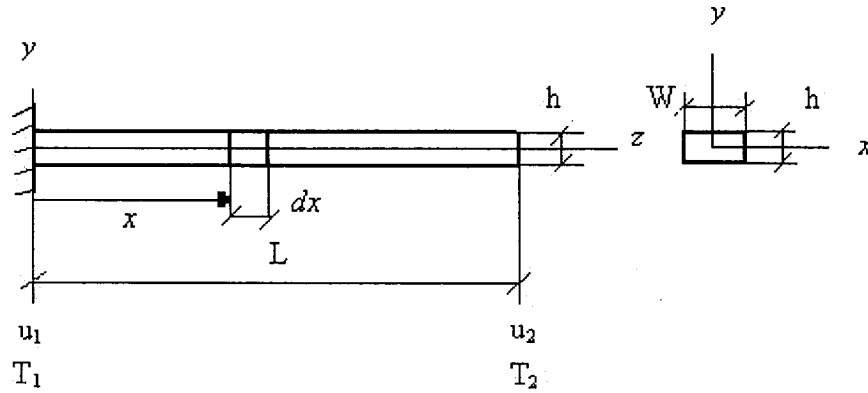
Time (sec.)	speed (rpm)	T4 (i) (Deg.F)	$T_4 \left(\frac{\min}{\max} \right)$	$T_{blade} \left(\frac{\min}{\max} \right)$			
				node 1	node 2	node 3	node 4
0.0500	29980.6	1719.6	1700.0	1281.1	1296.05	1311	1315.43
45.0000	29980.6	1719.6	1776.8	1320.1	1336.4	1352.7	1357.53
50.0000	29980.6	1720.9	0.0000	0.0000	0.0000	0.0000	0.0000
650.000	29980.6	1720.9	0.0000	0.0000	0.0000	0.0000	0.0000
15040.0	29980.6	1742.0	0.0000	0.0000	0.0000	0.0000	0.0000
15045.0	29980.6	1742.0	0.0000	0.0000	0.0000	0.0000	0.0000

Appendix D

The results of the effect of creep ratio on lifetime and rupture creep strain.



Appendix E



Based on the figure, for the small element at distance x we have:

$$\delta L = dx(1 + \alpha[T(x) - T_0])$$

where $T(x) = T_0 + \left(\frac{T_2 - T_0}{L}\right)x$ then

$$\delta L = dx \left(1 + \alpha \left[T_0 + \left(\frac{T_2 - T_0}{L} \right) x - T_0 \right] \right) = dx \left(1 + \alpha \left(\frac{T_2 - T_0}{L} \right) x \right)$$

$$L = \int_0^L \left(1 + \alpha \left(\frac{T_2 - T_0}{L} \right) x \right) dx = \left[x + \alpha \left(\frac{T_2 - T_0}{L} \right) \frac{x^2}{2} \right]_0^L = L \left[1 + \frac{\alpha}{2} (T_2 - T_0) \right]$$

Appendix F

SELECTION OF BASIC QUANTITIES

For obvious reasons the first standards to be established were those dealing with the measurement of the three relatively simple quantities, F, L, and T. It soon became evident that certain other quantities could be expressed or defined in terms of these three. For example, it was found that the magnitude of an area may be expressed in terms of the lengths of the sides or other pertinent dimensions, and velocity may be expressed in terms of length and time ($V=LT^{-1}$). As a result, certain measurable quantities have come to be considered as fundamental or basic, since other quantities may readily be evaluated or defined in terms of them. For scientific measurements the three quantities, mass, lengths, and time, are usually regarded as basic; while for engineering purposes; force, length, and time are usually more convenient. The four quantities are interrelated through Newton's Second Law of Motion,

$$F=Ma \tag{1}$$

or dimensionally,

$$F= M L T^{-2} \tag{2}$$

so that any one may be evaluated in terms of the other three. Any combination of measurable quantities may be used as basic quantities, provided that a sufficient number of independent quantities are included in the combination.

1. DIMENSIONAL ANALYSIS AND THEORY OF MODELS

Consider some physical system, called the prototype, about which it is desired to make certain predictions or draw certain conclusions. For such a physical system, the natural laws governing this particular system, together with the n physical parameters which are significant, lead to a relationship of the form

$$f(x_1, x_2, \dots, x_n) = 0 \quad (3)$$

If this equation is unique in the sense that only one relation exists between the parameters, then the need for dimensional homogeneity leads to the requirement that there exist an equivalent relation

$$\Phi(\pi_1, \pi_2, \dots, \pi_m) = 0 \quad (4)$$

among m independent dimensionless group (π_i) of the original dimensional parameters where $m=n-s$ and s is the minimum number of physical dimensions necessary for description of the n parameters. This is general statement of the well-known Buckingham π theorem. In those cases where the governing equation of the system is known, in the form of a differential equation, etc., the Buckingham Theorem gives assurance that the equation may be put in dimensionless form. It is in the general case, however, where the form of the equation is not known, that the π theorem is of greatest value. For that case, it is noted that the π terms must be independent and dimensionless but that the set is not necessarily unique.

2. SCALE MODEL OF CANTILEVER BEAM IN CREEP-FATIGUE

To use the Buckingham Pi Theorem, the first step in the analysis is to list the variables and their dimensions as follows:

Table 21 Parameters involved in modeling.

	Symbol	Measured Quantity	Dimension
1	l	Characteristic Length	L
2	I	Moment of Inertia	L^4
3	ρ	Density	ML^{-3}
4	E	Modulus of Elasticity	$ML^{-1}T^{-2}$
5	t	Characteristic Time	T
6	ω	Characteristic Frequency	T^{-1}
7	σ	Stress	$ML^{-1}T^{-2}$
8	ϵ	Strain	-----
9	T	Temperature	θ
10	F	Force	MLT^{-2}
11	Δ	Elongation	L
12	δ	Deflection	L
13	α	Thermal Expansion Coefficient	θ^{-1}
14	M	Mass	M
15	a	Characteristic Acceleration of Vibration	LT^{-2}

The dimension matrix is

	l	M	I	ρ	E	t	ω	σ	ε	T	F	Δ	δ	α	a
L	1	0	4	-3	-1	0	0	-1	0	0	1	1	1	0	1
T	0	0	0	0	-2	1	-1	1	0	0	-2	0	0	0	-2
M	0	1	0	1	1	0	0	1	0	0	1	0	0	1	0
Θ	0	0	0	0	0	0	0	0	0	1	0	0	0	1	0

Consider now the determinant on the left side of the matrix:

$$\begin{vmatrix} 1 & 0 & 4 & -3 \\ 0 & 0 & 0 & 0 \\ 0 & 1 & 0 & 1 \\ 0 & 0 & 0 & 0 \end{vmatrix} = -1 \Rightarrow \text{Rank of the matrix} = 4$$

Since this is nonzero, it follows that the rank of the dimensional matrix is four and there are 11 dimensionless products required to describe this problem.

Number of parameters = 15 and number of Pi's = 15 - 4 = 11. In essence, dimensional analysis allows us to study the problem described by the functional relationship

$$f(l, M, I, \rho, E, t, \omega, \sigma, \varepsilon, T, F, \Delta, \delta, \alpha, a) = 0 \tag{5}$$

This functional can be expressed in terms of the primary quantities in the form

$$(L)^a (a)^b (M)^c (I)^d (\rho)^e (E)^f (t)^g (\omega)^h (\sigma)^i (\varepsilon)^j (T)^k (F)^l (\Delta)^m (\delta)^n (\alpha)^p = M^0 L^0 T^0 \Theta^0 \quad (6)$$

This can be expressed

$$(L)^a (LT^{-2})^b (M)^c (L^4)^d (ML^{-3})^e (ML^{-1}T^{-2})^f (T)^g (T^{-1})^h (ML^{-1}T)^i (\Theta)^k (MLT^{-2})^l (L)^m (L)^n (\Theta^{-1})^p = M^0 L^0 T^0 \Theta^0 \quad (7)$$

It can be rearranged in terms of the primary quantities and their exponents as

$$M^{(c+e+f+i+l+p)} L^{(a+b+4d-3e-f-i+l+m+n+2p)} T^{(-2b+2f-h+i-2l-3p)} \Theta^{(k-p)} = M^0 L^0 T^0 \Theta^0 \quad (8)$$

In order that the products be dimensionless, the exponents of the various basic dimensions must combine to give a zero value for each basic dimension. For instance for the exponent of M we should have $c + e + f + I + l + p = 0$, Thus we will have 11 Pi's.

$$\pi_1 = \frac{at^2}{L}, \pi_2 = \frac{Et^2}{\rho L^2}, \pi_3 = \frac{\sigma t^2}{\rho L^2}, \pi_4 = \frac{I}{\Delta \delta L^2}, \pi_5 = \frac{Ft^2}{\rho L^4}, \pi_6 = \frac{\delta}{L}, \pi_7 = \frac{\Delta}{L}, \pi_8 = \omega t, \pi_9 = \varepsilon, \pi_{10} = \frac{E}{\sigma},$$

$$\pi_{11} = \frac{\rho A \omega^2}{T \alpha E} \quad (9)$$

For complete similarity:

$$(\Pi_n)_{\text{Prototype}} = (\Pi_n)_{\text{Model}} \quad (10)$$

and the scale factor is:

$$\lambda_i = \frac{i^{\text{th}} \text{ quantity of Prototype}}{i^{\text{th}} \text{ quantity of Model}} \quad (11)$$

Since the gravity acceleration for model and prototype cannot be changed, the characteristic acceleration of prototype and model should be the same:

$$(a)_p = (a)_m \quad (12)$$

From Equation (9):

$$(1) \Rightarrow \Pi_1 = \left(\frac{at^2}{L}\right)_p = \left(\frac{at^2}{L}\right)_m \Rightarrow \lambda_t = \lambda_L^{1/2}$$

$$(2) \Rightarrow \Pi_2 = \left(\frac{Et^2}{\rho L^2}\right)_p = \left(\frac{Et^2}{\rho L^2}\right)_m \Rightarrow \lambda_E = \frac{\lambda_\rho \lambda_L^2}{\lambda_t^2} = \lambda_\rho \lambda_L$$

$$(3) \Rightarrow \Pi_3 = \left(\frac{Et^2}{\rho L^2}\right)_p = \left(\frac{\sigma t^2}{\rho L^2}\right)_m \Rightarrow \lambda_\sigma = \lambda_\rho \lambda_L$$

$$(4) \Rightarrow \Pi_4 = \left(\frac{I}{\Delta \delta L^2}\right)_p = \left(\frac{I}{\Delta \delta L^2}\right)_m \Rightarrow \lambda_I = (\lambda_L)^4$$

$$(5) \Rightarrow \Pi_5 = \left(\frac{Ft^2}{\rho L^4}\right)_p = \left(\frac{Ft^2}{\rho L^4}\right)_m \Rightarrow \lambda_F = \lambda_\rho (\lambda_L)^3$$

$$(6) \Rightarrow \Pi_6 = \left(\frac{\delta}{L}\right)_p = \left(\frac{\delta}{L}\right)_m \Rightarrow \lambda_\delta = \lambda_L$$

$$(7) \Rightarrow \Pi_7 = \left(\frac{\Delta}{L}\right)_p = \left(\frac{\Delta}{L}\right)_m \Rightarrow \lambda_\Delta = \lambda_L$$

$$(8) \Rightarrow \Pi_8 = (\omega t)_p = (\omega t)_m \Rightarrow \lambda_\omega = (\lambda_L)^{-1/2}$$

$$(9) \Rightarrow \Pi_9 = (\varepsilon)_p = (\varepsilon)_m \Rightarrow \lambda_\varepsilon = 1$$

$$(10) \Rightarrow \Pi_{10} = \left(\frac{E}{\sigma}\right)_p = \left(\frac{E}{\sigma}\right)_m \Rightarrow \lambda_E = \lambda_\sigma = \lambda_\rho \lambda_L$$

$$(11) \Rightarrow \Pi_{11} = \left(\frac{\rho A \omega^2}{T \alpha E}\right)_p = \left(\frac{\rho A \omega^2}{T \alpha E}\right)_m \Rightarrow \lambda_{\Delta T} \lambda_\alpha \lambda_E = \lambda_\rho \lambda_A \lambda_\omega^2 \Rightarrow \lambda_{\Delta T} = \frac{\lambda_\rho \lambda_A \lambda_\omega^2}{\lambda_\alpha \lambda_E}$$

$$\text{also we have } (\varepsilon_T)_p = (\varepsilon_T)_m \Rightarrow \lambda_{\Delta T} = \lambda_T = \lambda_k^{-1} = \frac{\lambda_\rho \lambda_A \lambda_\omega^2}{\lambda_\alpha \lambda_E} \quad (13)$$

Bibliography

- [1] S. Hansheng, W. Zhongtang, *Creep-Fatigue Behavior of Ni-Base Single Crystal Alloy DD3 and Its Life Prediction*, Acta Metallurgica Sinica (English Edition), Series A (1000-9442), Vol. 6A, No. 4, pp. 226-232, July 1993.
- [2] M. Masaaki, N. Akito, K. Kazuo, *Creep-Fatigue Strength of a Ni-Base Single Crystal Superalloy*, Japan Society of Materials Science, Journal, Vol. 39, pp. 723-729, June 1990.
- [3] R. S. Bellows, J.K. Tien, *Orientation Effects on the Creep-Fatigue Behavior of Single Crystal Ni₃Al (B,Hf)*, Scripta Metallurgica , Vol. 21, pp. 653-656, May 1987.
- [4] A. Pineau, *Fatigue and Creep-Fatigue Behavior of Ni-Base Superalloys- Microstructural and Environmental Effects*, High Technology, Vol. 15, pp. 135-154, 1996.
- [5] L. Gang, W. Zhong, G. Guo, J. Ting, *Relationship between Creep-Fatigue Interaction and Fracture Life of Ni₃Al (B) Alloy*, Scripta Metallurgica et Materialia (0956-716X), Vol. 31, No. 5, pp. 631-634, September 1994.
- [6] X. Xie, X. Sun, H. Jiang, J. Liang, R.M. Pelloux, *Effect on High Temperature Fatigue and Creep-Fatigue Behavior of Nickel-Base and Iron-Base Superalloys*, Chinese Journal of Metal Science and Technology, Vol. 6, pp. 1-7, February 1990.
- [7] M.R. Winstone, K.M. Nikbin, G.A. Webster, *Modes of Failure under Creep-Fatigue Loading of a Nickel-Based Superalloy*, Journal of Materials Science (ISSN 0022-2461), Vol. 20, pp. 2471-2476, July 1985.

- [8] J. He, Z. Duan, Y. Ning, D. Zhao, *Strain Energy Partitioning and its Application to GH33A Ni-Base Superalloy and 1Cr18Ni9Ti Stainless Steel*, Acta Metallurgica Sinica (ISSN 0412-1961), Vol. 21, pp. A54-A63, February 1985.
- [9] G. L. Chen, L.G. Fritzemeier, J.K. Tien, X. Xie, *Creep and Creep-Fatigue of a Nickel-Base Superalloy at Ambient Temperatures*, Metallurgical Transactions A – Physical Metallurgy and Materials Science, Vol. 13A, pp. 1951-1955, November 1982.
- [10] S. S. Manson, *Fatigue and Creep-Fatigue Deformation of Several Nickel-Base Superalloys at 650 °C*, Metallurgical Transactions A - Physical Metallurgy and Materials Science, Vol. 13A, pp. 1755-1765, October 1982.
- [11] H. L. Bernstein, *An Evaluation of Four Creep-Fatigue Models for a Nickel-Base Superalloy*, Low-Cycle Fatigue and Life Prediction (A83-13901 03-39) Philadelphia, PA, American Society for Testing and Materials, pp. 105-134, 1982.
- [12] T. Beck, K. H. Lang, G. Pitz, D. Lohe, *The Influence of Superimposed Creep Loadings on the Thermal- Mechanical Fatigue Behavior of the Ni-Base Superalloy in 792 cc.*, Mechanics of Time Dependent Materials, Vol.6, Issue 3, pp. 271-282, 2002.
- [13] J. Tong, S. Dalby, J. Byrne, M. B. Henderson, M. C. Hardy, *Creep, Fatigue and Oxidation in Crack Growth in Advanced Nickel Base Superalloys*, International Journal of Fatigue, Vol. 23, Issue 10, pp. 897-902, November 2001.
- [14] L. J. Chen, Z. G. Wang, G. Yao, J. F. Tian, *An assessment of Three Creep-Fatigue Life Prediction Methods for Ni-Based Superalloy GH4049*, Fatigue and Fracture of Engineering Materials and Structures, Vol. 23, Issue 6, pp. 509-519, June 2000.

- [15] K. Sadananda, P. Shahinian, *Hold-Time Effects on High Temperature Fatigue Crack Growth in Udimet 700*, Journal of Materials Science, Vol. 13, pp. 2347-2353, November 1978.
- [16] R. B. Bhat, *Natural Frequencies of Rectangular Plates Using Characteristic Orthogonal Polynomials in Rayleigh Ritz Method*. Journal of Sound and Vibration, Vol. 102, No. 4, pp. 493-499, 1985.
- [17] T. S. Chihara, *An Introduction to Orthogonal Polynomials*, Gordon and Breach, New York, 1978.
- [18] I. A. Stegun, and M. Abramowitz, *Handbook of Mathematical Functions*, Dover, New York, 1976.
- [19] C. S. Kim, *The Vibration of Beams and Plates Studied Using Orthogonal Polynomials*, Ph.D. Thesis, The University of Western Ontario, 1988.
- [20] M. M. Leven, *Experimental Mechanics*, Vol. 353, September 1973.
- [21] K. Kuwabara and A. Nitta, *Estimation of Thermal Fatigue Damage in Steam Turbine Rotors*, Report 277001, Central Research Institute for the Electric Power Industry (Japan), July 1977.